Multiphysics simulation of drug-coated balloon deployment and drug delivery

André Fensterseifer Schmidt

Submitted in fulfilment of the requirements for the
Degree of Doctor of Philosophy

James Watt School of Engineering
College of Science and Engineering
University of Glasgow

June 2024

Abstract

The treatment of ischaemic arterial disease has improved substantially in recent decades largely due to the inclusion of local delivery of anti-restenotic drugs in percutaneous intervention. To perform drug delivery without an implant, a drug-coated balloon (DCB) is inflated endovascularly for a one-time drug transfer from its coating to the target artery upon contact, serving as an alternative or complementary therapy to drug-eluting stents. While this therapy may avoid the potential complications of implants, namely in-stent restenosis and thrombosis, its greatest challenge is providing sufficient drug delivery and subsequent retention in the tissue without sustained release from a permanent drug reservoir. The mechanisms of drug delivery from DCBs are not completely understood, and the literature lacks models that describe the mechanics and drug release parts of the problem simultaneously. Aiming to improve this understanding, this work proposes modelling efforts towards an *in silico* simulation framework of simultaneous DCB deployment and drug delivery that studies procedural parameters such as inflation pressure, inflation duration, and drug loading and their effect on drug delivery performance.

First, the foundation for the modelling assumptions is set with a drug delivery problem considering an idealised 2D-axisymmetric multilayered arterial wall and a prescribed set of boundary conditions to represent the DCB's role. Then, a more realistic geometrical representation of a DCB is proposed based on the specifications of a DCB that has undergone clinical trials, along with the modelling of the inflation procedure and drug release from the coating. Ultimately, the two previous models are combined, culminating in a novel multiphysics simulation of DCB deployment that includes time-dependent structural mechanics, contact interaction, transmural filtration, and drug transport and retention simultaneously. All models are implemented in COMSOL Multiphysics® based on the finite element method. Results are assessed throughout the simulation of DCB deployment and 28-day follow-up, evaluating safety and efficacy indicators common to preclinical testing (drug content and receptor saturation) from the spatiotemporal drug distribution.

Although further studies and experimental data are still required to improve the model validation and achieve clinical utility, this work demonstrates the potential of *in silico* modelling as a powerful tool to complement traditional methods of medical device testing. The valuable mechanistic insights obtained can enhance the design process of DCBs and improve drug-delivery therapies, substantially reduce development costs, and expedite the technology.

Contents

"An absurd extravagance of energy"
—Sir Arthur Conan Doyle, *The Valley of Fear*

Chapter 1

Introduction

Engineering as a science relies deeply on the ability to mathematically represent physical processes. These creative representations, referred to as "models", come in different formats and degrees of abstraction, with their characteristics being intimately associated with the phenomenon of interest and the application at hand. In essence, "all models are wrong" as they are simplified and flawed representations of reality, "but some are useful". This aphorism, attributed to George E. P. Box in [1], acknowledges the importance of devising simple, pragmatic, yet representative models. While inherently limited, models can have remarkably useful applications. Mathematical models are particularly useful in scenarios where real-world experimentation is inconvenient or prohibitively difficult e.g. due to financial or ethical reasons.

Biomedical Engineering especially benefits from modelling, since the design process of its technological solutions is both costly and potentially life-threatening. New technologies in this field go through the progressive stages of preclinical and clinical testing. Typically, preclinical testing employs the traditional *in vivo*, *ex vivo*, and *in vitro* techniques, conducted on models that are living animals, tissue excised from their usual biological surroundings, and isolated microorganisms or cells, respectively, before moving into humans. Meanwhile, "*in silico*" is a pseudo-Latin term for a computational environment, where virtual simulations of mathematical models can be carried out. *In silico* models can provide insights into understanding the performance and enhancing the design of medical devices, as an emerging alternative to trial-and-error practices and hypothesis testing, from the safety and convenience of a computational simulation. This is crucial, as it can (I) expedite the development of new life-saving techniques, (II) minimise premature clinical testing involving human lives, and (III) reduce costs substantially, considering that every experiment and device iteration has an associated cost. Therefore, this work is motivated by the potential of *in silico* modelling to reduce and refine the process of medical device development.

1.1 The clinical problem and the evolution of the technology

Ischaemic heart disease is the primary cause of death worldwide, accounting for about 9 million deaths globally in 2019, according to the World Health Organization [2]. The most common type of this condition is when a coronary artery — a small blood vessel located around the heart and responsible for its irrigation — becomes dangerously narrowed due to fatty plaque build-up (atherosclerosis), leading to insufficient blood supply and ultimately to cardiac death.

Accordingly, one of the most common medical procedures worldwide is a particular treatment of coronary artery disease, called percutaneous coronary intervention (PCI) [3]. It is an endovascular procedure. That is, the artery disease is reached from the inside of the vessel. In the last fifty years, remarkable progress has been made in endovascular treatment techniques. The historical progress of the technology of endovascular intervention has been extensively described in the literature [3–9]. Notably, the evolution of the technology overlaps the clinical problem, since the progressive introduction of treatment modalities provoked new iatrogenic complications — which, in turn, demanded further innovative solutions. A chronological summary is provided for contextualisation, culminating in an implantless treatment alternative for endovascular drug delivery.

Balloon angioplasty

Since 1977, when the advent of minimally invasive procedures revolutionised the treatment of cardiovascular diseases [5], a substantial and continuous evolution has taken place in the field of interventional cardiology and medical devices technology [10]. At first, the main way to promote the widening of a narrowed artery (revascularisation) was to insert a flexible wire-like device (catheter) through a small incision in the patient, navigate it via the circulatory system, and inflate a balloon at the site of the abnormal narrowing (stenosis). This repair, known as balloon angioplasty (from Greek "*angio*", vessel; and "*plastos*", moulded), would diminish the lipidic blockage and restore the proper size of the channel (lumen) for blood to flow.

However, it was observed that the balloon procedure was followed by acute elastic recoil of the newly widened artery, compromising more than 10% of the vessel lumen [11]. Moreover, the commonly provoked barotrauma resulted in exuberant growth and migration of smooth muscle cells towards the arterial lumen, forming a new layer of tissue (neointimal hyperplasia). The recurrence of luminal narrowing greater than 50%, defined as the phenomenon of restenosis, shortened the effectiveness of this solution and in many cases demanded repeated revascularisation procedures on the same target lesion [12]. These two issues — acute recoil and restenosis — proved a major drawback of this minimally invasive treatment modality and stimulated the pursuit and discovery of novel technologies and techniques.

Bare-metal stents

The stenting technique, introduced in 1986, consisted of the implantation of an intravascular metallic scaffold to provide mechanical support to the artery post-balloon dilatation (Figure 1.1). This tubular device, named "stent", is delivered through the same minimally invasive procedure using a catheter. The stent concept was perceived at that time as the specific solution for the problem of acute vessel occlusion, successfully reducing the frequency and the severity of restenosis [13].

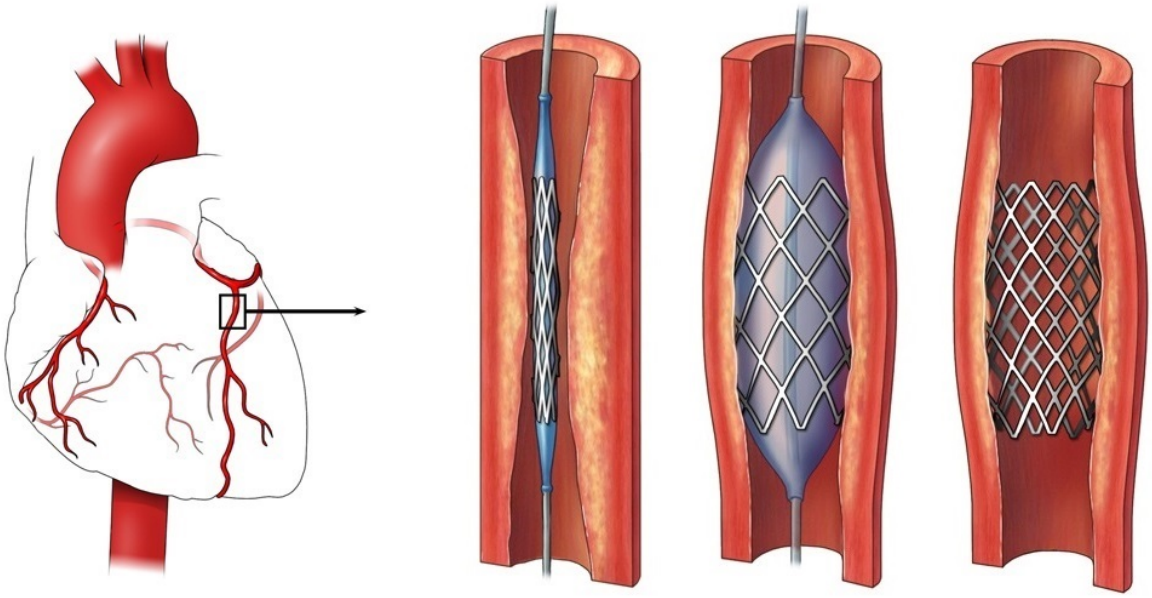

Figure 1.1: Schematic illustration of a typical percutaneous coronary intervention: catheter insertion into a narrowed coronary artery, then balloon dilatation followed by stent deployment. Adapted from [14].

Like most novel technologies, the first iterations of stents were flawed and unaware of complex outcomes. Above all, the severe vascular trauma caused by stent deployment often triggered an excessive healing and immunological response, and the presence of a foreign body, metallic and uncovered, configured an environment highly susceptible to platelet aggregation and clot formation (thrombogenic) [5]. Although stenting is a “minimally invasive” technique, this refers to the method of percutaneous introduction of the devices; these, however, remain considerably invasive to the vessel targeted for treatment [4]. To mitigate the risk of thrombosis after having a stent, dual antiplatelet therapy (DAPT) was administered. DAPT is the regular use of a concoction of medication to control platelet behaviour, inhibiting platelet aggregation and clot formation. However, since platelets are responsible for counteracting bleeding, this temporary platelet debilitation dramatically increases the severity of potential bleeding events. Moreover, while on DAPT the patient is rendered unsuitable for undergoing surgical operations. Although effective, reliance on DAPT posed considerable risks for the patient and often created a lengthy, even lifelong, dependency in fear of late stent thrombosis.

Stenting also created a new medical-induced disease: in-stent restenosis (ISR). As a result of deployment damage, neointimal hyperplasia continuously re-narrowed the lumen and restricted blood flow inside the stent. Thus, reverting the beneficial state achieved with the interventional procedure. Nevertheless, the adoption of stents in the field of angioplasty has been considered an advance [3].

Solving the initial stenosis of the vessel via implantation of a stent proved more challenging. The complex cascade of biological events triggering restenosis is out of the scope of this work. A detailed discussion on this subject is provided in [15]. The anticipated rate of repeat revascularisation procedures as 30–50% was deemed unacceptable, and a solution was urged [16]. Reasonably, the technology advanced to tackle this problem.

Drug-eluting stents

The main leap in stent technology happened in 1999 when the inclusion of drugs to be eluted from the stent surface drastically inhibited the body's inflammatory response and neointimal hyperplasia after stenting [17]. The addition of this functionality, initially through the use of a polymeric coating embedded with antiproliferative drugs, set the stage for a new generation of devices named drug-eluting stents (DESs).

Precursor DESs CYPHER (Cordis) and TAXUS (Boston Scientific) represented the first generation of this technology in the early 2000s with considerable success [7, 18]. The anti-restenotic drugs, mainly sirolimus and paclitaxel, were incorporated within the stent platform and programmed to be released slowly over a few weeks after deployment. This addressed the important issue of the disproportional inflammatory response and exuberant cell proliferation after stent implantation, decreasing the body's initial rejection of the foreign implanted device and the long-term re-narrowing of the vessel. With time, further technological development has allowed the use of more biocompatible materials for stents and better-designed stent struts and manufacturing processes, incrementally improving their clinical performance. Stainless steel was replaced by titanium and cobalt-based alloys, and the decrease in strut size was shown to be a tendency [19]. The stent problem became divisible into several parts: structural scaffold (backbone), drug vehicle (coating) and drug elution (therapeutics release). Remarkably, stent design grew in complexity, having now the need to understand and control the entwined events of drug release and polymer behaviour [20]. Controlled drug release became a critical part of DES design to meet the requirements of delivering the drug at an adequate rate and magnitude to avoid both toxicity and ineffectiveness [21]. Initially, durable polymer coatings were used to carry the drug in the DES but were found to provoke inflammatory responses and delay healing. The technology then moved onto degradable polymer or even polymer-free coatings, largely eliminating these complications [3]. With the advent of second-generation DESs, the technology became more mature and rapidly established the standard for the treatment of coronary artery disease. Newer stents, such as XIENCE (Abbott) and SYNERGY (Boston Scientific), became

great examples of problem-solving through technological innovation. Compared with bare-metal stents, DESs consistently lowered the occurrence of restenosis from about 30% to less than 10% [3]. Recent studies report the ISR rate of modern DESs as 1–2% [22]. But, despite the many improvements, ISR and late stent thrombosis have not been eliminated and remain an unsolved problem affecting hundreds of thousands of patients annually, especially for complex disease [22, 23].

A remarkable initiative to eliminate long-term exposure to polymers in the vascular environment is the design of polymer-free stents. For example, BioFreedom (Biosensors) is a pharmacological stent with drugs embedded in its abluminal microstructured surface [24]. The absence of polymer allows an exceptionally short DAPT duration (one month), decreasing delayed reendothelialisation and the likeliness of potential bleeding events. Consequently, the enhancement of post-implantation healing speed dramatically improved the outcome of the treatment of diabetic or high-risk-of-bleeding patients [25].

The long-term issues associated with the permanence of a permanent implant led the technology to attempt an ambitious concept — a stent that completely disappears after the lesion is treated.

Bioresorbable stents

A bold innovative step in stent evolution has been the design of bioresorbable stents (also known as "absorbable stents" or “bioresorbable vascular scaffolds”) as an alternative to permanent stents. These stents are programmed to dissolve and completely disappear from the blood vessel after the disease is treated. Ideally, this type of temporary implant would provide the early scaffolding benefits of stenting while avoiding its potential long-term complications, overcoming the irreversible aspect of the procedure. This technological pursuit is particularly important, given the potential benefits to the patient of a stent that disappears: decrease of late adverse events such as ISR and late stent thrombosis, compatibility with computed tomography and magnetic resonance imaging, paediatric use on growing arteries, reduced disturbance of blood flow, shorter dependence on antiplatelet therapy, potential of future unimpeded revascularisation procedures, and restoration of endothelial function and vasomotion [5, 26–28]. Although potentially promising and relevant, this technology still has some way to go before being widely accepted in clinical practice. A major challenge is that the structural scaffold made of degradable polymer or metallic alloy must balance several design properties, such as programmed degradation, decomposition by-products, controlled drug release, deliverability, biocompatibility, radial strength, conformability, drug-eluting capacity, radiopacity, etc. [3, 29]. The technical feasibility of bioresorbable stents is out of the scope of the present work; nonetheless, it brings attention to implantless alternatives of endovascular therapy.

Lesion preparation

Beyond implanting medical devices, considering the disease of the artery segment to be treated, referred to as the "lesion", is critical for the outcome of the interventional procedure [30]. Its condition is often severe, including fatty and calcified plaque deposits. For brevity, lesion preparation is the process of clearing the lesion site endovascularly. It is an interventional strategy aimed at facilitating the operation of a medical device and improving its outcome. In general, lesion preparation pre-dilates the stenosed artery via plain balloon angioplasty and removes the bulk of the plaque burden (atherectomy). A plethora of minimally invasive techniques is available for clearing the lesion. For instance, standard semi-compliant balloons, specialty balloons (scoring, cutting, non-compliant), atheroablation, and lithotripsy [22, 23]. Intravascular ultrasound (IVUS) provides a means of scanning the interior of the lesion to guide the procedure.

The urge for lesion preparation was motivated, to some extent, by the problem of ISR. When a stented lesion undergoes repeated revascularisation, therapeutic strategies are contemplated. Deploying a second stent overlapping the first stent has been common practice. However, multiple metallic stent layers are associated with a progressively higher risk of recurrent ISR, and thus must be avoided [22]. This indicates a finite number of irreversible interventional procedures in a given lesion. As ultimately suggested by Shlofmitz et al. [23], the best way to address ISR in DESs is to prevent it.

Therapeutic guidelines are suggested depending on the outcome of lesion preparation [30]. The decision of whether to implant a stent or not in a new coronary lesion, treated for the first time (*de novo*), precedes a quantitative evaluation based on residual restenosis and flow limitation. "Suboptimal" lesion preparation is characterised by angiographic results with residual stenosis $> 30\%$ of lumen area and fractional flow reserve ≤ 0.80. This outcome leads to the implantation of a stent, even called a "stent bail-out" because of the dire circumstances. Otherwise, if "optimal" lesion preparation is achieved, it is recommended that no stent is used. Notwithstanding, a dose of an antiproliferative drug is still desired to suppress the neointimal hyperplasia induced by the interventional procedure. The technology has advanced to provide an implantless modality of endovascular drug delivery. After all, the avoidance of long-term complications of implants — permanent or transient — may be accomplished by not having an implant at all.

Recapitulating, several treatment strategies have been developed over the years, ranging from balloon angioplasty to the placement of therapeutic vascular scaffolds, with each procedure having its own set of limitations. Despite significant advances, several severe complications still affect this procedure performed millions of times worldwide each year, particularly the re-narrowing of the artery (restenosis) and clot formation (thrombosis) [6, 22, 31]. While the former may often be treated with further revascularisation procedures, the latter is potentially fatal without warning. This provides sufficient motivation to investigate the development of alternative treatment strategies.

Drug-coated balloons

The last technology presented in this Chapter is an alternative to deliver drugs to arteries without an implant and will be the focus of the subsequent modelling endeavours.

A drug-coated balloon (DCB) is a minimally invasive medical device designed to provide a one-time localised delivery of anti-restenotic drugs to the arterial wall on contact. The DCB is homologous to the angioplasty balloon, as it is a balloon of polymeric material designed to be inflated endovascularly. However, as the name implies, the DCB is coated with a drug formulation. The function of the DCB is solely drug delivery, instead of mechanical dilation to restore vessel patency as with the plain angioplasty balloon. Figure 1.2 illustrates the principle of the DCB. Once the lesion site is accessed via percutaneous procedure, the device is inflated for about one minute to transfer the drug from its coating to the target artery segment on contact. After that short time window, the balloon is deflated, and the balloon catheter is withdrawn from the body. Ultimately, only the drug delivered remains in the treated artery.

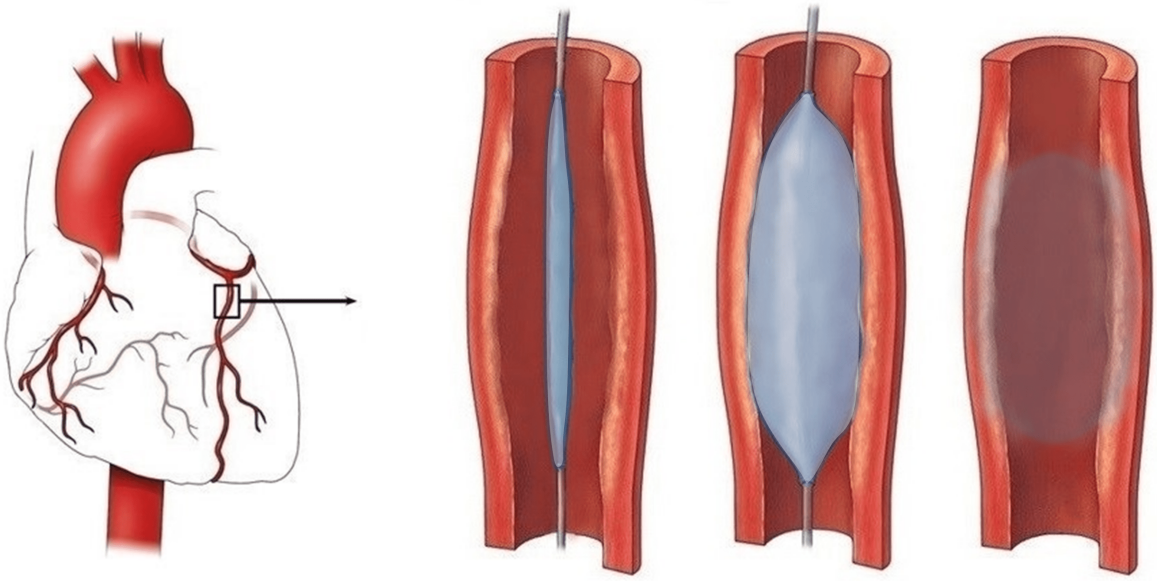

Figure 1.2: Schematic illustration of endovascular DCB deployment and localised drug delivery in a coronary artery, followed by drug retention in the arterial wall. Notably, the vessel depicted was already patent due to lesion preparation before the drug delivery. Adapted from [14].

These devices are routinely used as an alternative strategy to treat arterial disease when localised drug delivery is desired but without a permanent implant [32]. For example, in the treatment of delicate and complex geometries such as small vessels (of lumen diameter < 3.0 mm) and bifurcation lesions, where stenting is particularly challenging [30]. While this technology might avoid long-term complications associated with stents, it lacks the mechanical support and sustained drug release from permanent implants. The short contact duration between the DCB and the artery must be sufficient to transfer the required drug dose — which, once delivered, must be retained for weeks within the arterial wall for its therapeutic purpose [33, 34].

Therefore, there are challenges to understanding the mechanisms governing drug delivery from the device and the subsequent pharmacokinetics in the arterial tissue.

The DCB was initially conceived for use in peripheral arteries, where stent implantation led to poor outcomes due to severe and varied biomechanical stresses [35]. There, it served as a complement to the technique of plain angioplasty. Pioneer studies worked towards providing preliminary evidence of a clinical benefit of DCB for coronary artery use [36]. Then, its usefulness became also evident in the pharmacological treatment of already stented vessels troubled with ISR [37]. Its main advantage was the ability to provide favourable results without repeated implantation adding a new stent layer [38]. Since then, the efficacy and safety of DCBs for *de novo* lesions have also been proved [39, 40]. Currently, DCBs are an established treatment modality for remediating recurring ISR and some types of *de novo* lesions [22]. The possibility of DCB-only intervention is promising in the field of PCI.

In the beginning, the first DCBs preferred lipophilic drugs, such as paclitaxel, due to their relative ease of delivery and retention in the vessel wall. As the technology developed, sirolimus and its analogues (the "-limus" drugs) have been introduced to DCBs, based on the evidence that the drug has a better efficacy-safety profile than paclitaxel and also following the trend of DESs, in which sirolimus is the default pharmacotherapy [30, 41]. The choice of drug was enabled, to a great extent, by the development of supporting substances (under the names of excipient, binder, carrier, or matrix) and also improved balloon techniques (such as folding and pleating), which tackled the problem of DCBs losing a considerable part of their drug loading en route to the lesion site [42]. Due to the cytostatic mechanism of -limus drugs, they necessitate longer persistence in tissue [43] and every greater technical effort is required to deliver and sustain it in the arterial wall of the treated lesion.

DCBs offer important opportunities for safer, simplified, and repeatable treatments. Due to the absence of implantation with a DCB-only procedure, the intervention provokes less arterial disturbance and has a relatively low biological impact [38]. The vascular trauma caused by the balloon procedure is less severe, thus not critically damaging the endothelium and triggering the excessive healing and immunological response often observed post-stent deployment. Moreover, the lack of persisting inflammatory stimuli and foreign structure considerably reduces the risk of thrombosis and hence the length of DAPT required, greatly favouring patients at high bleeding risk [30]. The sole use of a DCB over a stent has the advantage of allowing the vessel to remodel in the future, as blood flow is undisturbed and vasomotion is unrestricted [44]. All these aspects contribute towards the indicators of complete vascular healing and reducing adverse events. The use of DCBs as an alternative to stents in several cases is motivated by some technological and therapeutic limitations of stents, such as poor outcome in small vessel disease, the possibility of incomplete apposition, long duration of DAPT (with an increase in both thrombotic and haemorrhagic risk), treatment failure leading to ISR and late stent thrombosis, and multiple stent layering when treating ISR resulting in excessive stiffening and threat

of injury to the ends of the vessel [38].

According to a recent report of the International DCB Consensus Group, every PCI should aim at using the DCB-only strategy [30]. Notably, lesion preparation has been essential for doing so [38, 39, 45]. Depending on its outcome, the decision is made on whether to use a DCB or stent. When lesion preparation is deemed satisfactory, a balloon is enough to solve the stenosis; otherwise, a stent should be placed. Reference interventional cardiologists estimated that in 70% of the time a sole DCB should be enough, and in 30% a stent would be necessary [44]. In summary, the DCB is a situational and selective technology and should be used accordingly. That is, it is a complementary tool expected to be employed in indications where DES have limitations. While there are factors favouring each of the therapies, having alternatives that cover a wider range of clinical conditions is highly valuable.

To obtain the certification of the Conformité Européenne (CE) or U.S. Food and Drug Administration (FDA), devices are progressively tested and compared in preclinical, then clinical non-inferiority and superiority comparisons with existing, more established, techniques. Most commercially available DCBs have only the CE mark, treat ISR or small vessel disease, and feature paclitaxel as the therapeutic agent [30]. Initially, there was only solid evidence of the superiority of DCB for the treatment of ISR and small vessel disease. New trials are shedding light on the efficacy and safety of DCBs and there is growing evidence that a variety of clinical situations, including *de novo* lesions, may benefit from a DCB-only approach [46, 47].

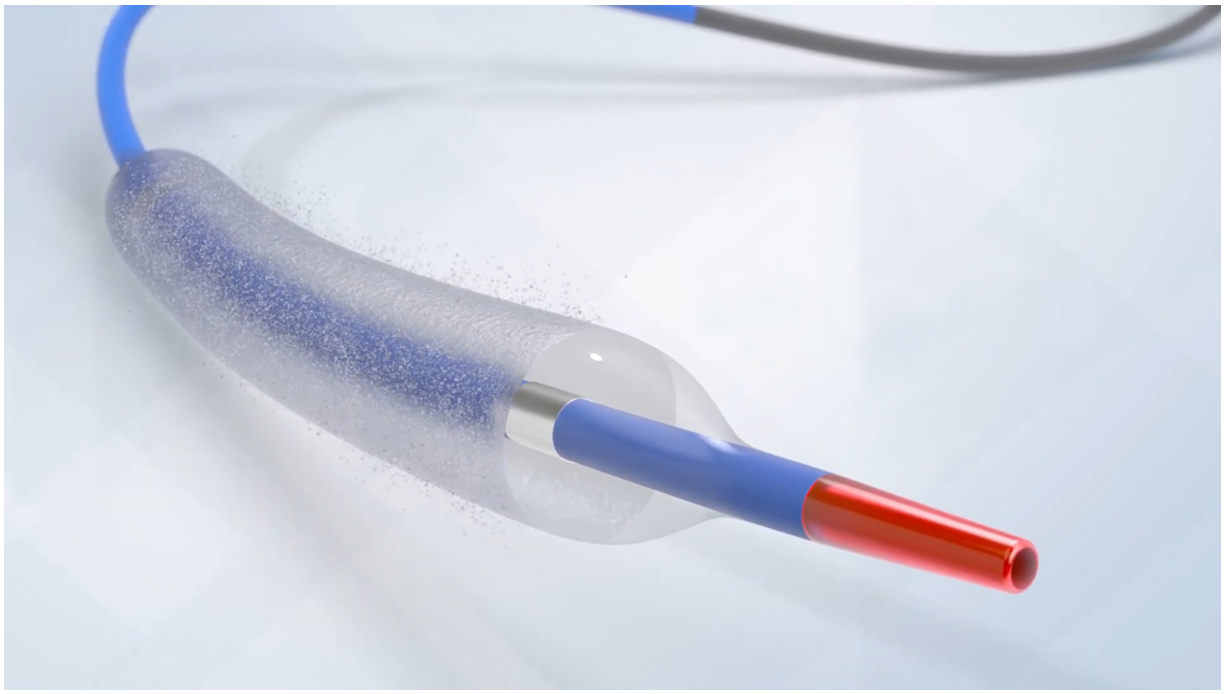

Figure 1.3: Illustration of the AGENT™ Drug-Coated Balloon (Boston Scientific). It is the first FDA-approved DCB for endovascular therapy of coronary artery disease. Adapted from [48].

Recently, on the 1st of March 2024, the first DCB was approved for use in coronary artery disease in the USA [49]. A series of randomised trials provided the required clinical evidence to

convince both the FDA and the clinical community of the utility of DCBs in coronary application [50].

The DCB is a pharmacotherapy technology of increasing importance [51]. Its early challenges are being overcome and improvements in DCBs are synergistic with advances in imaging, lesion preparation, pharmacology, excipients, and balloon design [44, 52]. Drug delivery from DCBs notably needs to be different than from DESs — and there is still a critical need to improve the understanding of the underlying factors and pharmacokinetics governing the efficacy and safety of DCBs [53]. This provides the motivation for the study and use of mathematical modelling and computational simulation approaches to complement the current *in vitro* and *in vivo* experimentation, which are still useful and indispensable but may lack mechanistic understanding and lead to inefficient design development.

Specifically, this thesis aims to understand how the procedural and design parameters of the DCB, e.g. inflation pressure, inflation duration, and drug load, may influence the performance of drug delivery during the short time window of deployment and the subsequent long-term retention in the arterial tissue. The modelling literature of endovascular drug delivery is presented progressively in Chapter 2. Currently, the computational literature lacks models capable of depicting the inherently simultaneous aspects of the DCB problem — inflation-induced deformation and drug delivery upon contact. To address this knowledge gap, the sequential objectives of the work are to develop *in silico* models of endovascular drug delivery in an arterial wall, the DCB device and its inflation procedure, and the combination of the previous models to describe the DCB deployment procedure and drug delivery in a novel simultaneous fashion. The potential impact of the work will be elaborated throughout the forthcoming Chapters. Concisely, it is to improve the mechanistic understanding of DCBs and thus allow more informed decisions on the development of this technology.

1.2 Outline of Thesis

This Thesis is structured in the following sequence of Chapters:

Chapter 1 introduced the context of modelling and endovascular medical device technology. Chapter 2 exemplifies existing modelling approaches for endovascular drug delivery devices and unmet needs. Chapter 3 presents the arterial wall model devised, as an idealised artery segment subjected to a prescribed drug influx. Chapter 4 presents the DCB model devised, utilising a drug release test performed in the industry for parameter calibration and preliminary validation. Chapter 5 combines the models from the previous Chapters to represent DCB deployment into an arterial wall. Structural and contact mechanics are added to the artery model. The notable multiphysics model devised involves the simultaneous simulation of deformation, contact, drug transfer, and subsequent drug transport and retention in tissue. Chapter 6 provides concluding remarks.

Chapter 2

In silico modelling of endovascular drug delivery

This Chapter aims to provide an overview of the relevant modelling works that provided the foundation for this Thesis, instead of an exhaustive review of the literature.

2.1 A historical perspective

Studies of endovascular drug delivery date back to 1990, when Edelman, Adams, and Karnovsky [54] considered the delivery of heparin as a prospective means to suppress smooth muscle cell proliferation in endothelial injury in rats. Initial attempts with heparin were frustrated in terms of clinical success — but built much of the theoretical foundation for the future of the technology, particularly for paclitaxel and sirolimus and its analogues. The advances in the field of controlled-release technologies depend on the mechanistic understanding of drug transport and retention properties in the tissue, i.e. pharmacokinetics. Before endovascular drug delivery was a consolidated clinical technique, early experimental works illuminated the principles and mechanisms of pharmacokinetics. In particular, Creel, Lovich, and Edelman [55] appreciated the effect of reversible drug binding competing with the forward motion of transmural advection, due to the physiological pressure gradient across the arterial wall, and the simultaneous diffusive transport. Therefore, drug mobility via diffusion and advection is resumed only after dissociation from binding sites. This provided a remarkably vivid description of the multifaceted mechanisms of drug transport and retention in tissue, which later became increasingly implemented as numerical models in *in silico* form. Still, vascular pharmacokinetics studies generally consisted of harvesting arteries at sequential times for quantifying the total drug deposition, greatly limiting their possible insights.

Models of endovascular drug delivery have been proposed ever since with varied complexity [7, 56]. According to McGinty et al. [21], simpler mathematical models could have analytical solutions and provide useful insights into drug release from devices and penetration in the tis-

sue. However, more sophisticated models may ultimately be required to characterise complex situations. Concerning model geometry, for instance, the simplest unidimensional (1D) models can represent a unidimensional path of drug concentration through the arterial wall; two-dimensional (2D) can represent a cross-section of an artery; 2D-axisymmetric can represent a cylindrical, idealised vessel; and three-dimensional (3D) can represent complex geometries with great detail and inhomogeneity. Likewise, drug transport mechanisms can be modelled with varied complexity.

In the precursor computational modelling study, in 1996, Lovich and Edelman [57] considered a 1D diffusion-only problem to represent the transport of heparin radially through an arterial wall, in the context of treating coronary artery disease. Results strongly suggested that hydrophilic drugs require a form of sustained release to maintain therapeutic levels in tissue and are unfeasible for single-dose localised delivery, such as from a drug-coated balloon (DCB). Also, the discussion provided in this work demonstrates the valuable advantages of augmenting experiments with simulation, allowing for mechanistic interpretation with spatial resolution and sparing a "tremendous" number of costly animal experiments.

In silico modelling efforts have been prolific in parallel to the clinical progress, considering that the first experience of drug-eluting stent (DES) implantation in human coronary arteries dates from 1999, as reported in Sousa et al. [17]. Notably, initial modelling efforts have been almost exclusively for DESs, since this technology has been *en vogue* since its adoption prior to DCBs. Although DES models are not the focus of the present work, they built the foundation for its modelling assumptions and thus deserve mentioning.

A subsequent modelling example from 2001, Hwang, Wu, and Edelman [58], considered a 2D cross-sectional artery ring, representing the transport of paclitaxel via a diffusion-advection equation. Here, the "physiological transport forces" causing transmural filtration were regarded with the advective term in the governing equation of drug transport. Drug release from a stent was modelled as a simplified drug flux, spatially distributed to represent the stent strut disposition over the endothelial interface. The geometrical structure of the stent was not depicted in the model.

The theoretical foundation for pharmacokinetics was developed over the years. Initially, Levin et al. [59] provided an in-depth investigation of how the antiproliferative drugs sirolimus and paclitaxel interact with the arterial tissue. Then, Zunino [60] proposed a simplified binding behaviour derived from the drug availability in tissue (constant equilibrium), on a 2D diffusion-advection model. Later, in 2009 Tzafriri, Levin, and Edelman [61] described drug binding to cell receptors in more detail, including a non-linear, saturable, and reversible reaction term in the governing equation of drug distribution. This study provided several pertinent conclusions, drawn from the modelling simplicity of a 1D diffusion-reaction problem. First, it concluded that saturable binding must be accounted for to capture the distribution behaviour of sirolimus and paclitaxel. Since then, there has been a modelling distinction between drug phases — free

and bound. The form of the reaction term that denotes the binding rate, i.e. the transformation between phases, varied in the literature [7]. Second, it related the penetration and retention success of drug types (namely sirolimus and paclitaxel over heparin) to their pharmacological parameters. Third, it acknowledged the promising endovascular drug delivery modality of the DCB but warned of the absence of a clear mechanistic understanding of its pharmacokinetics. The DCB delivers a large drug dose over a short time, which is referred to as a "bolus infusion". After the modelling insights obtained on drug binding, it became evident that a bolus infusion may rapidly saturate the target receptors — and the drug excess may be washed away in free phase. This question illustrates a main challenge in the design of controlled drug release.

Increasing sophistication, in 2014 Bozsak et al. [62] employed 2D-axisymmetry to represent the cylindrical features of the arterial wall as a straight tubular geometry, depicting the intima and media layers. An idealised stent was included in this model, half-embedded in the artery, as a series of equally-spaced round struts (resembling disconnected rings in a 2D-axisymmetric perspective). In the interest of drug delivery, these struts were surrounded by a domain to represent a non-erodible drug-embedded coating. The coating and adjacent artery were connected via continuity of concentration, permitting a continuous diffusive drug flow between domains. This modelling work featured diffusion-advection-reaction equations, considering a single mode of drug binding in the reaction term.

Building upon the latter, in 2020 Escuer et al. [63] represented DES deployment on a 2D-axisymmetric multilayered arterial wall, depicting the intima, media, and adventitia. Drug transport followed diffusion-advection-reaction equations and the process of drug binding was implemented as two separate phases, to account for drug binding to both cellular and non-cellular receptors in the tissue e.g. extracellular matrix and interstitial tissue, as recommended in Tzafriri et al. [64] and McGinty and Pontrelli [65]. Remarkably, their model incorporated a sophisticated description of arterial structural mechanics, defined on a layer-specific basis. Simplified steady-state fluid dynamics of blood in the lumen (haemodynamics) were also included. Although not simultaneously, multiple physics were included in this model, where the stationary simulations of deformation, fluid dynamics, and transmural filtration precede a time-dependent simulation of drug transport.

2.2 Existing approaches for drug-coated balloons

The aforementioned examples illustrated a progressive advance in modelling complexity for the relevant physics of interest: drug transport and retention, transmural filtration, and structural mechanics.

It is noticeable throughout the modelling literature of endovascular drug delivery that, regardless of the simulated scenario e.g. bolus release or sustained reservoir, similar governing equations have been used to describe the drug distribution in the arterial tissue, only by adapting drug-specific parameters and boundary conditions. Early studies [55, 57, 61], emphasised that the principles and mechanisms of drug transport and retention — pharmacokinetics — are defined as individual physicochemical properties of the combination of a given therapeutic compound and tissue. These assumptions have been considered adequate for modelling the arterial distribution of small hydrophobic drugs e.g. paclitaxel and rapamycin once delivered to the target arterial tissue by a device, and should apply to other similar therapeutic compounds and local drug delivery systems. Therefore, this motivates the same pharmacokinetics principles used for DESs to be considered for modelling DCBs, namely drug distribution calculated via diffusion-advection-reaction equations, considering the mode of release and tissue penetration and distribution as distinct parts of the problem. Next, the focus is on the existing modelling approaches for DCB.

Kolachalama et al. [66] examined the pharmacokinetics of zotarolimus, aiming to improve the understanding of the mechanisms of tissue uptake and retention after delivery via DCB. This study combined animal studies, bench-top experiments, and computational modelling — the full trio. This permitted the estimation of important parameters for characterising the model e.g. diffusion coefficients and binding rates. Drug release kinetics were measured by inflating balloons in a solution medium (whole blood), then translating the results to time-dependent exponential expressions of drug mass released per balloon surface area, and flux, obtained from its derivative:

$$\begin{cases} M_{\mathrm{b}}(t) \;= A\left(1 - e^{-k\,t}\right) \\ \\ J_{\mathrm{b}}(t) \;= \dfrac{1}{\mathrm{M_M}} \dfrac{dM_{\mathrm{b}}(t)}{dt} = \dfrac{k\,A}{\mathrm{M_M}}\, e^{-k\,t} \end{cases} \tag{2.2.1}$$

where A and k were empirically estimated via exponential curve fitting, and $\mathrm{M_M}$ is the molar mass of the drug.

The drug flux derived empirically was exported to the *in silico* model and applied as a boundary condition to the inner surface of a homogeneous 2D ring representing an artery. The application time was intended to match the delivery duration of a DCB. Afterwards, the boundary condition was replaced by either a zero-flux or a perfect sink condition, to observe the effect of luminal drug wash-off. This work revealed key insights into bolus release behaviour. One was

that the magnitude of drug uptake depends on the duration of delivery, i.e. the time the DCB stays in contact with the vessel. Another was that subsequent drug transport and retention in tissue depend on diffusion and binding parameters, respectively. The zero-flux condition showed better results, supporting the argument that coating adhering to the wall surface may act as a shield against luminal drug wash-off. However, caution must be taken on this evidence since pressure gradients, transmural filtration, and multiple artery layers were absent in the model and should influence this behaviour. Finally, an efficient DCB therapy was deemed bound by (I) a need for delivering a large amount of drug within a short period and (II) the nature of drug binding in tissue.

Similarly, Anbalakan et al. [67] modelled DCB drug delivery in an idealised 2D artery using a prescribed flux according to an exponential function. The drug release behaviour was measured experimentally using a different sirolimus-coated balloon inflated and in a much harsher solution medium (acetonitrile). Besides the temporary drug flux, a temporary increase of transmural pressure during DCB application was proposed. While the artery was assumed rigid in this model, i.e. structural mechanics were absent, this increase should affect transmural filtration. The effect of different disease types hindering both diffusive and advective drug transport was also probed.

Tzafriri et al. [68] asserted the modelling principles for DCB delivery and persistence in the tissue, including the mechanism of coating adhesion. Patches of drug adhered to the artery during DCB application should experience dissolution, of declining magnitude over time, via diffusion then penetrate the arterial wall according to the usual mechanisms. Despite consistent simulation results, using a 1D model, the behaviour of coating adhesion was still insufficiently understood. Much of the existing knowledge was based on DESs, which is not synonymous with DCBs. As DCBs inherently lack sustained release from a permanent reservoir, understanding the drug transfer from the coating is crucial for perceiving the requirements for adequate drug levels throughout the therapeutic window.

The DCB drug transfer mechanisms were investigated deeper in Tzafriri et al. [69], by assessing the role of contact stress during balloon angioplasty *in silico* using a 2D-axisymmetric balloon and artery model. The balloon geometry mimicked a commercial device and the arterial tissue was represented as an idealised single-layer tube. Despite not calculating the spatiotemporal distribution of drug over the model geometries, the contact pressure along the balloon-tissue interface was correlated with surface drug deposition maps from animal studies, partly for investigating the behaviour of coating adhesion. The balloon deformation was described phenomenologically using a hyperelastic Arruda-Boyce material model. The contact mechanics between the pair and the artery material model (third-order Mooney Rivlin) were derived from Shukla et al. [70].

Modelling studies became increasingly interested in the contact interaction between the DCB and the arterial wall. More recently, Stratakos et al. [71] investigated balloon contact pressure

in great detail with a complex 3D DCB geometry featuring a complete folding and unfolding procedure. The focus was on structural mechanics; the drug delivery part of the problem was left untouched. As mentioned in this study, several balloon inflation and deployment models of increasing complexity have been developed over the years, but largely in the context of plain angioplasty or stent deployment.

Escuer, Fensterseifer Schmidt, et al. [72] provided a comprehensive *in silico* comparison between DCBs and DESs, in a 2D-axisymmetric multilayered arterial wall with layer-specific properties. This work highlighted the key differences in drug release profiles between the modalities and how that may affect the therapeutic indicators of safety and efficacy. The cases differed in terms of drug source: a domain with an initial drug concentration for the DES model versus a temporary boundary condition of drug influx for the DCB. In both cases, drug transport and retention in the tissue were governed by diffusion-advection-reaction equations, featuring nonlinear, reversible, and saturable binding. Different drug flux expressions and delivery durations were probed, based on the empirical expressions from [66] and Anbalakan et al. [67]. Due to the use of vastly different experimental approaches in the aforementioned studies, their resulting expressions for drug released per surface area differ dramatically, as illustrated in Figure 2.1. Still, the DCB model lacked a geometrical representation of the DCB itself and relied on such prescribed expressions. Importantly, it also appreciated the potential effect of increased pressure during DCB application on the early flow-mediated transport and late drug retention performance.

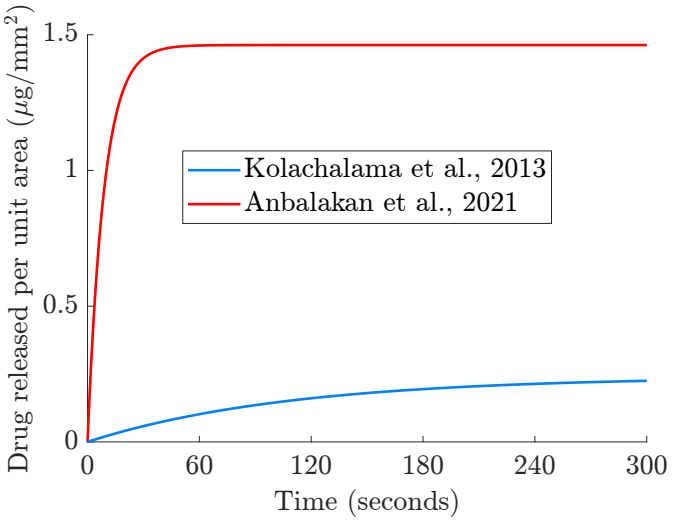

Figure 2.1: Comparison of empirically estimated exponential expressions for drug mass released per balloon surface area from a DCB inflated in a solution medium.

Although devices are often tested during preclinical stages in healthy animal models, the end user is a diseased patient; thus, the disease must, to some extent, be considered. Recent models incorporated disease in the context of DCBs. Colombo et al. [73] created a 3D artery geometry incorporating homogeneous disease, emphasising that drug diffusion is significantly

hindered through calcified plaque. Procedural aspects such as inflation time and multiple DCB applications were probed. The interaction between the drug delivery device and the vessel was simplified as an imposed boundary condition of drug flux, without representing the DCB. The integration of structural mechanics in the 3D setting was suggested as a potential feature in future works, to depict the deformation caused by DCB applications.

Sarifuddin and Mandal [74] characterised heterogeneous disease in a cross-sectional patient-specific artery, obtained from virtual histology IVUS imaging, and performed drug transport simulations. Drug delivery was simulated with a boundary condition of drug flux, also without including a geometrical representation of the DCB.

In conclusion, the importance of these two key studies must be emphasised, as they provide the theoretical and modelling foundations for the present work. The potential contribution of this thesis is to create a multiphysics representation of DCB deployment and drug delivery, applying the theoretical foundation of endovascular drug transport and retention described in Tzafriri, Levin, and Edelman [61] and building upon the computational modelling implementation of Escuer et al. [63]. The resulting model simulation shall replicate the drug delivery procedure of a DCB in a time-dependent fashion, accounting for all physics of the problem simultaneously. Concisely, Figure 2.2 summarises the main features of the DCB problem. Most of the principles were derived from previous modelling literature for DESs, which did not consider a time-dependent deforming artery geometry. Since the DCB delivery is characterised by a short period combining acute deformation and drug transfer, the deployment step will be an important focus of the modelling efforts of the present work.

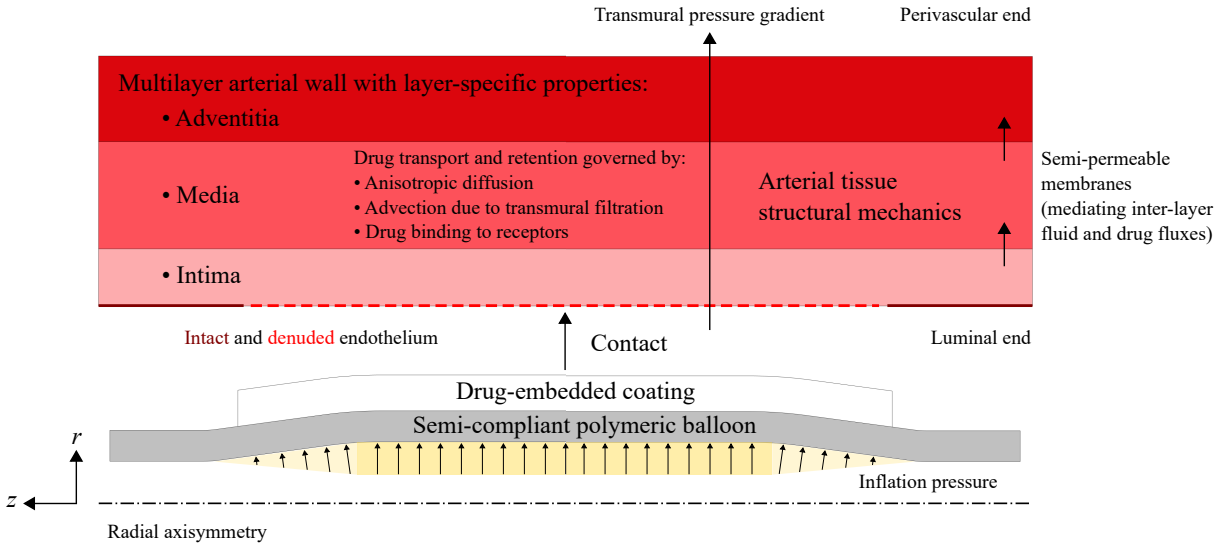

Figure 2.2: Diagram of the main features of modelling DCB deployment. Each of these parts will be explained progressively in the subsequent Chapters.

2.3 The proposed modelling endeavour

In silico modelling has evolved considerably over this relatively short time, considering that the first modelling study dates from 1996 [57]. Most *in silico* models reported in the relevant literature are based on a continuum modelling approach, which traditionally describes physical phenomena through deterministic mathematical expressions defined over continuous intervals. The finite element method is widely used for the numerical solution of these, calculating the model governing equations over discretised parts of its geometry and combining their information usually to form spatiotemporal behaviours e.g. drug transport, fluid flow, and structural deformation. Occasionally, continuum modelling is combined with discrete modelling in a complementary way [75].

Propelled by the massive increase in computational power over the years [76], numerical models became capable of performing more computationally demanding simulations, such as the simultaneous simulation of multiple interdependent physics, referred to as "multiphysics". The key structures of the problem, i.e. the arterial wall and the drug delivery device, have been progressively represented with increased sophistication [56]. Models evolved until 3D patient-specific artery geometries, diffusion-advection-reaction equations, and even considering inhomogeneous atherosclerotic disease. Despite all these advances, there is still no DCB model that incorporates simultaneous deformation and drug delivery.

Therefore, the general aim of this work is to develop a novel *in silico* model of DCB that depicts the two inherent aspects of the DCB — deformation and drug delivery — simultaneously. It will be used as a tool to assess DCB technology, improving on the limitations of previous DCB modelling literature, which are particularly limited to either the deformation or the drug delivery part of the problem.

The specific objectives of this work are as follows:

(I) Create detailed geometrical representations for the key entities of the problem of interest: the DCB and the arterial wall

(II) Represent the procedure of DCB deployment into the arterial wall, describing the simultaneous multiphysics aspects of the contact interaction

(III) Calculate the spatiotemporal drug distribution over the DCB coating and the arterial wall, featuring state-of-the-art drug transport and retention mechanisms

(IV) Calibrate the model using *in vitro* and/or *in vivo* experimental data available

(V) Validate the model by predicting results comparable to preclinical and clinical data available

Using a continuum modelling approach, the proposed model will produce a fully time-dependent multiphysics simulation of the DCB deployment procedure into a multilayered ar-

terial wall. The model will be based on a set of refined modelling assumptions provided by the aforementioned references in this Chapter, and focus on a DCB-only approach for *de novo* coronary artery intervention.

DCBs are still very much under investigation. To date, there are plenty of technical problems, challenges, and understudied factors of DCBs [52, 53]. Medical device companies are spending money developing these devices, and they are not always successful [77]. *In silico* models can elucidate their shortcomings and, as emphasised in Tzafriri and Edelman [78], can help further drive innovation at a reduced cost. This work is motivated by the challenge of modelling the complex interaction between the DCB and the arterial wall, and by the prospects of *in silico* models to improve the next generations of devices.

Chapter 3

Modelling endovascular drug delivery from drug-coated balloons

This Chapter presents the basic modelling assumptions of endovascular drug delivery in an idealised artery. The model aims to describe (I) the brief and localised drug delivery from a DCB, and (II) the long-term spatiotemporal distribution of the drug delivered in the target vessel following the procedure. The arterial wall is modelled as a 2D-axisymmetric geometry, representing a wet porous structure composed of multiple layers (intima, media, and adventitia) separated by semi-permeable membranes. It is pressurised internally by blood flow, propelling fluid flow through the arterial wall (transmural filtration).

The artery geometry is assumed rigid, and thus solid mechanics are not considered in this model. This is consistent with previous modelling works focussed on the problem of drug distribution [62, 66, 67, 72]. Similarly to these, drug traverses the artery layers according to the transport mechanisms of diffusion and advection, and is simultaneously retained by reversible binding reactions. The combination of drug transport and retention physics and transmural filtration physics configures a multiphysics model.

A crucial aspect of modelling the DCB is depicting the time window of the DCB procedure — when the device delivers part of its drug load to the target vessel on contact. Prior literature has simplified the simulation of drug delivery from DCBs using a flux expression [66, 67]. The behaviour of drug release from a DCB was obtained experimentally and fitted to an exponential function of flux. Active for a short duration, this prescribed flux expression provided a simplified representation of the drug transfer from the DCB in the simulation of drug delivery without modelling the device itself.

The present model is related to the previous modelling study in [72]. Authorship and substantial contribution in this previous work must be recognised. In summary, it proposed an *in silico* comparison of the rapid delivery from a DCB versus the sustained release from a DES, considering a rigid multilayered arterial wall built as a 2D-axisymmetric geometry. Drug delivery from the DCB was represented using the aforementioned approach of prescribed drug flux.

This Chapter builds upon the DCB model of [72].

Outline

Firstly, this Chapter presents the set-up of an idealised arterial wall geometry, followed by the definition of the drug transport and retention physics within its model domains and at its boundaries. Once the behaviour of drug is established, the source of drug is then introduced — proposing a simplified representation of drug delivery from the DCB as a temporary drug flux expression. The model is solved computationally using a finite element method framework. Key drug quantities, such as drug release profile, drug content, and receptor saturation, are presented and assessed in the simulation results while investigating the influence of procedural parameters. Finally, a discussion is provided on the significance of the results, simplifying assumptions, and the path towards modelling a more realistic representation of the DCB deployment procedure.

3.1 Model geometry

To represent the environment of endovascular drug delivery, this Chapter proposes an idealised model of the multilayered arterial wall. Notably, this model does not feature a geometrical representation of the DCB.

3.1.1 Lumen simplification

The lumen is the internal channel of the artery where blood flows. The effect of blood motion within the lumen, called "haemodynamics", is an important part of the problem of endovascular drug delivery, mainly because (I) it pressurises the arterial wall and (II) acts as a drug sink, washing off the superficial drug. However, due to the complexity of pulsatile and transient blood flow, simulating haemodynamics is computationally intensive and may detract the modelling efforts from its focus — drug distribution in the arterial wall. Previous computational studies have proposed simplifying assumptions, such as neglecting pulsatile flow in the lumen, considering blood as a Newtonian fluid, and calculating steady-state fluid dynamics [62, 63]. Over time, *in silico* observations prompted further simplifications.

According to the study in Escuer et al. [72], where blood flow is modelled as steady-state Navier-Stokes equations in a straight idealised artery geometry, the pressure distribution along the lumen-wall interface is approximately constant. Furthermore, Vijayaratnam et al. [79] verified the rapid superficial drug wash-off at the lumen interface. Motivated by the observations above, a simplification of the lumen that regards (I) and (II) is proposed. In line with the simplifying assumptions of [72] and [80], the effects of luminal blood flow are approximated by a constant pressure (p_{lum}) and a constant drug concentration ($c_{\text{lum}} = 0$), respectively representing the luminal blood pressure and drug sink, defined over the lumen-wall interface. Under these assumptions, there is no need to model blood flow coupled with drug transport physics in the lumen. As a consequence, disregarding the lumen as a domain in the model geometry greatly reduces the complexity of haemodynamics and drug transport physics in the model.

3.1.2 Model domains

The arterial wall model was then designed as a straight and tubular geometry composed of three concentric layers. It represents a segment of a blood vessel that will be subjected to drug delivery from a DCB. The motivation for considering an idealised artery is that these devices are tested preclinically in healthy animal models [81]. The generative process of the model geometry is depicted in Figure 3.1:

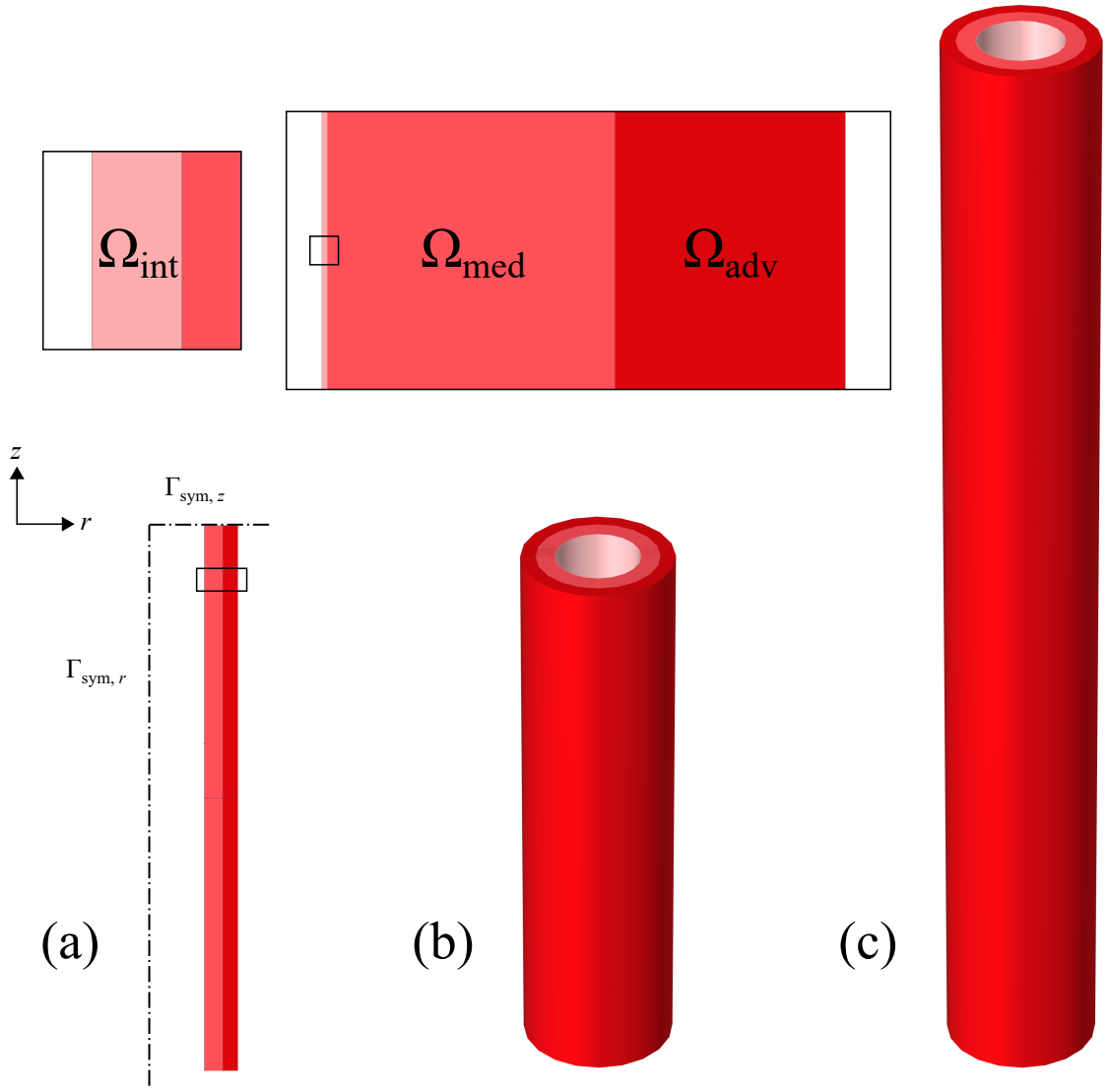

Figure 3.1: Schematic of the arterial wall model. From left to right, the labels indicate (a) the starting 2D-axisymmetric geometry, (b) the resultant revolved geometry, and (c) the resultant mirrored geometry. The magnified insets highlight the intima, media, and adventitia domains composing the multilayer structure of the wall, listed in Table 3.1. Due to the lumen simplification, the hollow part of the tubular geometry is not regarded as a domain.

The geometrical idealisations of the lumen and arterial wall enabled the use of two modelling strategies:

Two-dimensional (2D) axisymmetry A rectangular geometry with delimited domains is the starting point of the 2D-axisymmetric model. Once rotated around the axis of radial symmetry ($\Gamma_{sym,\,r}$), it forms a hollowed and multilayered structure. Therefore, the model geometry is symmetric around the axis $\Gamma_{sym,\,r}$, following the radial direction. The 2D-axisymmetric model geometry is defined employing a cylindrical coordinate system, i.e. in radial (r) and longitudinal (z) coordinates, similarly to in [62, 63, 82, 83].

Longitudinal mirroring The geometry is replicated over a line of longitudinal symmetry ($\Gamma_{\text{sym, } z}$) producing a longer structure with the full artery length desired. Therefore, the model geometry is symmetric over the line $\Gamma_{\text{sym, } z}$, following the longitudinal direction. More information on the modelling assumptions that enable longitudinal mirroring is available in [72]. This procedure aims to ultimately reduce computational costs by about half.

The multilayer aspect is a distinctive part of the arterial wall model, depicted in detail in the insets of Figure 3.1. The arterial wall geometry is composed of separate regions, referred to as "domains", representing each one of the arterial layers — intima (Ω_{int}), media (Ω_{med}), and adventitia (Ω_{adv}). This permits the modelling descriptions in this Chapter, concerning drug transport and retention physics, to be considered on a layer-specific basis over the composite geometry. There are three domains in total, as illustrated in Figure 3.1 and listed in Table 3.1.

Table 3.1: Summary of the model domains.

Domain name	Description
Ω_{int}	Intima layer of arterial wall
Ω_{med}	Media layer of arterial wall
Ω_{adv}	Adventitia layer of arterial wall

3.1.3 Model boundaries

Special attention is required at the edges of the domains, which are referred to as "boundaries". The behaviour at the boundaries must be explicitly defined to provide cohesion between all the physics simulated within the domains. The relevant boundaries of the model geometry, where boundary conditions will be assigned, are identified in Figure 3.2 and listed in Table 3.2.

Table 3.2: Summary of the model boundaries.

Boundary name	Description
$\Gamma_{\text{sym, } r}$	Axis of radial symmetry
$\Gamma_{\text{sym, } z}$	Line of longitudinal symmetry
$\Gamma_{\text{ET, de}}$	Denuded endothelium
$\Gamma_{\text{ET, in}}$	Intact endothelium
Γ_{IEL}	Internal elastic lamina
Γ_{EEL}	External elastic lamina
Γ_{periv}	Perivascular end
$\Gamma^{\text{wall}}_{\text{sym, } z}$	Mirroring extremity of arterial wall
$\Gamma^{\text{wall}}_{\text{ext}}$	Proximal extremity of arterial wall

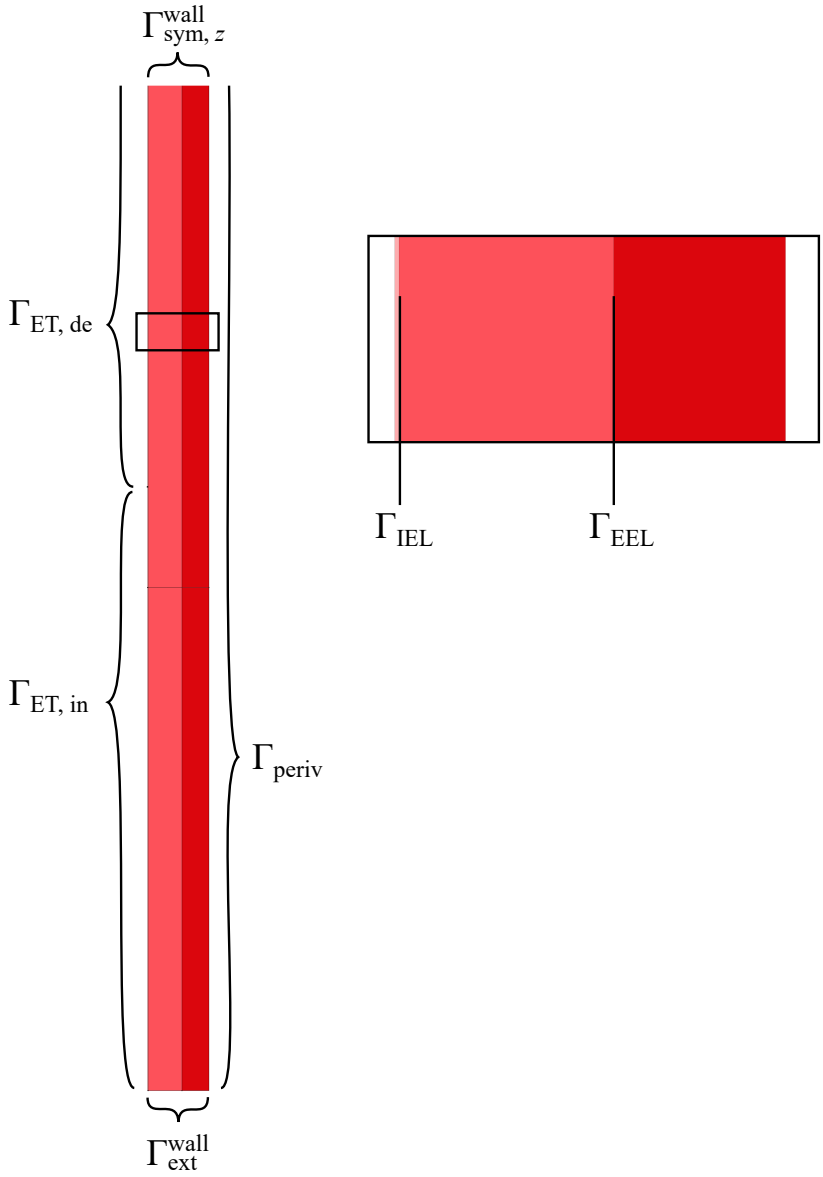

Figure 3.2: Definition of relevant boundaries in the model geometry. The magnified inset depicts the arterial wall and its elastic laminae, Γ_{IEL} and Γ_{EEL}, which separate the layers. Notation refers to Table 3.2.

The domains and boundaries listed in Tables 3.1 and 3.2 will be referenced in the subsequent sections where the multiphysics phenomena are defined.

3.1.4 Model dimensions

The idealised blood vessel segment resembles the physiological dimensions of a human distal left anterior descending coronary artery (LAD), which is a small blood vessel responsible for supplying blood to the left side of the heart muscle [84]. At this point, it is crucial to emphasise that this model represents a healthy artery completely absent of atherosclerotic disease or nar-

rowing (stenosis). This mimics the preclinical scenario, where the medical devices are tested in healthy animal models.

In preclinical testing of DCB in animal models, a segment of the tested artery is harvested at varied time points after the procedure for the measurement of drug distribution. The excised segment includes a middle therapeutic domain, where drug mass is quantified, and proximal and distal appendant segments, which are disregarded for the measurement. The definition of artery segment and therapeutic domain lengths in the *in silico* model, as highlighted in blue in Figure 3.3, is based on referential preclinical experiments. Therefore, the total segment must be sufficiently long to capture the unrestricted distribution of drug and allow posterior comparisons between simulation and experimental results for validation. Table 3.3 displays the complete model dimensions.

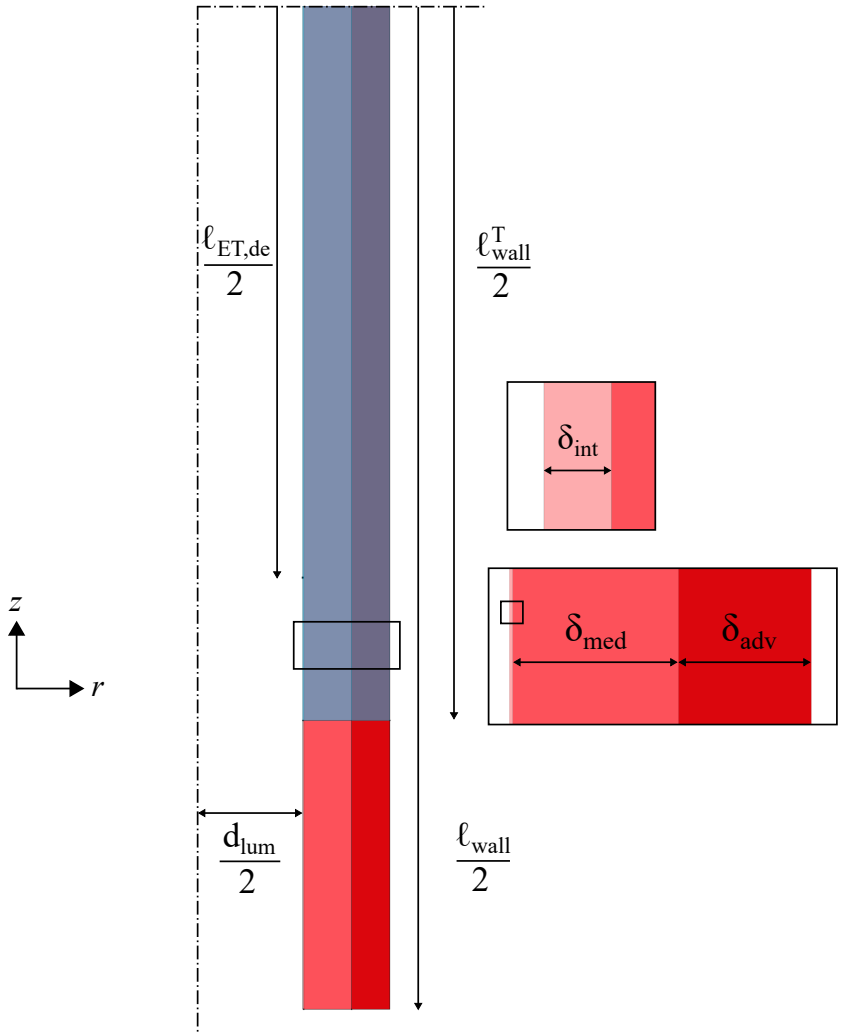

Figure 3.3: Schematic overview of the arterial wall model dimensions. The therapeutic domain is highlighted in blue. The magnified inset depicts the thicknesses of each of the arterial layers. Due to axisymmetry, some dimensions appear halved. Notation refers to Table 3.3.

Table 3.3: Summary of arterial wall model dimensions.

Parameter	Description	Value	Reference
d_{lum}	Diameter of artery lumen	2.25 mm	[63]
ℓ_{wall}	Total length of artery segment	30 mm	Estimated
$\ell_{\text{wall}}^{\text{T}}$	Length of therapeutic artery segment	15 mm	Estimated
$\ell_{\text{ET, de}}$	Length of denuded endothelium segment	12 mm	[72]
δ_{int}	Thickness of intima layer	0.01 mm	[63]
δ_{med}	Thickness of media layer	0.5 mm	[63]
δ_{adv}	Thickness of adventitia layer	0.4 mm	[63]

Drug transport and retention

This work aims to represent the delivery of a therapeutic agent from a medical device, the DCB, and its subsequent distribution in the arterial tissue. The therapeutic agent considered in this model is the antiproliferative drug sirolimus, also known as rapamycin. It will be simply referred to as the "drug". Since the current modelling efforts are focussed on the drug delivery and spatial distribution processes, the effect of the drug on the arterial tissue, for example, cell proliferation and tissue remodelling, is beyond the scope of this work. The reader may refer to McQueen et al. [85] and [80] for approaches that consider the effect of the drug.

Fundamentally, the model studies the distribution of three spatiotemporal variables, $c(r, z, t)$, $b^{\text{s}}(r, z, t)$, and $b^{\text{ns}}(r, z, t)$, over the model domains. These represent drug concentrations, assuming that the drug may coexist in free (c) and bound phases, distinctively bound to specific (b^{s}) and non-specific (b^{ns}) binding sites. The free drug is allowed to move via diffusion, spreading over domains driven by the gradient of concentration, and via advection, being simultaneously carried away by fluid flow due to transmural filtration through the porous arterial wall. In contrast, the bound drug is deprived of mobility and is fixed in space. A more detailed explanation of the binding process is provided in Section 3.4.

In summary, drug distribution in the arterial wall is modelled as a transport of diluted species phenomenon governed by three mechanisms — diffusion, advection, and reaction — combined depending on the model domain (Table 3.4). The domains are connected with boundary conditions, enabling the interchange of fluid and solute (drug) between domains. These are described in detail, respectively, in Sections 3.3.2 and 3.6.

Table 3.4: Summary of the drug transport and retention mechanisms in each model domain.

Domain	Mechanisms
Ω_{int}	Diffusion-Advection
Ω_{med}	Diffusion-Advection-Reaction
Ω_{adv}	Diffusion-Advection

At the beginning of the time-dependent simulation, i.e. at $t = 0$ s, all arterial wall domains are assumed to be empty of drug:

$$\begin{cases} c = 0 & \text{in } \Omega_{\text{int}} \\ c = 0;\ b^{\text{s}} = 0;\ b^{\text{ns}} = 0 & \text{in } \Omega_{\text{med}} \\ c = 0 & \text{in } \Omega_{\text{adv}}. \end{cases} \tag{3.1.1}$$

The following Sections describe the behaviour of drug transport and retention, firstly within model domains and then at its boundaries via boundary conditions.

3.2 Diffusion

Diffusion is the first drug transport mechanism assumed in the arterial wall. Diffusion, as a transport phenomenon, governs the spread of a particular substance through a medium. Its rate depends on the gradient of concentration and a coefficient of proportionality in that medium, named diffusion coefficient.

3.2.1 Layer-specific diffusion coefficients

It is assumed that drug diffusion may behave differently in each layer of the arterial wall and according to its direction. Generically, the layer-specific diffusion coefficient can be described in tensor form as:

$$\mathbf{D}_i = \begin{pmatrix} D_{i,\,r} & 0 \\ 0 & D_{i,\,z} \end{pmatrix} \qquad \text{for } i = \{\text{int, med, adv}\}, \tag{3.2.1}$$

where i denotes each of the artery layers, and r and z are the radial and longitudinal coordinates.

Based on previous modelling works considering multilayered vessels [63, 72], diffusive transport is assumed to behave with equal magnitude in the radial and longitudinal directions in the intima (Ω_{int}) and adventitia (Ω_{adv}) layers. Therefore, a single isotropic diffusion coefficient is considered there, i.e. $D_{\text{int},\,r} = D_{\text{int},\,z} = D_{\text{int}}$ and $D_{\text{adv},\,r} = D_{\text{adv},\,z} = D_{\text{adv}}$.

Distinctively, diffusive transport in the media layer (Ω_{med}) is assumed to be governed by an anisotropic diffusion coefficient. This implies different magnitudes of diffusion in the radial and longitudinal directions, i.e. $D_{\text{med},\,r} \neq D_{\text{med},\,z}$, due to the effect of fibre orientation of smooth muscle cells on the transport of drug as observed in [59]. Table 3.5 summarises the parameters used in the modelling of drug transport within artery layers via diffusion.

Table 3.5: Summary of model parameters relevant to drug transport via diffusion. All drug-related parameters refer to sirolimus as the therapeutic agent.

Parameter	Description	Value	Reference
D_{int}	Diffusion coefficient in intima	$1.67 \cdot 10^{-11}$ m^2/s	[62]
$D_{\text{med},\,r}$	Radial diffusion coefficient in media	$7 \cdot 10^{-12}$ m^2/s	[59]
$D_{\text{med},\,z}$	Longitudinal diffusion coefficient in media	$4 \cdot 10^{-11}$ m^2/s	[59]
D_{adv}	Diffusion coefficient in adventitia	$4 \cdot 10^{-12}$ m^2/s	[63]

Based on a continuum modelling approach, the arterial wall model simulates the behaviour of drug concentrations over space and time by calculating partial differential equations over a finite element mesh. These are the governing equations of drug transport and retention, defined on a layer-specific basis as:

- Diffusion-advection equations in the intima:

$$\frac{\partial c}{\partial t} = \nabla \cdot (\mathbf{D}_{\text{int}} \nabla c - \mathbf{u}^* c) \qquad \text{in } \Omega_{\text{int}}, \tag{3.2.2}$$

- Diffusion-advection-reaction equations in the media:

$$\frac{\partial c}{\partial t} = \nabla \cdot (\mathbf{D}_{\text{med}} \nabla c - \mathbf{u}^* c) - R \qquad \text{in } \Omega_{\text{med}}, \tag{3.2.3}$$

- Diffusion-advection equations in the adventitia:

$$\frac{\partial c}{\partial t} = \nabla \cdot (\mathbf{D}_{\text{adv}} \nabla c - \mathbf{u}^* c) \qquad \text{in } \Omega_{\text{adv}}. \tag{3.2.4}$$

The next Sections present the mechanisms of advection and reaction and elaborate on the meaning of the terms $\mathbf{u}^*$ and R in the Equations above. Combined with diffusion, these mechanisms will produce the governing equations of drug transport and retention in the arterial wall model.

3.3 Advection

Advection is the second mechanism of drug transport assumed in the arterial wall. It represents the transport of the drug, as a diluted solute, due to the motion of a fluid. In the current model, the advective transport of drug in the arterial wall stems from the concept of transmural filtration.

3.3.1 Transmural filtration

The arterial wall is often modelled as a wet porous material subjected to pressure constraints. As pressurised blood flows in the lumen, part of the fluid — plasma — is continuously driven perpendicular to the flow direction through the permeable artery layers. This phenomenon is named transmural filtration (from Latin "*trans*", through; and "*murus*", wall), and it facilitates the transport of substances radially outwards through the arterial wall. In this model, this flow is assumed to be governed by Darcy's Law.

Darcy's Law

Darcy's Law generally states that the fluid flow across a wet porous medium is driven by its pressure gradient:

$$\mathbf{u} = -\frac{\kappa_i}{\mu_{\text{plasma}}}(\nabla p + \mathbf{f}), \tag{3.3.1}$$

where the transmural convective field ($\mathbf{u}$) is proportional to the gradient of the transmural pressure field (∇p), plus an external force ($\mathbf{f}$), if present. Proportionality is given by the relation between the layer-specific porous medium permeability (κ_i) and dynamic fluid viscosity (μ_{plasma}). The constant κ_i quantifies the ease of passage of the transmural fluid through the respective porous medium, $i = \{\text{int, med, adv}\}$ in the current multilayered model, and will be referred to as Darcy permeability to distinguish it from other constants. The transmural convective field is defined in all layers of the arterial wall. Remarkably, the negative sign in Equation 3.3.1 means that fluid flow is propelled towards the direction of pressure drop.

Convective field

The main output of Darcy's Law calculations is the transmural convective field, $\mathbf{u}(r, z, t)$, which is derived from the transmural pressure field, $p(r, z, t)$. It contains the direction and magnitude of the fluid flow velocity of transmural filtration over the entire arterial wall, in the radial and longitudinal directions. Its utility in the current modelling problem is to inform the advective contribution towards drug transport over the arterial wall throughout the simulation. Effectively, advection represents the drug carried by the fluid flow of plasma filtration through the porous wall. The convective field $\mathbf{u}$ may be presented in a general vector form in terms of its radial and

longitudinal components, underlining the directional character of convection:

$$\mathbf{u} = \begin{pmatrix} u_r & u_z \end{pmatrix} \qquad \text{in } \Omega_i, \text{ for } i = \{\text{int, med, adv}\}. \tag{3.3.2}$$

3.3.2 Boundary conditions on fluid flow

Transmural filtration within the arterial wall domains is characterised by the constraints of its surroundings. In the current model, these are modelled as boundary conditions pressure and fluid flux. These boundary conditions are presented next, categorised based on their boundary of effect.

Denuded/intact endothelium

The deployment of endovascular devices such as angioplasty balloons, stents, and to a lesser extent imaging guide wires, causes damage to the lining of the arterial wall. In the most extreme cases, the endothelial layer of cells is completely removed — a process referred to as endothelial denudation. The complete or even partial denudation of the endothelium alters the barrier function of the arterial wall and increases permeability substantially until the endothelium fully recovers [86]. In this work, in line with other modelling literature [62, 63], the region of the arterial wall that the balloon contacts has been assumed to be denuded, effectively increasing plasma filtration rates and drug clearance. This determined the choice of boundary conditions as presented in the subsequent modelling.

Based on the approach of previous modelling works [63, 72, 82], the lumen-wall interface is divided into two zones: the denuded ($\Gamma_{\text{ET, de}}$) and intact ($\Gamma_{\text{ET, in}}$) endothelia. The denuded endothelium ($\Gamma_{\text{ET, de}}$) represents the region affected by the percutaneous intervention, where the superficial layer of endothelium cells is assumed to be completely removed. Due to the lack of a protective barrier, continuity of pressure is prescribed to this boundary. Considering the transient DCB therapy, this region is either affected by the DCB deployment or is exposed to the blood flow in the lumen. The internal surface of the artery is named "luminal" as it faces the lumen. It is constrained by blood pressure, which, under normal circumstances, stems from complex haemodynamics. However, disregarding pulsatile blood flow allows an idealised model to use steady-state or even constant values for luminal pressure constraints, as described earlier.

Following the previous modelling assumption of [67] and [72], the pressure behaviour over $\Gamma_{\text{ET, de}}$ is modelled as a transient multistep boundary condition of pressure, defined as:

$$p_{\text{ET, de}} = \begin{cases} p_{\text{DCB}} & 0 < t < t_0 \\ p_{\text{lum}} & t \geq t_0, \end{cases} \tag{3.3.3}$$

where p_{DCB} is an estimate of the temporary pressure exerted by DCB inflation on the arterial wall, p_{lum} is the luminal blood pressure, and t_0 is the duration of the DCB drug delivery. The

value of t_0 is estimated as 60 seconds, based on typical usage of DCBs in coronary intervention [32].

On the other hand, the intact endothelium ($\Gamma_{\text{ET, in}}$) represents a region unaffected by the DCB deployment. It is the remaining length of the lumen-wall interface farther away from the intervention site, and it can fulfil its usual protective purpose of mediating the transmission of pressure from the lumen. The intact endothelium is described as a semi-permeable barrier according to the Kedem-Katchalsky equations [87], and the fluid flux across it, $J_{\text{v, ET}}$, is presented as:

$$J_{\text{v, ET}} = L_{\text{p, ET}} \left(\Delta p_{\text{ET, in}}\right) \qquad \text{on } \Gamma_{\text{ET, in}}, \tag{3.3.4}$$

where $L_{\text{p, ET}}$ is the hydraulic conductivity of the intact endothelium, and $\Delta p_{\text{ET, in}}$ is the pressure difference across the respective boundary. Since the endothelium separates the lumen and intima, the pressure difference is defined over its length as $\Delta p_{\text{ET, in}} = p_{\text{lum}} - p_{\text{int}}$.

Remarkably, the effect of blood pressure on the intact endothelium is modelled as a fluid flux boundary condition (in units of velocity) rather than a pressure boundary condition as in the denuded counterpart.

Perivascular end

There is known to be a pressure gradient across the vascular wall, from the luminal side, where blood is flowing, to its external surface, named "perivascular", which is constrained by intrathoracic pressure. Similarly to the lumen simplification of pulsatile blood flow, disregarding inspiratory-expiratory cycles also allows the perivascular pressure constraint to be idealised as a constant value of magnitude derived from physiological values ($p_{\text{periv}} = 30$ mmHg, as in [88]). Together, the set of luminal and perivascular pressure constraints represents the pressurised vascular environment where a coronary artery resides. That provides the baseline of the transmural pressure gradient along the simulation: an idealised constant pressure load $p_{\text{lum}} = 100$ mmHg acting on the denuded endothelium, and $p_{\text{periv}} = 30$ mmHg acting on the perivascular end, emulating a physiologically realistic pressure drop of 70 mmHg across the arterial wall.

Elastic laminae

Transmural filtration is a process assumed to occur in the entire arterial wall. The behaviour of the transmural velocity field between the artery layers is mediated by two thin barriers, named elastic laminae. They act as semi-permeable membranes separating the intima and media (internal elastic lamina, IEL, at Γ_{IEL}) and the media and adventitia (external elastic lamina, EEL, at Γ_{EEL}). In the current model, the effect of the elastic laminae is described with a set of fluid

fluxes, $J_{\text{v, IEL}}$ and $J_{\text{v, EEL}}$, according to the Kedem-Katchalsky equations:

$$\begin{cases} J_{\text{v, IEL}} = L_{\text{p, IEL}} \left(\Delta p_{\text{IEL}}\right) & \text{on } \Gamma_{\text{IEL}} \\ J_{\text{v, EEL}} = L_{\text{p, EEL}} \left(\Delta p_{\text{EEL}}\right) & \text{on } \Gamma_{\text{EEL}}, \end{cases} \tag{3.3.5}$$

where $L_{\text{p, IEL}}$ and $L_{\text{p, EEL}}$ are the hydraulic conductivities of the IEL and EEL membranes, respectively; and Δp_{IEL} and Δp_{EEL} are the pressure differences across each membrane. For example, the pressure difference across the IEL is calculated using the pressure values from the intima (p_{int}) and media (p_{med}), immediately adjacent to the lamina, as $\Delta p_{\text{IEL}} = p_{\text{int}} - p_{\text{med}}$. Effectively, the flux boundary conditions of the elastic laminae produce pressure discontinuities across the transmural pressure field of the multilayer arterial wall.

In a more general way, the Kedem-Katchalsky equation of flux through a semi-permeable barrier can be described as:

$$J_{\text{v, }i} = L_{\text{p, }i} \left(\Delta p_i\right) \qquad \text{on } \Gamma_i, \tag{3.3.6}$$

where $J_{\text{v, }i}$ is the fluid flux across a boundary of arbitrary name i, $L_{\text{p, }i}$ is its hydraulic conductivity, and $\Delta p_i = p_{\text{down}} - p_{\text{up}}$. In the model, three boundaries are modelled as semi-permeable membranes (the intact endothelium and elastic laminae), so that $i = \{\text{ET, in; IEL; EEL}\}$. The subscripts "down" and "up" denote the pressure field values downstream and upstream of that respective boundary, i.e. immediately before and after it in the positive radial direction. The resulting flux $J_{\text{v, }i}$, given in units of velocity, has spatiotemporal-dependent values over its respective boundary since (I) pressure is distributed unequally over the model geometry and (II) dynamic stimuli may disturb the pressure fields along the simulation. The parameters for the fluid fluxes across the membranes are listed in Table 3.7.

For a greater understanding of the concept of hydraulic conductivity, this constant may be defined for each elastic laminae as

$$\begin{cases} L_{\text{p, IEL}} = \dfrac{\kappa_{\text{med}}}{\mu_{\text{plasma}}\, h_{\text{EL}}} & \text{on } \Gamma_{\text{IEL}} \\ L_{\text{p, EEL}} = \dfrac{\kappa_{\text{adv}}}{\mu_{\text{plasma}}\, h_{\text{EL}}} & \text{on } \Gamma_{\text{EEL}}, \end{cases} \tag{3.3.7}$$

where κ_{med} and κ_{adv} are the Darcy permeability values for the corresponding layers, μ_{plasma} is the dynamic fluid viscosity, and h_{EL} is the approximate thickness of an elastic lamina, in line with [89]. This relation derives from the representation of a thin barrier of thickness h_{EL} as permeable as the upstream domain. Despite the use of a thickness value, the present model represents the elastic laminae as boundary conditions without geometrical features.

Remaining constraints

Additionally, sufficient boundary conditions must be assigned to the longitudinal extremities of the arterial wall to properly enclose its domains. These are located where the artery meets the line of longitudinal symmetry ($\Gamma^{\text{wall}}_{\text{sym, }z}$) and at the upstream and downstream ends of the artery ($\Gamma^{\text{wall}}_{\text{ext}}$). Both boundaries are regarded with the imposition of a zero-flow condition, expressed as:

$$-\mathbf{n} \cdot \mathbf{u} = 0 \qquad \text{on } \Gamma^{\text{wall}}_{\text{sym, }z} \text{ and } \Gamma^{\text{wall}}_{\text{ext}}, \tag{3.3.8}$$

where $\mathbf{n}$ is the unit outward normal vector to the corresponding boundary, and $\mathbf{u}$ is the local advective velocity. In chorus with previous modelling works, the geometry length is chosen such that the upstream and downstream ends are sufficiently far from the therapeutic domain that they do not impact the results of the simulation [83]. Moreover, the behaviour of transmural fluid flow is assumed symmetric over the middle line of symmetry, following the longitudinal mirroring procedure [72].

3.3.3 Lag coefficients

After defining the baseline advective field over the arterial wall, calculated with Darcy's Law, considerations are made on the solute transport in wet porous media. To distinguish the effect of layer-specific properties on advection, the model uses constant and layer-specific advective multipliers that are named "lag coefficients". This approach is based on the previous modelling works [63] and [72]. In summary, lag coefficients attempt to account for the effects of hindrance and porosity of the arterial tissue on the advective drug transport through its multilayered structure. Hindrance represents possible friction between the drug molecules and the porous medium (none if $= 1$), while porosity refers to its fraction of void space (none if $= 0$). Equation 3.3.9 defines these coefficients on a layer-specific basis:

$$\text{lag}_i = \frac{\gamma_i}{\phi_i} \qquad \text{for } i = \{\text{int, med, adv}\}, \tag{3.3.9}$$

where γ_i is the hindrance coefficient, and ϕ_i is the porosity of a given layer i.

The layer-specific lag coefficients are constants that amplify the transmural advective field $\mathbf{u}$, leading to an updated transmural advective field renamed as $\mathbf{u}^*$. Equation 3.3.10 generalises this procedure:

$$\begin{aligned} \mathbf{u}^* &= \mathbf{u}\ \text{lag}_i \\ &= \begin{pmatrix} u_r\ \text{lag}_i & u_z\ \text{lag}_i \end{pmatrix} \end{aligned} \qquad \text{in } \Omega_i, \text{ for } i = \{\text{int, med, adv}\}. \tag{3.3.10}$$

Table 3.6 summarises the set of boundary conditions of pressure and flow constraining the multilayered arterial wall, and Table 3.7 summarises the parameters utilised in the simulation of transmural filtration.

Table 3.6: Summary of boundary conditions concerning transmural filtration. The transient boundary condition, presented in Equation 3.3.3, is indicated as "condition during drug delivery / condition after drug delivery".

Type	Expression	Boundary
Pressure	p_{DCB} / p_{lum}	$\Gamma_{\text{ET, de}}$
Flow	$J_{\text{v, ET}}$	$\Gamma_{\text{ET, in}}$
Flow	$J_{\text{v, IEL}}$	Γ_{IEL}
Flow	$J_{\text{v, EEL}}$	Γ_{EEL}
Pressure	p_{periv}	Γ_{periv}
Zero-flow	$-\mathbf{n} \cdot \mathbf{u} = 0$	$\Gamma^{\text{wall}}_{\text{sym, } z}$
Zero-flow	$-\mathbf{n} \cdot \mathbf{u} = 0$	$\Gamma^{\text{wall}}_{\text{ext}}$

In conclusion, the main output of the modelling of transmural filtration physics is the advective field $\mathbf{u}^*$ — which is used to inform the advective term of the governing equations of drug transport and retention. Advection is a complementary mechanism in the process of drug distribution in the arterial wall following DCB therapy and essentially depends on pressure constraints between the ends of the arterial wall. It is expected that the high-pressure inflation of a DCB temporarily affects the pressure value at the contacting region, denoted in the model as the denuded endothelium ($\Gamma_{\text{ET, de}}$). This was modelled by employing the multistep boundary condition expressed in Equation 3.3.3. The magnitude of this pressure, p_{DCB}, is a major topic of discussion in this work and is featured in Section 5.7.

Table 3.7: Summary of parameters for the modelling of transmural filtration.

Parameter	Description	Value	Reference
ρ	Density of wet arterial tissue	0.983 g / ml	[64]
μ_{plasma}	Dynamic viscosity of plasma	$7.2 \cdot 10^{-4}$ Pa s	[60]
κ_{int}	Darcy permeability in intima	$2.2 \cdot 10^{-16}$ m^2	[88]
κ_{med}	Darcy permeability in media	$2.0 \cdot 10^{-18}$ m^2	[60]
κ_{adv}	Darcy permeability in adventitia	$2.0 \cdot 10^{-18}$ m^2	[90]
p_{lum}	Physiological luminal pressure	100 mmHg	[88]
p_{DCB}	DCB deployment pressure	8 atm	[67]
t_0	DCB deployment duration	60 s	[32]
p_{periv}	Physiological perivascular pressure	30 mmHg	[88]
h_{EL}	Thickness of elastic lamina	1.263 μm	Estimated
$L_{\text{p, ET}}$	Hydraulic conductivity of endothelium	$2.2 \cdot 10^{-12}$ m^2 s / kg	[62]
$L_{\text{p, IEL}}$	Hydraulic conductivity of IEL	$2.2 \cdot 10^{-9}$ m^2 s / kg	[62]
$L_{\text{p, EEL}}$	Hydraulic conductivity of EEL	$2.2 \cdot 10^{-9}$ m^2 s / kg	[63]
γ_{int}	Hindrance coefficient of intima	1	[63]
γ_{med}	Hindrance coefficient of media	0.845	[63]
γ_{adv}	Hindrance coefficient of adventitia	1	[63]
ϕ_{int}	Porosity of intima	0.983	[88]
ϕ_{med}	Porosity of media	0.258	[88]
ϕ_{adv}	Porosity of adventitia	0.85	[57]
lag_{int}	Lag coefficient of intima	1.0173	Calculated
lag_{med}	Lag coefficient of media	3.38	Calculated
lag_{adv}	Lag coefficient of adventitia	1.1765	Calculated

3.4 Reaction

While the drug is transported through the multilayer wall via diffusion and advection, it is assumed to behave as a ligant and be retained by the drug receptors in the tissue in a process named "drug binding" [91]. In chorus with contemporary modelling works, drug binding is modelled as a two-phase, non-linear, reversible, and saturable process [7, 61, 78]. This is implemented *in silico* with the inclusion of a reaction rate R to the drug transport equation. The term R is composed of the formation rates of specific and non-specific bound drug concentrations:

$$R \;=\; \frac{\partial b^{\mathrm{s}}}{\partial t} \;+\; \frac{\partial b^{\mathrm{ns}}}{\partial t}, \tag{3.4.1}$$

each defined as:

$$\begin{cases} \dfrac{\partial b^{\mathrm{s}}}{\partial t} \;=\; k^{\mathrm{s}}_{\mathrm{on}}\, c\, (b^{\mathrm{s}}_{\mathrm{max}} - b^{\mathrm{s}}) \;-\; k^{\mathrm{s}}_{\mathrm{off}}\, b^{\mathrm{s}} \\[2ex] \dfrac{\partial b^{\mathrm{ns}}}{\partial t} \;=\; k^{\mathrm{ns}}_{\mathrm{on}}\, c\, (b^{\mathrm{ns}}_{\mathrm{max}} - b^{\mathrm{ns}}) \;-\; k^{\mathrm{ns}}_{\mathrm{off}}\, b^{\mathrm{ns}}. \end{cases} \tag{3.4.2}$$

The main features of drug binding in this model are synthesised below:

Two-phase The antiproliferative drugs used in DCBs are designed to halt smooth muscle cell proliferation in the arterial tissue — this represents the therapeutic purpose of drug delivery. In the model, drug binding creates two new spatiotemporal variables of interest, b^{s} and b^{ns}, defined over part of the arterial wall. Respectively, they represent the two ways drug may bind: to drug receptors within cells (generating drug in specifically-bound phase, b^{s}) and to interstitial tissue and extracellular matrix sites (generating drug in non-specifically-bound phase, b^{ns}).

Reversible Each rate of Equation 3.4.1 represents the net transformation of drug between phases. They may have positive or negative values, contributing to the evolution of free drug concentration in a reversible fashion. For instance, if the rate $\frac{\partial b^i}{\partial t}$ is positive (for $i = \{\mathrm{s}, \mathrm{ns}\}$), drug concentration will be transformed from free to that respective bound drug phase, i.e., subtracted from free and added to bound phase. If the rate is negative, drug concentration will be transformed from bound to free drug phase, i.e., subtracted from bound and added to free phase. The rate of drug binding is composed of two parts: "binding-on" and "binding-off". They are identified respectively as the positive and negative terms in Equation 3.4.2. The balance between the two determines the net behaviour of binding.

Non-linear The pace at which the drug binds to the binding sites depends on the local availability of free drug as well as the current bound drug concentration. This non-linear dependency is indicated by the product of both the free and bound drug concentrations, c and

b^i, in the "binding-on" part of the binding rates. In contrast, the drug unbinding process is solely dependent on the current amount of bound drug, indicated in the "binding-off" terms.

Saturable The model assumes the existence of a finite number of drug receptors in the arterial tissue; thus capable of capturing a limited amount of drug particles at a given moment. This behaviour is incorporated by imposing a ceiling for the binding-on rate in the binding equations. Notably, drug binding stops when the bound drug concentration b^i reaches a maximum value, defined as the binding site density b^i_{max} (for $i = \{\text{s, ns}\}$). Then, the term in brackets $(b^i_{\text{max}} - b^i)$ becomes null, which, due to multiplication by zero, causes the entire binding on rate to be nullified. In this scenario, the binding-off term will likely dominate the expression, resulting in a negative rate.

Binding site location

The antiproliferative effect of sirolimus on inhibiting the cascade of biological events provoked by vascular injury is attributed to the binding of drug to the FKBP12 receptor, resulting in the inhibition of mTOR signalling, and thus cell proliferation [64, 80]. Therefore, supplying drug to these specific receptors represents the main target of the pharmacological therapy post-endovascular intervention. These relevant drug receptors are located within smooth muscle cells, which are the principal constituent of the media layer. Therefore, vascular pharmacotherapies target smooth muscle cells in the media [57]. While it is acknowledged that drug binding should also happen, to cellular and non-cellular (non-specific) components, in all layers of the arterial wall, the majority of the binding is expected to occur in the media layer. Based on a simplifying assumption in line with the multilayered works of [63], [72], [80], the current model considers that drug binding happens exclusively in the media domain (Ω_{med}).

Table 3.8 lists the parameters required to characterise drug binding in the model.

Table 3.8: Summary of model parameters relevant to drug retention via binding reactions. All drug-related parameters refer to sirolimus as the therapeutic agent.

Parameter	Description	Value	Reference
k^{s}_{on}	Specific binding-on rate	800 m^3/(mol s)	[92]
$k^{\text{s}}_{\text{off}}$	Specific binding-off rate	$1.6 \cdot 10^{-4}$ 1/s	[61]
$b^{\text{s}}_{\text{max}}$	Specific binding site density	0.0033 mol/m^3	[64]
$k^{\text{ns}}_{\text{on}}$	Non-specific binding-on rate	2 m^3/(mol·s)	[61]
$k^{\text{ns}}_{\text{off}}$	Non-specific binding-off rate	$5.2 \cdot 10^{-3}$ 1/s	[61]
$b^{\text{ns}}_{\text{max}}$	Non-specific binding site density	0.363 mol/m^3	[64]

Finally, combining the reaction term R with the drug transport equation forms diffusion-advection-reaction equations.

$$\frac{\partial c}{\partial t} = \nabla \cdot \left(\mathbf{D}^{*}_{\text{med}} \nabla c - \mathbf{u}^{*} c \right) - R \qquad \text{in } \Omega_{\text{med}}. \tag{3.4.3}$$

Expressing R in terms of the binding rates $\frac{\partial b^{\text{s}}}{\partial t}$ and $\frac{\partial b^{\text{ns}}}{\partial t}$, Equation 3.4.4 presents the spatiotemporal evolution of the three phases of drug considered within the media domain:

$$\begin{cases} \dfrac{\partial c}{\partial t} = \nabla \cdot \left(\mathbf{D}_{\text{med}} \nabla c - \mathbf{u}^{*} c \right) - \dfrac{\partial b^{\text{s}}}{\partial t} - \dfrac{\partial b^{\text{ns}}}{\partial t} \\ \dfrac{\partial b^{\text{s}}}{\partial t} = k^{\text{s}}_{\text{on}} \, c \, (b^{\text{s}}_{\text{max}} - b^{\text{s}}) - k^{\text{s}}_{\text{off}} \, b^{\text{s}} \qquad \text{in } \Omega_{\text{med}}. \\ \dfrac{\partial b^{\text{ns}}}{\partial t} = k^{\text{ns}}_{\text{on}} \, c \, (b^{\text{ns}}_{\text{max}} - b^{\text{ns}}) - k^{\text{ns}}_{\text{off}} \, b^{\text{ns}} \end{cases} \tag{3.4.4}$$

It must be emphasised that drug is assumed immobile while in bound phase. In that state, drug is not directly affected by transport phenomena, i.e., advection and diffusion. The reversible fashion of binding and unbinding, along with loss and regain of mobility, may predict a slow drift of drug through the arterial tissue with binding sites. Everywhere else, drug is freely mobile via diffusion and advection.

After regarding the behaviour of drug transport and retention in the model, it is timely to present the source of the drug — how the drug is introduced into the arterial wall in the simulation.

3.5 Drug source

In addition to the effect of the DCB on the transmural pressure constraints as presented in Section 3.3, the DCB's role in drug delivery must be regarded. This Chapter employs a simplified representation of the DCB as a prescribed flux to represent drug delivery from a DCB without modelling the device itself. It is modelled as a temporary boundary condition of solute flux, prescribed uniformly over the denuded endothelium ($\Gamma_{\text{ET, de}}$) and active during a brief time window (of duration t_0).

The drug delivery rate, $J_{\text{DCB}}(t)$, alongside its cumulative drug delivered, behaves according to exponential functions solely dependent on time, as presented in Equation 3.5.1:

$$\begin{cases} J_{\text{DCB}}(t) \;=\; \dfrac{k\,A}{M_{\text{sir}}}\, e^{-k\,t} \\ \\ \displaystyle\int_0^t J_{\text{DCB}}(t)\,dt = \frac{A}{M_{\text{sir}}}\,(1 - e^{-k\,t}) \end{cases} \qquad \text{on } \Gamma_{\text{ET, de}}, \text{ for } 0 < t < t_0, \tag{3.5.1}$$

where k and A are, respectively, the exponential and linear parameters that shape the functions, M_{sir} is the molar mass of the drug, and t is the independent variable of time in the simulation. While J_{DCB} expresses a time-variant drug flux per delivery area, in mol/(m^2 s), the cumulative drug delivered per delivery area may be obtained from the integration of the former over time, in mol/m^2.

The parameterisation of $J_{\text{DCB}}(t)$ is based on *in vitro* experiments. In chorus with [72], the current model simulates two vastly different drug flux expressions derived from experimental studies with DCBs to illustrate two scenarios of drug delivery. They are referred to as "Low dose" and "High dose":

Low dose Reported in the study of Kolachalama et al. [66]. The study is based on the drug zotarolimus, a sirolimus analogue. Assuming sufficient similarity between the analogues, the flux may be adapted to sirolimus simply by using its molar mass instead. Drug release kinetics were assessed *in vitro* using porcine blood.

High dose Reported in the study of Anbalakan et al. [67]. The study employed angioplasty balloon catheters (Biomatrix NeoFlex, Biosensors International, Singapore), coated with sirolimus as the drug and polyethylene oxide (PEO) as the excipient. Drug release kinetics were assessed *in vitro* using a harsh solution medium (acetonitrile) and fitted into an exponential curve.

Table 3.9 defines the two drug flux expressions considered in this work. Each expression is defined by the parameters k and A, which are constant values empirically estimated from experimental data in their respective references. The names "Low dose" and "High dose" denote

the magnitude of the flux expressions, which should be apparent in the presentation of simulation results in Section 3.8.

Table 3.9: Summary of the two drug flux expressions used to simulate DCB drug delivery in this Chapter.

Flux name	**Low dose**	**High dose**
Reference	Kolachalama et al., 2013 [66]	Anbalakan et al., 2021 [67]
k	0.009221 1/s	0.1135 1/s
A	0.24 μg/mm^2	1.4618 μg/mm^2
M_{sir}	914.187 g/mol	

A similar DCB simplification was performed in the previous modelling works [66], [67], [73], and [72], which notably did not include a geometrical representation of the DCB.

3.6 Boundary conditions on drug transport

Boundary conditions provide essential information on drug transport physics at the boundaries of the domains, permitting containment or cohesion of the physics of adjacent domains. The boundary conditions concerning the transport of drug in the model are presented next, categorised based on type:

- Semi-permeable barrier
- Perfect sink
- Zero-flux

Figure 3.4 summarises the physics considered in the model, as described in the previous Sections, and indicates the relevant boundaries where the remaining boundary conditions will be assigned.

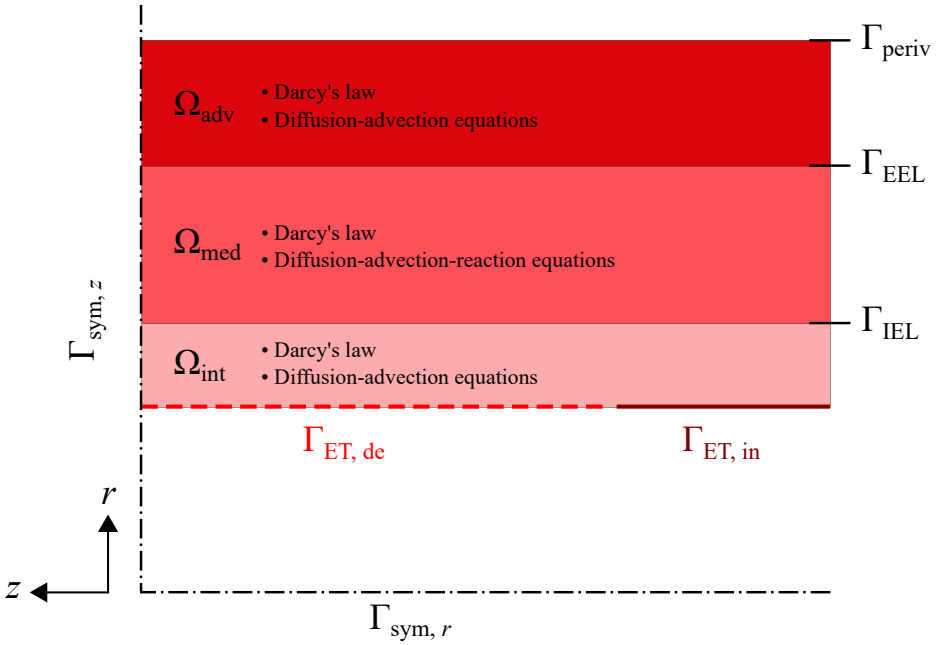

Figure 3.4: Schematic summary of physics considered in the model of Chapter 3. Geometry is not to scale.

3.6.1 Semi-permeable barrier

The problem of endovascular drug delivery involves drug transport as a solute through several membranes separating the arterial tissue, namely the endothelium and elastic laminae. In line with previous modelling works, the semi-permeable behaviour observed in the endovascular environment may be described with sufficient realism by the flux expressions formulated

by Kedem-Katchalsky (originated in [87], and implemented in [62] and [82]). Concisely, the Kedem-Katchalsky equations express solute flux, $J_{\text{s},\,i}$, through a semi-permeable barrier defined over an arbitrary boundary i, driven by fluid flow. Equation 3.6.1 presents a general form for them, decomposed into parts:

$$\begin{cases} J_{\text{s},\,i} = (P_i\ \Delta c_i) + (s_i\ \bar{c}_i\ J_{\text{v},\,i}) \\ \\ J_{\text{v},\,i} = L_{\text{p},\,i}\ \Delta p_i \end{cases} \qquad \text{on } \Gamma_i, \text{ for } i = \{\text{ET, in, IEL, EEL}\}, \tag{3.6.1}$$

where i is an arbitrary boundary name representing a membrane; $J_{\text{s},\,i}$ is the flux of solute crossing it; P_i and s_i are the permeability and sieving coefficient of the membrane, respectively; Δc_i is the drug concentration difference over the boundary, defined as $\Delta c_i = c_{\text{down}} - c_{\text{up}}$; $J_{\text{v},\,i}$ is the fluid flux through the boundary; $\bar{c}_i$ is a weighted average of drug concentration over the boundary, defined as:

$$\bar{c}_i = \frac{1}{2}\,(c_{\text{down}} + c_{\text{up}}) + \frac{1}{12}\,\frac{s_i\ J_{\text{v},\,i}}{P_i}\,\Delta c_i. \tag{3.6.2}$$

The fluid flux used here is identical to the one defined earlier, in Subsection 3.3.2, indicating that drug transport through the elastic laminae is assisted by transmural filtration.

Table 3.11 lists the set of parameters required to define the aforementioned equations. The subscripts "down" and "up" denote the field values downstream and upstream, i.e. immediately before and after the respective boundary following the positive radial direction. Over the endothelium boundary, downstream would refer to the lumen domain, which is simplified in this model. Due to the simplification, all drug concentrations related to the lumen domain are assumed null ($c_{\text{lum}} = 0$). The lumen simplification is described in more detail in subsection 3.1.1.

3.6.2 Perfect sink

Drug sinks are boundary conditions designed to allow the clearance of drug from the model domains. Essentially, they relate to the ephemerous behaviour of drug in the arterial environment. In this model, perfect drug sinks are defined as $c = 0$ over $\Gamma_{\text{ET, de}}$ and Γ_{periv}. To some extent, the semi-permeable barrier defined over the intact endothelium also allows "leakage" of drug from the arterial wall, according to the value of $J_{\text{s, ET, in}}$ in Equation 3.6.1.

The denuded endothelium boundary ($\Gamma_{\text{ET, de}}$) represents the intervention-struck superficial region of the artery, which is left devoid of its protective layer of endothelial cells after the DCB deployment. The regulation of pressure and drug concentration behaves differently at the denuded endothelium compared to its intact counterpart.

During the duration of drug delivery ($0 < t < t_0$), the drug flux J_{DCB} is prescribed over the $\Gamma_{\text{ET, de}}$ boundary length. Afterwards, the condition is overridden by a drug sink, allowing

drug clearance through this boundary. Due to the lumen simplification, the drug wash-off to the lumen may be reasonably approximated as a sink condition. Continuity of concentration is then enforced with the drug concentration in the lumen, $c_{\text{lum}=0}$, configuring a perfect sink. A perfect sink condition is characterised by continuity with a null concentration ($c = 0$), providing an endless gradient of the free drug as $\Delta c = c - 0 > 0$ for any value of positive concentration c. This essentially enables rapid clearance of drug at those boundaries.

The multistep transient condition at the denuded endothelium is given by:

$$\begin{cases} J_{\text{DCB}} & 0 < t < t_0 \\ c \;=\; 0 & t \geq t_0, \end{cases} \tag{3.6.3}$$

where J_{DCB} is the drug flux expression defined in Section 3.5, t_0 is the duration of DCB drug delivery, and $c = 0$ represents a perfect sink condition of free drug concentration.

Likewise, drug is allowed to exit the arterial wall through its outer surface, at the perivascular end (Γ_{periv}), via a perfect sink:

$$c \;=\; 0 \qquad \text{on } \Gamma_{\text{periv}}. \tag{3.6.4}$$

The modelling of drug sinks allows drug to continuously flow outwards through these boundaries over time, eventually leading to complete drug drainage from the arterial wall.

3.6.3 Zero-flux

The arterial wall is enclosed by zero-flux conditions at the remaining boundaries. Simply, that insulates the drug concentration fields within the domains delimited by these boundaries.

$$-\mathbf{n} \;\cdot\; (J + \mathbf{u}c) \;=\; 0 \qquad \text{on } \Gamma^{\text{wall}}_{\text{sym},\,z} \text{ and } \Gamma^{\text{wall}}_{\text{ext}}, \tag{3.6.5}$$

where J is the diffusive flux.

The arterial wall length was designed such that the boundary condition at the extremities does not have any notable impact on the quantities of interest calculated within the therapeutic domain. This rationale is based on [72]. Remarkably, the length of the artery segment considered in the model was found to resemble the common length of excised arteries in preclinical experiments, where similar measurements are taken [81].

Table 3.10 summarises the set of boundary conditions concerning drug transport between and out of the domains of the multilayered arterial wall, and Table 3.11 summarises the parameters utilised to define the semi-permeable membranes.

Table 3.10: Summary of boundary conditions on drug transport. The transient boundary condition, presented in Equation 3.6.3, is indicated as "condition during drug delivery / condition after drug delivery".

Type	Expression	Boundary
Prescribed flux / Perfect sink	J_{DCB} / $c = 0$	$\Gamma_{\text{ET, de}}$
Flux through semi-permeable membrane	$J_{\text{s, ET}}$	$\Gamma_{\text{ET, in}}$
Flux through semi-permeable membrane	$J_{\text{s, IEL}}$	Γ_{IEL}
Flux through semi-permeable membrane	$J_{\text{s, EEL}}$	Γ_{EEL}
Perfect sink	$c = 0$	Γ_{periv}
Zero-flux	$-\mathbf{n} \cdot (J + \mathbf{u}c) = 0$	$\Gamma^{\text{wall}}_{\text{sym, } z}$
Zero-flux	$-\mathbf{n} \cdot (J + \mathbf{u}c) = 0$	$\Gamma^{\text{wall}}_{\text{ext}}$

Table 3.11: Summary of model parameters relevant to fluid flux through the semi-permeable membranes, considering plasma as the fluid.

Parameter	Description	Value	Reference
$L_{\text{p, ET}}$	Hydraulic conductivity of endothelium	$2.2 \cdot 10^{-12}$ m^2 s / kg	[62]
$L_{\text{p, IEL}}$	Hydraulic conductivity of IEL	$2.2 \cdot 10^{-9}$ m^2 s / kg	[62]
$L_{\text{p, EEL}}$	Hydraulic conductivity of EEL	$2.2 \cdot 10^{-9}$ m^2 s / kg	[63]
P_{ET}	Permeability of endothelium	$3.6 \cdot 10^{-6}$ m / s	[62]
P_{IEL}	Permeability of IEL	$9.6 \cdot 10^{-6}$ m / s	[62]
P_{EEL}	Permeability of EEL	$9.6 \cdot 10^{-6}$ m / s	[63]
s_{ET}	Sieving coefficient of endothelium	0.855	[62]
s_{IEL}	Sieving coefficient of IEL	1	[62]
s_{EEL}	Sieving coefficient of EEL	1	[63]

3.7 Computational set-up

The model was set up in COMSOL Multiphysics® version 6.1 (COMSOL AB, Stockholm, Sweden), a commercial finite element analysis software that numerically solves differential equations based on the finite element method (FEM). The software choice was determined by three factors: (I) the need to model interdependent and simultaneous processes, (II) reliable expert assistance from both the software company's support service and fellow researchers, and (III) previous positive experiences with the software within the research group, demonstrating its feasibility.

In summary, the model geometry was created, its physics defined using a continuum modelling approach, discretised into a finite element mesh and then solved numerically. The software provided a somewhat intuitive interface for setting up multiphysics.

Study steps

The current model's multiphysics is composed of drug transport and retention physics coupled with transmural filtration physics. While the evolution of drug concentrations over the model domains must be calculated in a time-dependent fashion, i.e. at every time step of the simulation, the behaviour of transmural filtration does not require such temporal resolution. The conditions that affect transmural filtration in this model only change once, as previously indicated in Equation 3.3.3. In between this step-like change in pressure constraints, the transmural advective field is assumed to remain constant. Therefore, a stationary calculation of transmural filtration physics is proposed.

The calculation of transmural filtration is performed in two instalments of stationary simulations, using each of the transient boundary conditions of pressure as presented in Equation 3.3.3. The outcome of this is two constant transmural advective fields, which are used to sequentially inform the advective term of the drug transport equations, respectively during and after the DCB drug delivery.

The sequence of interconnected stationary and time-dependent steps, combining transmural filtration and drug transport and retention physics is organised as:

1. Stationary step to define the transmural advective field during DCB drug delivery, using the increased inflation pressure $p_{\text{ET, de}} = p_{\text{DCB}}$.

2. Time-dependent step to calculate the spatiotemporal evolution of drug concentrations, while applying the drug flux expression J_{DCB} to represent drug delivery from DCB, for $0 < t < t_0$.

3. Stationary step to update the transmural advective field after DCB drug delivery, using the physiological luminal pressure $p_{\text{ET, de}} = p_{\text{lum}}$.

4. Time-dependent step to calculate the spatiotemporal evolution of drug concentrations until the end of the simulation, for $t_0 \leq t \leq 28$ days.

Each subsequent step receives information from the previous step, effectively connecting the simulation results for post-processing convenience.

This model architecture was originally developed for the work in [72]. This design intends to avoid repeated and unnecessary calculations of the transmural fields throughout the simulation, with the benefit of reducing the number of degrees of freedom solved for.

The following text reports the efforts of setting up a robust numerical implementation for the governing equations and boundary conditions of the model. For brevity, a sufficient spatiotemporal resolution is required to capture the model's physics over its domains, and thus permit its simulation. In the model presented in this Chapter, the simulation of transmural filtration physics was found to be trivial. However, the greatest challenges were found to be related to simulating drug transport and retention phenomena, specifically at (I) the region near the drug source and (II) the region where drug binding is assumed to happen. The thin intima domain at (I) is marked by brisk drug concentration gradients, during the drug delivery from DCB and soon afterwards when the luminal drug sink is enabled. Meanwhile, the rate of drug binding onto specific receptors at (II) is of substantial magnitude due to the product of k_{on}^{s} and c, as introduced in Section 3.4, particularly at early moments when free drug availability is at its highest. Furthermore, the dependence on c causes the drug retention physics, and thereby the mesh resolution requirement, to depend on the amount of drug delivered to the tissue. For instance, the "High dose" scenario, defined earlier in Section 3.5, was found to be the most computationally challenging to simulate. An analysis of the non-dimensional Damköhler numbers, which relate the rates of reaction and mass transport, could enrich this understanding.

Together, these rapid behaviours demand a sufficient spatiotemporal resolution throughout (I) and (II). From the iterative inspection and manual tuning of meshing and solver settings, a satisfactory combination of those was eventually achieved, enabling the simulations of all case scenarios considered.

Meshing

As intrinsic to the FEM, the model equations were calculated spatially over a mesh of elements, which discretised the model geometry domains.

The model used a structured 2D quadrilateral mesh, mapped as a regular square grid of mesh elements defined onto each domain. This meshing technique allowed for the manipulation and tailoring of the mesh dimensions in the multidomain geometry of the model until the mesh element quality criteria were satisfactory. Following a largely empirical fine-tuning process, the satisfactory mesh configuration consisted of 31800 quadrilateral elements, 2559 edge elements, and 13 vertex elements in total, boasting average and minimum mesh element quality values of 1.0 and 0.9782, respectively, according to COMSOL's definition of mesh element quality ("0.0

represents a degenerated element, and 1.0 represents the best possible element." [93]). Boundary layer elements were employed to provide additional refinement at the edges of domains e.g. at $\Gamma_{\text{ET, de}}$ and Γ_{IEL} where sizeable gradients are expected. This mesh configuration, displayed in Figure 3.5, was devised to be utilised in all simulations of this Chapter.

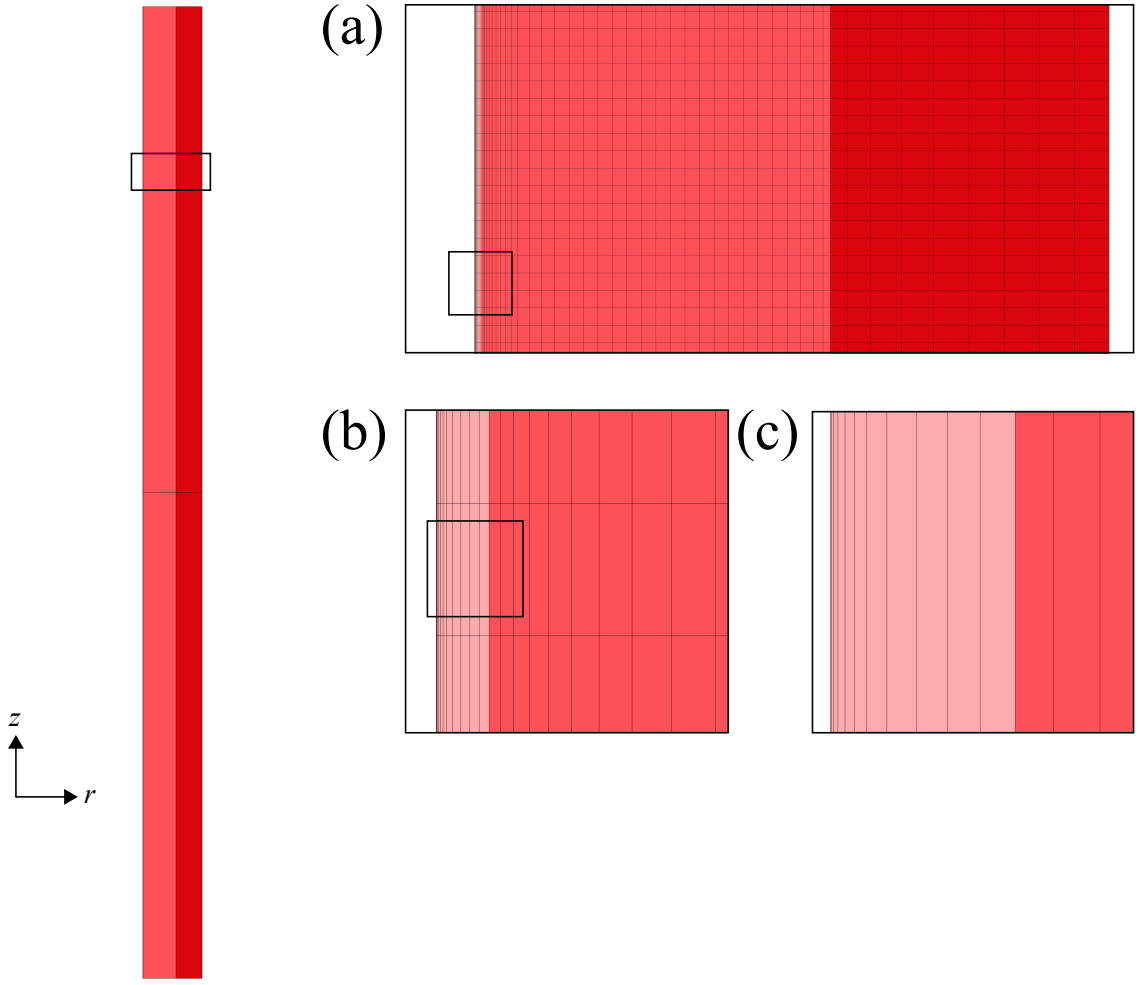

Figure 3.5: Schematic of mesh. The insets (a-c) detail the mesh composition of the multilayer arterial wall with increased magnification.

Solver settings

Alongside meshing, an exhaustive manual tuning of solver settings was performed to enable and improve the convergence of the model's multiphysics simulations. For consistency, a single solver settings configuration was devised and used in the different models presented in Chapters 3, 4 and 5 of this work. A more detailed explanation of the adjustment of solver settings can be found later in the computational set-up Section 5.5, where the worst-case scenario in terms of computationally challenging simulations was tackled.

Computational specifications and computation time

The resulting system of time-dependent partial differential equations (PDEs) was solved using a Parallel Direct Sparse Solver (PARDISO). The computation was performed using an AMD Ryzen 9 5950X 16-Core CPU @ 3401 MHz processor, with 32 Logical Processors. The computation time of the simulations carried out varied approximately between 4 and 6 hours.

3.8 Results

The previous Sections defined the governing physics of the model and its computational set-up. Once the model is simulated *in silico*, it generates spatiotemporal information on the drug distribution over the model domains, representing an idealised arterial wall undergoing pharmacological therapy from a DCB. Based on previous drug modelling principles [78], drug concentration is observed in three distinct phases: free (c), bound to specific binding sites (b^{s}), and bound to non-specific binding sites (b^{ns}). The drug concentration fields $c(r, z, t)$, $b^{\text{s}}(r, z, t)$, and $b^{\text{ns}}(r, z, t)$ are defined as scalar fields over their respective domains, and, for simplicity, referred to as c, b^{s}, and b^{ns}. Clinically relevant information can be quantified from these results, permitting the assessment of the drug delivery and subsequent drug retention in the tissue. The key drug quantities of interest proposed to be measured from the simulation results are presented next.

3.8.1 Drug release profile

The drug that is released from the DCB during deployment can be quantified and expressed in a drug release profile. The drug release profile is a relationship between the cumulative fraction of the drug released versus time. Because the fraction of drug released is a relative measurement, it requires information on the initial drug load of the device. While usually available from the manufacturer's specifications, the initial drug load on the medical device is unclear when modelling the DCB effect as a temporary drug influx. Therefore, this Chapter proposes a mass-based quantification of drug delivery from the DCB.

In the previous Section 3.5, a simplified drug source was defined in terms of a drug flux expression. To facilitate the comprehension of the drug delivery magnitude in the current problem of interest, the assessment of the amount of drug delivered by the DCB is proposed in terms of a total drug mass influx. Equation 3.8.1 expresses how the total drug mass influx is derived:

$$\dot{m}_{\text{DCB}}(t) \;=\; J_{\text{DCB}}\; A_{\text{ET, de}}\; M_{\text{sir}}, \tag{3.8.1}$$

where J_{DCB} is the prescribed drug flux expression, given in mol/(m^2 s); $A_{\text{ET, de}} = \pi\, d_{\text{lum}}\, \ell_{\text{ET, de}}$ is the drug delivery surface area, measured over the entire denuded endothelium surface; and M_{sir} is the molar mass of the drug. The choice of variable name as "influx" is designed to indicate the direction of the flux — as entering the arterial wall domains.

Similarly to the original flux presented in Section 3.5, the mass-based influx $\dot{m}_{\text{DCB}}(t)$ can be integrated over time to result in the cumulative drug mass delivered to the tissue by the DCB:

$$m_{\text{DCB}}(t) \;=\; \int_0^t \dot{m}_{\text{DCB}}(t)\, dt. \tag{3.8.2}$$

3.8.2 Drug content

Drug content (DC) is a mass relation that expresses the amount of drug present in a given mass of arterial tissue, commonly used in preclinical experiments and computational simulations to evaluate the permanence of drug following delivery [94]. The value of DC is commonly referred to as a preclinical indicator of the safety and performance of the drug therapy [7, 33]. It is a non-dimensional quantity, usually given in units of drug mass per unit mass of tissue (ng/mg or μg/g).

In preclinical studies, DC is measured over a section of an excised artery — the therapeutic domain defined earlier in Section 3.1. The measurement is usually taken at different time points after the drug delivery, e.g. at one hour, one day, three days, seven days, and 28 days [81]. Moreover, the measurement is carried out on different subjects for statistical significance. This provides some information on the long-term permanence of drug in the arterial tissue at discrete time intervals.

In silico, DC is calculated by combining the drug mass and tissue mass contributions of each artery layer in the therapeutic domain via spatial integrations. At any given moment of the simulation, DC is given by:

$$DC(t) \;= \sum_{i} \frac{M_{\text{sir}} \int_{\Omega_{\text{wall}}} (c + b^{\text{s}} + b^{\text{ns}})\; d\Omega_i}{\rho\; V_i} \qquad \text{for } i = \{\text{int, med, adv}\} \tag{3.8.3}$$

where M_{sir} is the molar mass of the drug; c, b^{s}, and b^{ns} are the spatiotemporal variables representing the free, specifically-bound, and non-specifically-bound drug concentrations, if applicable; ρ is the density of arterial tissue, assumed constant in all layers; V_i is the volume of layer i; and i is the name of any given artery layer.

Alternatively, the spatial integration may be performed over a combined domain that encompasses all artery layers within the therapeutic domain, $\Omega^T_{\text{wall}} := \Omega^T_{\text{int}} \cup \Omega^T_{\text{med}} \cup \Omega^T_{\text{adv}}$, corresponding to the domain highlighted in blue in the previous Figure 3.3.

3.8.3 Receptor saturation

The concepts of specific and non-specific receptor saturation (sRS and $nsRS$) are theoretical relations of drug retention capacity. They are defined as the amount of drug retained at a given moment compared to the maximum capacity of the receptor, assuming that the binding sites are limited and can saturate [61]. Both types of receptor saturation are non-dimensional quantities, usually given as percentages, and can range from 0% to 100%.

The value of sRS can serve as a potentially more objective and representative indicator of therapy efficacy in comparison to DC. This is because sRS is related directly to the drug retention capacity of the specific cell receptors that the therapy is targeting. Sustained saturation of specific binding sites throughout the healing period signifies a good performance of the drug

therapy at providing the cell receptors with an antiproliferative drug, which may indicate high therapeutic efficacy [64, 94].

Meanwhile, $nsRS$ represents a secondary pathway for drug retention. In a somewhat collateral fashion, the free drug is bound to non-specific receptors (e.g. interstitial tissue and extracellular matrix) following the same binding equation logic but with substantially different parameters. Although not the target of the therapy, non-specific receptor binding considerably influences the distribution of drug in the tissue. Additional comments are provided in the Discussion of Chapter 5.

Remarkably, it is currently unfeasible to measure these quantities experimentally *in vivo*. In the current model, receptor saturation is calculated in the therapeutic media domain, where binding is assumed to occur, as the total bound drug mass divided by the total binding site capacity. Respectively, sRS and $nsRS$ are:

$$\begin{aligned} sRS(t) &= \frac{\int_{\Omega_{\text{med}}} b^{\text{s}}\, d\Omega_{\text{med}}}{\int_{\Omega_{\text{med}}} b^{s}_{\text{max}}\, d\Omega_{\text{med}}} \\ &= \frac{\int_{\Omega_{\text{med}}} b^{\text{s}}\, d\Omega_{\text{med}}}{b^{s}_{\text{max}}\, V_{\text{med}}}, \end{aligned} \tag{3.8.4}$$

$$\begin{aligned} nsRS(t) &= \frac{\int_{\Omega_{\text{med}}} b^{\text{ns}}\, d\Omega_{\text{med}}}{\int_{\Omega_{\text{med}}} b^{\text{ns}}_{\text{max}}\, d\Omega_{\text{med}}} \\ &= \frac{\int_{\Omega_{\text{med}}} b^{\text{ns}}\, d\Omega_{\text{med}}}{b^{\text{ns}}_{\text{max}}\, V_{\text{med}}}. \end{aligned} \tag{3.8.5}$$

To achieve the therapeutic goals of drug delivery, the literature suggests that it is desired to maintain the value of DC above 1 ng/mg [33, 47], and the value of sRS as high as possible, i.e. 100%, during the therapy window. The model observes drug indicators over a period of 28 days, based on reference preclinical studies from the collaborating company [81].

3.8.4 Model verification

The inclusion of the longitudinal direction (z) in the model geometry is justified to allow comparability with the preclinical indicators of safety and efficacy (DC and sRS), which consider a certain length of artery segment. For this reason, a simpler model geometry such as a 1D model cannot produce comparable results for the desired measurements since these are calculated over a domain extended in the longitudinal direction. Nonetheless, aiming to strengthen the verification of the model, a series of comparisons are provided considering the following versions of the model:

(I) 1D, calculated over a uni-dimensional line with cylindrical coordinates

(II) Pseudo-1D, with a single element in the longitudinal direction

(III) 2D-Axisymmetric, featuring the full geometry as presented in Section 3.1.

Figure 3.6 compares the total drug concentration ($c + b^{s} + b^{ns}$) in the radial direction in the middle of the problem for (I), (II), and (III) at several time points throughout the simulation. The overlapping of curves of the three model versions (solid green, dashed blue, and dotted yellow) indicates that the results are reasonably comparable.

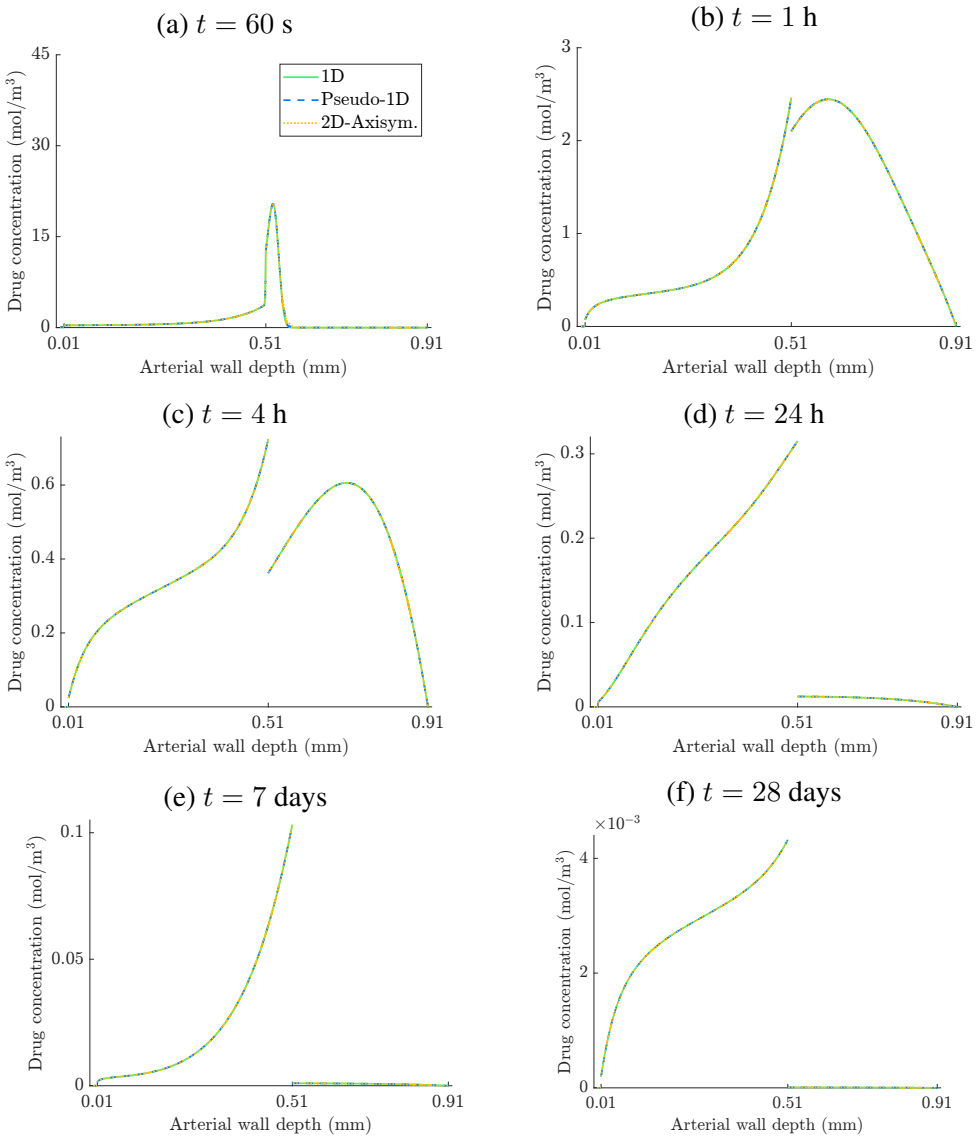

Figure 3.6: Comparison of total drug distribution ($c+b^{s}+b^{ns}$) over a middle radial line across the arterial wall, obtained via three different model versions. The case considered is "High dose", 60-s drug delivery, and increased inflation pressure enabled.

Additionally, a similar observation of drug concentrations over a central radial line is proposed to obtain insights into the contribution of each drug transport and retention mechanism.

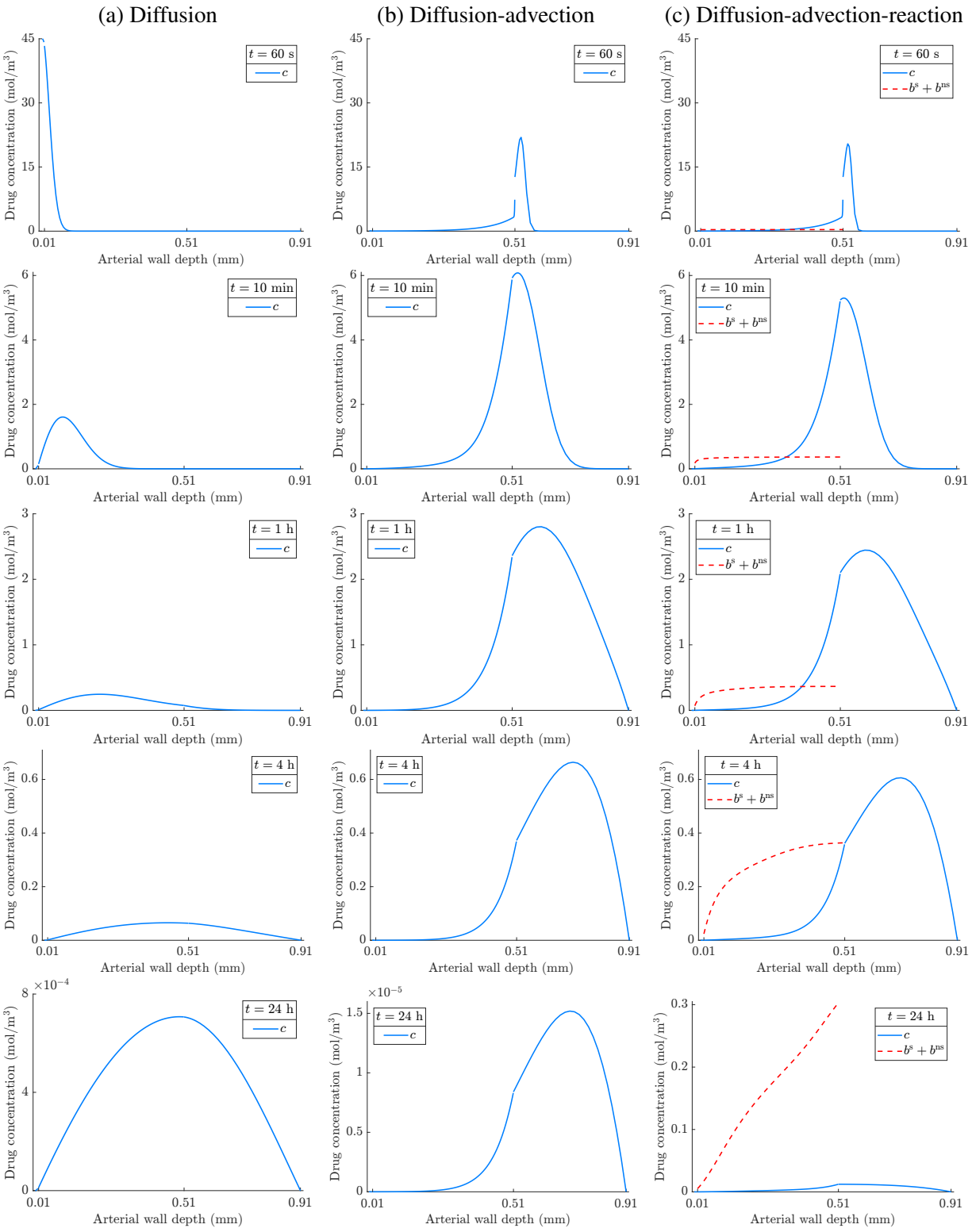

Figure 3.7: Temporal evolution of drug distribution over a radial line across the arterial wall, considering a "High dose" 60-s drug delivery. To observe the contribution of each drug transport mechanism, separate cases are simulated considering governing equations featuring a combination of (a) diffusion, (b) diffusion-advection, and (c) diffusion-advection-reaction. The values shown in the horizontal axis correspond to the spatial limits of each artery layer. Common vertical axes are used to facilitate comparison, except for the last set of figures, at $t = 24$ h.

Figure 3.7 provides pertinent observations about the role of each drug transport and retention mechanism. Solely with diffusion, the drug delivered concentrates near the luminal end of the arterial wall ($t = 60$ s). In contrast, the drug is transported deeper into the wall with the addition of advection at the same early times. A major consequence of this greater penetration is the lesser wash-off via luminal sink, favouring drug retention, which may be appreciated at subsequent times. The discontinuities in drug concentration observed at the extremes of each layer are due to the semi-permeable membranes (present at Γ_{IEL} and Γ_{EEL}). Also, when comparing drug concentration magnitudes one must account for the effect of radial coordinates in the problem; that is, elements farther in the radial direction are slightly larger and thus require more drug to achieve the same concentration (a top view may illustrate this).

The addition of the reaction term has a lesser effect at early times, when free drug availability is the highest, since the total bound drug capacity is of relatively modest magnitude ($b^{\text{s}}_{\text{max}} + b^{\text{ns}}_{\text{max}} = 0.3663$ mol/m^3). However, at later times free drug is practically depleted while bound drug persists. At $t = 24$ h, the last time featured in this observation, the order of magnitude of drug concentration differs greatly between cases (a), (b), and (c). The characteristic magnitude of each case is depicted in their vertical axes. Remarkably, the advection mechanism, which favoured drug retention early, also propels free drug towards the perivascular sink, propitiating drug wash-off at late times. At later times, retention in the arterial wall is almost exclusively in bound drug phase. Therefore, observing indicators objectively related to bound drug retention, such as receptor saturation, becomes increasingly relevant as the therapy progresses.

In silico models conveniently permit the experimentation of procedural parameters and modelling assumptions for hypothesis testing and gathering of mechanistic insights. This ability is exemplified by the simulation of a few scenarios and assessment of the drug quantities of interest, as listed in Table 5.14, followed by a brief interpretation of their results.

Table 3.12: Summary of simulation results presented.

Quantity	Description	Physical unit	Definition
$\dot{m}_{\text{DCB}}(t)$	Total drug mass influx	μg/s	Equation 3.8.1
$m_{\text{DCB}}(t)$	Cumulative drug mass delivered	μg	Equation 3.8.6
$DC(t)$	Drug content	ng/mg	Equation 3.8.3
$sRS(t)$	Specific receptor saturation	%	Equation 3.8.4
$nsRS(t)$	Non-specific receptor saturation	%	Equation 3.8.5

3.8.5 Varying drug dose

The first scenario featured in this study explored the effect of varying the drug flux expressions considered, "Low dose" and "High dose". Based on the usual values of DCB application duration as reported by [32], the delivery duration was chosen as $t_0 = 60$ s. This duration derives from empirical clinical knowledge and represents a balance between sufficient drug delivery and arterial disturbance, considering that DCB inflation partly or completely blocks blood flow in the lumen. Such an effect is tolerable for a small duration due to the coronary collateral circulation, which diverts blood supply.

Figure 3.8 presents the simulation results regarding the drug quantities of interest. Subfigures 3.8 (a) and (b) show a remarkable difference in the magnitude of the drug flux expressions, which justifies their naming convention. Intuitively, subfigure 3.8 (c) shows that a greater dose of drug delivery provides more drug mass delivered, thereby higher levels of drug in the tissue early. However, despite the different early peak values, late DC values are remarkably similar as shown in the adjacent table. Finally, subfigure 3.8 (d) suggests that the drug mass delivered by the "High dose" flux is almost sufficient to achieve complete specific binding site saturation at around 3 days, while the "Low dose" is insufficient. The long-term retention behaviour is remarkably comparable for either dose.

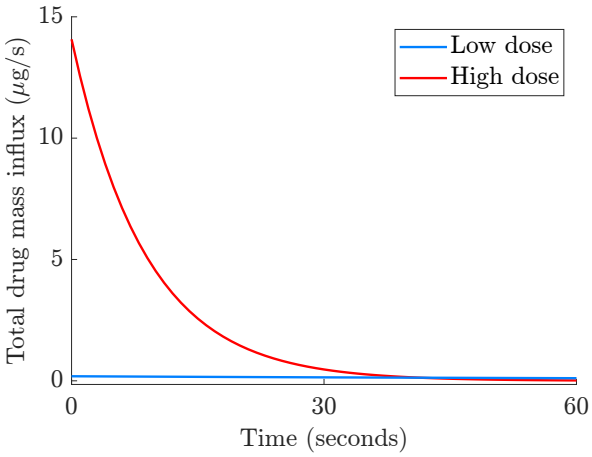

(a)

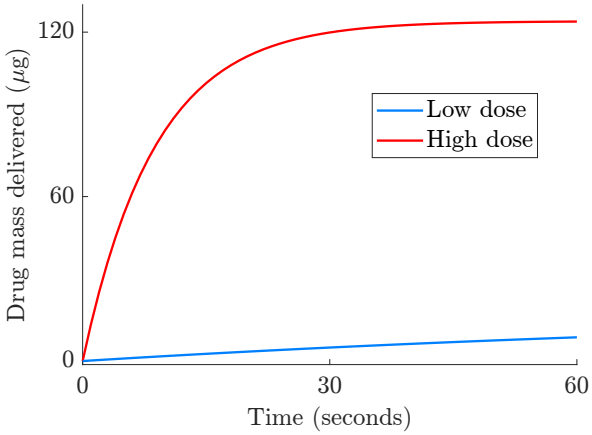

(b)

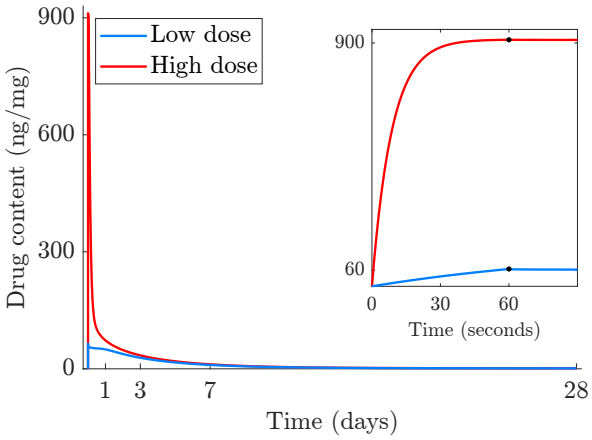

(c)

Case	Peak DC (ng/mg)	Final DC (ng/mg)
Low dose	63.98	1.22
High dose	911.73	1.27

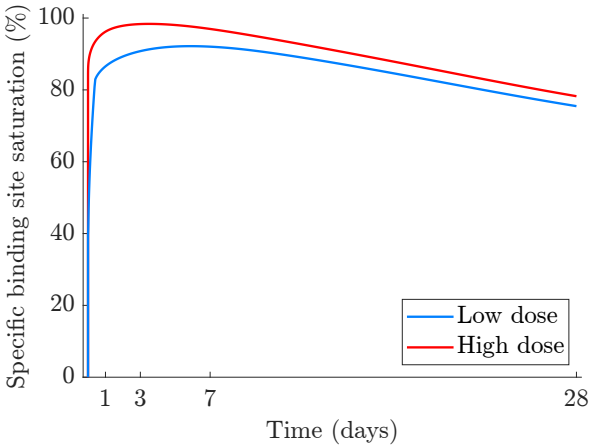

(d)

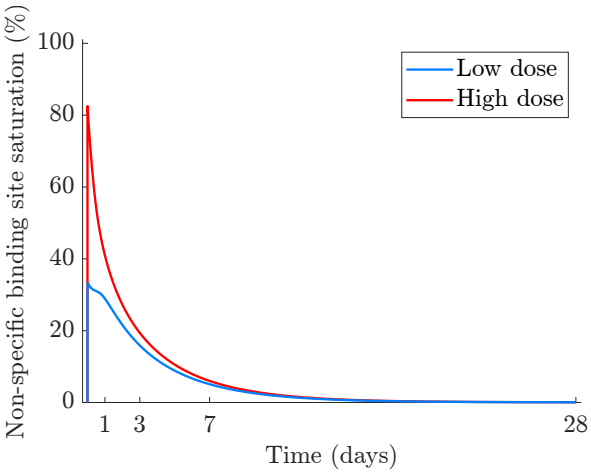

(e)

Figure 3.8: Overview of simulation results while varying the drug flux expression ("Low dose" and "High dose") for a single drug delivery duration (60 s), regarding (a) total drug mass influx, (b) cumulative drug mass delivered, (c) drug content, and (d) specific and (e) non-specific binding site saturation. The table beside (c) informs particular drug content values at its peak, soon after DCB delivery, and final, at 28 days.

3.8.6 Influence of increased inflation pressure

The second scenario featured in this study probed the influence of having an increased pressure value at the drug delivery surface. The rationale of this supposition is that a pressure increase, although temporary during the short time window of drug delivery, should amplify the transmural advective field and thus affect drug distribution to some extent. This analysis was originally proposed in [72].

Based on the assumptions of temporary increased pressure due to balloon inflation of [67], [95], and [72], two different pressure values were chosen for $p_{\text{ET, de}}$ during DCB delivery: $p_{\text{lum}} = 100$ mmHg or $p_{\text{DCB}} = 8$ atm. Respectively, they represent having the increased pressure disabled or enabled, such that "off":= physiological pressure only and "on":= increased pressure during DCB delivery. Again, each of the drug flux expressions is considered, "Low dose" and "High dose". In total, four cases were observed:

- Low dose, off
- Low dose, on
- High dose, off
- High dose, on

Figure 3.9 presents the simulation results regarding the drug quantities of interest for the aforementioned cases, except for $\dot{m}_{\text{DCB}}$ and m_{DCB} since they are solely dependent on the prescribed drug flux expression and indifferent to other procedural parameters. Remarkably, the same drug mass is delivered among curves of the same colour, as their delivery rate is given by the same prescribed drug flux expression. Subfigure 3.9 (a) shows a dramatic abrupt decay in DC levels when increased pressure is absent. Despite of it, the amount of drug delivered by the "High dose" flux is still sufficient to reach the binding sites with similar outcome. The slightly different peak DC values are attributed to the marginal wash-off at the edges of the denuded endothelium, through the intact endothelium, which behaves differently when the advective term is amplified. Subfigure 3.9 (b) shows that including increased pressure alters the long-term retention in the tissue, for the same given amount of drug mass delivered. This effect is more noticeable when less drug is available, as in the "Low dose" case.

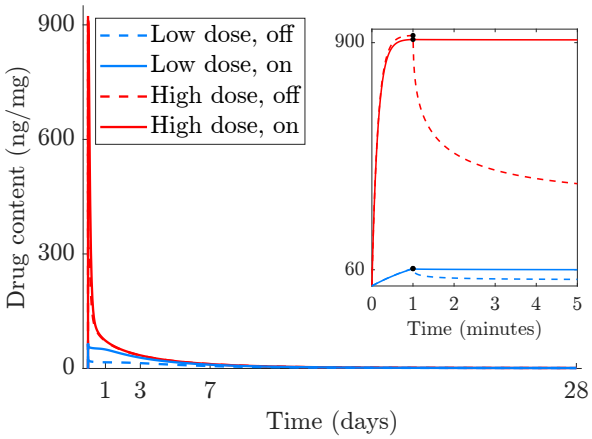

(a)

Case	Peak DC (ng/mg)	Final DC (ng/mg)
Low dose, off	64.81	1.16
Low dose, on	63.98	1.22
High dose, off	926.49	1.27
High dose, on	911.73	1.27

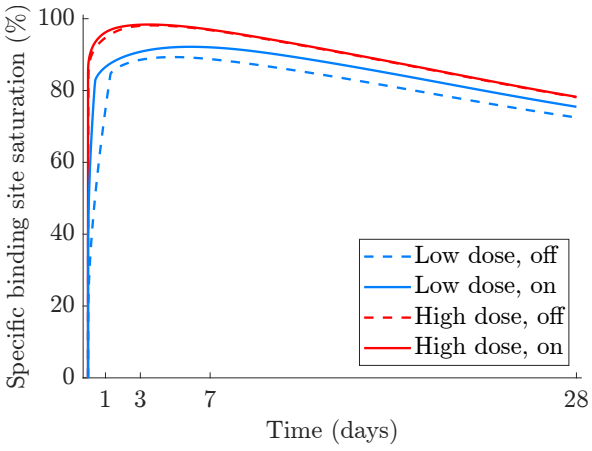

(b)

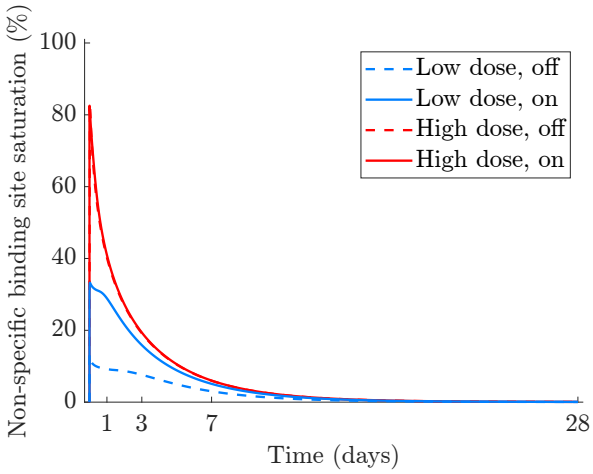

(c)

Figure 3.9: Overview of simulation results while varying the drug flux expression ("Low dose" and "High dose") and enabling increased inflation pressure ("off" and "on"), regarding (a) drug content, and (b) specific and (c) non-specific binding site saturation. Total drug mass influx and cumulative drug mass delivered are excluded for being expressions solely dependent on time. The table beside (a) informs particular drug content values at its peak, soon after DCB delivery, and final, at 28 days.

Beyond the indicators presented in Figure 3.9, it is of utmost interest to observe the spatial drug concentration between the cases "off" and "on". Figure 3.10 depicts qualitatively the spatial distribution of total drug concentration over the therapeutic domain at three instants, 60 seconds, 1 hour, and 1 day from the beginning of the simulation, considering the "High dose" drug flux expression. Subfigures 3.10 (d-f) show a deeper penetration of drug when the increased pressure is present.

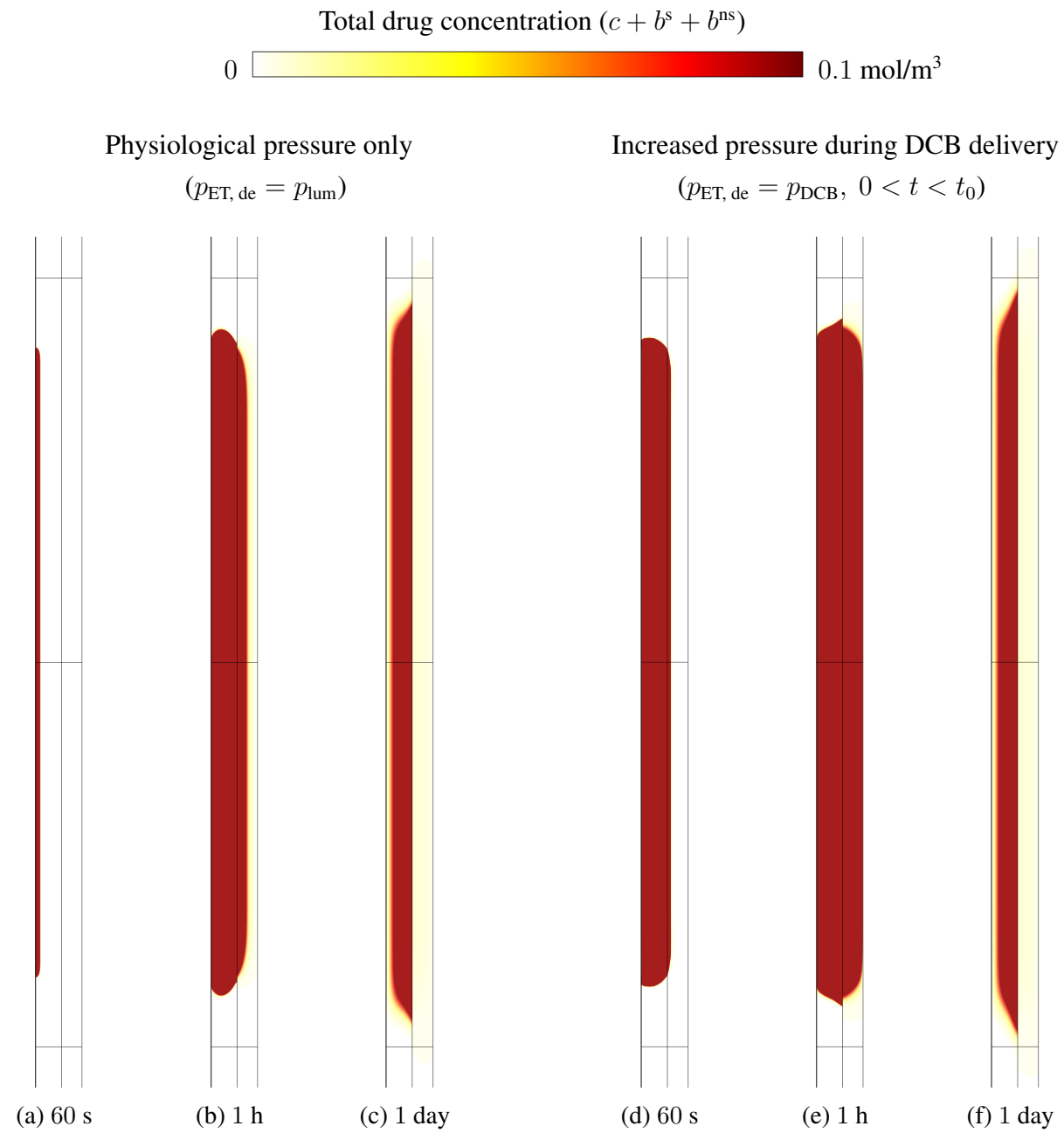

Figure 3.10: Spatial distribution of drug over the therapeutic domain at early times, depicting the effect of increased pressure during DCB delivery. Subfigures (a-c) exclude the increased pressure during DCB delivery, while subfigures (d-f) include it, assuming a pressure magnitude of $p_{DCB} = 8$ atm. The drug flux expression considered is "High dose". The magnitude of drug concentration is illustrated using a linear colour scale from 0 to 0.1 mol/m^3.

Furthermore, the magnitude of the transmural filtration convection may be quantified over the arterial wall. Figure 3.11 (a) and (b) compare, respectively, the transmural velocity for the "off" and "on" cases to highlight the effect provoked by increased pressure during DCB delivery. Additionally, Figure 3.11 (c) provides an analysis of the Péclet number on a layer-specific basis and Figure 3.12 measures the magnitude of radial convective velocity over a radial line to enrich this understanding. The Péclet number is a dimensionless number that relates the transport rates

of convection and diffusion. In the model, it may be on a layer-specific basis defined as:

$$Pe_i = \frac{\delta_i \, u_i}{D_i} \qquad \text{for } i = \{\text{int, med, adv}\}, \tag{3.8.6}$$

where δ_i is the layer thickness, u_i is the magnitude of convection, and D_i is the diffusion coefficient as in Table 3.5. The present observation considers the range of u_i within its minimum and maximum values in the radial direction and the radial diffusion coefficient in the media.

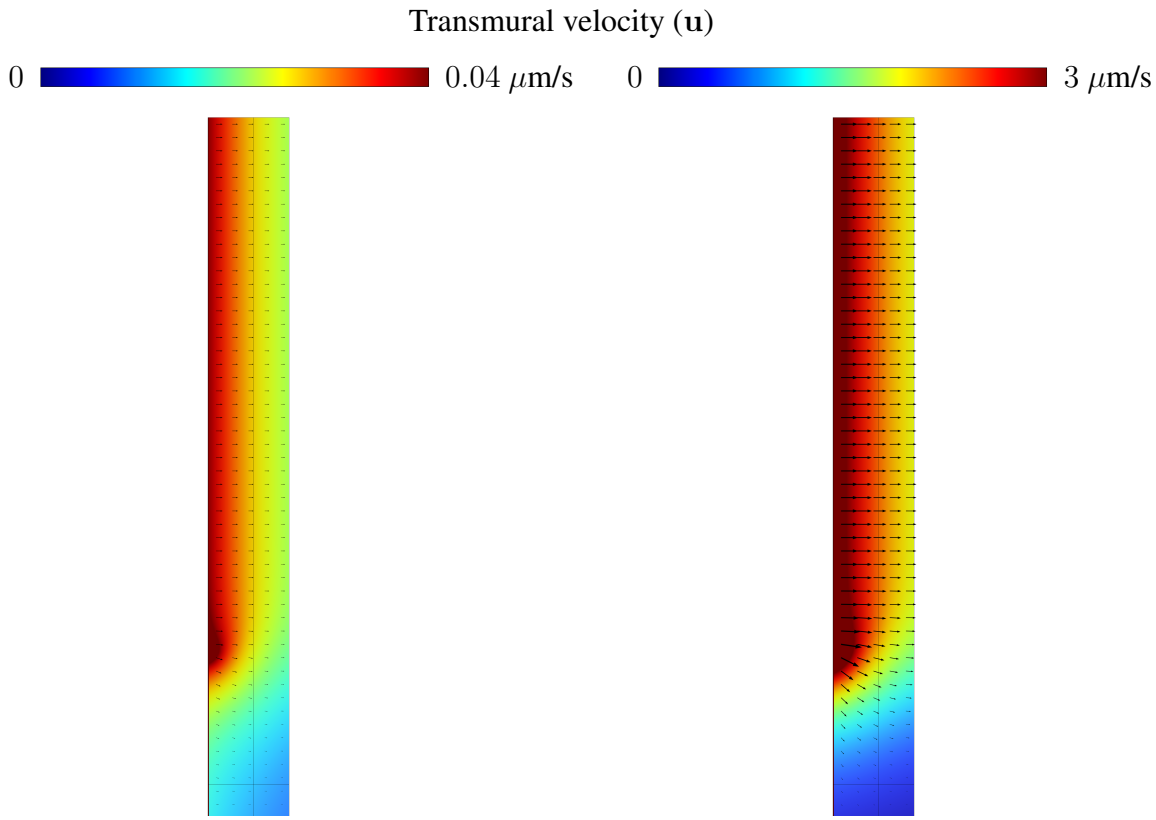

(a) $p_{\text{ET, de}} = p_{\text{lum}}$ (b) $p_{\text{ET, de}} = p_{\text{DCB}}, \; 0 < t < t_0$

Case	Pe_i range, for $i =$ int	med	adv
(a)	0.0233 – 0.0236	1.93 – 2.78	2.17 – 2.71
(b)	2.02 – 2.04	167.1 – 240.7	187.9 – 233.9

(c)

Figure 3.11: Transmural velocity field over half of the 2D-axisymmetric model geometry, with (a) physiological or (b) increased pressure applied. The magnitude of transmural velocity is illustrated qualitatively using different linear colour scales, from 0 to 0.04 μm/s or 3 μm/s. Black arrows illustrate the direction of convection. The table (c) compares the Péclet number ranges on a layer-specific basis in the arterial wall, i.e. min(Pe_i) – max(Pe_i) for the cases of (a) and (b).

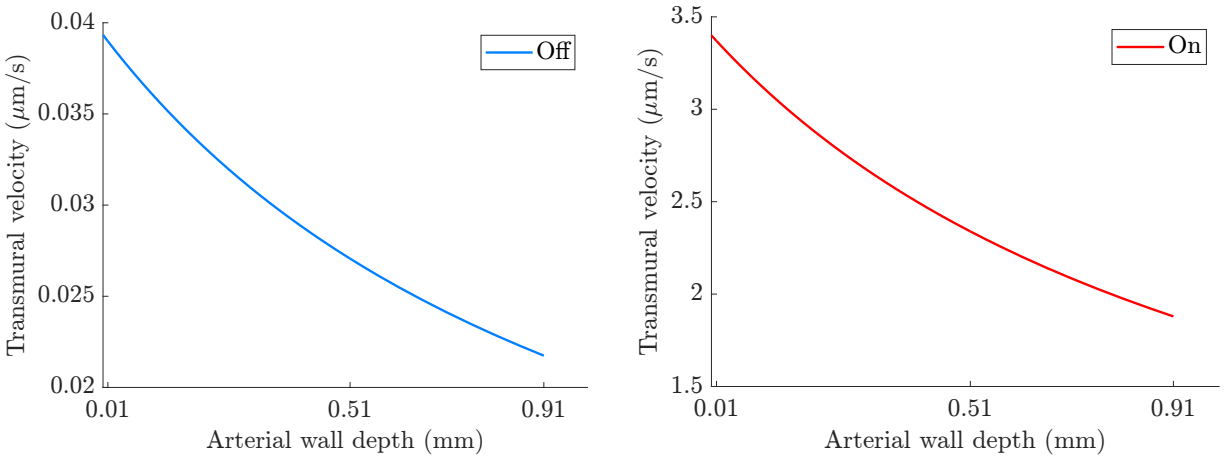

Figure 3.12: Transmural velocity magnitude in the radial direction over a middle radial line through the arterial wall. Due to the different order of magnitude between cases, they are observed separately.

In this model, the effect of having increased inflation pressure is represented as a temporary amplification of the pressure constraint, causing an increase in the convective field magnitude, which ultimately amplifies the advective mechanism of drug transport. For the duration of DCB delivery, that causes drug to be propelled deeper into the arterial wall. Such deeper penetration results in a greater reach of binding sites, of both types, as shown quantitatively in Figures 3.9 (b) and (c), and qualitatively in Figure 3.10 (d). This greater retention to binding sites is deemed to attenuate the drug wash-off via luminal sink after delivery, explaining the lesser subsequent decay in DC. A quantification of the drug loss to the luminal sink in each case is suggested to support this inference. Also, drug clearance occurring early, soon after delivery, via luminal sink, or late via perivascular sink may be assessed separately.

In conclusion, the comparison presented in subfigure 3.11 (c) indicates that drug transport is dominated by advective transport when increased pressure is applied. The assumption of increased pressure has also shown a substantial effect on the long-term drug retention behaviour in the arterial wall. However, a crucial point of discussion is about the magnitude of the increased pressure, p_{DCB}. Further discussion on this subject is provided in the next Section.

3.9 Discussion

This Section presents a summary of the modelling endeavour, mechanistic insights obtained, and limitations of the work developed, which motivates the next Chapters.

Model summary

This work aimed to produce an idealised simulation of the endovascular drug delivery procedure with a DCB. The model represented the delivery of antiproliferative drugs into a multilayered arterial wall, according to a prescribed drug flux expression. As a pressurised wet porous medium, the blood vessel exhibits transmural fluid flow (plasma) that propels the drug delivered through it. During delivery, increased pressure is applied to the lumen-wall interface to emulate the pressure due to balloon inflation — amplifying the transmural pressure gradient and thus the magnitude of advection. After delivery, both drug influx and increased pressure cease. They are replaced with a drug sink and pressure conditions, respectively, representing the luminal drug wash-off and a constant physiological blood pressure value. While traversing the wall via diffusion and advection, the drug binds reversibly to cellular and non-cellular binding sites. Drug delivery from the DCB and subsequent retention in the arterial tissue are quantified with indicators of safety and efficacy, common to what is done in the preclinical practice. The assessment of simulation results from a length-dependent and layer-specific drug distribution strongly motivates the use of a 2D-axisymmetric model.

Comparison with DES

The DCB model presented in this Chapter may be compared to models of drug delivery from drug-eluting stents (DESs) [62, 63, 80, 94, 96]. For brevity, the main difference between these two modalities relates to the presence of a reservoir for sustained release. Thereby, their time frame for drug delivery is largely different — a DCB has a 1-minute time window to deliver its full drug load, while a DES can slowly release the drug from its drug-embedded coating over months. The drug dose of DCBs is required to be higher as its time window for delivery is shorter. Consequently, the larger bolus of drug delivered from DCB results in a faster drug release profile, leading to an acute early peak in drug content in tissue versus a much smoother curve in the case of a DES.

A dedicated discussion regarding DCB versus DES is provided in [72].

Reduced binding equations

The computational burden of the simulation was a pertinent part of the model development as well as a side subject of study. It was found that the drug binding physics was responsible for most of the computational expense of the model, specifically the process of drug binding to

specific receptors. Therefore, preliminary efforts were made aiming to improve computation speed at a minimal loss of fidelity. In one of the approaches taken, a rapid binding assumption was used as a mathematical resource to simplify the computationally expensive specific binding equations. Assuming that the drug binding rate to the specific binding sites is approximately zero, b^{s} may be rearranged and expressed as:

$$\begin{aligned} \frac{\partial b^{\mathrm{s}}}{\partial t} &\approx 0 \\ k^{\mathrm{s}}_{\mathrm{on}}\, c\, (b^{\mathrm{s}}_{\mathrm{max}} - b^{\mathrm{s}}) \;-\; k^{\mathrm{s}}_{\mathrm{off}}\, b^{\mathrm{s}} &\approx 0 \\ b^{\mathrm{s}} \;&\approx \frac{b^{\mathrm{s}}_{\mathrm{max}}\, c}{\dfrac{k^{\mathrm{s}}_{\mathrm{off}}}{k^{\mathrm{s}}_{\mathrm{on}}} + c}. \end{aligned} \tag{3.9.1}$$

Effectively, this excludes one bound drug phase from the drug transport equation. The bound drug concentration b^{s} is then approximated analytically over space as a function of the free drug concentration, c. This results in an infringement of mass conservation that may be acceptable if negligible. Remarkably, $\lim_{c\to\infty} b^{\mathrm{s}} = b^{\mathrm{s}}_{\mathrm{max}}$, which is still consistent with the concept of binding site saturation. Although promising, this work is ongoing and its outcome is material for future work. To illustrate this subject, Figure 3.13 provides a preliminary comparison between pseudo-1D models with the full governing equations (diffusion-advection-reaction) and a reduced version, using the rapid binding assumption for specific drug binding. The critical difference between these approaches is the behaviour of the drug concentration in specifically-bound phase. Accordingly, the comparison features the observation of $b^{\mathrm{s}}(r, z, t)$ over a line following the radial coordinate (r), in the media layer only, where the occurrence of drug binding is assumed. The longitudinal coordinate (z) is disregarded since the pseudo-1D model features a single mesh element in that direction. A few time points are proposed to illustrate the behaviour of interest.

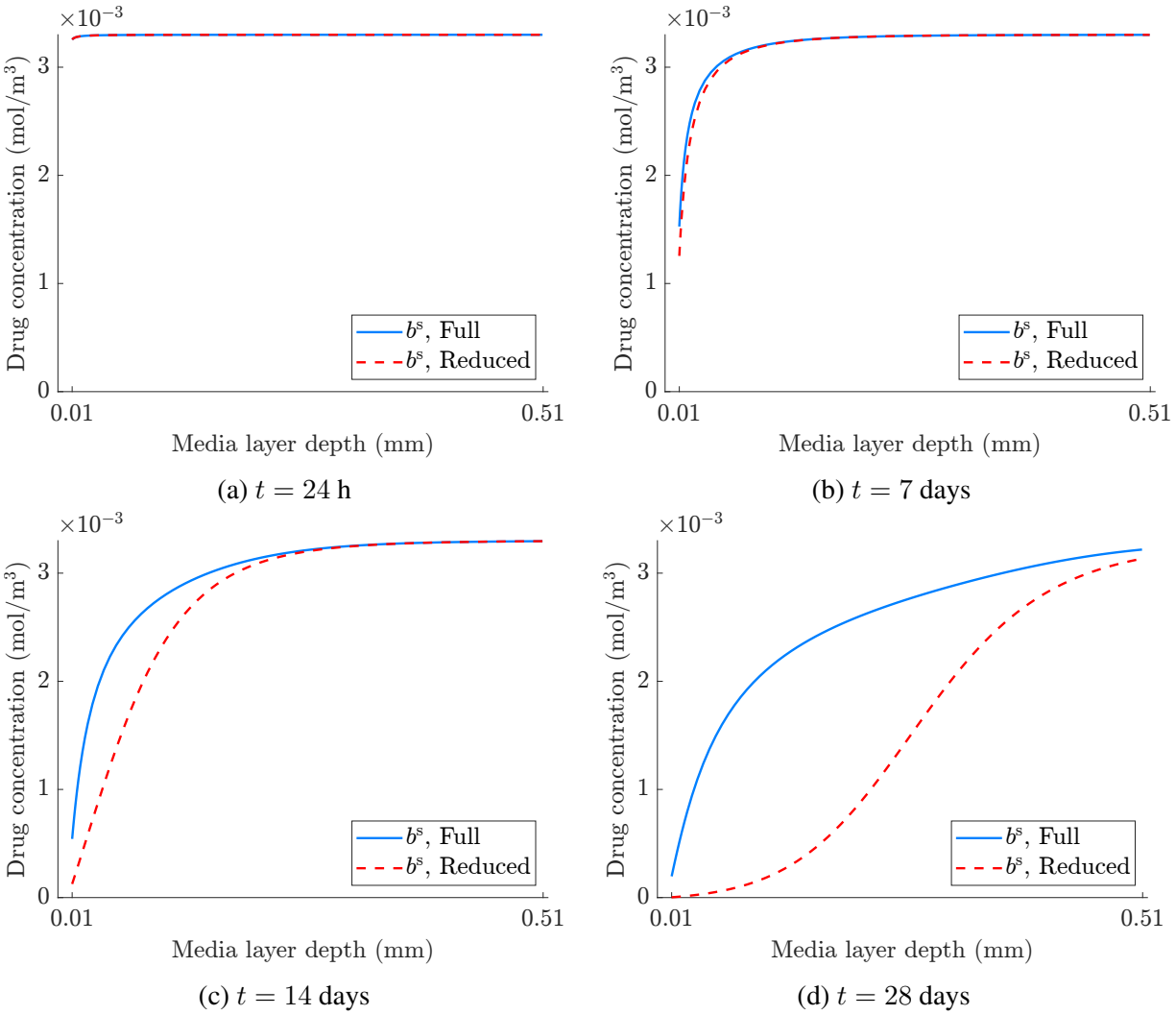

(a) $t = 24$ h (b) $t = 7$ days

(c) $t = 14$ days (d) $t = 28$ days

Figure 3.13: Temporal evolution of specifically-bound drug (b^s) distribution over a radial line across the arterial wall, following "High dose" 60-s drug delivery, at sequential time points (a–d). The values shown in the horizontal axis correspond to the spatial limits of each artery layer. Common vertical axes are used to facilitate comparison.

The behaviour of binding kinetics is summarised by the ratio of $\frac{k_{\text{off}}^s}{k_{\text{on}}^s}$, presented in Tzafriri et al. [61] as the equilibrium dissociation constant. Due to the strong specific binding, late drug retention is mainly in the specifically-bound drug phase. Therefore, the resemblance between the Full and Reduced cases in a temporal fashion can be provided simply by a receptor saturation plot.

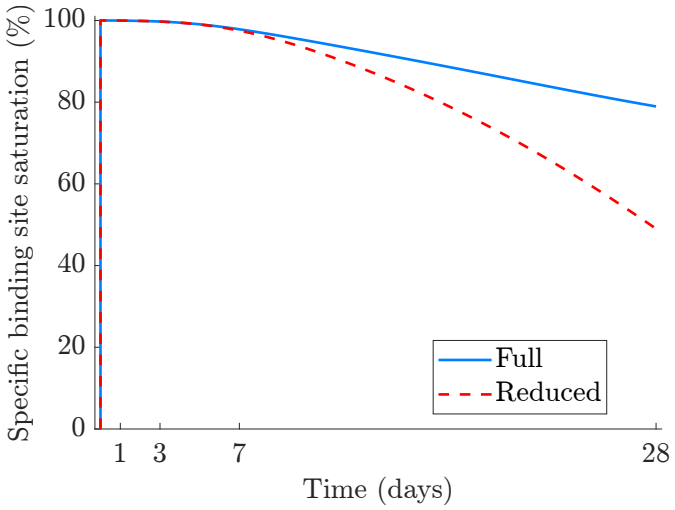

Figure 3.14: Specific receptor saturation results comparing Full and Reduced models. The monotonous behaviour is attributed to the geometrical simplicity of the pseudo-1D model.

Coating adhesion

Although modelling literature suggests that part of the coating adhering to the wall surface during delivery may act as a shield against luminal drug wash-off [66], this mechanism and its translation *in silico* are unexplored. Realistically, the perfect sink assumption used in this work may overestimate the drug losses to the lumen.

Lumen simplification

Haemodynamics are generally calculated to regard disturbed flow and wall shear stress in stented arteries. In strongly simplified geometries, such as in 2D-axisymmetric models, [72] has found haemodynamics to be largely irrelevant. For the effects of drug transport, luminal blood flow causes rapid clearance of drug from the lumen-wall interface surface and may therefore be simplified as a perfect sink. Moreover, during DCB application the luminal blood flow is impeded by the presence of the device itself.

Drug flux expressions

This modelling study explored different albeit simplified representations of drug delivery from a DCB. It is of interest to compare vastly different doses of DCBs to pose questions about the drug amount required to achieve sufficient therapeutic levels in the tissue. The "Low dose" and "High dose" expressions illustrate two examples of different drug delivery behaviours (release kinetics) and how this translates into different key indicators (DC and sRS).

Notwithstanding, the following points deserve questioning:

1. The flux expressions utilised, sourced from the literature, were derived from *in vitro* experiments using different procedural and device settings (e.g. different devices, drug types,

solution medium, inflation pressure), exhibiting weak comparability. These vastly different conditions should relate to their vastly different flux expression behaviours.

2. The flux expressions were derived from drug release measurements in a solution medium. How representative are these experiments of the actual drug release behaviour of a DCB when in contact with arterial tissue?

3. How does drug delivery depend on other parameters beyond delivery duration? For example, inflation pressure, drug load, drug type, balloon size, etc.

There are still many aspects to be explored. Models using prescribed drug flux expressions, such as the one presented in this Chapter, are unable to investigate these.

Increased balloon inflation pressure

During DCB application, the high-pressure inflation of the device against the arterial wall is expected to affect the pressure constraint at the contacting surface, and, consequently, the pressure gradient, magnitude of transmural filtration, and finally the drug transport via advection. Although temporary, a substantial increase in the advective term of the drug transport equation may result in a noticeably different distribution behaviour of drug concentration in the arterial wall. As originally observed *in silico* in [72], the outcome of drug delivery from a DCB is influenced by the temporary increase of pressure during its application. The experimentation with the current model also conveniently permitted insights into having increased pressure values during drug delivery. For instance, the comparison in subsection 3.8.6 considered hypothetical pressure cases: having (I) an increased pressure during DCB application versus (II) the physiological luminal pressure at all times of the simulation. As illustrated by Figure 3.11, the increased inflation pressure provoked an amplification of the Péclet number range across the arterial wall from 0.0233 – 2.78 to 2.02 – 240.7 in the radial direction. Although expected to affect advection, the magnitude of the amplification by about 2 orders of magnitude is glaring.

Previous modelling works [67] and [72], perhaps naively, assumed a magnitude of the increased pressure value as equal to the balloon inflation pressure ($p_{\text{DCB}} = 8$ atm), i.e. the inner pressure of balloon inflation. Although balloon inflation pressures inside the balloon may routinely reach 8 atm ($= 6080$ mmHg), which is about 61 times greater than the physiological pressure value considered ($p_{\text{lum}} = 100$ mmHg), the pressure and strain on the arterial wall provoked by the balloon inflation originate from the relative distention beyond the resting diameter of the vessel [97].

Moreover, a brief consideration of the safety of the problem of interest leads to the study of elasticity and distensibility of a blood vessel — posing serious doubts on the magnitude of p_{DCB}. Experimental works studied the mechanical stress values that triggered dissection lesions and rupture in human arteries. For instance, [98] reports the mean pressure value that triggers

dissections in human aortas as 596 ± 214 mmHg, which is considered as a very high non-physiological value – even for the largest calibre artery, the aorta. Abnormal transmural pressure values in the coronary artery exceeding its compliance can lead to rupture. Aggravating this, atherosclerotic disease results in decreased elasticity of the coronary artery, making it stiffer and prone to rupture due to sudden increases in transmural pressure [99]. Moreover, the binary aspect of the multistep increased pressure causes a brisk change in pressure over space and time, respectively around the boundary $\Gamma_{\text{ET, de}}$ and the instant t_0. These issues prompted subsequent scrutiny of the temporary boundary condition of pressure, particularly concerning the value of p_{DCB} assigned to it. A more sophisticated approach is considered in Chapter 5, where the contact pressure is calculated from a balloon deployment simulation.

Significance of results

As acknowledged earlier, the present model was a substantial contribution to the previous modelling work of [72]. For this Chapter, the model has been adjusted mainly to account for different artery dimensions and improve its computational implementation. Thereby, the behaviours of the safety and efficacy indicators, DC and sRS, are broadly in line with the previous results observed in [72]. The characteristic acute peak of DC shows a magnitude of about 900 and 60 ng/mg, respectively for the "High dose" and "Low dose" 60-s DCB application. The levels of saturation of binding sites is also similar between models, and interestingly indicate a decay in drug levels regardless of the drug load delivered. Aware of the aforementioned model limitations, a detailed comparison of the results with other experimental or simulation data is deferred until the next Chapters.

Conclusion

In this Chapter, the DCB is largely reduced to a pair of temporary boundary conditions, uniformly prescribed over the DCB application region: (I) a drug influx and (II) an increased constant pressure. The lack of a representation of the DCB causes the model to rely on prescribed resources to define the problem of interest — the role of DCB in drug delivery. Taken together, the simplifying assumptions of (I) and (II) limit the accuracy of the model and the potential insights it can provide. Therefore, a better understanding of p_{DCB} and the mechanism of drug transfer from DCB to the arterial wall on contact are major ambitions of the following Chapters. The next two Chapters propose, respectively, the creation of a DCB model including a geometrical representation of the device, and the coupling of DCB and arterial wall models — notably including structural mechanics and thus deformation. In conclusion, the assumptions of the model presented here and previous modelling works were questioned — leading to the development of the novel DCB model in the subsequent Chapters.

Chapter 4

Modelling drug-coated balloon drug release test

In the previous Chapter, the role of DCBs was modelled as a pair of temporary boundary conditions imposed at part of the lumen–wall interface. These were an increased pressure, representing the high balloon inflation pressure observed in the clinical angioplasty procedure; and a drug influx, introducing drug mass into the tissue at an experimentally-defined rate. This pair was active during the short balloon inflation time, then replaced with physiological conditions of pressure and drug wash-off by blood flow.

The modelling approach described above is a substantial simplification of the drug delivery procedure with DCBs. The DCB device lacked a geometrical representation and inflation procedure. Mainly, this neglects the important multiphysics interaction between the device and the arterial wall — involving simultaneous deformation and drug transfer on contact. Although these effects only take place during a short time window, they are fundamental for understanding the inherent mechanism of drug delivery from DCBs. Thus, it becomes pertinent to consider a more sophisticated representation of the DCB. The starting point of such a DCB model was a drug release experiment, referred to as the "drug release test".

Drug release test rationale

Medical devices of drug delivery are commonly subjected to *in vitro* drug release tests as an empirical step in their development and certification stages. The experiment considered in this work is based upon testing performed by the industrial partner, Biosensors International [81]. Figure 4.1 illustrates the steps of the drug release test. In this test, the DCB is immersed in a solution medium of 100% acetonitrile, a harsh solvent that acts as a sink medium. The total exposure duration is comprised of one minute with the DCB uninflated, followed by an additional one minute with the DCB inflated. At the end of the test, totalling two minutes, the DCB is removed from the solution medium and the amount of drug released is quantified. The amount of drug released by the DCB's coating is quantified through ultraviolet-visible spectrophotome-

try measurements of the solution medium (using wavelength 278 nm) [81]. These experimental evaluations only provide data on the final drug released after a certain exposure time, lacking relevant time-dependent information along the process. A computational model would be able to provide a drug release profile across the entire process.

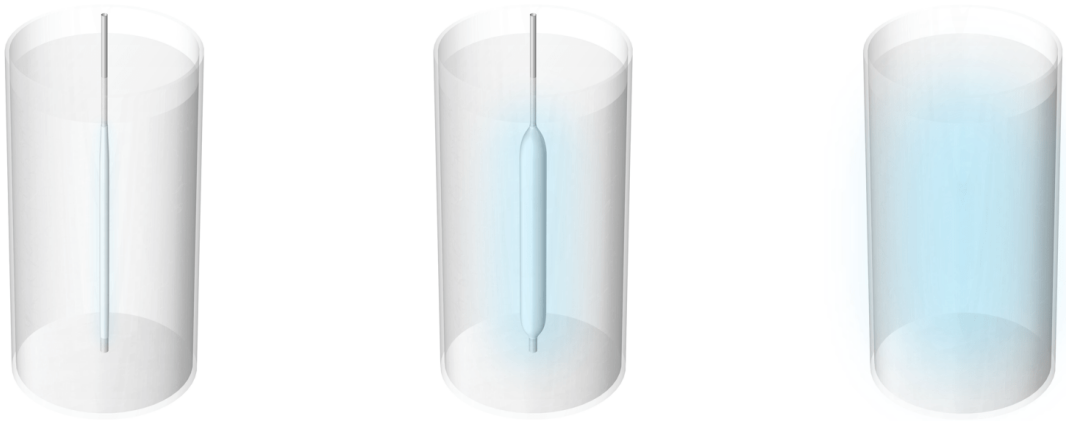

Figure 4.1: Schematic illustration of the steps of the drug release test, as described in the text.

A complete experimental procedure reproducing this drug release test was performed in [100], where drug release measurements were taken at regular intervals throughout the experiment. This experiment serves as an opportune reference for developing the current model. Thus, the present work combines new intermediate experimental data points from [100] and novel *in silico* modelling to expand the mechanistic understanding of drug release from DCBs.

Outline

This Chapter presents a multiphysics model capable of reproducing the DCB's drug release test, including the interdependent processes of balloon inflation and drug release into a sink medium. The specific objectives of the present work are to achieve a resemblance of the following aspects:

(I) Model geometry

(II) Structural mechanics

(III) Drug release kinetics

The modelling efforts to achieve each of these points will be described in the subsequent Sections, including the multiphysics coupling of balloon inflation and drug transport physics. Then, a parameter calibration routine is proposed to simultaneously adjust (I), (II), and (III), using the experimental data available. The model is set up and solved computationally using a finite element method framework. The simulation results are presented, and additional scenarios are probed to provide mechanistic insights. Finally, a discussion is provided on the model's achievements, limitations, and validation.

4.1 Model geometry

The model geometry represents a Biolimus A9™ Drug-Coated Balloon (BA9-DCB), a commercial device manufactured by Biosensors International [81].

The device core is a polymeric balloon with similar behaviour to a semi-compliant angioplasty balloon. Its material is the thermoplastic elastomer Pebax 72D, a polyether block amide (PEBA) composed of a flexible polyether and rigid polyamide [101]. Alternatively, it is referred to as PEBAX D72 or PEBAX 7233 SA 01 MED. For the purpose of drug delivery, the balloon is coated with a hybrid mixture of:

Excipient Poly(ethylene) oxide (PEO), a high-molecular-weight polymer with strong hydrophilic properties. It is approved by the United States Food and Drug Administration (U.S. FDA) for internal use in humans, as an inactive non-toxic and biocompatible agent [102]. Excipients are widely used in drug delivery applications within biomedical engineering. In this case, it acts as a vehicle or carrier that enables the attachment of the drug in the form of a coating embedded in the balloon. Supporting the adhesion of the drug to the balloon surface, PEO facilitates the transport of the drug load to the target lesion through the aqueous conditions of the circulatory system [95]. As an excipient in DCBs, PEO has been found to be effective in delivering paclitaxel to the vessel wall of the target lesion [103].

Drug Biolimus A9™, Biosensors's proprietary antiproliferative agent.

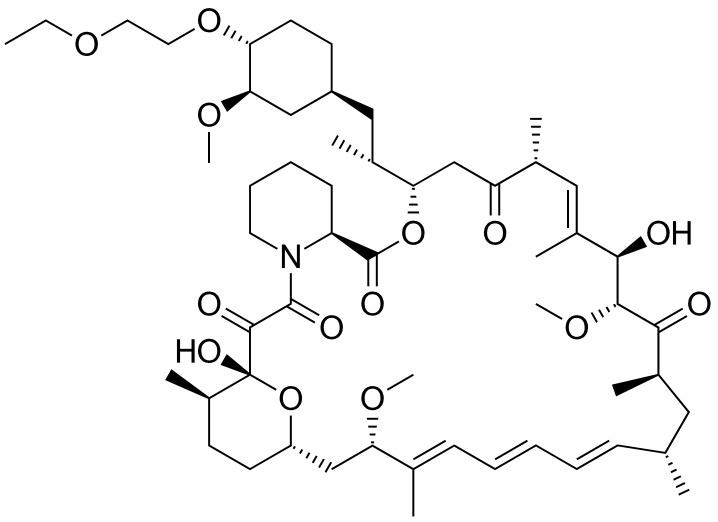

Figure 4.2: Chemical structure of Biolimus A9™, ($C_{55}H_{87}NO_{14}$). The drug is also known by the nonproprietary name umirolimus.

Biolimus A9™ is a highly lipophilic cytostatic drug, developed specifically for use in coronary vascular applications [81]. The drug's relatively high lipophilicity has been associated with improved retention by the tissue [104]. It is an analogue of sirolimus and

has been used in drug-eluting stents (DESs) suppressing neointimal formation with success according to [47]. Its role as an antiproliferative drug is to halt cell proliferation, control the healing response following the procedure, and alleviate undesirable effects [81]. It composes a smaller fraction of the coating mixture.

As emphasised in [105], the combination of excipient and drug is crucial to the performance of DCBs in drug delivery.

The device is mounted onto a balloon catheter, a long wire-like device designed to transport the crimped balloon through the circulatory system until the site of intervention. For convenience, the current model focusses on the modelling of the DCB and ignores the catheter. The efforts to replicate the DCB geometry *in silico* are presented next.

4.1.1 Model domains

The device is described as a hollowed cylinder-like structure (Ω_{B}) surrounded by a thin drug-embedded coating (Ω_{coat}) at its outer surface. It is modelled as a two-dimensional (2D) axisymmetric geometry, composed of two adjacent domains, via several geometric primitives and operations. Using axisymmetry allows for a simpler 2D geometry, built with radial and longitudinal dimensions (r, z). Once rotated around the axis of radial symmetry ($\Gamma_{\text{sym},\, r}$), it effectively represents a cylindrical three-dimensional (3D) geometry with volume. Accordingly, a general transformation of coordinate systems, from cartesian to cylindrical, is performed for all physics interfaces of the model.

These modelling choices produce a representation of the DCB device from a simplified two-dimensional geometry, greatly promoting computational efficiency for further simulations incorporating additional modelling complexities. As a notable disadvantage, this geometrical configuration does not account for the complex and unsymmetrical balloon folding and unfolding techniques, often performed in a helical fashion around its radial axis [71, 106]. Figure 4.3 depicts the generation process of the DCB model from a simplified two-dimensional geometry followed by axisymmetric revolution around $\Gamma_{\text{sym},\, r}$. The proximal, middle, and distal parts of the device are coated with drug, represented by the white domain Ω_{coat}. The resulting geometry is an idealised representation of a DCB in an uninflated state. Table 4.1 lists the model domains. The notation of domains is referent to the current (deformed) configuration, being altered according to deformation.

Table 4.1: Summary of the model domains.

Domain name	Description
Ω_{B}	Balloon
Ω_{coat}	Coating

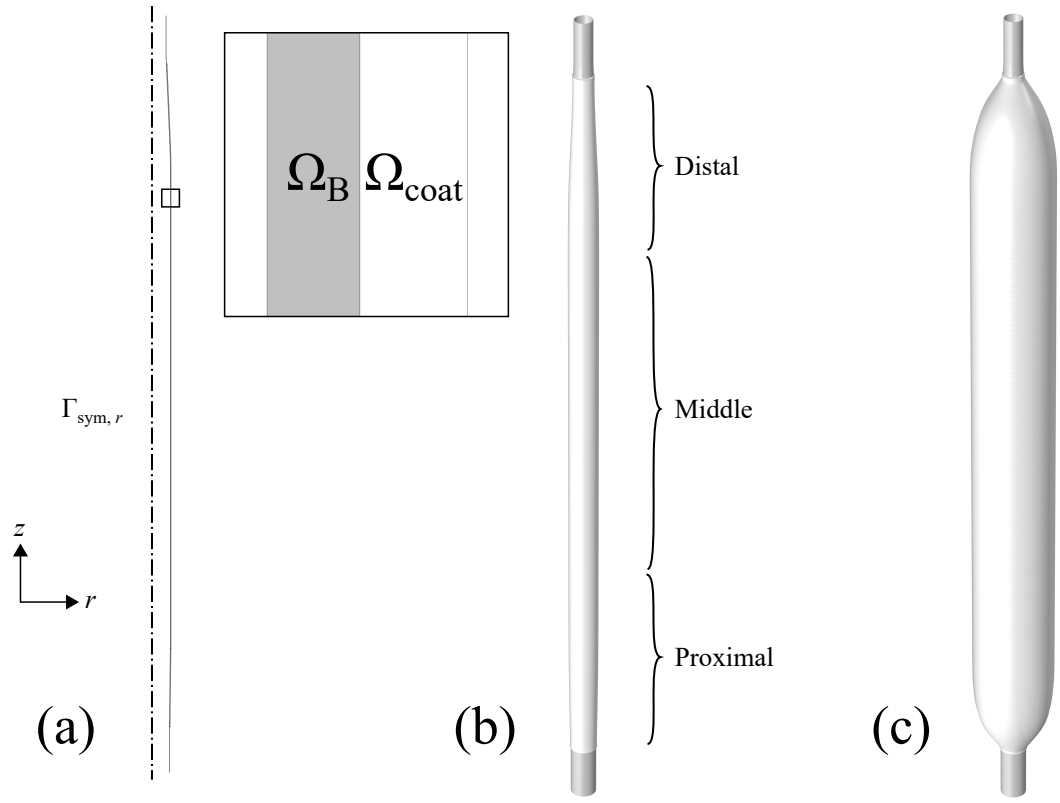

Figure 4.3: Schematic of the DCB model. From left to right, the labels indicate (a) the starting 2D axisymmetric geometry, (b) the resultant revolved geometry, uninflated, and (c) inflated to 11 atm. The magnified inset highlights the balloon and coating domains.

4.1.2 Model boundaries

For convenience, the relevant boundaries of the model domains are identified in Figure 4.4 (a) and listed in Table 4.2. They will be referenced in the subsequent sections where the model multiphysics are defined. The inner boundaries of Ω_B and outer boundaries of Ω_{coat} are of particular interest for the modelling in this Chapter. These were highlighted, respectively, in red and yellow, and blue in Figure 4.4 (a). Moreover, uncoated elongations of the proximal and distal extremities of the balloon (Γ^{ext}_{prox} and Γ^{ext}_{dist}) were designed to incorporate a small part of the catheter shaft into the model geometry.

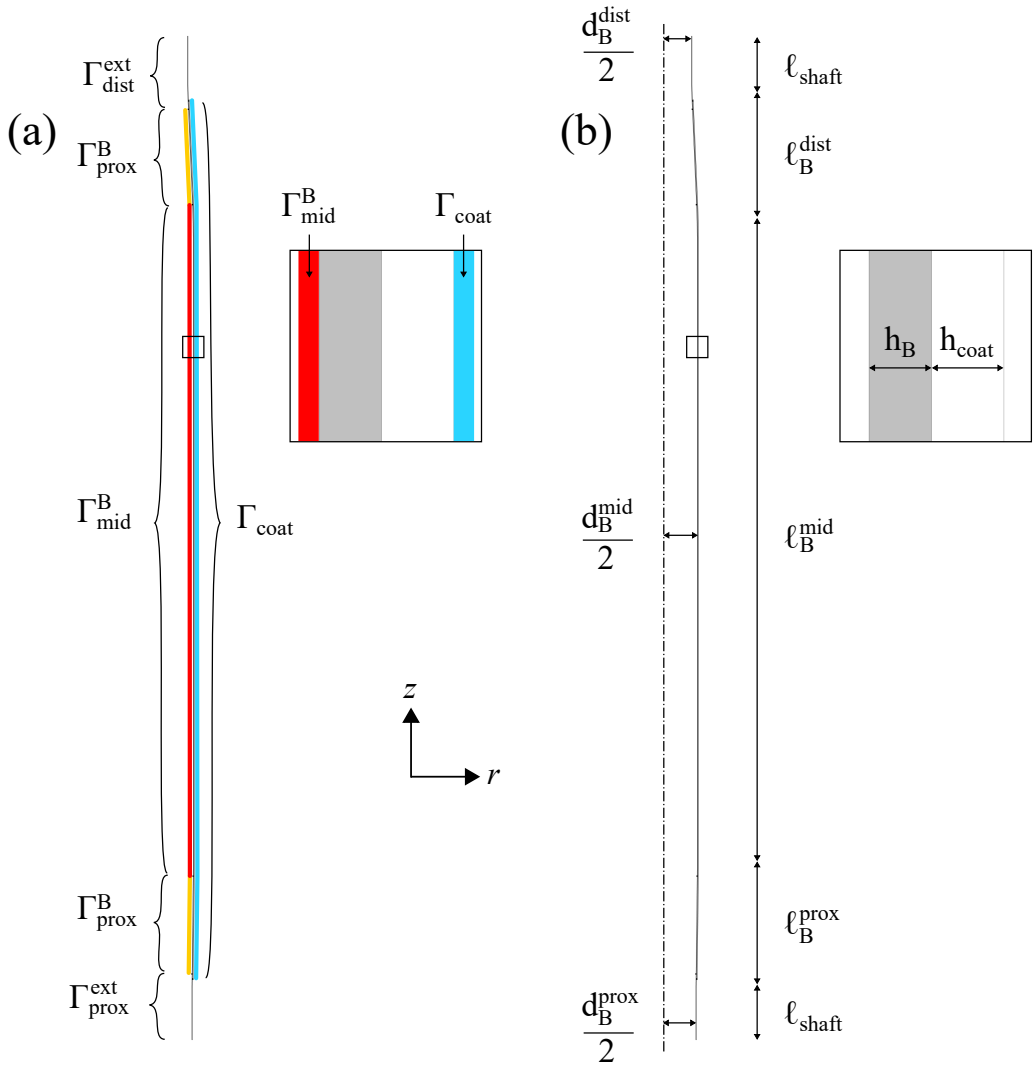

Figure 4.4: Schematic overview of (a) boundaries and (b) geometrical dimensions of the DCB model. The magnified insets depict the inner and outer boundaries and the thicknesses of the balloon and coating domains.

4.1.3 Model dimensions

The initial model geometry corresponds to the uninflated dimensions of a BA9-DCB of nominal size 3.5 x 25 mm (i.e. "nominal diameter", d_B^{nom}, x "middle section length", ℓ_B^{mid}). The nominal diameter refers to the DCB's outer diameter when inflated to nominal pressure (6 atm). Most geometrical dimensions of the model were directly informed by the device's manufacturer. The uninflated middle diameter of the DCB ($d_{B,0}^{mid}$), exceptionally, was estimated via the parameter calibration explained in Section 4.4. Remarkably, $d_{B,0}^{mid}$ relates to the concept of crossing profile. The crossing profile is a value used clinically to designate the accessibility of the minimally invasive device, measured as its maximum radial dimensions while in transit during the intervention.

The geometrical dimensions used to build the DCB model are identified in Figure 4.4 (b) and listed in Table 4.3.

Table 4.2: Summary of the model boundaries.

Boundary name	Description
$\Gamma_{\text{sym, } r}$	Axis of radial symmetry
Γ_{coat}	Outer coating surroundings
$\Gamma^{\text{B}}_{\text{mid}}$	Inner surface of balloon, middle
$\Gamma^{\text{B}}_{\text{prox}}$	Inner surface of balloon, proximal
$\Gamma^{\text{B}}_{\text{dist}}$	Inner surface of balloon, distal
$\Gamma^{\text{ext}}_{\text{prox}}$	Proximal extremity
$\Gamma^{\text{ext}}_{\text{dist}}$	Distal extremity

Table 4.3: Summary of the model dimensions. Most values were based on discussions with Biosensors International.

Parameter	Description	Value	Reference
$d_{\text{B}}^{\text{nom}}$	Nominal diameter	3.50 mm	[81]
$d_{\text{B, 0}}^{\text{mid}}$	Uninflated middle DCB diameter	1.302 mm	Estimated
$d_{\text{B}}^{\text{prox}}$	Proximal extremity diameter	1.143 mm	[81]
$d_{\text{B}}^{\text{dist}}$	Distal extremity diameter	0.813 mm	[81]
$\ell_{\text{B}}^{\text{mid}}$	Middle section length	25 mm	[81]
$\ell_{\text{B}}^{\text{prox}}$	Proximal section length	4.55 mm	[81]
$\ell_{\text{B}}^{\text{dist}}$	Distal section length	5.19 mm	[81]
ℓ_{shaft}	Shaft length	2 mm	Estimated
h_{B}	Balloon wall thickness	21.8 μm	[81]
h_{coat}	Coating thickness	25 μm	[81]

4.2 Structural mechanics

This Section presents the modelling efforts to characterise the structural mechanics of the DCB model, based on the inflation behaviour of the real device.

The DCB model geometry was presented in Section 4.1 as a thin-walled structure composed of two parts: balloon and coating. They are composed of different materials and exert different functions. The balloon is responsible for the device's compliance while the coating serves primarily as a carrier for the drug, having unknown structural resistance. Although they may differ in structural properties, the balloon and coating entities were observed to behave as a conjoined structure during the DCB inflation procedure, performed experimentally as depicted in Figure 4.5. Therefore, as a simplifying assumption, the domains of the balloon (Ω_{B}) and coating (Ω_{coat}) are merged into a single solid structure with a uniform material behaviour. A detailed explanation of this rationale can be found in this Chapter's discussion, in Section 4.7.

Models of varying complexity were reported in the literature to represent balloon inflation. Most modelling works were in the context of angioplasty balloons for stent deployment [106–110]. Fewer models were dedicated to DCBs [71]. According to this modelling literature, semi-compliant balloons are commonly modelled as isotropic linear elastic materials and are usually treated as compressible with a Poisson ratio in the range of 0.3 – 0.4. A strong incentive for linear elasticity is the linear pressure-diameter relationship of balloons over their operation range, as specified by their manufacturers. The deformation profile of the DCB is often quantified and informed by the device's manufacturer in a "compliance chart" — a table relating balloon diameter (mm) versus inflation pressure (atm) for a range of balloon sizes. As shown in previous modelling works, balloon compliance has a characteristic bi-phase behaviour: non-linear from uninflated to nominal pressure, and quasi-linear over the operation range. Preliminary *in silico* investigation of own authorship has found that this balloon compliance was unachievable in the 2D-axisymmetric model geometry with a linear elastic model. Therefore, the constitutive model and compressibility of the polymeric materials on balloons were questioned in the present modelling. As major differences, the present model features (I) a 2D-axisymmetric geometry and (II) a depiction of the coating conjointly to the balloon.

4.2.1 Material model

A phenomenological approach is proposed to capture both the nonlinear nature and strain-stiffening phenomenon of inflating polymeric balloons. A Gent hyperelastic material model is defined and implemented to govern the stress-strain response of the conjoined DCB structure ($\Omega_{\mathrm{B}} \cup \Omega_{\mathrm{coat}}$). The DCB is modelled as a non-porous, solid, and incompressible material, such that its deformation results in an isochoric process (from Greek "*iso*", equal; and "*choric*", space).

Equation 4.2.1 presents the basis of the Gent material model for an incompressible material:

$$\Psi_{\text{Gent}} = -\frac{\mu}{2}\, j_{\text{m}}\, \ln\left(1 - \frac{I_1 - 3}{j_{\text{m}}}\right), \tag{4.2.1}$$

where Ψ_{Gent} is a strain energy density function, parametrised by two material parameters: the macroscopic shear modulus, μ, and the limiting stretchability, j_{m}. This function depends solely on the first invariant of the Cauchy-Green deformation tensor, I_1, introduced non-linearly within a natural logarithmic expression ($\ln$). A discerning feature of the strain energy density function proposed by Gent is the concept of limiting polymeric chain extensibility. This effect is produced by a singularity in Ψ_{Gent} when $I_1 - 3$ tends towards j_{m}. When this happens, the argument of the natural logarithm function tends to zero, resulting in asymptotically high negative values. Meanwhile, the resulting strain energy density Ψ_{Gent} becomes infinitely large, halting deformation and effectively limiting the extensibility of the material at this threshold. This rubber-like response enabled the reproduction of the aforementioned bi-phase compliance behaviour. The Gent constitutive model for hyperelastic isotropic incompressible materials was chosen for its parametric simplicity, relative numerical stability, and application to polymeric materials [111, 112].

Phenomenological models are a practical alternative to replicate the macroscopic behaviour of polymers and may be determined in an inverse procedure from experimental data [113]. Although empirical, the Gent hyperelastic material model has been used in the context of soft biological tissues, demonstrating its ability to capture both the nonlinear nature and strain-stiffening phenomenon [114, 115]. Its usage in the context of inflating polymeric balloons in this work is somewhat innovative.

Moreover, in contrast to the previously referenced modelling works, the current model treats the DCB structure as an isotropic incompressible material (i.e. the density and volume of the DCB are maintained constant in the face of deformation). In the present multiphysics model, incompressibility has implications beyond beyond structural mechanics. These concern the calculation of drug transport in the coating — a novel feature compared to the previous modelling references. The modelling of the drug-embedded coating domain becomes evident in the next Section, 4.3. Since volume is conserved, the drug-embedded coating domain conserves its drug concentration over the domain. The assumption of incompressibility is a simplification used in the phenomenological approach taken and may be questioned for its physical realism; nevertheless, it facilitated the multiphysics modelling greatly.

Additional simplifications concern the assumption of quasi-static structural mechanics, which excludes inertial terms are excluded, and thus, density does not play a role in the simulation. Moreover, the system mass is assumed sufficiently small so the inertial terms, kinetic energy, and energy dissipation during the simulation can be ignored.

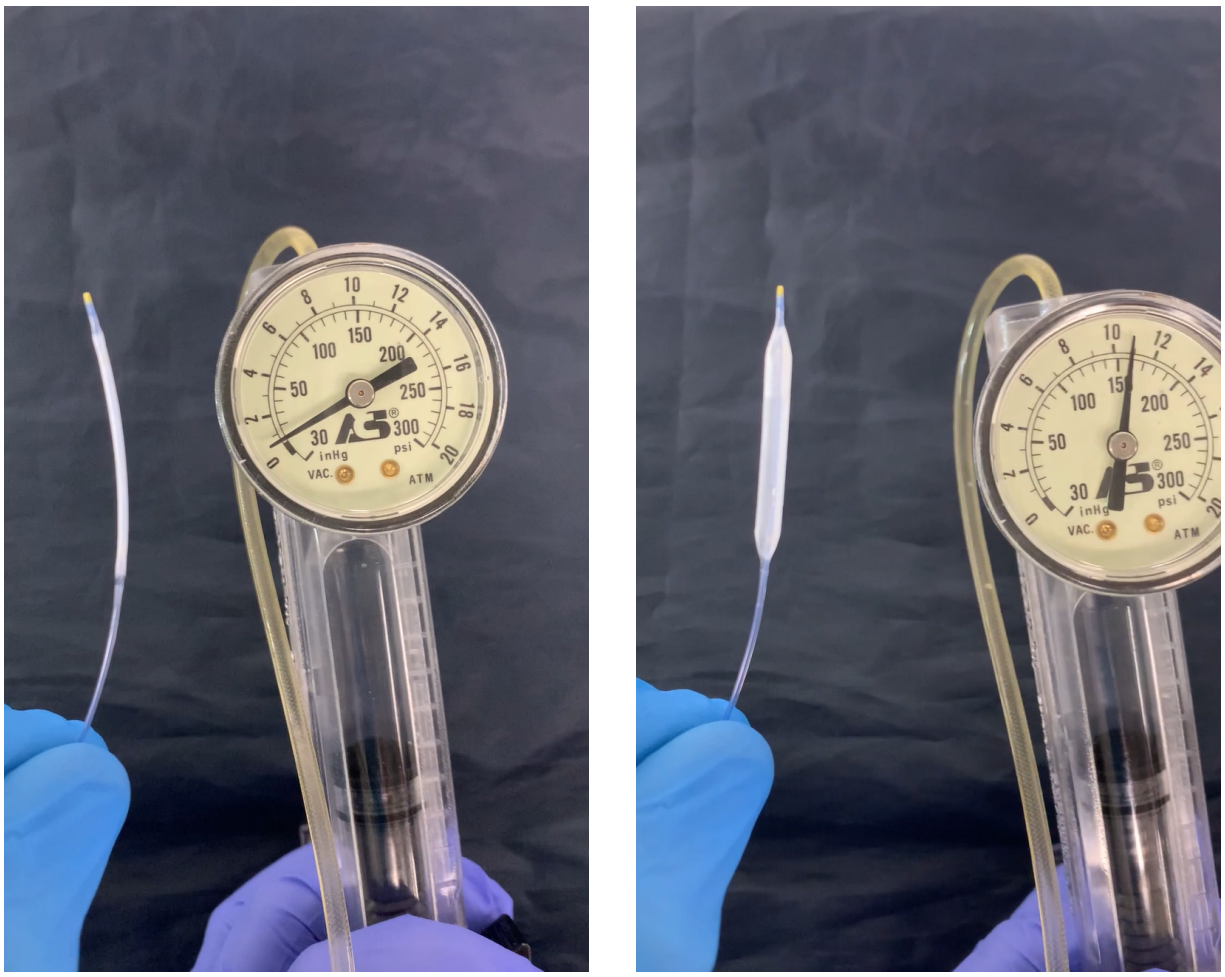

(a) $p_{\text{inf}} = 0$ atm (b) $p_{\text{inf}} = 11$ atm

Figure 4.5: Showcase of the experimental DCB inflation procedure, (a) uninflated and (b) inflated to 11 atm. This pressure range is the basis for the present modelling of balloon inflation. Reproduced from [100] with permission.

4.2.2 Balloon inflation

During the drug release test, the DCB remains uninflated for a period of one minute, then it is inflated to high pressure. To model the balloon inflation procedure *in silico*, a time-dependent pressure boundary load is devised using ramp functions. In the form of a boundary condition, it is applied to the internal surface of the DCB ($\Gamma^{\text{B}}_{\text{prox}}$, $\Gamma^{\text{B}}_{\text{mid}}$, and $\Gamma^{\text{B}}_{\text{dist}}$) to deform it accordingly. The desired pressure versus time behaviour is:

$$p_{\text{inf}}(t) = \begin{cases} 0 & 0 < t < 60 \text{ s} \\ \dfrac{t - 60}{t_{\text{ramp}}} p_{\text{max}} & 60 \text{ s} \leq t \leq 60 \text{ s} + t_{\text{ramp}} \\ p_{\text{max}} & 60 \text{ s} + t_{\text{ramp}} < t < 120 \text{ s}, \end{cases} \tag{4.2.2}$$

where t is the time variable; t_{ramp} is the ramp duration; and p_{max} is the target inflation pressure, considering a zero base pressure at the uninflated state.

Alternatively, the modal behaviour presented in Equation 4.2.2 can be described by a single time-dependent function valid for the entire deployment step:

$$p_{\text{inf}}(t) = \frac{1}{2}\min\left(\frac{t-60}{t_{\text{ramp}}} + \left|\frac{t-60}{t_{\text{ramp}}}\right| \, , \, 1\right) p_{\text{max}} \qquad 0 < t < 120 \text{ s}. \tag{4.2.3}$$

Combining minimum and modulus functions offsets the start of the ramp and limits its magnitude. The utility of Equation 4.2.3 is permitting the use of the independent time variable t over a continuous interval.

In summary, the boundary condition $p_{\text{inf}}(t)$ prescribes a pressure load of zero value for one minute; then briefly increases (during $t_{\text{ramp}} = 10$ s) until the predefined maximum inflation pressure value (p_{max}); and sustains it until the test duration has elapsed two minutes (Δt_{inf}). This inflation behaviour is illustrated in Figure 4.6. The pressure boundary load is applied to the inner surface of the DCB: $\Gamma^{\text{B}}_{\text{mid}}$, $\Gamma^{\text{B}}_{\text{prox}}$, and $\Gamma^{\text{B}}_{\text{dist}}$.

Spatiotemporal smoothing

The occurrence of abrupt pressure gradients over time, due to the linear behaviour of the ascending pressure ramp described in Equations 4.2.2 or 4.2.3, is inconvenient for the simulation. This problem is addressed with curvature smoothing of the time-dependent pressure ramp, providing two continuous derivatives over a one-second transition zone at the beginning and end of the ramps. Figure 4.6 presents the behaviour of $p_{\text{inf}}(t)$ as implemented in the model, highlighting the effect of the procedure referred to as temporal smoothing in its subfigures.

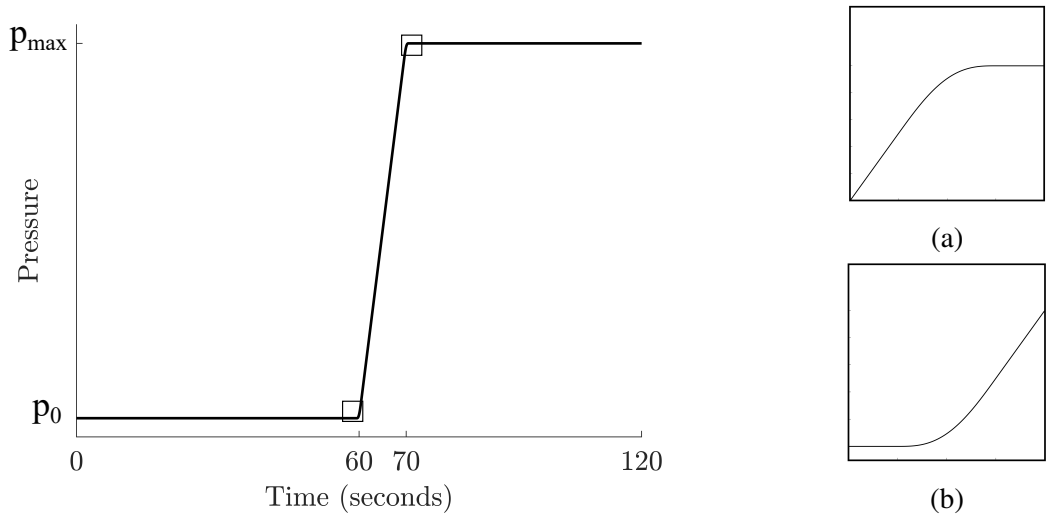

Figure 4.6: Magnitude of the time-dependent pressure load during the simulation, reproducing the DCB inflation procedure in the drug release test. The magnified insets show the temporal smoothing at the (a) top and (b) bottom parts of the ramp.

Furthermore, an equivalent problem over space was considered. Abrupt pressure gradients at the edges of the boundary subjected to pressure may cause the DCB to kink unnaturally in the inflation simulation, hindering realism and convergence. Moreover, the application of uniform pressure over these boundaries was found to produce unrealistic deformation unlike what was observed with the real device in Figure 4.5. This may be attributed to the oversimplification of the DCB geometry in the present model, modelled based on basic dimensions as in Figure 4.3, which resulted in a simplified structure of uniform thickness that disregards the internal parts of the balloon catheter system. Two modelling strategies were developed and implemented to avoid this undesired effect:

1. A space-dependent feature is added to the ramp: inflation pressure magnitude is also ramped linearly over space along the proximal and distal extremities. That is, while the full pressure magnitude $p_{\text{inf}}(t)$ is applied to $\Gamma^{\text{B}}_{\text{mid}}$, gradual magnitude is applied to $\Gamma^{\text{B}}_{\text{prox}}$ and $\Gamma^{\text{B}}_{\text{dist}}$, according to $\alpha_i(r, z)$. The linear relationship $\alpha_i(r, z)$, defined in Equation 4.2.4, ranges from 0 to 1 according to the relative position along each of the boundary's length. It is used as a space-dependent multiplier of the pressure load along its respective boundary, providing a transition zone over space.

$$\begin{aligned} \alpha_i(r, z) &= \frac{\Delta \ell}{\ell_i} \\ &= \frac{\sqrt{(\Delta r)^2 + (\Delta z)^2}}{\ell_i} \\ &= \frac{\sqrt{(r - r_{0,\,i})^2 + (z - z_{0,\,i})^2}}{\ell_i} \qquad \text{for } i = \{\text{prox, dist}\}, \end{aligned} \tag{4.2.4}$$

   where ℓ_i is the length of the respective boundary Γ^{B}_i; r and z are the radial and longitudinal coordinates; and $r_{0,\,i}$ and $z_{0,\,i}$ are the extreme points of each respective boundary, corresponding to the starting coordinates of their pressure ramps. All coordinates are given in the deformed configuration. For a schematic illustration of $p_{\text{inf}}(t)$ in the model, the reader may refer to Figure 4.7.

2. The initial starting state is assumed to be pre-stressed, by adding a normal stress contribution (σ_{pre}) to the longitudinal stress tensor component over the entire DCB domain. The value of σ_{pre} was estimated empirically based on the observance of computational robustness. Effectively, this condition creates a pre-tension in the DCB, so the geometry is reasonably taut before and during the inflation simulation.

These modelling techniques accomplish a smoother deformation profile across the length of the DCB during inflation and improve the simulation convergence by reducing mesh element distortion or inversion due to excessive localised deformation.

Spring foundation

The DCB model geometry represents only a finite section of the DCB. The extremities of the device, $\Gamma^{\text{ext}}_{\text{prox}}$ and $\Gamma^{\text{ext}}_{\text{dist}}$, must be constrained somehow in the simulation of inflation. Typically, the fixed constraint boundary condition is used, as in other endovascular modelling studies [83, 85], to prescribe zero degrees of freedom to the extremities. However, this model employs an alternative approach in the form of a spring foundation boundary condition instead of fixed constraints. The spring foundation prescribes artificial springs to partially immobilise the extremities of the model geometry, according to the linear relation shown below:

$$\mathbf{F}_{\text{spring}} = -k_{\text{spring}}\,(\Delta\mathbf{v}), \tag{4.2.5}$$

where $\mathbf{F}_{\text{spring}}$ is the opposing force generated by the spring; k_{spring} is the isotropic total spring constant; and $\Delta\mathbf{v} = \mathbf{v} - \mathbf{v}_0$ is the relative displacement deforming the spring.

The spring foundation is assigned to the boundaries $\Gamma^{\text{ext}}_{\text{prox}}$, and $\Gamma^{\text{ext}}_{\text{dist}}$, to effectively connect them to a reference "ground", as to oppose relative displacement. To achieve a less restrictive but still stiff constraint, a high total spring constant of estimated stiffness value $k_{\text{spring}} = 10^6$ N/m is selected. This choice is intended to produce a more natural and computationally stable deformation behaviour at the proximal and distal ends of the model geometry.

Free deformation

In the drug release test, the DCB is immersed and inflated within a solution medium. It is assumed that the mechanical resistance offered by the solution medium is negligible. Consequently, the remaining boundaries of the model geometry are allowed to deform freely. This means they experience unconstrained displacement in the radial and longitudinal directions.

Table 4.4 lists the parameters characterising the DCB inflation procedure.

Parameter	Description	Value	Reference
p_{max}	Target inflation pressure	11 atm	[100]
t_{inf}	Inflation time duration	60 s	[81]
t_{ramp}	Ramp up duration	10 s	Estimated
σ_{pre}	Balloon pre-stress	30 MPa	Estimated
k_{spring}	Spring foundation stiffness	10^6 N/m	Estimated

Table 4.4: Summary of procedural parameters for DCB inflation.

A design requirement of the *in silico* model is to capture the compliance behaviour when subjected to inflation pressure, as the DCB would in the clinical situation. In summary, the DCB has an initial small diameter when uninflated; reaches its nominal diameter when inflated to its nominal inflation pressure, i.e. 6 atm; and increases its size quasi-linearly over the operation

range (6 atm – 11 atm), according to the compliance chart informed by the manufacturer. Remarkably, there is no compliance information for inflation pressures below the nominal value; nonetheless, the estimated uninflated DCB dimension plus the compliance chart information were sufficient references to adjust the deformation behaviour of the DCB. The calibration procedure performed to obtain the material model parameter values is explained in Section 4.4.

4.3 Drug release kinetics

This section describes the modelling of drug distribution in the DCB's coating during the drug release test. The therapeutic agent considered in the coating of the DCB is Biolimus A9™. Throughout the modelling, it is referred to as the "drug".

4.3.1 Drug transport in the coating

Initial conditions

For simplicity, the coating domain is embedded with a homogeneous initial drug concentration, c_0, to match the drug load in the DCB as per the manufacturer's specifications:

$$c_0 = \frac{m_{\text{nom}}}{M_{\text{Bio}}\, V_{\text{coat}}}, \tag{4.3.1}$$

where m_{nom} is the nominal drug load, M_{Bio} is the molar mass of drug, and $V_{\text{coat}} = \int_{\Omega_{\text{coat}}} d\Omega_{\text{coat}}$ is the volume of the coating domain given by its spatial integration.

Similarly to in Chapter 3, the drug concentration in the DCB is regarded as a spatiotemporal variable $c(r, z, t)$ defined over the coating domain (Ω_{coat}). Drug transport in Ω_{coat} is assumed to be governed by a linear diffusion process. This was based on reference modelling works that considered drug transport via diffusion in the coating of drug-eluting stents [62, 63, 72, 80]. Before defining the governing equations of drug transport in Ω_{coat}, deformation must be regarded.

Moving domains

The current model calculates the transport of diluted species over the deformable coating geometry. Due to inflation pressure, the coating domain is deformed. Its drug distribution, given by the drug concentration field $c(r, z, t)$, must be updated accordingly to ensure that deformation is regarded and drug mass is conserved throughout the simulation.

The problem of drug transport over moving domains is addressed by using the deformation rate, $\mathbf{v}(r, z, t)$, as a pseudo-advective term in the drug transport equation in Ω_{coat}. It affects the drug concentration field in the coating in an additive, anisotropic, and time-dependent fashion, shifting the drug concentration over space as the geometry deforms. Additionally, incompressibility of the material model was assumed in Section 4.2, ensuring that the total volume of model geometries remains constant regardless of deformation. Together, these features corroborate the conservation of drug mass during deformation.

Equation 4.3.2 defines the local deformation rate over the model geometry in the radial and

longitudinal directions:

$$\mathbf{v}(r,z,t) = \begin{pmatrix} \dfrac{\partial r}{\partial t} \\ \dfrac{\partial z}{\partial t} \end{pmatrix}, \tag{4.3.2}$$

where r and z are the radial and longitudinal coordinates in the deformed configuration, and t is the time variable. The deformation rate components are expressed in units of velocity.

Governing equations

The definitive governing equations of drug transport incorporate the spatiotemporal rate of deformation, $\mathbf{v}(r,z,t)$, alongside the drug transport via diffusion. This ensures that the drug transport equations for all domains in the model are considered correctly in the current deformed configuration, while the drug-embedded coating domain deforms. Equation 4.3.3 describes the drug transport equation in the coating domain in the form of partial differential equations:

$$\frac{\partial c(r,z,t)}{\partial t} \;=\; \nabla \cdot \left(D_{\text{coat}}\, \nabla c(r,z,t) \;-\; \mathbf{v}(r,z,t)\, c(r,z,t) \right) \qquad \text{in } \Omega_{\text{coat}}, \tag{4.3.3}$$

where $c(r,z,t)$ is the spatiotemporal free drug concentration variable, D_{coat} is the diffusion coefficient in the coating, and $\mathbf{v}(r,z,t)$ is the spatiotemporal deformation rate.

Following the definition of drug within Ω_{coat}, boundary conditions must be defined to model the drug behaviour in its surroundings.

4.3.2 Drug sink

A perfect sink boundary condition is prescribed over the outer surroundings of the coating domain, Γ_{coat}. This represents the effect of the solution medium on draining the drug from the coating during the drug release test:

$$c \;=\; 0 \qquad\qquad \text{on } \Gamma_{\text{coat}}. \tag{4.3.4}$$

The process of drug clearance is modelled as continuous and irreversible. A detailed description of this boundary condition can be found in Chapter 3.

4.3.3 Zero-flux

To ensure the drug is allowed only to leave the coating domain through Γ_{coat}, a zero-flux boundary condition is prescribed over its remaining boundaries. Equation 4.3.5 expresses the zero-flux

boundary condition:

$$-\mathbf{n} \cdot (J + \mathbf{v}\, c) = 0, \tag{4.3.5}$$

where J is the total diffusive flux of drug; $\mathbf{v}$ is deformation rate, in this case, accounting for the total advective term in the coating; and c is the free drug concentration.

Table 4.5: Summary of model parameters of drug transport in the coating. All drug-related parameters refer to Biolimus A9™ as the therapeutic agent.

Parameter	Description	Value	Reference
m_{nom}	Nominal drug load	$1050\ \mu$g	[81]
M_{Bio}	Molar mass of Biolimus A9™	986.29 g / mol	[81]
D_{coat}	Isotropic diffusion coefficient in the coating	$8.2 \cdot 10^{-13}$ m^2 / s	Estimated

Another design requirement of the *in silico* model is to simulate drug release as the DCB would in the real drug release test. In the model, the DCB's drug release behaviour is shaped by a single drug-related parameter — the diffusion coefficient in the coating (D_{coat}). The calibration procedure performed to obtain the value of D_{coat} is explained in Section 4.4. Table 4.5 summarises the parameters used in the modelling of drug release.

4.3.4 Drug release profile

Drug released from a medical device is often quantified as a drug release profile, i.e. a curve relating cumulative drug released (%) versus time (s). It represents the cumulative amount of the DCB's drug load released until a given time t, defined continuously throughout the drug release test simulation and expressed as a percentage ranging from 0 to 100%. The drug release profile is calculated as

$$\begin{aligned} DRP(t) &= \frac{m_{\text{nom}} - m_{\text{coat}}(t)}{m_{\text{nom}}} \\ &= 1 - \frac{\int_{\Omega_{\text{coat}}} c(r,z,t)\, d\Omega_{\text{coat}}}{m_{\text{nom}}}, \end{aligned} \tag{4.3.6}$$

where m_{nom} is the initial drug load in the coating, and $m_{\text{coat}}(t)$ is the current drug mass in the coating domain, given by the spatial integration of the current drug concentration field, $c(r,z,t)$, over $d\Omega_{\text{coat}}$. The calculation of $DRP(t)$ is the main way of quantifying the outcome of the drug release test simulation.

4.4 Calibration of parameters

The previous Sections presented the modelling of DCB inflation in a solution medium, as summarised in Figure 4.7.

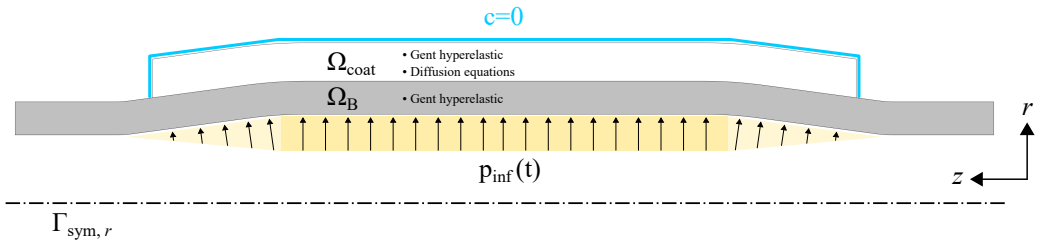

Figure 4.7: Schematic summary of physics considered in the model of Chapter 4. Geometry is not to scale.

The factors of DCB's geometry, structural mechanics, and drug release are entwined in the outcome of the drug release test through the following model parameters: the diffusion coefficient in the coating, D_{coat}; the material model parameters, μ and j_{m}; and the uninflated middle diameter of the DCB, $d_{\text{B, 0}}^{\text{mid}}$. Based on the premise that the model is capable of reproducing the *in vitro* results of the drug release test, there is a combination of these parameters that produces satisfactory simulation results in line with some given experimental data. In this case, the experimental data comes from the drug release test performed in [100]. The parameter calibration routine proposed to estimate these model parameters is presented in Figure 4.8 in the form of a flowchart. Essentially, it is an iterative process of selecting multiple parameters.

Uninflated drug release

A design requirement of the *in silico* model is to exhibit a drug release pattern similar to the drug release test. As introduced in Section 4.3, isotropic diffusion and a surrounding perfect sink are assumed to describe the entire drug transport behaviour in the DCB's coating. During the first part of the test (0 – 60 s), the DCB is submersed into the solution medium in an uninflated state. While undeformed, drug release from its coating solely depends on the diffusion behaviour in the coating and the initial geometrical configuration of the DCB. Therefore, the isotropic diffusion coefficient in the coating (D_{coat}) is the first parameter to be selected to shape drug release during the first part of the drug release test.

The calibration procedure begins with initial guesses of D_{coat}, $d_{\text{B, 0}}^{\text{mid}}$, μ and j_{m}. The initial value of D_{coat} was based on the diffusion coefficient used in the coating of DES models [72] and $d_{\text{B, 0}}^{\text{mid}}$ was based on the manufacturer's specifications on the crossing profile range of the device [81]. To obtain the initial guesses of μ and j_{m} for the simulation, an in-house Python package [116] was used as a parameter fitting tool considering a simplified thin-walled cylinder as a surrogate for the more complex problem of DCB inflation. In summary, the tool receives the

initial conditions of the problem and the expected pressure-deformation behaviour as inputs and provides the corresponding material model parameter values as outputs for the desired material model.

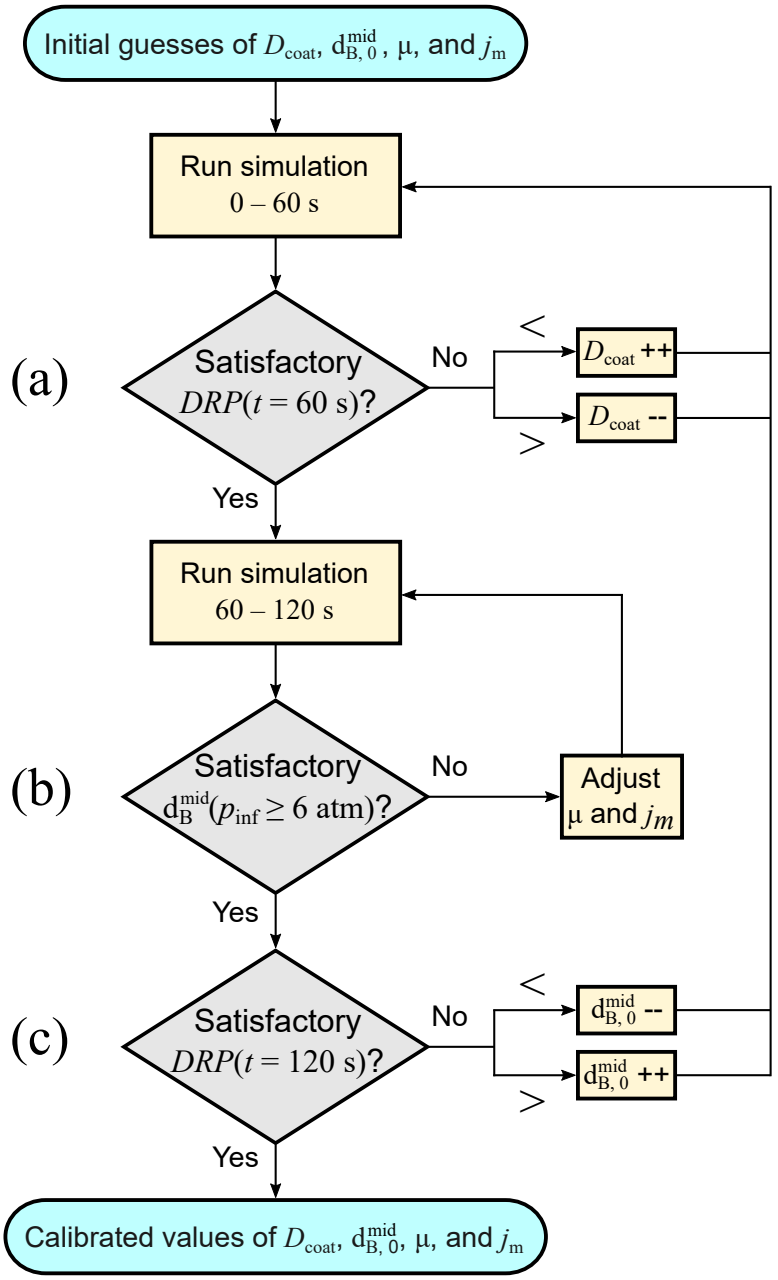

Figure 4.8: Schematic of the parameter calibration procedure. Sequentially, the DCB's (a) uninflated drug release, (b) compliance, and (c) inflated drug release behaviours are assessed and calibrated. A detailed explanation of this procedure can be found in the text.

Then, the first part of the drug release test is simulated (0 – 60 s). At the end of this interval, the drug release profile is quantified, as defined in Section 4.3, and $DRP(t = 60\ s)$ is compared to a reference experimental value [100], as indicated in Figure 4.8 (a). If the measured value is less than desired, diffusion must be faster — so D_{coat} is incremented and the simulation is

repeated. In contrast, if it is greater than desired then diffusion must be slower — so D_{coat} is decremented and the simulation is repeated. The magnitude of the increment or decrement (symbolised as ++ or --) was chosen empirically. Once $DRP(t = 60\,\text{s})$ corresponds to the desired value within a certain tolerance ($\pm 0.1\%$), this iterative subroutine ends.

Compliance

During the second part of the test (60 – 120 s), the DCB is inflated, which causes changes to its geometrical configuration. As introduced in Section 4.2, the structural mechanics behaviour of the DCB is shaped by two material model parameters: μ and j_{m}. From selecting these, its compliance may be adjusted as desired. Accordingly, the next step of the calibration routine aims to acquire a set of parameters capable of accurately reproducing the DCB compliance as expected by the device specifications. Then, the second part of the drug release test is simulated — featuring the DCB inflation with $p_{\text{max}} = 11$ atm, according to the reference experimental procedure in [100]. Figure 4.8 (b) indicates the calibration subroutine for the two material parameters. The parameter μ may be seen as an analogue of stiffness. This parameter dislocates the compliance curve (DCB diameter vs inflation pressure) vertically, with lower values allowing greater deformations. Meanwhile, j_{m} is related to stretchability. This parameter alters the slope of the curve, so lower values reduce mobility and flatten the compliance curve. These two parameters undergo iterative fine-tuning until compliance is deemed satisfactory — objectively, when the relation of the middle diameter of the DCB versus inflation pressure, $d_{\text{B}}^{\text{mid}}(p_{\text{inf}}(t))$, corresponds to the compliance chart data over the operation range (6 – 11 atm) within a certain tolerance, defined by root-mean-square error (RMSE) < 0.02 mm.

Inflated drug release

Now, the attention falls on the drug release from the DCB during inflation. Although the current configuration of selected parameters D_{coat}, μ, and j_{m}, may produce satisfactory behaviours concerning uninflated drug release and compliance, the drug released during the second part of the test (60 – 120 s) is still uncalibrated. The enlargement of balloon surface area provoked by inflation is presumed to increase the coating exposure to the solution medium and thus affect the drug release rate. The impact of this effect depends on the relative deformation of the DCB, i.e. between uninflated and inflated states. While the compliance behaviour within the operation range (6 – 11 atm) is constrained by the selection of material model parameters, the initial part of the compliance curve is still uncertain. Therefore, the remaining target of parameter calibration is the uninflated DCB diameter, $d_{\text{B},\,0}^{\text{mid}}$.

As indicated in Figure 4.8 (c), the final point of drug release at the end of the drug release test, $DRP(t = 120\,\text{s})$, is compared to a reference experimental value [100]. In case the assessed value is less than desired, the relative deformation must be larger — so $d_{\text{B},\,0}^{\text{mid}}$ is decremented. In contrast, if it is greater than desired then the relative deformation must be smaller — so

$d_{\mathrm{B},\,0}^{\mathrm{mid}}$ is incremented. Finally, the entire calibration routine is repeated since this change in the model geometry affects the other behaviours adjusted in (a) and (b). Once $DRP(t = 120\,\mathrm{s})$ corresponds to the desired value within a certain tolerance ($\pm 0.1\%$), the parameter calibration routine ends.

The outcome of the calibration routine is the selection of satisfactory values of D_{coat}, μ, j_{m}, and $d_{\mathrm{B},\,0}^{\mathrm{mid}}$, presented in Table 4.6. As intended, this means that the simulation results match the reference values for drug release and compliance. The simulation results are presented in Section 4.6, "Results".

In the decision blocks of Figure 4.8, the term "satisfactory" was used as a verbose logical operator. Objectively, it compares the simulated and experimental reference values to verify sufficient similarity according to a certain tolerance. The reference values indicated in Figures 4.8 (a) and (c) are the intermediate and final experimental data points (respectively, at $t = 60$ s and $t = 120$ s) from [100], where the same drug release test was performed. Namely, $DRP(t = 60\,\mathrm{s}) = 29.0 \pm 5.3\%$ and $DRP(t = 120\,\mathrm{s}) = 78.3 \pm 5.0\%$. Effectively, they serve as two "anchor points" used for the calibration of drug release. Simultaneously, the satisfaction condition indicated in Figure 4.8 (b) is met when the model compliance approximates the reference values from the compliance chart, provided by the device's manufacturer [81]. In total, the calibration routine performed a rough estimate of 50 simulations.

Table 4.6: Summary of calibrated parameters.

Parameter	Description	Value
D_{coat}	Isotropic diffusion coefficient in the coating	$8.2 \cdot 10^{-13}$ m^2 / s
μ	Macroscopic shear modulus of DCB	1.965 MPa
j_{m}	Limiting stretchability of DCB	5.35
$d_{\mathrm{B},\,0}^{\mathrm{mid}}$	Uninflated middle DCB diameter	1.302 mm

4.5 Computational set-up

The computational set-up of the model was performed in chorus with the previous Chapter 3, using COMSOL Multiphysics® version 6.1 as the modelling and simulation tool. A finite element method framework is developed, combining the governing equations and boundary conditions presented in the previous Sections, to pose a spatiotemporal problem over the 2D-axisymmetric model geometry.

Meshing

Figure 4.9 illustrates the quadrilateral mesh devised to discretise the model domains. Sufficient mesh resolution was required to depict all of the model multiphysics. The mesh was finer in Ω_{coat} since it features drug transport physics besides structural mechanics.

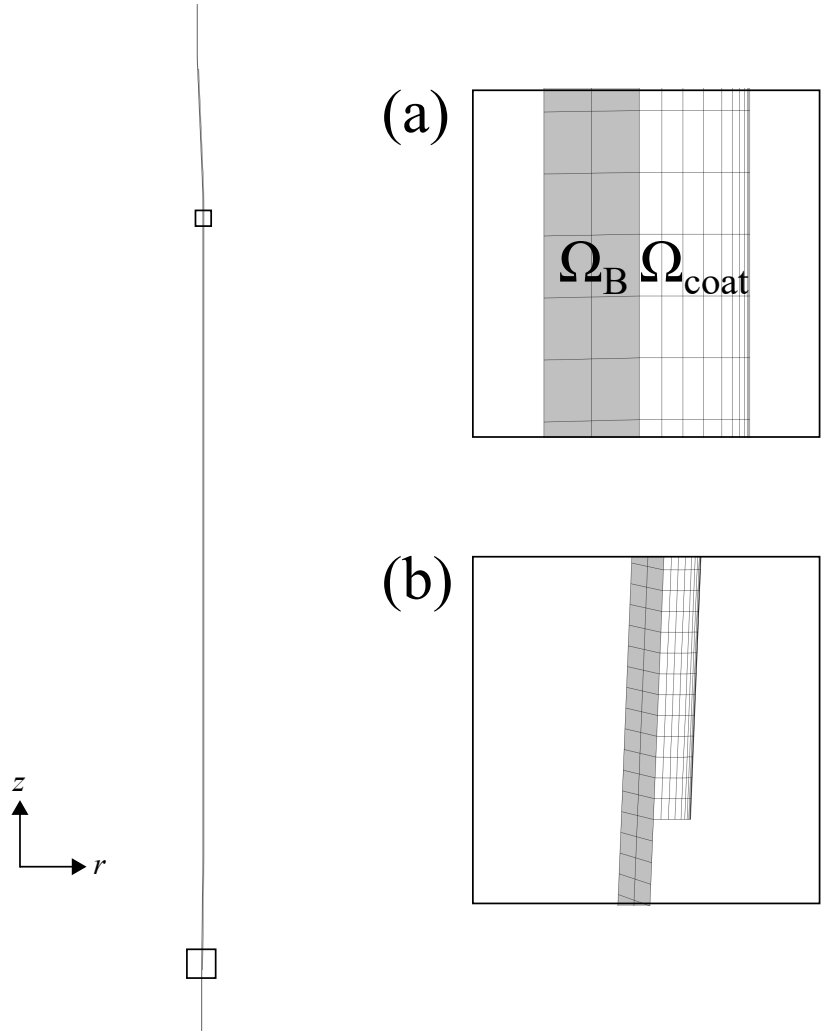

Figure 4.9: Schematic of mesh. The magnified insets detail the mesh composition at (a) the middle and (b) the proximal extremity of the DCB model geometry.

The most challenging computational aspect of the model was related to the perfect sink boundary condition. At the beginning of the simulation (at $t = 0$ s) an abrupt gradient occurs between the initial drug concentration in the coating, c_0, and the perfect sink, which prescribes $c = 0$. The mesh was iteratively refined and boundary layer elements (BLEs) were added at the sink boundary until the drug released at time zero was sufficiently low, i.e. $DRP(t = 0\text{ s}) < 0.2\%$. Additional actions could improve this value, such as further mesh refinement or artificially smoothing the initial drug distribution in the coating. However, the most important question is the awareness of such initial condition problems in diffusion models.

The total mesh consisted of 33442 quadrilateral elements, with average and minimum mesh element quality values of 0.825 and 0.220, respectively (for skewness as the quality measure).

The mesh devised was remarkably lean, featuring only two elements in the radial direction over Ω_{B} and five over Ω_{coat} in addition to four BLEs. Most of the computational burden of the simulation is due to the relatively long DCB geometry length in the longitudinal direction, totalling 38.74 mm (versus the approximate thickness of 0.05 mm in the radial direction). The DCB size of 3.5 x 25 mm (referring to its middle nominal dimensions) was chosen to match the experiments of [100].

Solver settings

Due to the simplified governing equation of drug transport, containing only isotropic diffusion and pseudo-advection, the simulation of the current model was computationally less challenging than the one from Chapter 3. For consistency, the same configuration of solver settings was used. A more detailed explanation of the adjustment of solver settings can be found later in the computational set-up Section 5.5, where the worst-case scenario in terms of computationally challenging simulations was tackled.

Computational specifications and computation time

The resulting system of time-dependent partial differential equations (PDEs) was solved using a Parallel Direct Sparse Solver (PARDISO). The computation was performed using an AMD Ryzen 9 5950X 16-Core CPU @ 3401 MHz processor, with 32 Logical Processors. Computation time was around 30 minutes for each simulation.

4.6 Results

This Section presents the performance of the drug release test model developed. Recapitulating, the main objective of the present model is to reproduce the drug release test — specifically, the behaviours of compliance and drug release. First, the model results were compared with the manufacturer's specifications and experimental data available. Then, additional simulation scenarios were probed to gather further mechanistic insights.

Table 4.7 lists the simulation outputs featured in this Section. Except for the compliance, all results observe the progression of quantities over time.

Table 4.7: Summary of simulation results presented.

Results	Physical unit	Inflation pressure
Compliance	mm/atm	11 atm
Drug release profile	%	
Drug release profile and rate	%, %/s	0 atm, 2 atm, 5 atm, 11 atm
Coating surface area	mm^2	
Coating thickness	mm	

4.6.1 Compliance

The deformation behaviour of the DCB when undergoing inflation is referred to as "compliance". In the model, it is measured as the middle diameter of the DCB versus the magnitude of inflation pressure, $d_{\mathrm{B}}^{\mathrm{mid}}(p_{\mathrm{inf}}(t))$.

Figure 4.10 compares the model compliance with the available device's specifications, informed by its manufacturer as linearly-spaced discrete points over the operation range (6 – 14 atm) [81]. The resulting simulated compliance matches the device's specifications well over the inflation pressure range of the drug release test (6 – 11 atm). The discrepancy between the curve and discrete measurements is quantified via root-mean-square error (RMSE) calculation as 0.0133 mm. The non-linear behaviour of the compliance curve is attributed to the combination of model geometry and hyperelastic material model. Remarkably, the starting value of the model compliance curve at (1.302 mm, 0 atm) is the uninflated middle DCB diameter, $d_{\mathrm{B},\,0}^{\mathrm{mid}}$, calibrated in Section 4.4.

Additionally, Figure 4.11 presents a qualitative depiction of the simulated inflation procedure. Despite the 2D-axisymmetric simplification, the DCB inflation behaviour resembles the reference device as presented earlier in Figure 4.5, and other DCB modelling studies [69, 71].

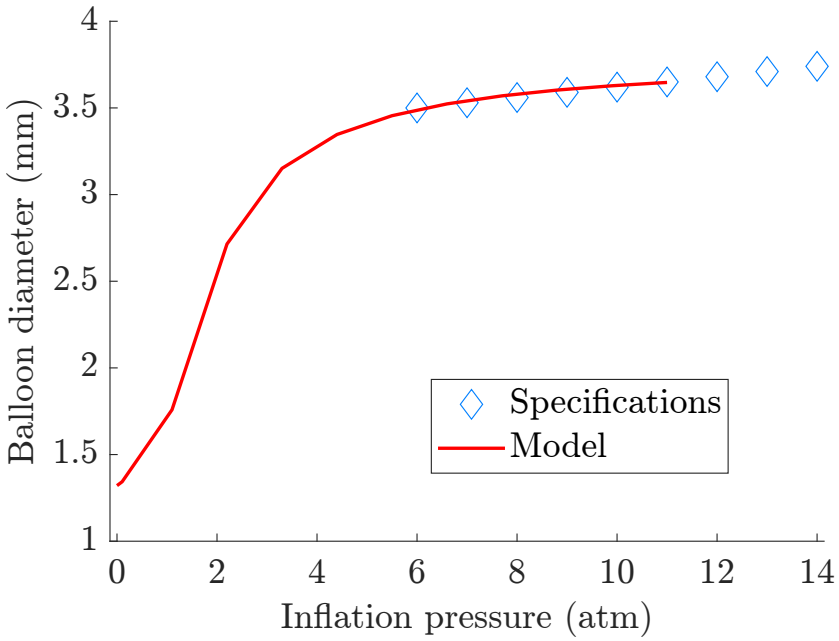

Figure 4.10: Comparison of device's compliance specifications against *in silico* model simulation results.

The middle section of the DCB ($\Gamma^{\mathrm{B}}_{\mathrm{mid}}$) was found to deform in a quasi-uniform fashion in the radial direction, justifying the usage of $d^{\mathrm{mid}}_{\mathrm{B}}$, a point-based value, in the previous measurement of DCB compliance. Also, the remarkably thin balloon thickness is observable in the 2D-axisymmetric perspective.

(a) $p_{\mathrm{inf}} = 0$ atm (b) $p_{\mathrm{inf}} = 11$ atm

Figure 4.11: Qualitative overview of the DCB model geometry's compliance, in 2D-axisymmetric and tridimensional perspectives, between (a) uninflated and (b) inflated states.

4.6.2 Drug release

Drug release from the DCB's coating can be quantified as a drug release profile, $DRP(t)$. As previously defined in Section 4.3, this value represents the cumulative amount of the DCB's drug load released throughout the drug release test simulation. The $DRP(t)$ produced *in silico* is comparable to the experimental results available. Figure 4.12 presents the main comparison of this study — the drug release profile from the model simulation versus the discrete experimental points from the drug release test performed in [100].

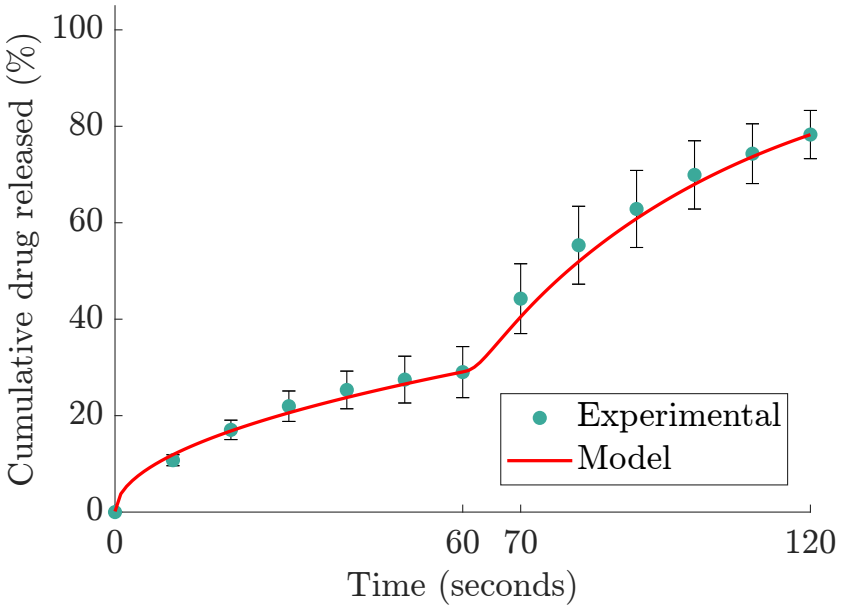

Figure 4.12: Comparison of experimental data of drug release against *in silico* model simulation results. The observed behaviour represents the DCB's drug release in the first sixty seconds of the test in an uninflated state, followed by sixty seconds in an inflated state. Balloon inflation occurs between $t = 60$ s and $t = 70$ s, as highlighted in the horizontal axis, when inflation pressure is ramped up from 0 to 11 atm.

A diffusion-only process satisfactorily described the drug release behaviour of the drug release test. The discrepancy between the curve and discrete measurements is quantified via RMSE calculation as 1.768%. Experimental uncertainty is indicated with the error bars featured in Figure 4.12, as reported in [100].

A pronounced increase in drug release is noticeable when inflation occurs, after sixty seconds into the drug release test. This is the subject of study in the next subsections.

4.6.3 Influence of inflation on drug release

The present model essentially combines drug transport and deformation physics. To improve the understanding of the entwined mechanisms of drug release in the drug release test, a few additional scenarios of varying inflation pressure were probed. The following Figures present the simulation results for different balloon inflation pressures: 0 atm, 2 atm, 5 atm, and 11

atm. In the scenario where the inflation pressure is zero (0 atm), the DCB remains uninflated throughout the simulation. The increasing magnitude of the varying pressure is denoted by the colour progression from green to yellow to red.

Figures 4.12 (a) and (b) show, respectively, $DRP(t)$ results and the rate of change of $DRP(t)$ with respect to time, given by its first-order derivative. In summary, drug release starts rather abruptly once the DCB is immersed in the harsh solution medium, and burst drug release occurs due to inflation.

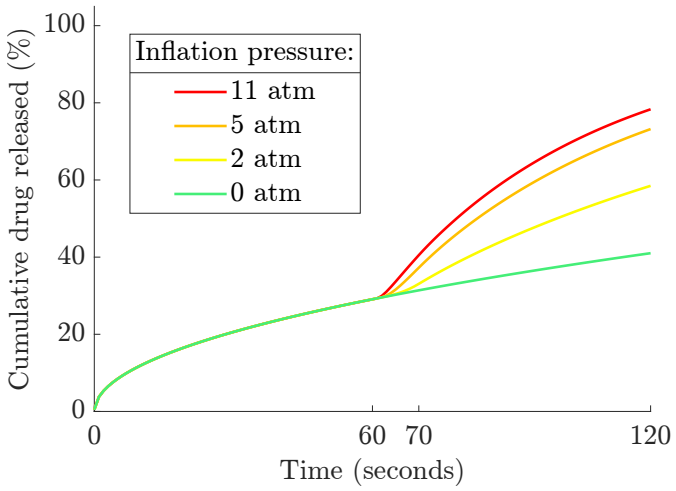

(a)

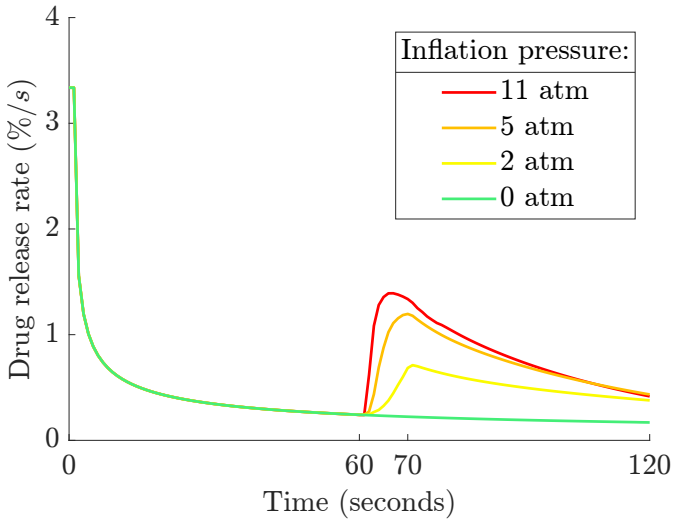

(b)

Figure 4.13: Influence of inflation pressure on (a) cumulative drug released, in %, and (b) drug release rate, in %/s. Drug release increases as the balloon is inflated with increasingly high pressures. When the DCB remains uninflated (0 atm), drug release follows a common diffusion pattern similar to a square root function.

As expected, as inflation pressure increases the drug released also increases. A preliminary investigation of the geometrical reasons for the phenomenon of burst release is proposed. In the model, the outer surroundings of the coating domain (Ω_{coat}) are subjected to a perfect sink

boundary condition. Inflating the DCB causes an increase in the surface area facing the perfect sink boundary condition, which may be translated as greater exposure to the solution medium in the drug release test. Figure 4.14 (a) observes the behaviour of coating surface area for different balloon inflation pressures. In the 2D-axisymmetric model, the coating surface area is obtained from the spatial integration of the outer boundaries of the coating domain (Ω_{coat}).

A complementary factor influencing the drug release is implied as the varying coating thickness. The decrease in coating thickness due to inflation may shorten the path of diffusion in the coating to the sink and increase drug release. Figure 4.14 (b) observes the behaviour of coating thickness, measured by tracking a pair of radially collinear points at the middle section of the DCB.

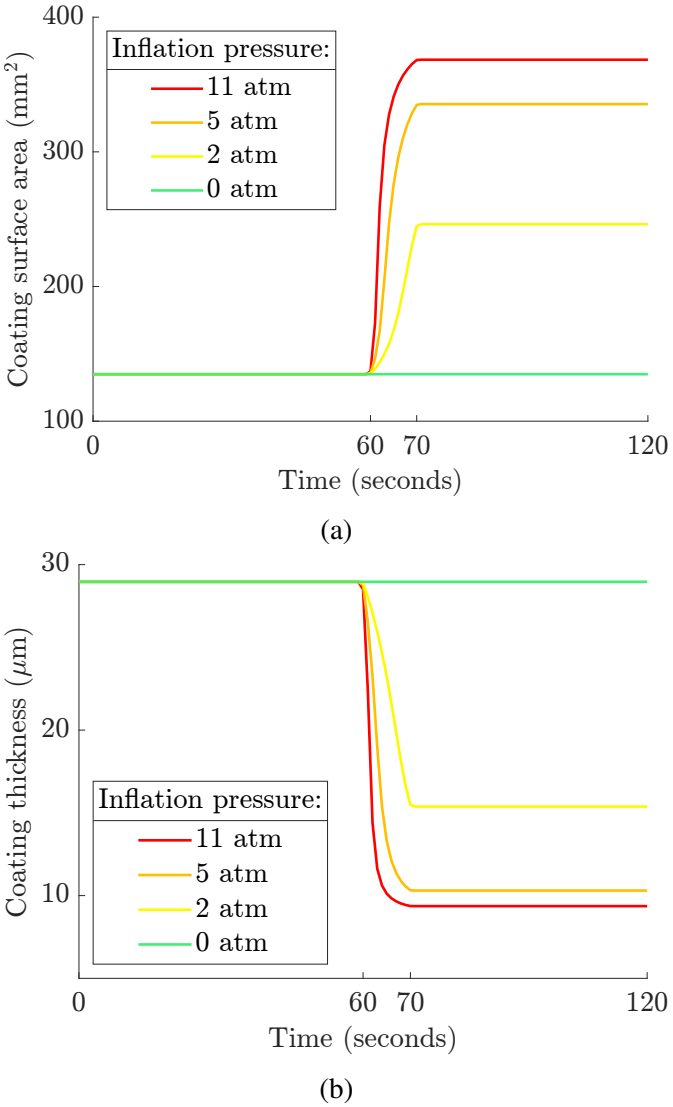

Figure 4.14: Influence of inflation pressure on (a) coating surface area and (b) coating thickness. As the balloon is inflated with increasingly high pressures, its surface area expands while its coating becomes thinner. Both measures are noticeably unchanged when the DCB remains uninflated (0 atm).

The behaviour of the coating in this model is inherent to its simplifying assumptions, which notably neglects the DCB unfolding and assumes an artificial structural resistance. A discussion on this is provided in the subsequent Section.

4.7 Discussion

The present work demonstrates the potential of *in silico* modelling as a tool to complement the traditional ways of experimental testing. For instance, the drug release test as performed in industry can be conveniently simulated for any given scenario of parameters. The model has produced a complete and continuous drug release profile, providing valuable additional insight into experimental measurements provided only at a discrete set of time points.

Overall, the model achieved all of its specific objectives:

(I) Model geometry was satisfactorily described with a series of geometric primitives, as showcased in Figure 4.3.

(II) Structural mechanics and compliance were satisfactorily described with a Gent hyperelastic material model, as showcased in Figure 4.10.

(III) Drug release kinetics were satisfactorily described with a diffusion-only mechanism, as showcased in Figure 4.12.

Exemplifying the potential of *in silico* experimentation, the model allowed investigation of the causes for burst drug release at inflation. Figure 4.14 suggested that burst release at inflation is related to the increase in balloon surface area, which increases the coating region exposed to the drug sink; and the decrease in coating thickness, which may shorten the path of diffusion for the drug to reach the drug sink.

Limitations

The drug release test is used to simulate, to some extent, the ability of the DCB to release its drug load. The immersion and inflation in acetonitrile represent an extreme scenario of exposure that seeks not to replicate the *in vivo* settings but to attest to the performance of the DCB for regulatory reasons. The test is a much simpler phenomenon than the actual application of DCB to arterial tissue; nonetheless, the extensive set of limitations that the drug release test may have is out of the scope of this work.

Given the thin aspect of the balloon geometry and the occurrence of large deformation, it is tempting to model it as a membrane or a shell — for the purpose of structural mechanics. The reader may refer to recent literature on the inflation of hyperelastic thin shells, although not in the context of biomedical engineering, in Liu et al. [117]. However, the main issue with that is how the drug delivery part of the model would work coupled with a shell or membrane.

The calculation of drug transport in the "layer of coating" surrounding the balloon is the main reason for justifying the current 2D-axisymmetric modelling approach used in the model. Another lesser issue is whether there is a shell or membrane formulation in COMSOL and how to implement it. Indeed, a future possibility is that the balloon inflation model can be modelled alternatively, ideally with an outcome that is computationally more accurate and cheaper. Then, the calculation of drug transport in the coating will require reconsideration.

The main limitations of the model are the geometrical simplifications of the DCB, namely (I) the use of 2D-axisymmetry and (II) the depiction of the coating as an immutable solid with structural properties equal to the polymeric balloon. The former ignores the balloon folding process, in which the DCB is folded helically around its radial axis to protect the drug-embedded coating while the DCB is in transit to the lesion site. The balloon folding and unfolding processes are unable to be depicted accurately when using 2D-axisymmetry. For that, a 3D or cross-sectional 2D geometry is necessary. *In silico* studies dedicated to the mechanisms of balloon unfolding in the context of DCBs can be found in [71].

Concerning (II), merging Ω_B and Ω_{coat} does produce an artificially thicker structure, which notably requires different material properties to achieve the desired compliance. An alternative approach could be to assign a much weaker mechanical resistance to Ω_{coat}, since the coating formulation should not pose structural resistance. Figure 4.15 exemplifies this scenario, considering a DCB with balloon and coating merged with the same structural properties and the extreme case of the absence of a coating ("Without coating").

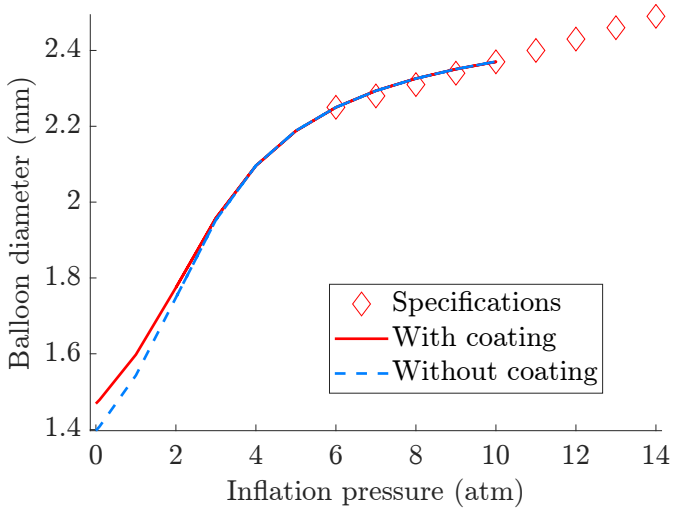

Figure 4.15: Comparison of compliance results between the inflation of a DCB with a coating, assuming the same structural properties for balloon and coating, and a balloon without a coating. The DCB nominal size is 2.25 x 10 mm.

The calibration procedure resulted in different Gent hyperelastic material model parameters to achieve the same compliance behaviour over the operation range (RMSE of approximately 0.01 mm over $6 - -10$ atm compared to the device's specifications). The DCB geometry be-

comes substantially thicker with a coating, and $\mu = 4.44$ MPa and $j_{\mathrm{m}} = 1.705$. Without a coating, the DCB is less thick and requires stiffer structural properties to deform in a comparable fashion subject to inflation pressure, requiring $\mu = 8.84$ MPa and $j_{\mathrm{m}} = 1.88$.

Indeed, an arbitrarily less stiff coating is feasible in the model of Chapter 4 where the DCB experiences free inflation, only requiring adjustments in the calibration procedure. However, it may be rather problematic once the DCB faces contact — as in the simulation of Chapter 5, where the DCB is deployed in an arterial wall. Therefore, the rationale for the simplifying assumption of a stiff coating in the proposed modelling is to avoid the crushing of Ω_{coat} in the forthcoming simulation of DCB deployment, facilitating the calculation of drug transport physics during the contact interaction. For a quantitative assessment of the impact of the simplification during contact the reader may refer to Section 5.7, the Discussion of Chapter 5. For brevity, having a thicker DCB structure with a coating produces about 6% smaller average values of contact pressure compared to a DCB without a mechanically resistive coating.

Future works shall revisit and develop the modelling of the coating domain. Moreover, the current coating assumption consciously neglects that the formulation of the drug and excipient in the coating of the DCB may be physically detached from the device during release. In the context of localised drug delivery from DCBs to arteries, this phenomenon is referred to as "coating adhesion" and is an understudied factor [53].

A lesser simplification concerns the solution medium which immerses the DCB, represented in the model as a perfect sink surrounding the coating domain. The volume of the solution medium, relative to the volume of the DCB, is assumed to be sufficiently large. Thus, it can provide an unlimited concentration gradient during the drug release test and act as a perfect sink in the model. Since the exposure time is limited to two minutes, the model disregards the potential effect of PEO swelling in an aqueous environment and its possible influence on the coating structure and drug transport properties [118].

Overall, the model has been shown to capture the experimental results; therefore, the model limitations were deemed acceptable.

Calibration and validation

A preliminary level of validation was achieved. Due to the availability of a single experimental data set, the model has not yet been tested against different scenarios unknown to the model (unlike the calibration data set) towards proper and formal validation. The discrepancy between the simulation results and the available discrete data points was quantified via RMSE calculation, resulting in values about two orders of magnitude smaller than the measurement range. The calibration procedure was satisfactory as it captured the characteristic behaviour of the problem of interest. A less “brute-force” calibration of parameters could be viable with the use of more sophisticated estimation methods as utilised in [119].

The simulation results suggested that a diffusion-only process is capable of describing the

behaviour of DCB's drug release in the drug release test and that a Gent hyperelastic material model is capable of describing the behaviour of DCB's compliance over the operation range. Despite satisfactory results somewhat fitting the data for a particular scenario, these assumptions might not accurately describe the DCB's behaviour over larger parameter ranges. Further studies are required to test the model against different conditions and achieve sufficient validation. Ultimately, this builds towards using *in silico* modelling as a powerful testing tool.

Conclusion

There is substantial room for improvement in the modelling of drug release from DCBs. This Chapter provides the foundation for representing a DCB *in silico*, advancing the understanding of the simultaneous phenomena of balloon inflation and drug transport in its coating. Despite idealisations, the model presented has shown satisfactory realism and the potential to provide valuable mechanistic insights. These can enhance the design process of DCBs and improve drug-delivery therapies, especially in conjunction with experimental testing. The general aim of this Chapter — to reproduce the drug release test *in silico* — was achieved, culminating in a more sophisticated model of drug release from DCBs. Importantly, an additional outcome of this modelling endeavour was an informed estimate of the diffusion coefficient in the coating of a DCB (D_{coat}), and of its uninflated dimensions ($d^{\text{mid}}_{\text{B},\,0}$). The knowledge obtained will be used in the next Chapter, where the DCB is combined with an arterial wall model to represent the procedure of DCB deployment into a coronary artery.

Acknowledgements

Acknowledgements must be given to the great work performed by Alasdair Hambrey, Hannah Kerr, Jake Miller, and Shona Rae, supervised by Christopher McCormick at the University of Strathclyde [100]. Their work provided the experimental results that served as a reference for the development of the DCB model. Moreover, the collaboration provided fruitful discussions about the subject.

Chapter 5

Modelling simultaneous drug-coated balloon deployment and drug delivery

In the previous Chapters, various models of increasing sophistication were developed to represent the drug delivery from DCB.

Chapter 3 presented the modelling of spatiotemporal drug delivery into a rigid multilayered arterial wall without a representation of the drug-coated balloon (DCB) geometry and its deployment procedure. Drug delivery from the device was simplified as a temporary flux of drug, active only during the brief time window of balloon inflation.

Chapter 4 presented the first steps towards a geometric depiction of the DCB, proposing a thin-walled structure surrounded by a drug-embedded coating. This geometry was made deformable to replicate the inflation behaviour of the actual device. The model was then used to simulate a drug release test within sink conditions, achieving excellent agreement with experimental data.

This Chapter combines the models above to produce a higher fidelity mechanistic description of drug delivery from DCBs, incorporating device design features and procedural parameters independently (e.g. DCB size, inflation pressure, inflation duration, drug load, etc.). That is, drug transfer behaviour will not be known *a priori*. Most of the modelling assumptions and parameters used originate from the previous Chapters. The interplay between the DCB and the arterial wall is modelled as a series of simultaneous, multiphysics, and time-dependent phenomena, emphasising the early events of the DCB inflation procedure — when the procedural factors of the DCB procedure may be entwined with its performance of drug delivery. Ultimately, the resulting model can be used as a powerful and convenient tool for hypothesis testing alongside the traditional experimental methods of preclinical and clinical testing of DCBs.

Outline

This Chapter concisely describes the *in silico* model of endovascular drug delivery from a DCB. The modelling approach is presented in a multilevel structure, with emphasis on the multiphys-

ical aspects of the problem. The modelling set-up is followed by a comprehensive summary of the computational set-up. Then, the main simulation outputs are highlighted, from which the results are quantified. Finally, a discussion is provided on the significance of the mechanistic insights obtained, the limitations of the model, and the prospects of *in silico* experimentation.

5.1 Model geometry

The model geometry is composed of two parts: the DCB and the arterial wall. It represents an idealised scenario of drug delivery, where an uninflated DCB is paired concentrically with a segment of a healthy coronary artery. The objective is to mimic the preclinical scenario where medical devices are tested in healthy animal models without stenosis or atherosclerotic disease.

As demonstrated in Chapters 3 and 4, within this idealised setting the problem of endovascular drug delivery has symmetrical features that can be exploited *in silico*. The model presented in the current Chapter proposes a 2D-axisymmetric geometry that includes the DCB and arterial wall, employing axial and longitudinal symmetries as modelling strategies.

Figure 5.1 shows the model geometry generation process, starting with a simplified two-dimensional geometry and followed by the steps of axial revolution and longitudinal mirroring. The radial (r) and longitudinal (z) directions are indicated with arrows in the Figure. The DCB geometry is inherently symmetric around its radial axis by design, making it suitable for 2D-axisymmetry. The device consists of three parts — proximal, middle, and distal — with different lengths. Nevertheless, if the proximal and distal parts are assumed sufficiently similar, then longitudinal symmetry can also be utilised as another modelling strategy. To implement longitudinal symmetry, only half of the model geometry is modelled and then mirrored longitudinally over a line of symmetry ($\Gamma_{\text{sym},\,z}$). Since the arterial wall geometry is highly idealised as a straight tube, both the radial and longitudinal symmetries also apply to it.

The present model proposes a halved 2D-axisymmetric geometry to produce the desired 3D geometry, once revolved around the axis of radial symmetry ($\Gamma_{\text{sym},\,r}$) and mirrored over the line of symmetry ($\Gamma_{\text{sym},\,z}$). This procedure is illustrated in Figure 5.1. The practical effect of exploiting symmetry is reducing the model size, number of mesh elements, degrees of freedom, number of required calculations, and thus computation time. This confers a large computational advantage to the model, permitting the intensive multiphysics calculations of the model to be completed in a reasonable time. The DCB model architecture was developed in Chapter 4. Similarly, the foundation of the arterial wall model originated from Chapter 3. The notable differences in this Chapter are that the DCB and artery sizes are different, and the mirroring procedure is used.

The resulting geometry depicts the medical device at the beginning of an interventional procedure: uninflated and positioned at the lesion site. Ultimately, one of the model features is to replicate the deformation behaviour of the pair during inflation of the DCB, as exemplified in

Figure 5.1 (d).

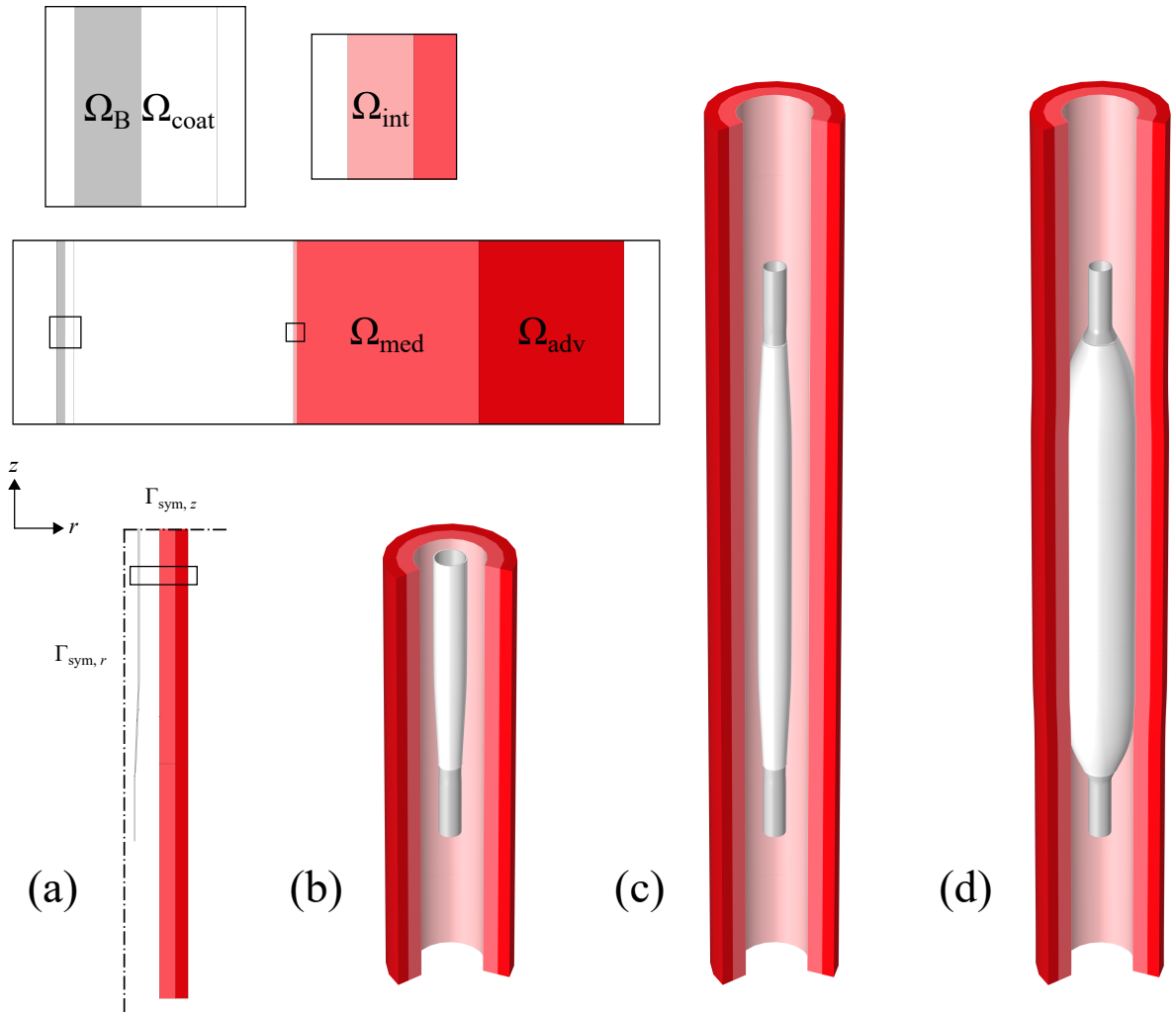

Figure 5.1: Schematic overview of the model geometry, which is composed of DCB and arterial wall. From left to right, labels indicate (a) the starting halved 2D-axisymmetric geometry, (b) the resultant revolved geometry after radial symmetry, (c) the resultant mirrored geometry after longitudinal symmetry, and (d) the deformed geometry when the DCB is inflated, for example with 8 atm of pressure. To enhance visualisation, a sector of $60°$ of the arterial wall is hidden. The multiple domains that compose the model are depicted in detail in the magnified insets of the Figure and summarised in Table 5.1.

The crimping procedure and intravascular transportation of the DCB are not included in the simulation since the model focuses on the interaction between the DCB and arterial wall.

5.1.1 Model domains

The procedure described above creates the basic model geometry that will be used throughout the modelling and simulation of this Chapter. The resulting geometry is composed of separate interior regions, referred to as "domains". There are five domains in total, depicted in detail in the

insets of Figure 5.1 and summarised in Table 5.1. The equations that govern the physics of the model will be defined over these domains, which are notably referent to the current (deformed) configuration, being altered according to deformation.

Table 5.1: Summary of the model domains.

Domain name	Description
Ω_{B}	Balloon
Ω_{coat}	Coating
Ω_{int}	Intima layer of arterial wall
Ω_{med}	Media layer of arterial wall
Ω_{adv}	Adventitia layer of arterial wall

5.1.2 Model boundaries

The edges of the model domains, named "boundaries", are identified and illustrated in Figure 5.2. Boundary names are consistent with the arterial wall model, from Chapter 3, and the DCB model, from Chapter 4, to facilitate comparison.

Table 5.2: Summary of the model boundaries.

Boundary name	Description
$\Gamma_{\mathrm{sym},\,r}$	Axis of radial symmetry
$\Gamma_{\mathrm{sym},\,z}$	Line of longitudinal symmetry
Γ_{coat}	Outer middle surface of coating
$\Gamma^{\mathrm{B}}_{\mathrm{mid}}$	Inner surface of balloon, middle
$\Gamma^{\mathrm{B}}_{\mathrm{prox}}$	Inner surface of balloon, proximal
Γ_{shaft}	Inner surface of catheter shaft
$\Gamma^{\mathrm{DCB}}_{\mathrm{sym},\,z}$	Mirroring extremity of balloon and coating
$\Gamma^{\mathrm{B}}_{\mathrm{ext}}$	Proximal extremity of balloon
$\Gamma_{\mathrm{ET,\,de}}$	Denuded endothelium
$\Gamma_{\mathrm{ET,\,in}}$	Intact endothelium
Γ_{IEL}	Internal elastic lamina
Γ_{EEL}	External elastic lamina
Γ_{periv}	Perivascular end
$\Gamma^{\mathrm{wall}}_{\mathrm{sym},\,z}$	Mirroring extremity of arterial wall
$\Gamma^{\mathrm{wall}}_{\mathrm{ext}}$	Proximal extremity of arterial wall

The domains and boundaries listed in Tables 5.1 and 5.2 will be referenced in the subsequent sections where the multiphysics phenomena are defined.

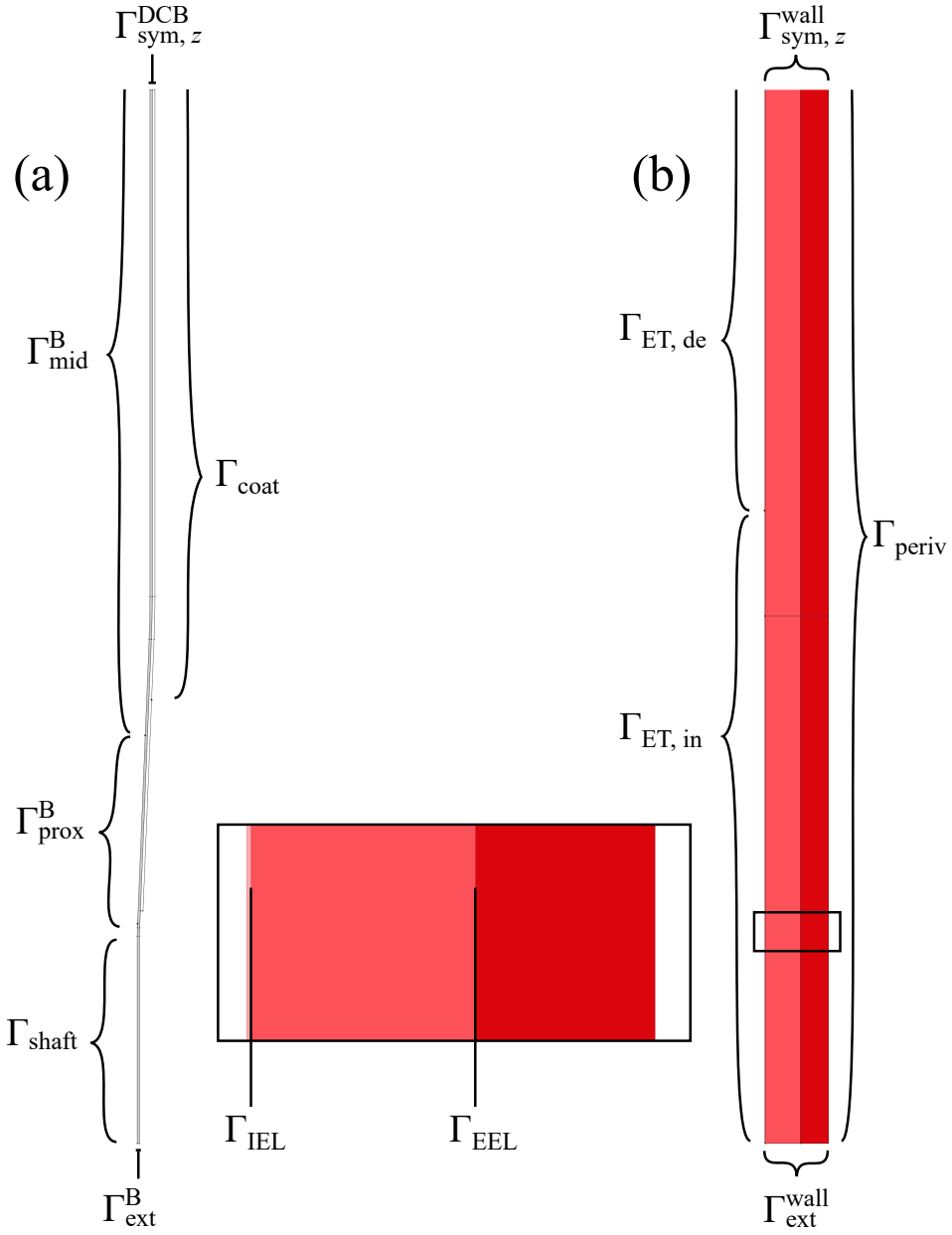

Figure 5.2: Schematic overview of the relevant model boundaries of (a) the DCB and (b) the arterial wall. The magnified inset depicts the arterial wall and its elastic laminae, which separate the layers. All boundary names are listed in Table 5.2.

5.1.3 Model dimensions

The dimensions used for building the model geometry are presented in Figure 5.3 and listed in Table 5.3. These are equivalent to the arterial wall model employed in Chapter 3. Due to

the assumption of longitudinal symmetry, the DCB is depicted as having its proximal and distal parts of equivalent size, unlike as in Chapter 4. This is another simplifying assumption, and any small differences in the proximal and distal parts of the DCB should have a negligible effect on the simulation results because the device's deformation and drug delivery are assumed to be dictated by its middle part.

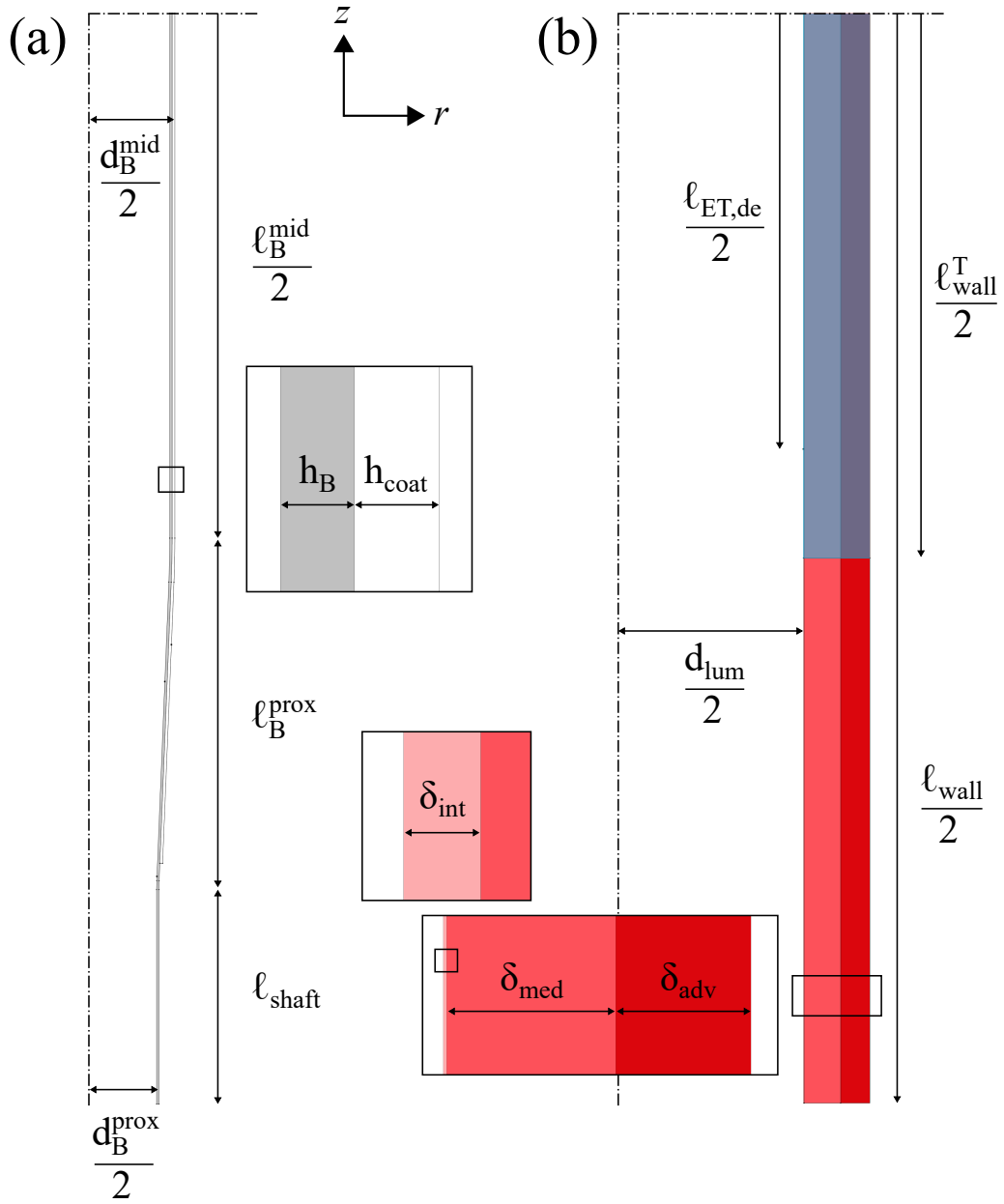

Figure 5.3: Schematic overview of the model dimensions of (a) the DCB and (b) the arterial wall. The magnified insets depict model domain thicknesses. Due to axisymmetry and mirroring, some dimensions appear halved or absent in the figure. All dimensions are listed in Table 5.3.

Noteworthy, the initial model dimensions aim to explicitly represent an already pressurised

arterial wall and no circumferential pretensioning is taken into consideration. Additionally, the model starts with uninflated balloon dimensions, estimated as per Chapter 4. The DCB nominal size chosen is 2.25 x 10 mm (i.e. "nominal diameter" x "middle section length") to ensure a $1:1$ balloon-to-artery ratio, as suggested in [47]. This ratio relates the outer diameter of the balloon when inflated to nominal pressure (6 atm) to the luminal diameter of the target artery. It is used clinically when selecting the DCB size for an intervention.

The therapeutic region, highlighted in blue in Figure 5.3, is the central part of the treated artery. It includes a part of each layer of the arterial wall and is where drug distribution will be assessed *in silico*, to mimic the measurement protocol performed in preclinical experiments.

Table 5.3: Summary of DCB model dimensions. The dimensions related to the DCB and preclinical assessment methods were estimated based on discussions with Biosensors International.

Parameter	Description	Value	Reference
$d_{\mathrm{B}}^{\mathrm{nom}}$	Nominal diameter	2.25 mm	[81]
$d_{\mathrm{B}}^{\mathrm{mid}}$	Crossing profile	1.00 mm	Estimated
$d_{\mathrm{B}}^{\mathrm{prox}}$	Proximal extremity diameter	0.7112 mm	[81]
$d_{\mathrm{B}}^{\mathrm{dist}}$	Distal extremity diameter	0.7112 mm	[81]
$\ell_{\mathrm{B}}^{\mathrm{mid}}$	Middle section length	10 mm	[81]
$\ell_{\mathrm{B}}^{\mathrm{prox}}$	Proximal section length	2.97 mm	[81]
$\ell_{\mathrm{B}}^{\mathrm{dist}}$	Distal section length	2.97 mm	[81]
ℓ_{shaft}	Shaft length	2 mm	Estimated
h_{B}	Balloon wall thickness	21.6 μm	[81]
h_{coat}	Coating thickness	25 μm	[81]
d_{lum}	Diameter of arterial lumen	2.25 mm	[63]
ℓ_{wall}	Length of total artery segment	30 mm	Estimated
$\ell_{\mathrm{wall}}^{\mathrm{T}}$	Length of therapeutic artery segment	15 mm	Estimated
$\ell_{\mathrm{ET,\,de}}$	Length of denuded endothelium segment	12 mm	[72]
δ_{int}	Thickness of intima layer	0.01 mm	[63]
δ_{med}	Thickness of media layer	0.5 mm	[63]
δ_{adv}	Thickness of adventitia layer	0.4 mm	[63]

Most of the DCB model dimensions are as per the manufacturer's specifications. Noteworthy, $d_{\mathrm{B}}^{\mathrm{nom}}$ is an implicit dimension that may only be observed mid-simulation when the DCB is inflated to its nominal pressure.

The definition of the model geometry is followed by a presentation on the modelling of the multiple physics involved in the problem of endovascular drug delivery.

System of Levels

A system is proposed to provide a structured depiction of the multiphysics architecture of the model in Levels. Three levels are defined, characterising the interdependent parts of modelling DCB deployment and drug delivery into arterial tissue:

- Level 1: Solid mechanics
- Level 2: Transmural filtration
- Level 3: Drug transport and retention

The concept of Levels is illustrated in Figure 5.4. The influence of each Level is denoted by colour, encompassing the DCB and arterial wall separately, and arrows represent the interrelation between their features. This diagram synthesises the model's multiphysics architecture and serves as a map of the structure of the Chapter. It aims to help orient the reader throughout the presentation of the Levels.

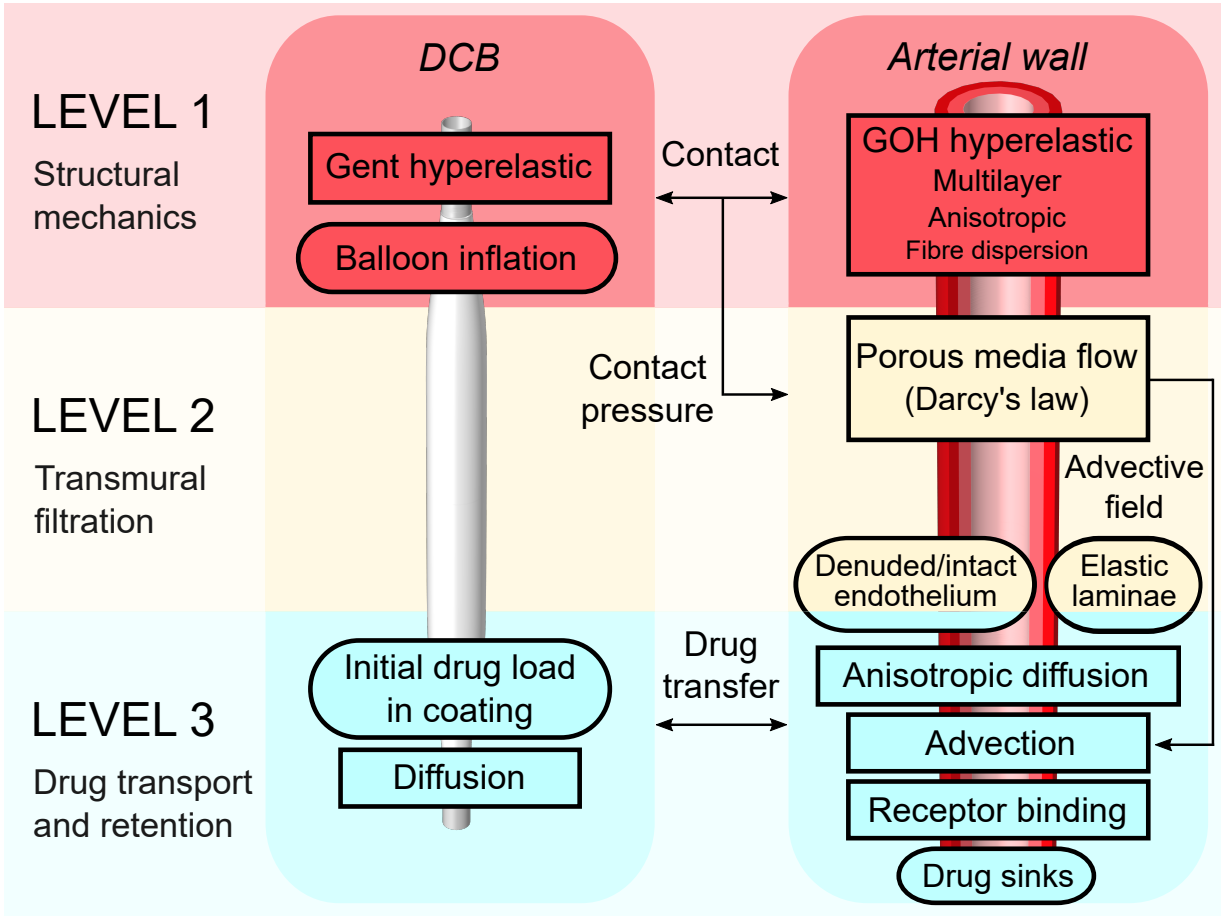

Figure 5.4: Schematic representation of the system of Levels, synthesising the model multiphysics. The colours express the coverage of each feature within Levels. Square boxes represent intrinsic mechanisms and definitions, while round boxes represent initial or boundary conditions. Arrows indicate interrelations between physics.

The simulation of the model presented in this Chapter comprises a stationary step, followed by two time-dependent steps:

- Initialisation step: An auxiliary step to set up initial conditions of the model multiphysics at $t = 0$ s.
- Deployment step: A short initial period of approximately one minute focussed on the DCB deployment procedure.
- Follow-up step: A subsequent prolonged observation period of 28 days after removing the DCB focussed on the drug distribution in the tissue. The terminology is based on the clinical concept of "follow-up" [120], where the patient status is continuously evaluated.

Briefly, the stationary step is proposed to provide computational stability at the beginning of the simulation. The two time-dependent steps are designed to evaluate both early and long-term outcomes of the drug therapy, respectively the drug delivery procedure and the retention in the arterial tissue. All Levels are enabled during the Deployment step. Afterwards, during the Follow-up step, Level 1 is disabled completely since the DCB is removed from the arterial environment after the intervention and it is assumed that all mechanical stimuli cease to exist after the deployment procedure is completed.

The three Levels of the system function independently to some extent. However, their features notably intersect in the event of contact, which occurs during most of the Deployment step. Contact between the inflating device and the artery has three main modelling implications, intentionally spread across the Levels. These are (1) structure-structure interaction, (2) variation of the pressure constraint at the lumen-wall interface, and (3) drug transfer, enabled by connectivity between drug concentration fields. The main motivation of the modelling work presented here is to incorporate these factors simultaneously into a time-dependent simulation.

In Level-order, the following sections describe the modelling assumptions and techniques employed towards a multiphysics simulation of DCB deployment and drug delivery.

5.2 Level 1: Structural mechanics

The procedure of endovascular balloon deployment involves inflation at high pressure against an artery, which induces deformation in both parts of the pair. The first Level of the system characterises the structural mechanics of each component of the model pair — DCB and multilayered arterial wall — by defining: constitutive laws to govern the material deformation behaviour; boundary conditions to constrain or allow spatial movement; a varying pressure load to represent the event of balloon inflation; and the contact interaction between the pair during deployment. As a result, the mechanical deformation and stress distribution of the model are obtained throughout the simulation of DCB deployment. When the balloon is deflated, the contact interaction lessens until disconnection, and the arterial wall returns to its original geometrical configuration. The equations of structural mechanics are solved only for the Deployment step, which occurs briefly until approximately one minute into the simulation. After the balloon is deflated and removed, the deformation stimuli are assumed to cease, and the remaining physics continue to be solved over a rigid arterial wall geometry for the rest of the simulation.

5.2.1 Material models

In solid mechanics, a material model is a relationship that describes how bodies behave in terms of stresses and deformation when subjected to forces. This subsection presents two types of hyperelastic material models used to characterise the mechanical behaviour of the DCB and arterial wall.

DCB: Gent

The structural behaviour of the DCB is similar to what was presented in Chapter 4. In summary, the DCB is described by an incompressible Gent hyperelastic material model assuming balloon and coating as a merged structure with the same mechanical properties.

Arterial wall: Gasser-Ogden-Holzapfel

The arterial wall model was introduced in Chapter 3 as a rigid geometry without a description of the deformation behaviour. This subsection presents the inclusion of solid mechanics for the arterial wall model in the form of a constitutive model. By assigning structural mechanics properties to the artery, it can experience deformation along with drug transfer when it comes into contact with the inflating DCB.

A Gasser-Ogden-Holzapfel (GOH) hyperelastic material model is chosen to describe the structural mechanics of the artery, based on [121]. This material model proposes an invariant-based strain energy density function, accounting for the nonlinear response and distributed orientation of collagen fibres in the arterial tissue. Similarly to the simplifying assumption for

the DCB, the arterial wall is modelled as an incompressible material. The incompressibility of arterial tissue is an acceptable assumption for the practical purpose of this modelling work, as evidenced by [122] and supported by [123]. Then, a GOH material model is used to describe each of the arterial wall layers (Ω_{int}, Ω_{med}, and Ω_{adv}) as incompressible anisotropic hyperelastic materials.

The implementation logic of the material model is presented below, starting with a compound strain energy density function in Equation 5.2.1:

$$\Psi_{\text{GOH}} = W_1 + W_4 + W_6, \tag{5.2.1}$$

where the isochoric strain energy density, Ψ_{GOH}, results from the combination of the isotropic isochoric strain energy density (W_1), the anisotropic mechanical contributions of the first fibre family (W_4), and the anisotropic mechanical contributions of the second fibre family (W_6). Respectively, these three terms characterise the mechanical response of elastin as isotropic and elastic, and of the anisotropic fibres in their two preferential directions as in [123].

Each of the components above is defined on a layer-specific basis, with i denoting a generic artery layer, in Equation 5.2.2:

$$\begin{cases} W_1 = \mu_i \, (I_1 - 3) \\ \\ W_4 = \dfrac{k_{1,\,i}}{2k_{2,\,i}} \left(\exp\left\{ k_{2,\,i} \left[\kappa_i \, I_1 + (1 - 3\kappa_i) \, I_4 - 1 \right]^2 \right\} - 1 \right) & \text{for } i = \{\text{int, med, adv}\}, \\ \\ W_6 = \dfrac{k_{1,\,i}}{2k_{2,\,i}} \left(\exp\left\{ k_{2,\,i} \left[\kappa_i \, I_1 + (1 - 3\kappa_i) \, I_6 - 1 \right]^2 \right\} - 1 \right) \end{cases} \tag{5.2.2}$$

where the parameters μ_i, $k_{1,\,i}$, and $k_{2,\,i}$ are obtained through mechanical testing of the tissue and represent neo-Hookean, stress-like, and nonlinearity characteristics, respectively. The first invariant of the right Cauchy-Green deformation tensor is denoted by I_1 as in [124]. The terms I_4 and I_6 are strain invariants, defined as equal to the square of the stretch in the direction of the fibres, respectively for the first and second fibre families, given by the mean orientation angle β_i [121]. Assuming that the strain energy from anisotropic terms only contributes to the global structural response of the tissue when stretched and bears no load when compressed, I_4 and I_6 are only considered for values greater than one [63]. This is intended to avoid some unexpected behaviour in shear, reported in detail in [125]. It is noteworthy that κ_i indicates the degree of fibre dispersion in that respective layer, characterising the distribution of collagen fibres within the two families. When $\kappa_i = 0$, it means that the fibres are perfectly aligned, while $\kappa_i = \frac{1}{3}$ indicates randomly-oriented fibres leading to an isotropic response. The parameters κ_i and β_i are determined from histological data of the tissue.

Using a sophisticated material model such as GOH permits the combination of anisotropy, in the form of collagen fibre dispersion, with the multilayer properties of the arterial wall model. By assigning layer-specific material parameters to each artery layer, additional anisotropic depth can be introduced to the model. Ideally, it provides a better depiction of the complex microstructure structure of soft biological tissues to make the simulated deformation behaviour more realistic. Hence, aiming to meet the prerequisite of realistic constitutive modelling for quantifying changes in the arterial wall in response to stimulus, as proposed by [121]. The material parameters used for each layer are summarised in Table 5.4).

Table 5.4: Summary of layer-specific GOH material model parameters. All parameters originated from the indicated reference and were fitted according to [63].

Name	Description	Unit	Layer-specific value, for $i =$			Reference
			int	med	adv	
μ_i	Neo-Hookean parameter	kPa	26.16	1.93	8.17	[126]
$k_{1,\,i}$	Stress-like parameter	kPa	10485.17	149.10	695.61	[126]
$k_{2,\,i}$	Nonlinearity parameter	—	20.00	51.74	604.79	[126]
κ_i	Dispersion parameter	—	0.165	0.262	0.265	[126]
β_i	Mean orientation angle	°	50.02	37.47	60.33	[126]

The density of wet arterial tissue is irrelevant since the deformation is assumed quasi-static.

5.2.2 Time-invariant boundary conditions

This subsection describes a set of physical constraints that enclose the model domains. Particularly, these boundary conditions feature unchangeable behaviour over time.

Spring foundation

The model geometries represent only a finite section of the DCB and arterial wall. These are virtually limited at the proximal and distal extremities by $\Gamma^{\mathrm{B}}_{\mathrm{ext}}$ and $\Gamma^{\mathrm{wall}}_{\mathrm{ext}}$, respectively. Since these boundaries are sufficiently far from the deployment region, they are assumed to be immobilised in terms of solid mechanics. Similarly, the catheter shaft where the balloon is mounted (represented by Γ_{shaft}) is also assumed to be immobile during the inflation procedure. Over these boundaries, the model employs a spring foundation as an alternative to fixed constraints. A detailed definition of the spring foundation boundary condition can be found in Chapter 4.

Roller

The DCB and arterial wall are also limited by the longitudinal line of symmetry ($\Gamma_{\mathrm{sym},\,z}$) at $\Gamma^{DCB}_{\mathrm{sym},\,z}$ and $\Gamma^{wall}_{\mathrm{sym},\,z}$, respectively. To allow free displacement in the tangential direction (r) but prevent

any movement in the perpendicular direction (z), a "roller" boundary condition was proposed over these boundaries. This constraint is somewhat analogue to a "symmetry" condition, as used in [72] and [80] to mirror the model geometries, but intended here to represent also the sliding motion over $\Gamma_{\text{sym},\,z}$. It is described in Equation 5.2.3 as:

$$\mathbf{v} \cdot \mathbf{n} = 0, \tag{5.2.3}$$

where $\mathbf{v}$ is the geometry displacement, and $\mathbf{n}$ is a unitary normal vector at that boundary. This boundary condition effectively causes the model geometries to "slide" in the direction tangential to the boundary of effect. Since balloon inflation is assumed to be symmetric in this model, it is reasonable to assume pure radial displacement at these boundaries. Free deformation is prescribed to the remaining boundaries of the model geometry.

The following subsections describe separately the two boundary conditions exhibiting variable behaviour over time. These are the primary mechanisms that characterise the time-dependent features of the deployment simulation: balloon inflation and contact.

5.2.3 Balloon inflation

In the clinical setting, the DCB is positioned at the intervention site and then inflated with high pressure (6 – 10 atm) to engage the interior surface of the blood vessel. This pressure range is in line with the manufacturer's procedural guidelines, given in the usage instructions of Biosensors's BA9™ DCB [81]. The pressure is then maintained for a sufficient duration to allow drug transfer to the arterial wall [36]. This duration is estimated, based on typical values for coronary applications [32], as 60 seconds.

Pressure ramp

Similarly to Chapter 4, a time-dependent pressure load $p_{\text{inf}}(t)$ is proposed to simulate the balloon inflation procedure. Additionally, the pressure function includes the deflation of the DCB after the prescribed inflation duration is reached.

The pressure load boundary condition is devised with the use of ramp functions applied to the inner surface of the DCB ($\Gamma^{\text{B}}_{\text{mid}}$ and $\Gamma^{\text{B}}_{\text{prox}}$). Inflation pressure magnitude is applied to $\Gamma^{\text{B}}_{\text{mid}}$ in full, while is applied to $\Gamma^{\text{B}}_{\text{prox}}$ in a spatially gradual fashion. The distal part of the ramp is absent due to longitudinal symmetry, and the entire DCB structure is pre-tensioned before inflation. A detailed definition of ramp smoothing and balloon pre-tensioning can be found in Chapter 4.

Equation 5.2.4 states the desired pressure versus time behaviour:

$$p_{\text{inf}}(t) = \begin{cases} \dfrac{t}{t_{\text{ramp}}}\, p_{\text{max}} & 0 < t < t_i \\ p_{\text{max}} & t_i \leq t \leq t_f \\ p_{\text{max}} - \dfrac{t - t_f}{t_{\text{ramp}}}\, p_{\text{max}} & t_f < t < t_f + t_{\text{ramp}}, \end{cases} \tag{5.2.4}$$

where $t_i = t_{\text{ramp}}$ and $t_f = t_i + \Delta t_{\text{inf}}$ are the initial and final time limits of inflation at nominal pressure, assuming the starting time of the ramp as zero for simplicity; and p_{max} is the target inflation pressure, considering a zero base pressure inside the balloon at the uninflated state. As the arterial lumen is largely simplified, any effects of the pressurised lumen resisting balloon inflation are neglected in this model. Thus, inflation occurs as a free expansion.

The modal behaviour presented above can be described by a single time-dependent function valid for the entire Deployment step, as in Equation 5.2.5:

$$\begin{aligned} p_{\text{inf}}(t) = \; & \min\left(\frac{t}{t_{\text{ramp}}}, 1\right) p_{\text{max}} \\ & - \max\left(0, \frac{t - t_f}{t_{\text{ramp}}}\right) p_{\text{max}} \qquad 0 < t < t_f + t_{\text{ramp}}, \end{aligned} \tag{5.2.5}$$

where min and max are minimum and maximum functions. Their usage limits the values of the ramps, permitting the use of the independent time variable t over a continuous interval.

Figure 5.5 shows the behaviour of magnitude of inflation pressure load versus time. It also illustrates the definition of inflation duration as $\Delta t_{\text{inf}} = t_f - t_i$. In summary, the boundary condition $p_{\text{inf}}(t)$ prescribes a pressure load that rises in magnitude briefly ($t_{\text{ramp}} = 10$ s) until the predefined maximum inflation pressure value (p_{max}) is reached; sustains it for the predefined inflation duration (Δt_{inf}); then ramps down over 10 seconds ($t_{\text{ramp}} = 10$ s), returning to its starting value and retracting the balloon to its deflated state.

Calibration of compliance

As per a similar iterative parameter calibration routine as in Chapter 4, the deformation behaviour of the inflating DCB, known as "compliance", was adjusted for a clinically relevant pressure range (6 – 10 atm). The fine-tuned material parameters for the Gent hyperelastic material model are $\mu = 1.965$ MPa and $j_{\text{m}} = 5.35$. Figure 5.6 compares the resulting compliance from a simulation of free inflation against the device's specifications as provided by the manufacturer [81]. The model behaviour matches the compliance data well over the chosen operation range.

Table 5.5 lists the set of parameters that characterise the inflation procedure in the model.

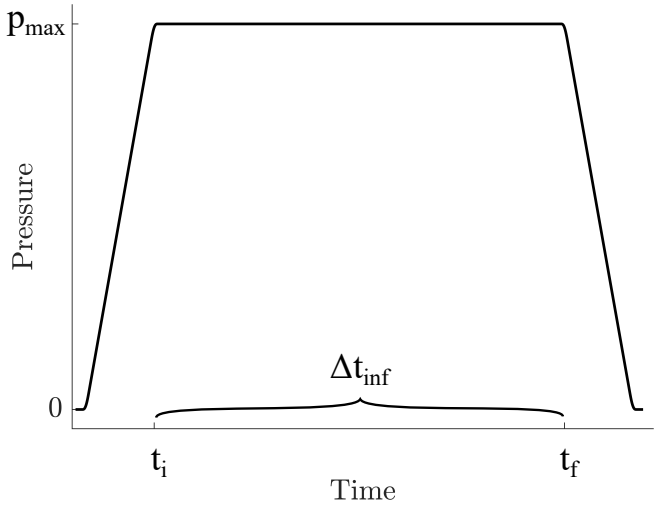

Figure 5.5: Magnitude of the time-dependent pressure load versus time, characterising the DCB inflation and deflation during the Deployment step.

Table 5.5: Summary of procedural parameters involved in the DCB inflation model. Procedural values were estimated from discussions with Biosensors, and the pre-stress value from own *in silico* experimentation.

Parameter	Description	Value	Reference
p_{max}	Target inflation pressure	6 – 10 atm	[81]
Δt_{inf}	Inflation time duration	60 s	[32]
t_{ramp}	Ramp up / down duration	10 s	Estimated
σ_{pre}	Balloon prestress	20 MPa	Estimated

It is assumed that the role of the DCB in the procedure ends after deflation. Therefore, after deflation the DCB is removed from the simulation along with all of its coexistent physics.

5.2.4 Contact

In Level 1, the solid mechanics interaction between DCB and arterial wall during contact is considered. The two entities of the model — DCB and arterial wall — are modelled as initially disconnected geometries. This represents the preclinical/clinical pre-intervention scenario, where the medical device is positioned at the lesion site and is ready to be inflated. In the model, the nominal diameter of the DCB is compatible with the internal artery diameter at a $1 : 1$ balloon-to-artery ratio. When the DCB is inflated to the nominal inflation pressure of 6 atm, its external surface will barely come in contact with the inner surface of the arterial wall without exerting any pressure. If the pressure is increased beyond that threshold value, the two surfaces will mechanically interact with each other, exerting equal and opposite pressure. To model this interaction, a contact algorithm is used.

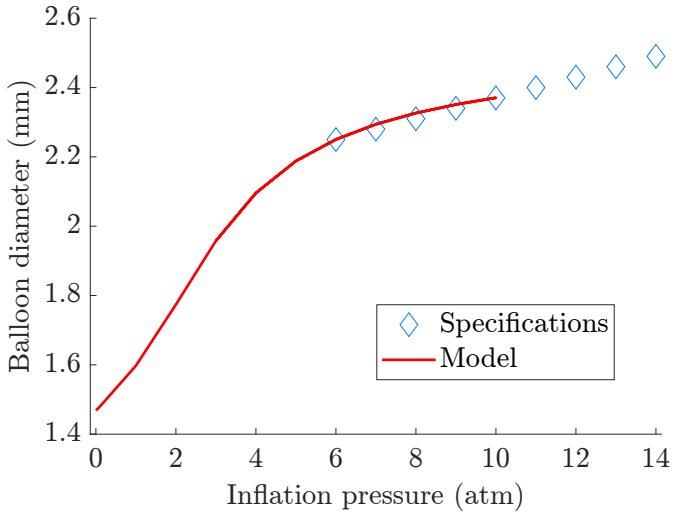

Figure 5.6: Comparison of compliance between DCB model results and device's specifications, expressed as middle section balloon diameter versus inflation pressure. This compliance curve notably differs from the previous Figure 4.10, in Chapter 4, due to the different DCB sizes considered.

Contact pair

The implementation of contact physics in the model starts with defining a "contact pair", which comprises the pair of potentially interacting boundaries. The selected boundaries are (I) a central part of the outer surface of the coating, Γ_{coat}, as the "source" and (II) an adjacent segment of the arterial wall that will receive contact, i.e. the denuded endothelium boundary $\Gamma_{\text{ET, de}}$ as the "destination".

Contact constraint is an inequality. It can be expressed using three conditions, known as the Karush–Kuhn–Tucker conditions, as explained in detail in [127]. The deformed positions of the contact pair surfaces are denoted as X_{Src} and X_{Dst}, respectively, for "source" and "destination", and the distance between the contacting pair is defined with a simplified physical gap function as $\Delta X = (X_{\text{Dst}} - X_{\text{Src}})$. The contact pressure between the two surfaces is defined as T_n, assumed positive in compression and in the normal direction to the contacting boundaries. Some notations are simplified for the sake of the theoretical set-up of the model. Therefore, a penalty method of contact is proposed to approximately impose the Karush–Kuhn–Tucker conditions in the model.

Penalty contact method

The penalty method governs the contact interaction between bodies in this model. For brevity, it works by imposing a stiff spring between the contacting surfaces when the contact clause is satisfied ($\Delta X < 0$). It is measured in the normal direction and in the spatial frame of the model, which varies with deformation along the time-dependent simulation. As the term becomes less than zero, a small penetration condition occurs. The penetration is then "penalised" by the insertion of a stiff compression-only spring between the contacting points, which pushes them apart.

The spring exerts increasing force as the boundaries engage contact, consequently contributing to structural stresses and triggering deformation in accordance with the material models. More details can be found in Section 5.5, "Computational set-up".

Assuming no pressure is transmitted at zero gap, the contact pressure relation between the contacting boundaries of the pair may be described by Equation 5.2.6:

$$T_n = \begin{cases} -f_p \, \Delta X & \text{if } \Delta X < 0 \\ 0 & \text{if } \Delta X \geq 0, \end{cases} \tag{5.2.6}$$

where T_n is the contact pressure in the normal direction, and f_p is the stiffness-like parameter. The two cases in the equation indicate that T_n is null if the distance between surfaces is greater than or equal to zero, i.e. while not in contact.

The term f_p is an important parameter in the penalty method. Its value determines the proportionality of the penalty relationship, as the stiffness of a spring, between the contacting boundaries of the pair. For instance, a high value of f_p indicates a stiff contact behaviour and a low value represents a soft contact behaviour. Notably, both extremes can pose numerical ill-conditioning of the problem. In the current model, an iterative trial-and-error process was used to adjust the penalty factor, eventually selecting a penalty factor value of $f_p = 4 \cdot 10^{11}$ Pa/m. The value is based on the characteristic stiffness and mesh size of the arterial wall, then adjusted iteratively. This choice ensured computational stability and acceptable penetration between contacting domains (less than 1 μm).

Figure 5.7 illustrates the evolution of the contacting boundary length during balloon deployment and the effect of the penalty factor method as springs in compression deforming the pair. At the end of the Deployment step, the balloon is deflated, and contact is terminated.

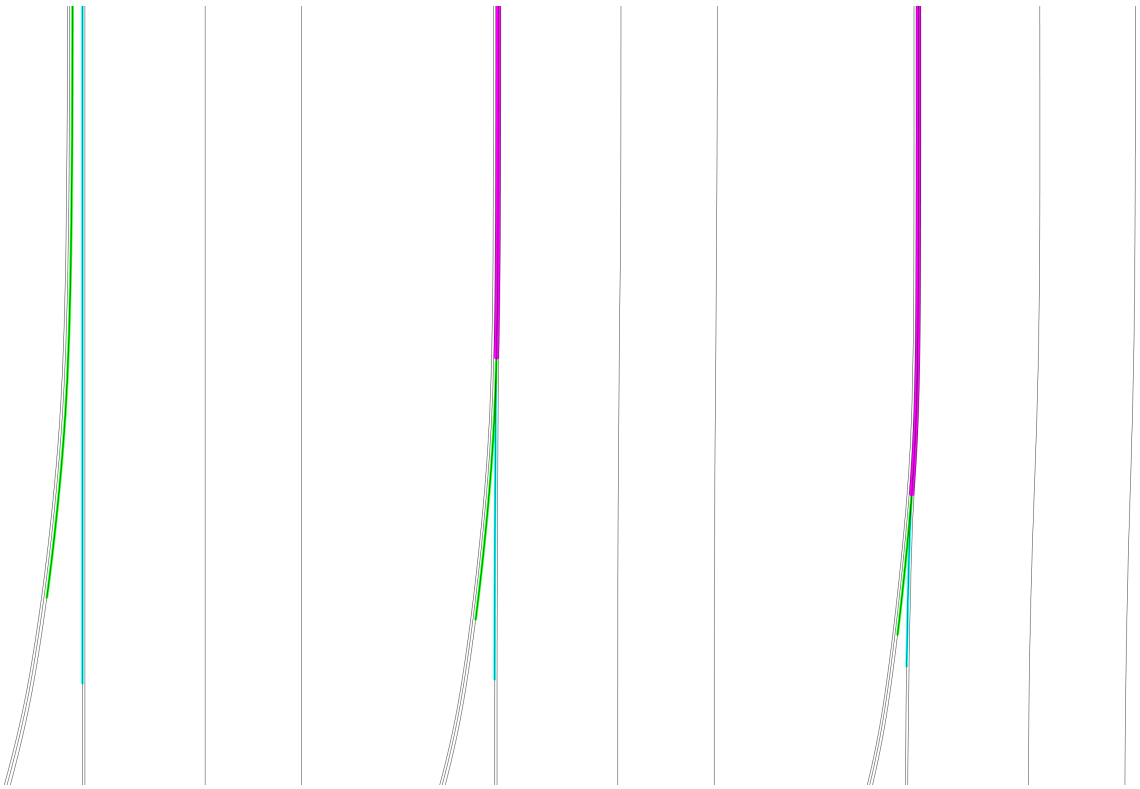

(a) $t = 8$ s (b) $t = 10$ s (c) $t = 12$ s

Figure 5.7: Qualitative illustration of the contact constraint progression along the time-dependent simulation of DCB deployment, for an example scenario with an inflation pressure of 8 atm. The reverse behaviour is observed as the balloon is deflated. The "source" and "destination" boundaries are illustrated in green and cyan, respectively, and the satisfaction of the contact clause is illustrated in magenta.

This concludes the characterisation of the solid mechanics of the model. In summary, Level 1 defines the solid mechanics behaviour of the model geometry and provides coherence for the spatial frame of the simulation. The contact interaction may be seen as an input that makes the inflation of the DCB affect the arterial wall. As a result, the contact pressure causes the pair to deform, altering their position in the spatial frame accordingly during the inflation procedure. Nevertheless, in the context of endovascular DCB deployment, the contact pressure between the device and the vessel has implications beyond solid mechanics. The following section considers how contact affects the fluid flow through the arterial wall.

5.3 Level 2: Transmural filtration

The second Level of the system describes the fluid flow occurring through the porous and permeable arterial wall, i.e. transmural filtration, during and after DCB deployment. A detailed definition of this phenomenon can be found in Chapter 3. Here, the contact stimulus between the DCB and arterial wall, presented in the last section, is proposed as a time-dependent input that couples Levels 1 and 2.

The magnitude and direction of transmural filtration are derived from Darcy's Law, detailed in Chapter 3, as:

$$\mathbf{u} = -\frac{\kappa_i}{\mu_{\text{plasma}}}(\nabla p + \mathbf{f}), \tag{5.3.1}$$

where $\mathbf{u}$ is the transmural convective field, κ_i is the layer-specific porous media permeability, μ_{plasma} is the dynamic fluid viscosity, ∇p the gradient of the transmural pressure field, and $\mathbf{f}$ is an external force. The subscript "i" denote each of the artery layers (i.e. $i = \{\text{int, med, adv}\}$).

The term $\mathbf{f}$ represents a contribution of an external force to the transmural pressure gradient. In the model presented in this Chapter, it is assumed that the contact pressure due to DCB deployment (T_{n}) fulfils this role at the contacting boundaries, where it temporarily increases the transmural pressure gradient, thereby amplifying the magnitude of advection.

Since the DCB is modelled as a solid geometry made of non-permeable material, the entire DCB domain (Ω_{B} and Ω_{coat}) is excluded from Level 2.

Pressure constraints

Based on previous computational studies [62, 72, 90, 128], and in chorus with Chapter 3, this model simplifies the effect of haemodynamics as a constant pressure. Then, a simplified set of constant pressures is assumed to represent the luminal and perivascular pressure constraints. Notwithstanding, the pressure stimulus from DCB deployment on the arterial wall must be considered.

Often in the case of DES models, the starting point of the simulation is an implant already embedded in a static artery [63, 72, 80, 85]. Without time-dependent stimuli, the pressure profile over the luminal interface would remain constant throughout the simulation, resulting in stable pressure configuration and thus permitting a reasonable steady-state assumption. In the case of DCB, however, there are more pronounced time-dependent stimuli during the time frame of drug delivery — which takes place entirely during the deployment procedure. Models have tried to incorporate the temporary albeit substantial pressure increase effect due to balloon inflation [66, 67, 72, 73]. Some works proposed a bi-modal pressure constraint: a high value during the inflation stage followed by a physiological value at the post-inflation stage once the delivery is completed. Three important limiting aspects of these works must be pointed out: (I) the absence of a material representation of the drug delivery device or its inflation procedure; (II)

the assumption of a rigid artery, unaffected by time-dependent deformation; and (III) the high value used in the bi-modal pressure constraint. Only revisiting (I) and (II), and including their missing effects, it is likely for models to have a more realistic assumption of (III).

The current model seeks to improve the realism of DCBs *in silico* by simulating the contact interaction between the device and arterial wall, to obtain the contact pressure as a spatiotemporal variable over the contacting interface.

5.3.1 Boundary conditions

The basic boundary conditions concerning transmural filtration are in Chapter 3, where the arterial wall model is described in detail. The same terminology is used for the boundaries to facilitate comparison. Exceptionally, this subsection presents the differences compared to the previous model. These are: (I) the boundary conditions regarding the DCB deployment effect will be updated accordingly, and (II) the model equations are calculated over moving domains due to deformation.

The pressure boundary conditions in this Level are designed to impact only the transmural filtration physics and not the solid mechanics physics of Level 1. This excludes the potential problem of a positive pressure and deformation feedback loop between the Levels.

Denuded endothelium

As in Chapter 3, the lumen-wall interface is divided into two zones: the denuded ($\Gamma_{\text{ET, de}}$) and intact endothelia ($\Gamma_{\text{ET, in}}$). The denuded endothelium represents the region affected by the DCB deployment, where the superficial layer of endothelial cells is assumed to be completely removed. Upon contact, the pressure disturbance due to DCB deployment is introduced as an additive pressure term in the contacting region, amplifying the base pressure:

$$\sum p \; = p_{\text{lum}} \; + \; T_{\text{n}} \qquad \text{on } \Gamma_{\text{ET, de}}, \tag{5.3.2}$$

where $\sum p$ denotes the additive contributions of pressures, composed of the luminal pressure p_{lum} and the contact pressure T_{n}. The contribution of the variable T_{n} is limited to where contact occurs. Elsewhere, it is null. Since T_{n} originated in Level 1, the boundary condition expressed in Equation 5.3.2 links Levels 1 and 2.

Semi-permeable barriers

The intact endothelium and elastic laminae are modelled as semi-permeable barriers according to the Kedem-Katchalsky equations, as introduced in Chapter 3. The resulting volume flow $J_{\text{v},\,i}$, given in units of velocity, has spatiotemporal-dependent values over its respective boundary since (I) pressure is distributed unequally over the model geometry and (II) dynamic stimuli

disturb the pressure fields along the simulation.

Finally, Table 5.6 summarises the complete set of boundary conditions of pressure and flow constraining the multilayered arterial wall. Zero-flow conditions are imposed over the longitudinal extremities to contain the transmural flow as in [62] and [72]. As justified in these works, this assumption considers an arterial wall that is both axially homogeneous and sufficiently long — so that the boundary conditions at the longitudinal extremities should have negligible effects on the simulation results in the therapeutic domain. A detailed definition of the modelling assumptions and parameters utilised in Level 2 can be found in Chapter 3.

Transmural fields

The outcomes of the porous media flow calculations are the transmural fields of pressure (p) and convective ($\mathbf{u}$). These fields are computed over all artery layers (Ω_{int}, Ω_{med}, and Ω_{adv}) in a time-dependent manner, spanning across Deployment and Follow-up steps. Pressure is expressed as a scalar in units of millimetres of mercury (mmHg) while convective velocity is expressed as a vector oriented in space with magnitude in units of micrometres per second (μm/s). Due to the cessation of dynamic stimuli after the Deployment step, the transmural fields will remain constant throughout the Follow-up step.

In conclusion, the spatiotemporal convective field $\mathbf{u}$ will inform the drug transport mechanism of advection, complementary in the process of drug distribution in the arterial wall following DCB therapy, as presented in the upcoming Level.

Table 5.6: Summary of boundary conditions used in Level 2.

Type	Expression	Boundary of effect
Pressure	$p_{\text{lum}} + T_{\text{n}}$	$\Gamma_{\text{ET, de}}$
Flow	$J_{\text{v, ET}}$	$\Gamma_{\text{ET, in}}$
Flow	$J_{\text{v, IEL}}$	Γ_{IEL}
Flow	$J_{\text{v, EEL}}$	Γ_{EEL}
Pressure	p_{periv}	Γ_{periv}
Zero-flow	$-\mathbf{n} \cdot \mathbf{u} = 0$	$\Gamma^{\text{wall}}_{\text{sym, } z}$
Zero-flow	$-\mathbf{n} \cdot \mathbf{u} = 0$	$\Gamma^{\text{wall}}_{\text{ext}}$

Table 5.7: Summary of Level 2 model parameters for transmural filtration.

Parameter	Description	Value	Reference
p_{lum}	Physiological luminal pressure	100 mmHg	[63]
p_{peri}	Perivascular pressure	30 mmHg	[63]
γ_{int}	Hindrance coefficient of intima	1	[63]
γ_{med}	Hindrance coefficient of media	0.845	[63]
γ_{adv}	Hindrance coefficient of adventitia	1	[63]
ϕ_{int}	Porosity of intima	0.983	[88]
ϕ_{med}	Porosity of media	0.258	[88]
ϕ_{adv}	Porosity of adventitia	0.85	[57]
lag_{int}	Lag coefficient of intima	1.0173	Calculated
lag_{med}	Lag coefficient of media	3.38	Calculated
lag_{adv}	Lag coefficient of adventitia	1.1765	Calculated
κ_{ET}	Permeability of endothelium	$3.6 \cdot 10^{-6}$ m/s	[62]
κ_{IEL}	Permeability of IEL	$9.6 \cdot 10^{-6}$ m/s	[62]
κ_{EEL}	Permeability of EEL	$9.6 \cdot 10^{-6}$ m/s	[63]
μ_{plasma}	Dynamic viscosity of plasma	$7.2 \cdot 10^{-4}$ Pa s	[60]

5.4 Level 3: Drug transport and retention

The last Level of the system elaborates on the modelling of drug delivery from DCB and subsequent distribution in the tissue, considering its underlying parts as "mechanisms". Level 3 aims to simulate the drug distribution over the coating and arterial wall domains throughout the time-dependent events of DCB inflation, drug delivery on contact, long-term retention in the tissue, and wash-off. While the basic definitions and assumptions of drug transport and retention come from Chapter 3, the novelty of this Chapter is the drug source implicitly derived from the simulation of DCB deployment. Moreover, drug calculations are performed over deformable domains.

The therapeutic agent considered in this model is the antiproliferative drug sirolimus, also known as rapamycin. It will be simply referred to as the "drug". Since the modelling efforts are focussed on the drug delivery process and subsequent long-term spatial distribution, considerations about the antiproliferative effect of the drug on the arterial tissue are beyond the scope of this work.

In this section, the behaviour of the drug is described first within the model domains and then at its surrounding boundaries.

5.4.1 Initial conditions

The initial conditions in the simulation represent a DCB already positioned at the intervention site, with its coating embedded with a uniform drug concentration, c_0. Throughout its entire time inside the circulatory system, the DCB is exposed to rapid blood flow in the lumen, causing loss of superficial drug from its coating. It is estimated that the majority of drug losses occur during the one-minute journey of the device to the intervention site [81]. As a simplifying assumption, the effect of drug loss in transit to the intervention site, known as "tracking loss", is included in this model as a uniform deduction from the drug load in the coating. This deduction is applied once, at $t = 0$ s, and subsequent drug wash-off during the time-dependent DCB deployment procedure is ignored.

Equation 5.4.1 expresses how the initial drug concentration in the coating is derived:

$$c_0 \;=\; \frac{m_{\text{nom}}\,(1-TL)}{M_{\text{sir}}\;V_{\text{coat}}}, \tag{5.4.1}$$

where m_{nom} the nominal drug load according to the device specifications, in μg; $(1-TL)$ is the remaining fraction of drug load in the coating after tracking loss, non-dimensional; M_{sir} is the molar mass of the drug, in g/mol; and V_{coat} is the volume of the coating, in m^3, resulting from the volumetric integration of the coating domain $\left(V_{\text{coat}} = \int_{\Omega_{\text{coat}}} d\Omega_{\text{coat}}\right)$.

The expected values of tracking loss are based on experimental literature as well as internal studies from the collaborating company [67, 95, 129]. The resulting value of Equation 5.4.1

defines a uniform initial concentration of drug in the coating, c_0, in mol/m^3. At the beginning of the time-dependent simulation, i.e. at $t = 0$ s, the DCB is positioned at the intervention site, concentric with the artery lumen, and all drug is localised in the coating domain. It is assumed that all other domains are devoid of drug.

Table 5.8 summarises the mechanisms of drug transport and retention and the initial conditions of drug concentration assigned to each of the model domains. Some domains exhibit a combination of multiple mechanisms. Transport of drug is governed by diffusion partial differential equations in the coating (Ω_{coat}), by diffusion-advection equations in the intima (Ω_{int}) and adventitia (Ω_{adv}) layers, and by diffusion-advection-reaction equations in the media (Ω_{med}) layer. The reaction term is included solely in the media, as justified in the further subsection 5.4.4, to account for the effect of drug retention in that domain. The balloon domain (Ω_{B}) is excluded from the drug transport and retention simulation.

Table 5.8: Overview of the Level 3 mechanisms and initial conditions in each model domain.

Domain	Mechanisms	Initial conditions (at $t = 0$)
Ω_{B}	—	—
Ω_{coat}	Diffusion	$c = c_0$ (Equation 5.4.1)
Ω_{int}	Diffusion-Advection	$c = 0$
Ω_{med}	Diffusion-Advection-Reaction	$c = 0$, $b^{\text{s}} = 0$, $b^{\text{ns}} = 0$
Ω_{adv}	Diffusion-Advection	$c = 0$

The following subsections describe each of the mechanisms of drug transport and retention in detail.

5.4.2 Diffusion

Diffusion in the coating

In line with the modelling work explained in detail in Chapter 4, the behaviour of the drug in the coating is based on an isotropic diffusion coefficient derived from experimental testing using the drug Biolimus A9™. However, the current model considers sirolimus as the drug. Biolimus A9™ is an analogue of sirolimus, obtained from altering a single radical group of the chemical compound. Since sirolimus and Biolimus A9™ are similar in terms of molecular size and weight, their diffusive transport properties are expected to be almost identical. Therefore, the diffusion coefficient derived from a Biolimus A9™ experiment will be adapted to describe the transport of sirolimus in this model.

At the beginning of the simulation, the entire drug load is assumed to be distributed uniformly and confined within the coating domain. Any further wash-off of drug due to blood flow during the time-dependent simulation is disregarded. Diffusion in the coating plays its role in drug delivery at the event of contact — when the drug load is "discharged" to the arterial

wall. The process of drug transfer between DCB and the arterial wall is described in the further subsection 5.4.5, "Boundary conditions".

Diffusion in the arterial wall

Diffusion is a drug transport mechanism assumed present in all layers of the arterial wall, behaving according to layer-specific diffusion coefficients. A detailed definition of this mechanism can be found in Chapter 3.

Deformation-dependent diffusion

In chorus with recent modelling studies that consider arterial deformation [63, 72], the effect of arterial deformation on the transport properties of the drug in the tissue is included in this model. The localised arterial deformations that occur during the Deployment step are assumed to temporarily alter the magnitude of the diffusive transport of the drug.

This effect is modelled with the introduction of deformation-dependent diffusion coefficients, $\mathbf{D}_i^*(r, z, t)$, acting as effective diffusion coefficients that incorporate effects of porosity and tortuosity. As the tissue deforms, the spatiotemporal deformation gradients $\varepsilon_r(r, t)$ and $\varepsilon_z(z, t)$ are translated as changes in the tortuosity in the arterial tissue. The change in tortuosity affects the diffusion coefficients $\mathbf{D}_i^*$ in a each layer, as $i = \{\text{int, med, adv}\}$. During the events of inflation and deflation, each layer-specific diffusion coefficient is updated on a spatiotemporal basis according to the local deformation experienced. After deployment, deformation ceases and so does the altering effect as both deformation gradients remain null for the rest of the simulation.

Equation 5.4.2 proposes that the arterial deformation caused by DCB deployment affects each layer-specific diffusion coefficient, exerting a localised and temporary effect on diffusion:

$$\mathbf{D}_i^*(r, z, t) = \begin{pmatrix} D_{i,\,r}\,(1+\varepsilon_r) & D_{i,\,z}\,(1+\varepsilon_z) \end{pmatrix} \qquad \text{for } i = \{\text{int, med, adv}\}, \tag{5.4.2}$$

where ε_r and ε_z are the local radial and longitudinal strains, respectively.

Local strains in the arterial wall are defined in Equation 5.4.3 as:

$$\begin{cases} \varepsilon_r = \dfrac{\Delta r}{r_0} \\ \varepsilon_z = \dfrac{\Delta z}{z_0}, \end{cases} \tag{5.4.3}$$

where Δr and Δz are the deformation gradients, and r_0 and z_0 are the original spatial configuration in radial and longitudinal coordinates, respectively.

5.4.3 Advection

Advection is primarily guided by the convective field ($\mathbf{u}$) in the simulation. It is obtained from the porous media flow calculations of Level 2 and fed into Level 3, as a spatiotemporal input effectively linking the Levels. A detailed definition of this mechanism can be found in Chapter 3.

Moving domains

The advective term is finalised with a consideration of moving domains. During the deployment simulation, the coating and arterial wall domains are deformed due to inflation, contact, and deflation. Drug distribution is calculated over these domains. Accordingly, all model domains containing drug concentration fields, whether in free or bound drug phases, need to shift their drug distribution as the geometry deforms to ensure that drug mass is conserved throughout the simulation.

The proposed implementation in this model closely resembles the one presented in Chapter 4. In summary, the drug transport equation implicitly incorporates the deformation rate, $\mathbf{v}$, alongside the effect of the regular transmural convective velocity, $\mathbf{u}$. The total convective term is then defined as $\mathbf{U} = \mathbf{u}+\mathbf{v}$. This ensures that the drug transport equations for all domains in the model are considered correctly in the current deformed configuration whilst the drug-embedded domains are deformed in the Deployment step of the simulation.

As diffusion is combined with advection, diffusion-advection equations are formed. Equations 5.4.4 and 5.4.5 govern the evolution of free drug concentration in Ω_{int} and Ω_{adv}, respectively:

$$\frac{\partial c}{\partial t} = \nabla \cdot (\mathbf{D}^*_{\text{int}} \nabla c - \mathbf{U}^* c) \qquad \text{in } \Omega_{\text{int}} \tag{5.4.4}$$

$$\frac{\partial c}{\partial t} = \nabla \cdot (\mathbf{D}^*_{\text{adv}} \nabla c - \mathbf{U}^* c) \qquad \text{in } \Omega_{\text{adv}}, \tag{5.4.5}$$

where c is the free drug concentration, t is time, $\mathbf{D}^*_i$ is the layer-specific modified diffusion coefficient, and $\mathbf{U}^*$ is the modified total advective velocity field, including the lag coefficients as defined in Chapter 3.

The equations describing drug transport in the media (Ω_{med}) require additional physics and are described in Section 5.4.4.

5.4.4 Reaction

As drug is transported through the multilayer wall via diffusion and advection, it may also be retained in the tissue in a process named "drug binding" [61]. To account for this effect, a reaction term R is added to the drug transport equation in the media layer, where the majority of

the target drug receptors are located. Effectively, the reaction rate R transforms drug concentration between free (c) and bound (b^{s} and b^{ns}) phases over time, simultaneously with the transport phenomena. A detailed definition of drug binding can be found in Chapter 3. While the bound drug is also assumed immobile here, unaffected by the transport phenomena of advection and diffusion, it artificially follows the deformation of the arterial wall during the Deployment step according to the aforementioned pseudo-advective term.

Finally, diffusion-advection-reaction equations govern the transport and retention of drug in the media:

$$\frac{\partial c}{\partial t} = \nabla \cdot \left(\mathbf{D}^{*}_{\text{med}} \nabla c - \mathbf{U}^{*} c \right) - R \qquad \text{in } \Omega_{\text{med}}, \tag{5.4.6}$$

where $R = \dfrac{\partial b^{\text{s}}}{\partial t} + \dfrac{\partial b^{\text{ns}}}{\partial t}$ is the reaction rate symbolising the simultaneous binding of drug to specific and non-specific binding sites.

Table 5.9 presents all governing equations of drug transport and retention in the model by domain, along with their main features.

Table 5.9: Summary of drug transport and retention mechanisms in each of the model domains.

Domain	Diffusion	Advection	Reaction	Full governing equation
Ω_{B}	—	—	—	—
Ω_{coat}	Isotropic	Deformation	—	$\frac{\partial c}{\partial t} = \nabla \cdot (\mathbf{D}_{\text{coat}} \nabla c - c)$
Ω_{int}	Isotropic	Deformation + transmural filtration	—	$\frac{\partial c}{\partial t} = \nabla \cdot (\mathbf{D}^{*}_{\text{int}} \nabla c - \mathbf{U}^{*} c)$
Ω_{med}	Anisotropic	Deformation + transmural filtration	Two-phase binding	$\frac{\partial c}{\partial t} = \nabla \cdot (\mathbf{D}^{*}_{\text{med}} \nabla c - \mathbf{U}^{*} c) - \frac{\partial b^{\text{s}}}{\partial t} - \frac{\partial b^{\text{ns}}}{\partial t}$
Ω_{adv}	Isotropic	Deformation + transmural filtration	—	$\frac{\partial c}{\partial t} = \nabla \cdot (\mathbf{D}^{*}_{\text{adv}} \nabla c - \mathbf{U}^{*} c)$

5.4.5 Boundary conditions

The previous subsections within Level 3 regarded the properties of drug phases within the model domains where they are valid: free drug concentration c, over the coating and entire arterial wall domains; and bound drug concentrations b^{s} and b^{ns} exclusively within the media layer.

Boundary conditions are essential to detail the behaviour of drug at the boundaries of each domain. A description of the basic boundary conditions of the arterial wall model can be found in Chapter 3. In this subsection, the key differences in boundary conditions due to having a depiction of the DCB deployment in the model are presented. These are related to (I) the drug source, (II) halved DCB geometry, and (III) drug-embedded moving domains.

Thin diffusion barrier

During the deployment procedure, the deformation experienced by the inflating DCB causes the coating to reach the intima layer. When these domains are sufficiently close, contact occurs. In retrospect, Level 1 used a contact pair boundary condition to model the connectivity between the geometrical fields of the DCB and arterial wall when engaged in mechanical interaction. Here, a somewhat analogous pair definition is proposed, but to establish communication between the drug concentration fields of Ω_{coat} and Ω_{int} during contact. This intends to enable the transmission of drug from the drug-embedded coating to the innermost artery layer, similarly to the dissolution process described in [68]. To this end, the boundaries that will experience drug transfer are selected as a pair, namely:

Source ("Src") Where the drug is sourced from, defined in this model as the outer boundary of the coating domain, Γ_{coat}.

Destination ("Dst") The target of drug delivery, defined as the innermost boundary of the arterial wall subjected to the drug delivery procedure, $\Gamma_{\text{ET, de}}$.

During DCB deployment, part of the source and destination boundaries engage contact. Temporarily while it occurs, the drug concentration fields of these should interact to exchange drug mass. The default way of modelling this would be to enforce continuity of drug concentration between the fields of the pair of Src and Dst. However, from preliminary modelling experimentation performed, the continuity boundary condition presents two main problems: (I) computation time, (II) need for matching mesh.

As an alternative to a continuity condition, a pair of boundary conditions of flux, J_{Src} and J_{Dst}, is prescribed over the respective contacting boundaries. The pair is assumed to behave as a thin diffusion barrier promoting the inter-flow of species solute, i.e. drug, through the contact interface and between the coating and intima domains. To provide generality and sufficient orientation to the pair of fluxes, each flux is combined with a negative unitary normal vector to its respective boundary, $-\mathbf{n}$, which points inwards to its respective domain. Then, the resulting

configuration is a pair of complementary boundary conditions of inward fluxes of solute, as presented in Equation 5.4.7:

$$\begin{cases} -\mathbf{n} \cdot J_{\text{Src}} = \dfrac{D_{\text{coat}}}{h_{\text{coat}}}(c_{\text{Dst}} - c_{\text{Src}}) & \text{on } \Gamma_{\text{coat}} \\ -\mathbf{n} \cdot J_{\text{Dst}} = \dfrac{D_{\text{coat}}}{h_{\text{coat}}}(c_{\text{Src}} - c_{\text{Dst}}) & \text{on } \Gamma_{\text{ET, de}}, \end{cases} \tag{5.4.7}$$

where $\mathbf{n}$ is the unit outward normal vector to the corresponding boundary; J_{Src} and J_{Dst} are the inward boundary fluxes at the source and destination contacting boundary, respectively, in units of mol/(m^2 s); D_{coat} is the diffusion coefficient in the coating; h_{coat} is the coating thickness; and c_{Dst} and c_{Src} are the drug concentrations immediately at the destination and source boundaries.

During the temporary contact window when the fluxes are active, there is a large concentration of drug in the source ($c_{\text{Src}} >> c_{\text{Dst}}$), causing J_{Src} to behave as a negative inward flux on Γ_{coat}, draining solute from the source. Simultaneously, J_{Dst} has equal magnitude but is positive, so that it injects drug into the destination through $\Gamma_{\text{ET, de}}$. The symmetry of the pair of boundary fluxes is necessary to conserve the total mass of drug in the system during the exchange.

The time window of contact is roughly equal to the inflation duration (Δt_{inf}), commonly reported as up to 60 seconds for coronary applications [32, 130]. After deflation, contact is removed and drug transfer is assumed to cease to exist for the rest of the simulation. The thin diffusion barrier condition is then replaced with a perfect sink. The drug delivered traverses the multilayered arterial wall according to the mechanisms of transport and retention described in the remainder of this Chapter.

In summary, the process of drug delivery from DCB is modelled with a thin diffusion barrier, composed of a pair of complementary fluxes of solute, J_{Src} and J_{Dst}, active respectively over the contacting boundaries of source and destination upon contact. This is proposed as an alternative to a continuity condition, which would connect the drug concentration fields of the contacting domains. The distinctive features of the thin diffusion barrier are (I) the additional dependency on coating parameters, namely D_{coat} and h_{coat}, and (II) reduced computational expense, as observed in preliminary *in silico* experimentation of own authorship. In Section 5.7, Discussion, a comparison between the performance of these is provided, justifying that their similarity is acceptable.

Semi-permeable barrier

The general Kedem-Katchalsky equations as presented in Equation 3.6.1 of Chapter 3 are used to model the effect of the intact endothelium and the two elastic laminae as semi-permeable membranes. These membranes mediate the transport of drug between artery layers based on local pressure and drug concentration information between the lumen and intima, at Γ_{IEL}; between intima and media, at $\Gamma_{\text{ET, de}}$; and between the media and adventitia, at Γ_{EEL}. The resulting

fluxes of drug — the solute — passing through each of the membranes are respectively $J_{\text{s, ET}}$, $J_{\text{s, IEL}}$, and $J_{\text{s, EEL}}$. Due to the time-dependent simulation of DCB deployment in this model, these fluxes are calculated over each respective boundary in a spatiotemporal fashion.

Perfect sink

The perfect sink is employed to allow drug clearance from the model domains. A detailed description of this boundary condition can be found in Chapter 3. In this model, perfect drug sinks are defined over Γ_{periv} and $\Gamma_{\text{ET, de}}$ after the Deployment step.

Zero-flux

The DCB geometry in this model is halved due to the usage of symmetry (mirroring over $\Gamma_{\text{sym, }z}$). To ensure drug is contained within the coating domain, a zero-flux boundary condition is prescribed over the region sectioned by the symmetry procedure, the boundary $\Gamma^{\text{DCB}}_{\text{sym, }z}$. Equation 5.4.8 expresses the zero-flux boundary condition:

$$-\mathbf{n} \cdot (J + \mathbf{U}^* c) = 0 \qquad \text{on } \Gamma^{\text{DCB}}_{\text{sym, }z}, \tag{5.4.8}$$

where J is the total diffusive flux of drug; $\mathbf{U}$ is the total advective term in the coating, in this case, formed solely by the deformation rate $\mathbf{v}$; and c is the free drug concentration.

Inflow

In the previous subsection 5.4.3, the conservation of drug within the deforming domains was addressed using an implicit pseudo-advective term. Here, an auxiliary boundary inflow condition is proposed to account for the deformation rate ($\mathbf{v}$) on the boundaries of all drug concentration fields (c, b^{s}, and b^{ns}). The need for such manual intervention is due to the seemingly disconnected physics of structural mechanics and drug transport in the modelling software, which does not account for their relationship by default and may calculate the pair in different coordinate systems (or "frames"). In the model, the inflow is imposed as an additive flux to the external boundaries of all drug-containing domains (Equations 5.4.9 5.4.10, and 5.4.11), excluding where zero-flux is applied, as an alternative to constraining drug concentrations to fixed values. Where applicable, it supplements the flux at inlet and outlet boundaries of the multilayered geometry such as the laminae surrounding the media layer. This boundary condition prescribes a total flux based on the upstream drug concentration and the total velocity at a boundary, to preserve both the conservation of flux and continuity of drug concentration around domains undergoing deformation and drug distribution.

$$-\mathbf{n} \cdot (J + \mathbf{U}^* c_{\text{down}}) = -\mathbf{n} \cdot (\mathbf{v}\, c_{\text{up}}) \qquad \text{on } \Gamma_i \tag{5.4.9}$$

$$-\mathbf{n} \cdot (J + \mathbf{U}^* b^{\text{s}}_{\text{down}}) = -\mathbf{n} \cdot (\mathbf{v}\, b^{\text{s}}_{\text{up}}) \qquad \text{on } \Gamma_i \tag{5.4.10}$$

$$-\mathbf{n} \cdot (J + \mathbf{U}^* \, b^{\text{ns}}_{\text{down}}) = -\mathbf{n} \cdot (\mathbf{v} \, b^{\text{ns}}_{\text{up}}) \qquad \text{on } \Gamma_i, \tag{5.4.11}$$

where $\mathbf{n}$ is the unit outward normal vector to the corresponding boundary; J is the diffusive flux of drug; $\mathbf{U}^*$ is the total advective term, composed of deformation and amplified transmural velocities if applicable; $\mathbf{v}$ is the spatiotemporal deformation rate; c_{down} and c_{up} are the free drug concentrations downstream and upstream of the boundary, respectively, and analogously for the bound drug concentrations b^{s} and b^{ns}; and i is an arbitrary boundary name surrounding a drug-containing domain.

It was observed that including this inflow condition effectively dislocates the drug concentration fields as they deform, resulting in the accurate containment of drug within domains to satisfy the conservation of drug mass. Despite not being affected by advection, the bound drug concentration fields still need to perceive the effect of arterial wall deformation and dislocate accordingly; thus, it is reasonable to apply the same inflow condition to the drug concentrations in bound phase. For bound drug, the inflow surrounds the media layer and is only active during the Deployment step — when the deformation rate is present.

In chemical engineering, this boundary condition is occasionally referred to as the Danckwerts inflow condition as presented in [131]. In that context, it has been reported as helpful when having high reaction rates in the vicinity of the substance inlet, perhaps as in the media layer near the denuded endothelium in the present model. In the present model, distinctively, it is used to include the effect of brisk deformation rates on drug transport and retention physics.

Figure 5.8 summarises the main physics of the model. Notably, it evokes a combination of the models of Chapters 3 and 4.

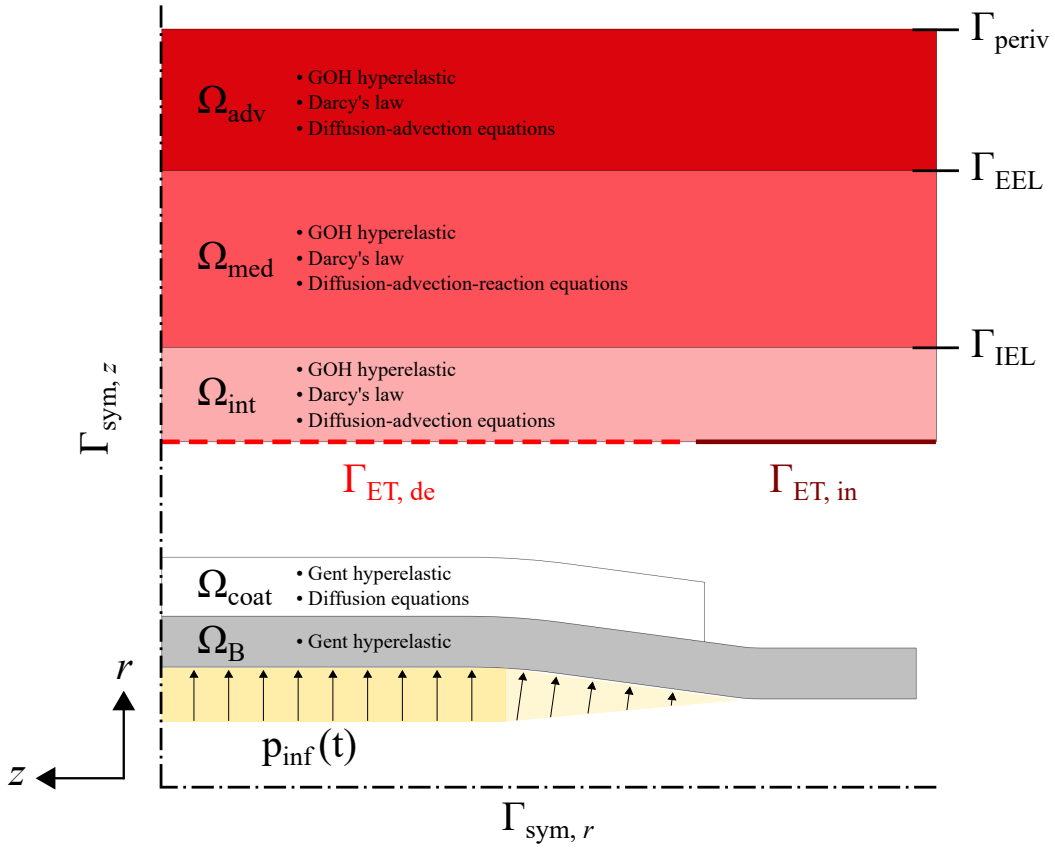

Figure 5.8: Schematic summary of physics considered in the model of Chapter 5. Geometry is not to scale.

A set of tables is presented next to overview and finalise the description of Levels.

- Table 5.10 overviews the main model variables and observes their coverage within Levels.
- Table 5.11 lists the model parameters used to characterise drug transport and retention.
- Table 5.12 summarises all boundary conditions for all multiphysics Levels, categorised by boundary. The boundary names may be consulted in Figure 5.2, in section 5.1.

Table 5.10: Overview of the main model variables.

Variable	Description	Unit	Level of effect
p_{inf}	Balloon inflation pressure	atm	1
T_{n}	Contact pressure between DCB and arterial wall	mmHg	1 & 2
ε_r	Local strain in the radial direction	—	1 & 3
ε_z	Local strain in the longitudinal direction	—	1 & 3
p	Pressure field in the arterial wall	mmHg	2
$\mathbf{u}$	Advective field in the aterial wall	μm/s	2 & 3
c	Free drug concentration	mol/m^3	3
b^{s}	Specifically-bound drug concentration	mol/m^3	3
b^{ns}	Non-specifically-bound drug concentration	mol/m^3	3

Table 5.11: Summary of Level 3 model parameters for drug transport and retention. Except for D_{coat}, all drug-related parameters refer to sirolimus as the therapeutic agent.

Parameter	Description	Value	Reference
m_{nom}	Nominal drug load in coating	300 μg	[81]
TL	Drug fraction lost during tracking	22 %	[81]
M_{sir}	Molar mass of sirolimus	914.187 g / mol	[59]
ρ	Density of wet arterial tissue	0.983 g / ml	[64]
D_{coat}	Diffusion coefficient in coating	$8.2 \cdot 10^{-13}$ m^2 / s	Estimated
D_{int}	Diffusion coefficient in intima	$1.67 \cdot 10^{-11}$ m^2 / s	[62]
$D_{\text{med, }r}$	Radial diffusion coefficient in media	$7 \cdot 10^{-12}$ m^2 / s	[59]
$D_{\text{med, }z}$	Longitudinal diffusion coefficient in media	$4 \cdot 10^{-11}$ m^2 / s	[59]
D_{adv}	Diffusion coefficient in adventitia	$4 \cdot 10^{-12}$ m^2 / s	[63]
k^s_{on}	Specific binding-on rate	800 m^3 / (mol s)	[92]
k^s_{off}	Specific binding-off rate	$1.6 \cdot 10^{-4}$ 1 / s	[91]
b^s_{max}	Specific binding site density	0.0033 mol / m^3	[64]
$k^{\text{ns}}_{\text{on}}$	Non-specific binding-on rate	2 m^3 / (mol s)	[61], [63]
$k^{\text{ns}}_{\text{off}}$	Non-specific binding-off rate	$5.2 \cdot 10^{-3}$ 1 / s	[91]
$b^{\text{ns}}_{\text{max}}$	Non-specific binding site density	0.363 mol / m^3	[61], [64]

Table 5.12: Summary of boundary conditions prescribed at each of the model boundaries, in each of the Levels. Transient boundary conditions are indicated in the format "condition at Deployment step / condition at Follow-up step".

Boundary	Condition		
	Level 1	Level 2	Level 3
Γ_{coat}	Contact pair	—	Thin diffusion barrier (Source) / —
$\Gamma^{\text{B}}_{\text{mid}}$	Full pressure ramp	—	—
$\Gamma^{\text{B}}_{\text{prox}}$	Gradual pressure ramp	—	—
Γ_{shaft}	Spring foundation	—	—
$\Gamma^{\text{DCB}}_{\text{sym, }z}$	Roller	—	Zero-flux / —
$\Gamma^{\text{B}}_{\text{ext}}$	Spring foundation	—	—
$\Gamma_{\text{ET, de}}$	Contact	Luminal pressure + contact pressure	Thin diffusion barrier (Destination) / Perfect sink
$\Gamma_{\text{ET, in}}$	Free	Flow through semi-permeable membrane	Flux through semi-permeable membrane
Γ_{IEL}	—	Flow through semi-permeable membrane	Flux through semi-permeable membrane
Γ_{EEL}	—	Flow through semi-permeable membrane	Flux through semi-permeable membrane
Γ_{periv}	Free	Perivascular pressure	Perfect sink
$\Gamma^{\text{wall}}_{\text{sym, }z}$	Roller	Zero-flow	Zero-flux
$\Gamma^{\text{wall}}_{ext}$	Spring foundation	Zero-flow	Zero-flux

5.5 Computational set-up

The computational set-up of the model was performed in chorus with the previous Chapters 3 and 4, using COMSOL Multiphysics® version 6.1. In this Section, the main differences and challenges involved in simulating DCB deployment are explained in detail.

Contact

During the deployment simulation, a penalty contact method is employed to depict the contact interaction between the DCB and the arterial wall. As introduced in Section 5.2, it exerts a spring-like response based on the distance between the contacting surfaces. In the numerical simulation, a search method is used to map the deformed configuration of the model geometry. This method determines, identifying in a binary fashion, whether parts of the pair are in contact or not. The condition for this is satisfied if the search criterion is met, which is a minimum distance of 10^{-3} mm between the pair. This value was empirically chosen as the tenth part of the intima layer thickness value (i.e. $\delta_{\text{int}}/10$). The deforming model geometry and the length of the contacting boundary are updated at every time step. To improve the accuracy of the numerical integration of contact, a fourth-degree integration order is used.

The penalty method is an advantageous approach for its robustness and suitability for problems involving multiple physics and time-dependent studies, according to [132]. Also, it does not require a special solver to be used. It is important to acknowledge that the penalty contact method involves a trade-off between accuracy and stability, which was deemed satisfactory in this model.

Simulation architecture

The model's multiphysics was structured in Levels (Solid mechanics, Transmural filtration, and Drug transport and retention), spanning two sequential time-dependent steps (Deployment and Follow-up). Additionally, a stationary Initialisation step was devised as an auxiliary step to set up the initial conditions of the simulation, i.e. at $t = 0$ s.

In summary, each step receives the values of dependent and independent variable fields from the previous step. The spatiotemporal solutions of each time-dependent step were stored in solution stores and merged after the simulation was completed. Then, the combined solution store was mirrored over the line of longitudinal symmetry, and then rotated around the axis of radial symmetry, finally resulting in the full 2D-axisymmetric results. This process forms the complete simulation results used to produce all plots and figures in Section 5.6, "Results".

Discretisation

The governing equations of the model were calculated with the FEM over a mesh of elements. To guarantee cohesion and, to some extent, continuity, the resulting information needs to be con-

nected between elements with respect to space and time. The solid mechanics physics described in Level 1 employed quadratic serendipity discretisation. This term enunciates the element order and shape function type, respectively. Quadratic order ensured a sufficiently smooth deformation profile, while the use of serendipity elements was preferred due to computational efficiency in terms of the required number of mesh elements and computation speed.

The spatial discretisation employed quadratic Lagrange elements for both the porous media flow physics of Level 2 and for the drug transport and retention physics of Level 3. The choice for the quadratic order was justified for consistency over the physics of all Levels, and the Lagrange elements were preferred for the computational stability observed in previous modelling studies [62, 63, 72].

Meshing

The meshing strategy was similar to that described in the previous Chapters 3 and 4. Sufficient mesh resolution is required to depict all of the model multiphysics and allow computational stability. Meshing parameters initially underwent iterative refinement based on the following criteria:

- Simulation convergence, in terms of binary success/failure.
- Conservation of mass due to deformation and drug transfer, satisfying $< 1\%$ increase of total drug mass in the simulation during DCB drug transfer.
- Mesh element quality above 0.5, for the quality measures of skewness, maximum angle, growth rate, and curved skewness, according to COMSOL's definition of mesh element quality ("0.0 represents a degenerated element, and 1.0 represents the best possible element." [93]).

Boundary layer elements were employed to produce a denser element distribution in the normal direction along specific boundaries, improving the local resolution in regions of large gradients, such as the contacting interfaces and elastic laminae. Overall, the meshing process was largely empirical.

Additionally, a mesh sensitivity analysis was performed to evaluate the influence of the mesh size on the solution. Specifically, the evaluation was based on the results of drug content, a key quantity of interest defined earlier in Chapter 3. The mesh was assumed satisfactory when further mesh refinement would differ the result of drug content by less than 1% in terms of maximum relative difference and less than 0.1% in average relative difference, measured throughout the entire 28 days.

Three mesh configurations are featured to illustrate the mesh sensitivity analysis. They are named qualitatively as "Coarse", "Fine", and "Finer", consisting of 30341, 36644, and 52066 mesh elements, respectively. Figure 5.9 compares drug content (DC) results while varying

mesh resolution. The results obtained with the three meshes are practically identical, as highlighted in the magnified inset of the figure and with the use of dotted and dashed lines to allow visualisation. Also, the table beside Figure 5.9 (a) summarises the peak and final DC values for each mesh configuration. This emphasises the marginal differences between results despite mesh resolution. The mesh satisfaction criteria are fulfilled in the example in subfigure (b), where the maximum difference between the DC results with the "Fine" and "Finer" meshes is 0.99%, and the average difference is -0.06%. At this point, the solution is assumed mesh-independent.

Considering the information obtained in this analysis, the definitive mesh chosen for the simulation was the "Fine" mesh. The mesh consisted of 36644 quadrilateral elements, 4796 edge elements, and 33 vertex elements in total, boasting average and minimum mesh element quality values of 0.9944 and 0.6092, respectively (for skewness as the quality measure). A leaner mesh was envisaged since it is crucial for permitting simulations at a reasonable duration. The mesh used is assessed before every simulation employing mesh quality evaluation, performed within COMSOL, and throughout the simulation in the form of a convergence plot. The convergence plot informs the reciprocal of step size, which, for the nonlinear solver, means an error estimate against the iteration number. In essence, this reflects the overall convergence of the simulated results and indicates whether the combination of mesh and solver settings is suitable for the problem (assuming that the physics are well-posed). A detailed discussion on convergence is interesting but was deemed out of the scope of the current work. It may be featured in more focussed content in the future.

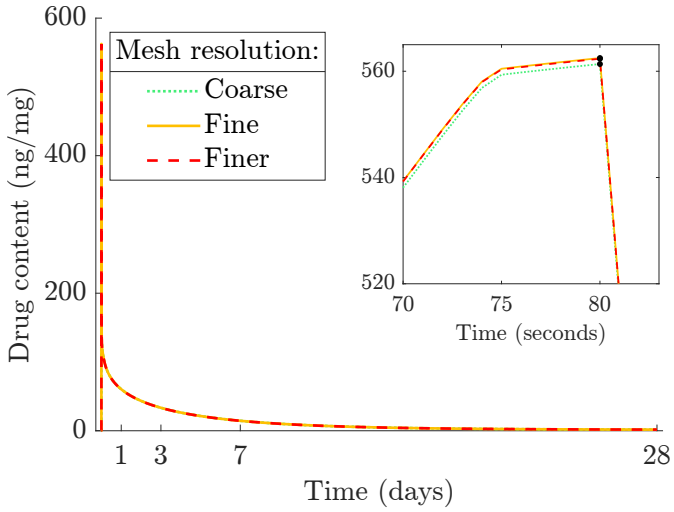

(a)

Mesh resolution	Peak DC (ng/mg)	Final DC (ng/mg)
Coarse	561.36	1.67
Fine	562.49	1.66
Finer	562.35	1.66

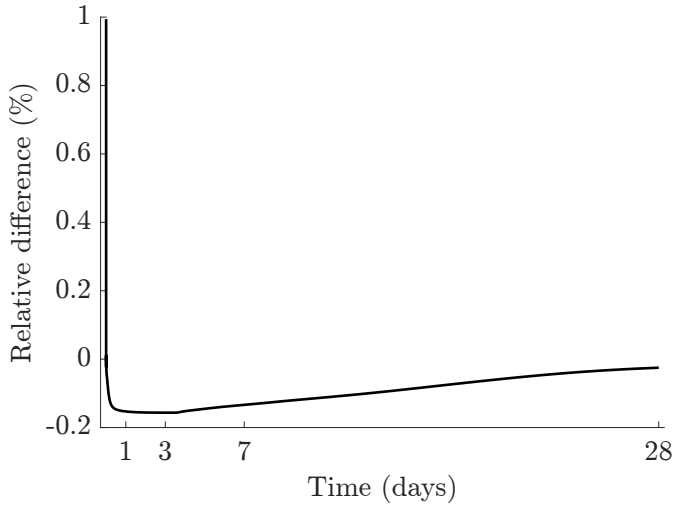

(b)

Figure 5.9: Summary of the mesh sensitivity analysis, reporting (a) the drug content results for three mesh sizes, and (b) the relative difference between drug content results with "Fine" and "Finer" meshes.

The schematic in Figure 5.11 provides an overview of the final mesh configuration. The mesh refinement strategy was mainly based on the complexity, and thus computational intensity, of the physics modelled in each model region. For instance, the contacting interfaces undergo contact interaction and sharp drug concentration gradients during DCB deployment, and the media layer features a highly non-linear process of drug binding. Therefore, both regions require a particularly regular and fine mesh. Also, the simulation of drug transport demands a finer mesh in its preferential direction, i.e. the radial direction, where the combination of diffusive and advective velocities is the highest. This can be observed in the insets of Figure 5.11.

A general sanity check was performed to study the sufficiency of the mesh to capture the gradients in the longitudinal direction. This particularly concerns the contact pressure over the contacting interface and the transmural fluid velocity through the media layer. The chosen

instants, i.e. $t = 9$, 10, 11, and 12 s, illustrate the early moments of deployment: immediately before the DCB engages contact, the intermediate states, and when inflation reaches its apex and the physics of Levels 1 and 2 stabilise. For instance, measuring the radial and longitudinal components of the transmural velocity field, $\mathbf{u} = (u_r \; u_z)$, over a longitudinal line through the media layer during the early instants of DCB deployment:

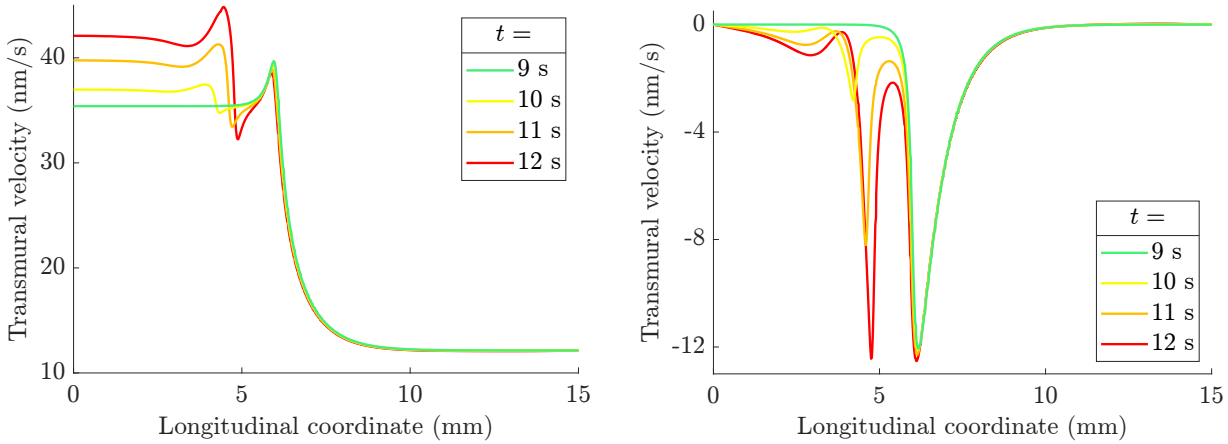

(a) u_r (b) u_z

Figure 5.10: Transmural velocity magnitude in the (a) radial and (b) longitudinal direction over a longitudinal line through the media layer ($r = 1.25$ mm), for different instants during DCB deployment. The baseline scenario of procedural parameters is considered in the simulation (inflation pressure of 8 atm, inflation duration of 60 s, and nominal drug load m_0).

Refining the mesh in the longitudinal direction does produce smoother curves e.g. contact pressure along the contacting length and transmural velocity albeit with comparable magnitude. For the simulation focus — drug distribution — the physics of faster dynamics occur in the radial direction, where radial diffusion is combined with advective transport due to transmural filtration, largely in the radial direction. In addition to the mesh sensitivity analysis presented in this Section, this justifies the relatively high refinement along the r-direction in detriment to the z-direction.

Remarkably, a single mesh was used to simulate all multiphysics of the model simultaneously. Exhaustive mesh tailoring and refinements were undertaken to arrive at a mesh configuration that satisfies both simulation convergence and mesh independence. Future studies may explore mesh sensitivity concerning other aspects of the results, such as contact interaction, drug mass conservation and receptor saturation.

Solver settings

Alongside meshing, an exhaustive manual tuning of solver settings was crucial to enable the convergence of the model's multiphysics simulations. Some of the modelling techniques used in the adjustment of solver settings are listed and outlined below:

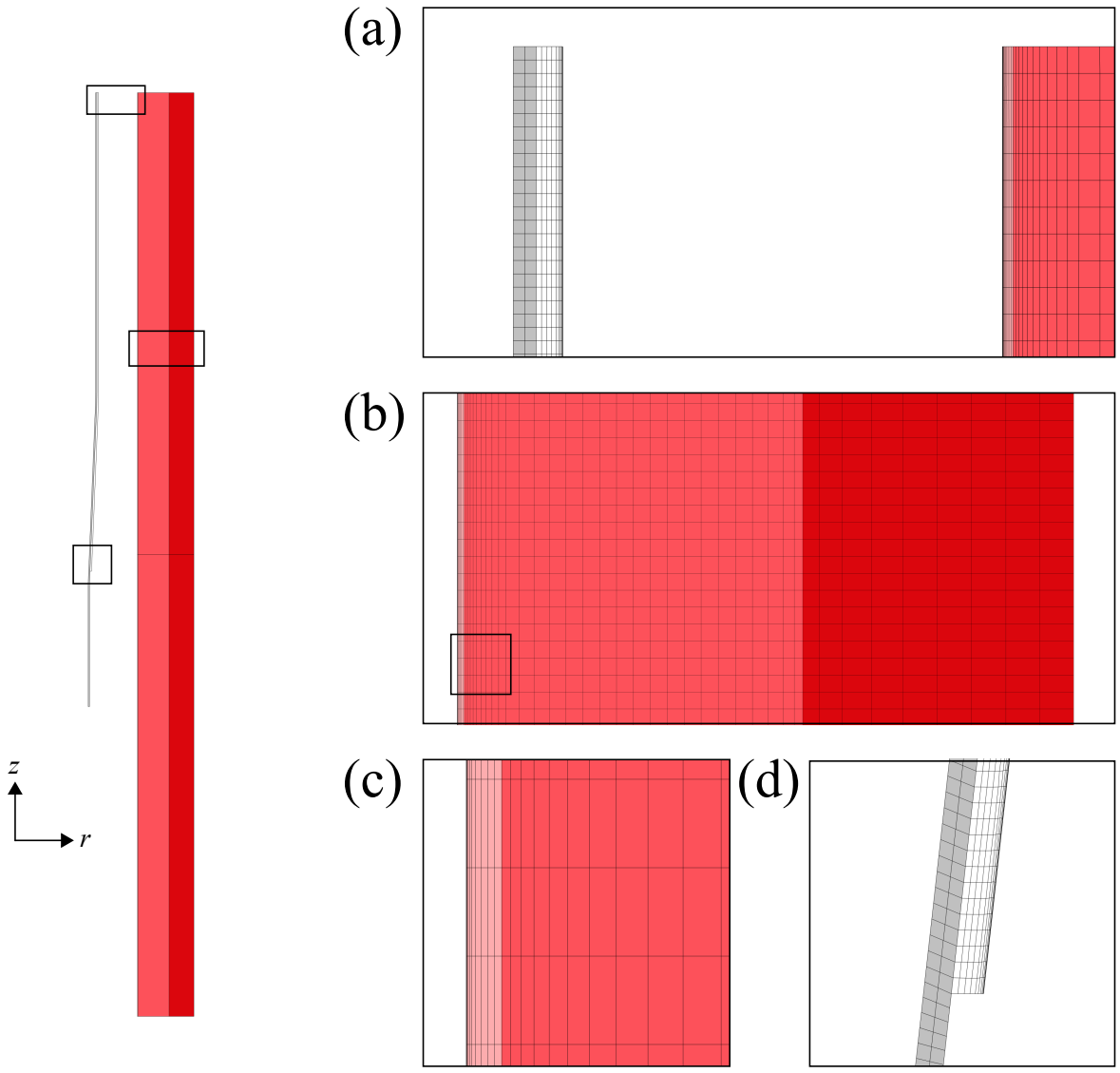

Figure 5.11: Schematic of mesh. The magnified insets detail the mesh composition of (a) contacting regions, (b) multilayer arterial wall, (c) intima layer, and (d) edge of coating.

Choice of solvers and tolerance A Multifrontal Massively Parallel Sparse (MUMPS) direct solver was used to solve the stationary step (Initialisation) with a tolerance for the relative error of the solution of 10^{-3}, while the time-dependent steps (Deployment and Follow-up) employed a Parallel Direct Sparse Solver (PARDISO), with relative and absolute tolerances set to 10^{-3} and 10^{-4}, respectively. These tolerance values were selected based on previous computational works of endovascular drug delivery [62, 63, 72].

Method An implicit Backward Differentiation Formula (BDF) method was used for the discretisation of the time-dependent steps, with an order of accuracy varying between 1 and 5. Low orders are automatically employed by the solver when necessary to obtain stability.

Time stepping The size of the time step was constrained by (I) an initial time step of 10^{-4}

seconds, and (II) a maximum time step of 3600 seconds, equivalent to one hour. The chosen values should provide sufficient resolution to capture the early and late instants of the drug transport and retention phenomena. Between these constraints, the time step size was variable throughout the simulation, adjusting automatically according to the COMSOL's automatic time-stepping algorithm. The "Strict" option for time steps taken was selected within the software to produce a more conservative progression of time-stepping, improving the simulation stability during the computationally demanding Deployment step.

Minimum damping factor A low damping factor of 0.1 for the non-linear Newton method improved simulation robustness, by essentially trading computation speed for stability in terms of convergence.

Maximum number of iterations A large number of iterations (50) for the non-linear Newton method also improved simulation robustness, permitting the solver to perform a more liberal number of iterations until convergence is achieved during the computationally demanding event of contact.

Manual scaling of independent variables Providing the solver with suggestions of the magnitude of each model variable was found to be crucial for simulation convergence. This process was performed iteratively and progressively, as initial guesses for the expected range of each variable were updated based on observations from simulations with increasing complexity, i.e. enabling different Levels.

Model development was marked by extensive research and experimentation of (I) physics parameters, (II) meshing, and (III) solver settings. When solving the equations of a model, COMSOL outputs the convergence plot, a graphical expression of how the time step evolves during the time-dependent solution process. Interpretation of the convergence plot was crucial for the adjustment of (I), (II), and (III).

Computational specifications and computation time

Finally, the model was simulated using the "Fine" mesh from the previous sensitivity analysis. The resulting system of time-dependent partial differential equations (PDEs) was solved using a Parallel Direct Sparse Solver (PARDISO). The computation was performed using an AMD Ryzen 9 5950X 16-Core CPU @ 3401 MHz processor, with 32 Logical Processors. The computation time reported varies depending on the combination of procedural parameters. For a default case scenario, characterised by inflation pressure of 8 atm, inflation duration of 60 s, and nominal drug load m_0, computation time was 10 hours and 40 minutes. In general, the computation time of the simulations carried out varied approximately between 8 and 16 hours.

5.6 Results

The Results section presents the exploration of different scenarios in the DCB deployment simulation. Three Case Studies are proposed, with each of them varying a single relevant procedural parameter. This exemplifies the usage of the model as an experimental platform for hypothesis testing — aimed at understanding the effect of varying procedural parameters on the simulation output. Table 5.13 presents the simulation cases considered:

Table 5.13: Study Cases considered *in silico*. Inflation pressure and duration are varied within clinical ranges, and drug load is varied experimentally to smaller and larger values (equal to half and two-fold the nominal drug load value, m_0). The baseline values for the three parameters are, respectively: 8 atm, 60 s, and m_0.

Case	Inflation pressure	Inflation duration	Drug load
1	6 atm, 8 atm, 10 atm	60 s	m_0
2	8 atm	30 s, 60 s, 90 s	m_0
3	8 atm	60 s	$\frac{1}{2}\, m_0$, m_0, $2\, m_0$

Extensive experimentation of other design and procedural parameters, such as drug type, balloon-to-artery-ratio, balloon design, and multiple inflations, is beyond the scope of this study but is encouraged for future research.

Table 5.14 lists the simulation outputs featured in the current presentation. These results concern the spatiotemporal evolution of the main model variables, encompassing all three multiphysics Levels of the system.

Table 5.14: Summary of results presented, per Level.

Results	Physical unit	Level
Balloon compliance	mm	Level 1
Contact pressure profile	mmHg	
Deformation field	—	
Transmural pressure field	mmHg	Level 2
Transmural advective field	μm/s	
Drug release profile	%, μg	Level 3
Drug distribution	mol/m^3, μg	
Drug content	ng/mg	
Specific receptor saturation	%	
Non-specific receptor saturation	%	

The colour scheme in the following time-dependent plotting represents the increasing magnitude of the varying parameters from green to yellow to red. Axes ranges are often equivalent to facilitate comparison between cases, and the values shown in the horizontal axes have particular relevance, e.g. the time points of usual preclinical evaluations (1, 3, 7, and 28 days after the procedure).

The spatial plotting presented next uses a rainbow colour scale (from blue to green to red) for non-drug variables, and a thermal colour scale (from white to yellow to red) for drug variables.

5.6.1 Balloon compliance

This subsection observes the behaviour of balloon compliance in each of the Case Studies.

In the model, balloon inflation is governed by a time-dependent pressure boundary load of maximum magnitude defined by the inflation pressure parameter. Altering this parameter, as proposed in Case 1, produces the following behaviour:

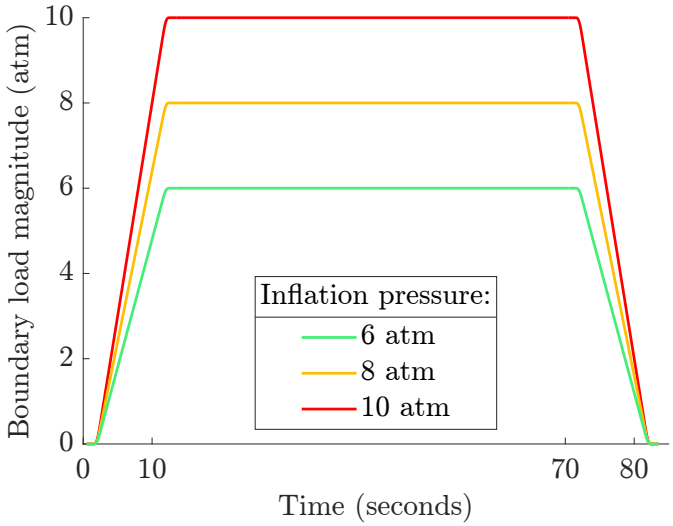

Figure 5.12: Magnitude of the pressure boundary load applied over the internal surface of the DCB during the Deployment step while varying the inflation pressure parameter.

The parameter variation in Cases 2 and 3 does not impact the amplitude of deformation. Notwithstanding, they will be featured in the observation of compliance.

Figure 5.13 shows the behaviour of DCB compliance in each of the Case Studies. The subfigures indicate that (a) increasing inflation pressure increases deformation amplitude, i.e. the DCB outer diameter at full inflation; (b) changing the duration of inflation only impacts the period of deployment; and that (c) drug dose variation has no impact on compliance (all curves are overlapping). From the simulation scenarios proposed, Case 1 is the only case that alters the DCB diameter at full inflation, thus affecting solid mechanics and transmural filtration. Therefore, further observations regarding Levels 1 and 2 are focussed on the variation of inflation pressure in Case 1.

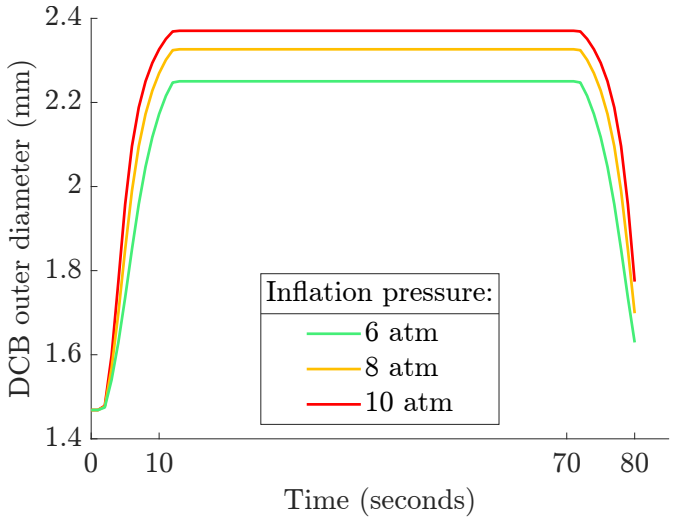

(a)

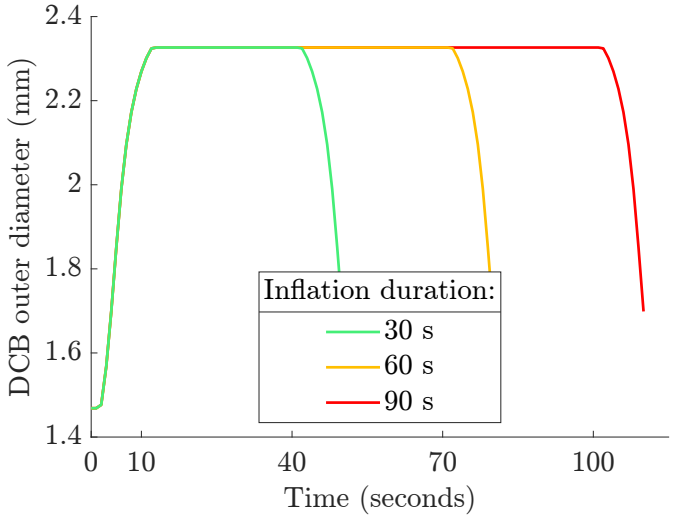

(b)

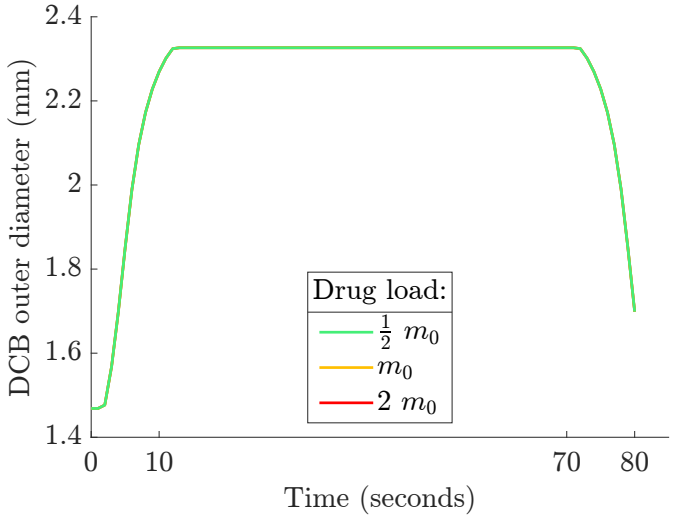

(c)

Figure 5.13: Balloon compliance results while varying (a) inflation pressure, (b) inflation duration, and (c) drug load.

5.6.2 Contact pressure profile

When the DCB is inflated to sufficiently high pressure values it engages the arterial wall. Having the DCB and the arterial wall as separated geometries in the model permits the contact interaction between them to be quantified. This addresses the important question of how much pressure is transmitted between the bodies on contact during deployment.

Assuming inflation is mainly perpendicular to the inner surface of the arterial wall, the magnitude of normal contact pressure is measured over the denuded endothelium, which comprises the contacting region:

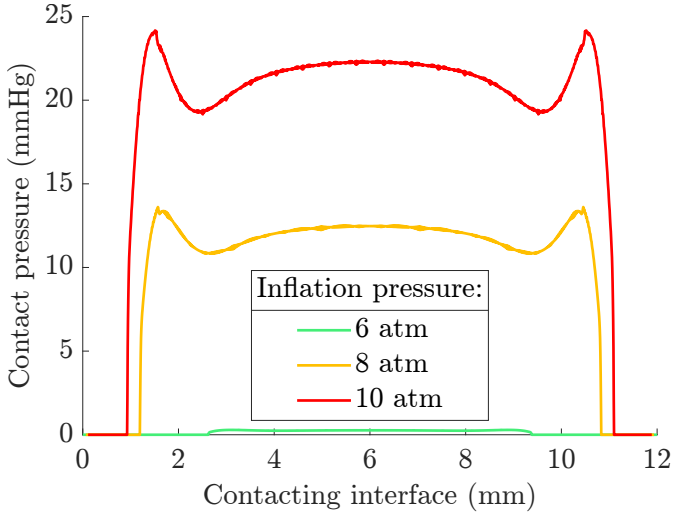

Figure 5.14: Magnitude of normal contact pressure over the contacting interface between the coating and denuded endothelium boundaries (in mmHg), while varying the inflation pressure parameter (in atm). The observation instant is mid-deployment ($t = 40$ s).

Figure 5.14 indicates that inflation pressure is only partially transmitted to the artery on contact. Increasing inflation pressure above the nominal inflation pressure amplifies contact pressure and thus deformation of the arterial wall. For reference, 6 atm, 8 atm, and 10 atm correspond to 4560 mmHg, 6080 mmHg, and 7600 mmHg.

A simple example is at an inflation pressure of 6 atm, where the DCB outer diameter is approximately equal to the artery inner diameter. Despite the high pressure inflating the DCB, about 45-fold the physiological luminal pressure, the device and artery barely touch and negligible pressure is transmitted. This is remarkably different to previous modelling assumptions, where the full inflation pressure values, such as 8 atm, were imposed over the drug delivery interface [67, 72]. This work encourages further discussion and exploration of contact pressure. Comparable contact pressure profiles and relatively low values were also reported in [71], for different balloon-to-artery ratios and inflation pressures.

Observing early instants in the time-dependent deployment simulation may show how contact pressure develops. The chosen instants, i.e. $t = 9$, 10, 11, and 12 s, illustrate the early moments of deployment: immediately before the DCB engages contact, the intermediate states,

and when inflation reaches its apex and the contact pressure stabilises (Figure 5.15). The sharp peaks in pressure seem to increase as contact intensifies.

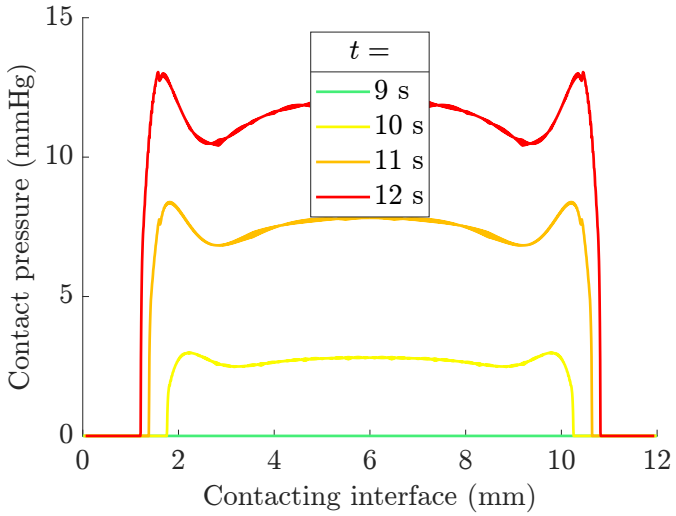

Figure 5.15: Magnitude of normal contact pressure over the contacting interface (in mmHg), during the early instants of the deployment simulation with the baseline pressure value ($p_{\max} = 8$ atm).

Figures 5.14 and 5.15 show peaks of contact pressure at the edges of the contacting interface between the DCB and arterial wall. The occurrence of non-uniform pressure over the contacting interface has been observed in the literature before. Teodorescu et al. [133] studied the contact pressure from the indentation of beam-like objects into a soft base material. This was to simulate stent implantation into an arterial wall, regarding the individual effect of each stent strut. From their perspective, the sharper edges or corners of the contacting object promote higher local stresses, described as "pressure spikes". In their work, they attribute it to geometry-related stress distribution.

The occurrence of non-uniform pressure over the contacting interface is present even in realistic 3D deployment simulations, such as [71]. This study identified non-uniform contact pressure gradients along the longitudinal direction and peaks are noticeable at the edges of the contacting interface. This may be somewhat related to the shape mismatch between the objects. In the present work, the sharp peaks of contact pressure are likely to be a result of the DCB geometry not being sufficiently rounded. Further geometry refinement via fillets with greater radius can attenuate the sharp corners and amend the issue if this is the case.

5.6.3 Deformation field

The contact interaction during DCB deployment temporarily impacts several aspects of the model. Initially, the altered pressure at the denuded endothelium affects the stress state of the arterial wall, causing deformation in Level 1, and also affects the pressure constraint of Level 2, amplifying transmural filtration. As these conditions are assumed to be constant and undisturbed except for during the event of DCB deployment, the mid-deployment scenario is of interest when concerning Levels 1 and 2. Therefore, the observations presented in the following figures take place mid-deployment, at $t = 40$ s, when the inflation pressure is stabilised at its maximum value, the DCB is fully inflated, and the influence of contact is the highest.

Figure 5.16 presents the mid-deployment 2D deformation behaviour of the arterial wall, specifically in the context of Case 1. Due to the predefined balloon-to-artery ratio ($1 : 1$), the DCB reaches the vessel's inner diameter when at its nominal inflation pressure value (6 atm). Despite establishing contact, this causes virtually no deformation in the arterial wall, as indicated in Figure 5.16 (a). In subfigures (b) and (c), the arterial wall increasingly deforms as the balloon is inflated to higher pressures. The maximum relative deformation of the arterial wall recorded in the radial direction was 0%, 3%, and 5%, respectively. These values are relatively low due to the chosen balloon-to-artery ratio. The high-pressure inflated balloon seems to dominate the overall deformation behaviour of the model, while the multilayered arterial wall complies with it.

It must be acknowledged that all observations on compliance relate to the simplifying modelling assumptions, namely the uniform geometry, incompressibility and hyperelasticity of the material models, and absence of disease. Considerations of the main limitations of the model are suggested in the next Section, "Discussion".

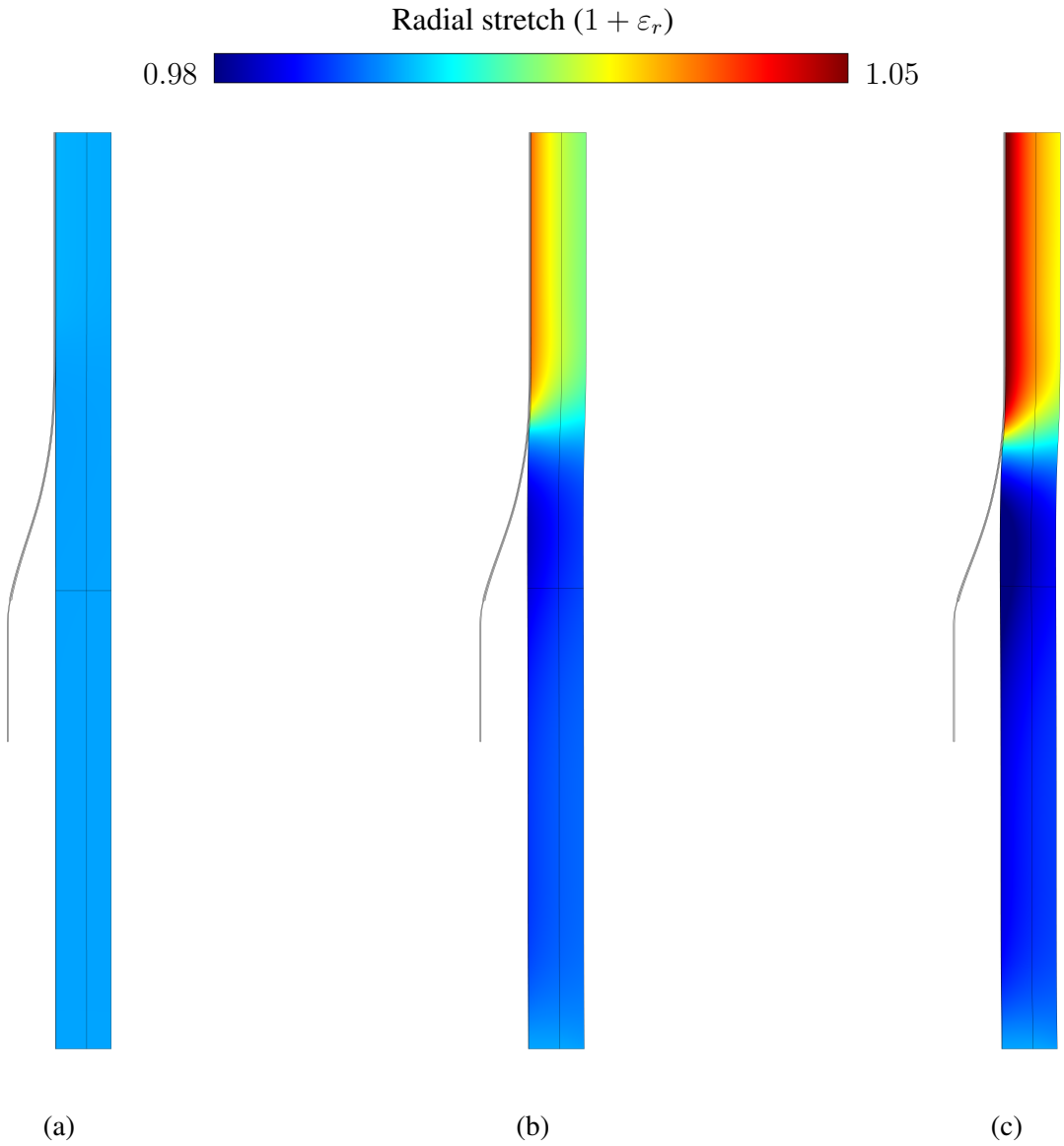

Figure 5.16: Mid-deployment deformation field, for inflation pressures of (a) 6 atm, (b) 8 atm, and (c) 10 atm, over half of the 2D-axisymmetric model geometry. The magnitude of arterial wall deformation is expressed as the radial stretch $(1 + \varepsilon_r)$, as illustrated with a linear colour scale.

5.6.4 Transmural filtration

The effect of DCB deployment on transmural filtration can be studied via assessment of the transmural pressure and advection fields. Contact pressure due to DCB inflation is added to the contacting interface, affecting the luminal constraint and, thus, the transmural fields.

Transmural pressure field

Figure 5.17 (a) indicates that the pressure constraint at the denuded endothelium exerts considerable influence on the transmural pressure field, even without the DCB effect.

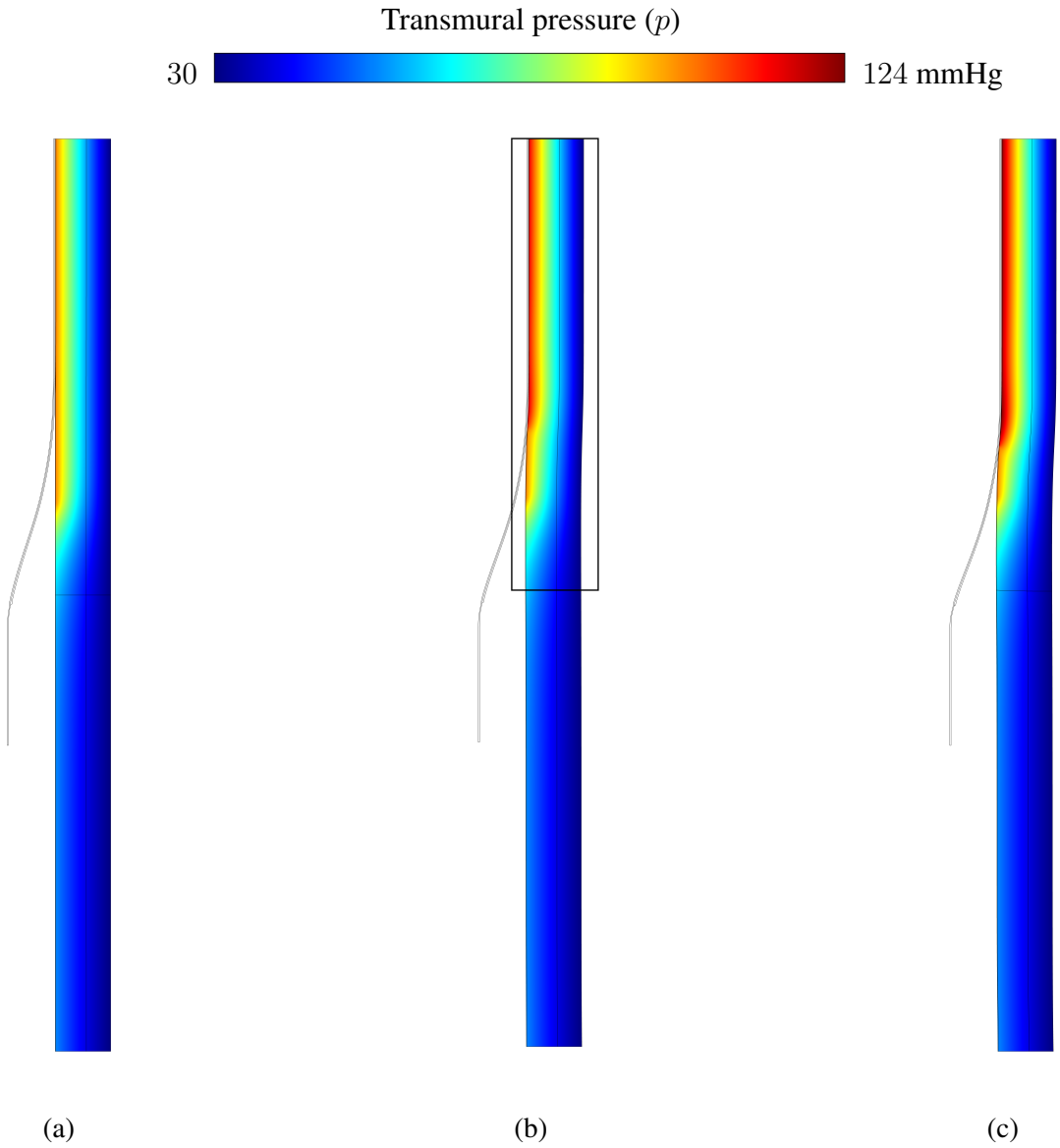

Figure 5.17: Mid-deployment transmural pressure field, for inflation pressures of (a) 6 atm, (b) 8 atm, and (c) 10 atm, over half of the 2D-axisymmetric model geometry. The magnitude of transmural pressure is illustrated using a linear colour scale from 30 to 124 mmHg.

This represents the physiological pressure of blood flow in the lumen, modelled as having a constant value of 100 mmHg, acting over the denuded region deprived of the protective layer of endothelial cells. Figures 5.17 (b) and (c) show that deploying the DCB with increasing inflation pressures contributes to the pressure constraint at the contacting interface, raising transmural pressure accordingly. When varying inflation pressure (Case 1), the maximum transmural pressure values recorded are 100 mmHg, 114 mmHg, and 124 mmHg. Such additive behaviour can be consulted in the previous Figure 5.14.

Figure 5.18 illustrates the transmural pressure behaviour over radial lines crossing the denuded and intact endothelium. The considered region is the therapeutic region, as an inset of the previous Figure 5.17 (b). Two moments are considered: at normal conditions when the

artery is subjected only to physiological pressure constraints and without external stimuli (i.e. before/after deployment), and mid-deployment (at $t = 40$ s).

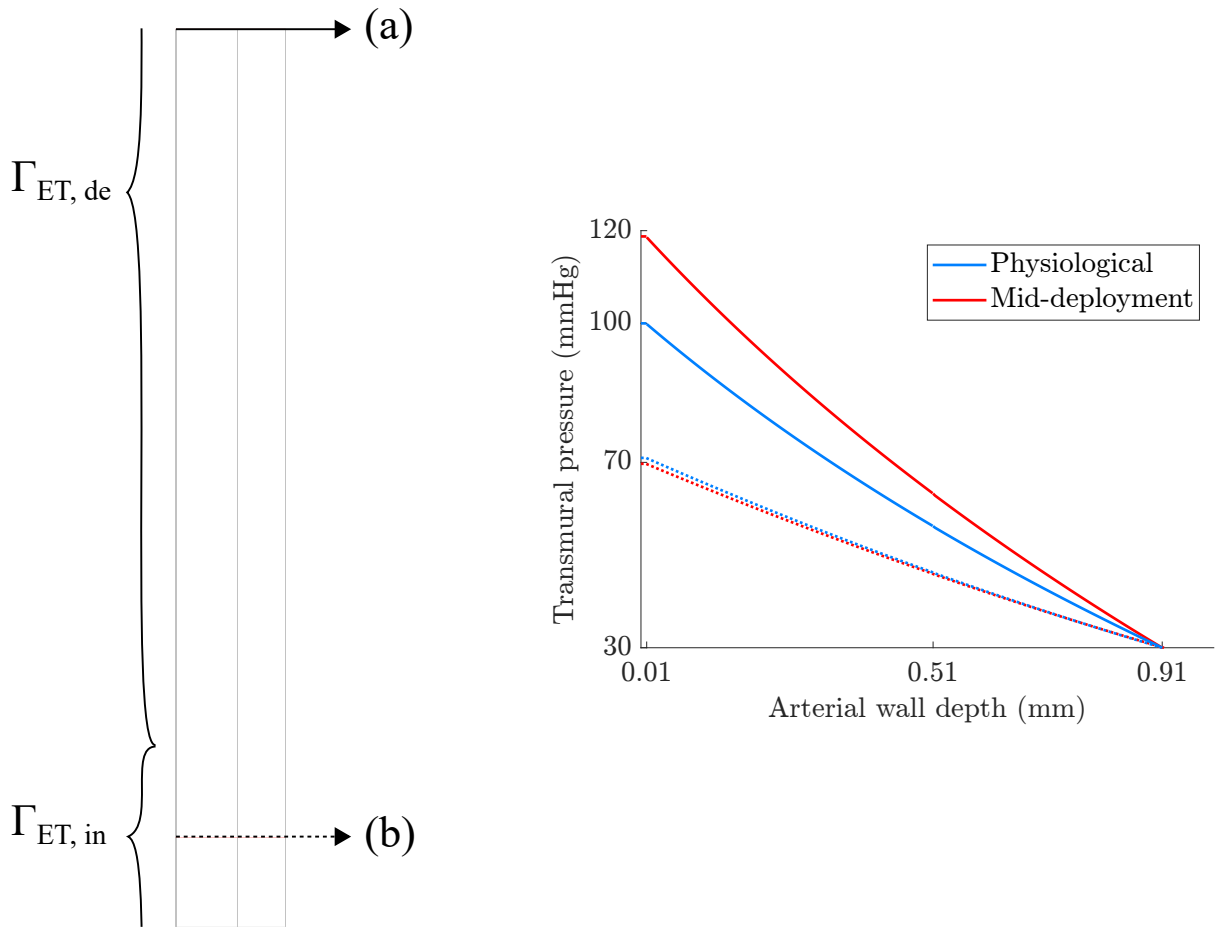

Figure 5.18: Schematic representation of the transmural pressure drop through the therapeutic region, over radial lines across (a) the denuded endothelium, as solid lines, and (b) the intact endothelium, as dotted lines. The values shown in the horizontal axis correspond to the spatial limits of each artery layer.

The denuded endothelium boundary ($\Gamma_{\text{ET, de}}$) represents the intervention-struck region of the artery. The solid line (a) in Figure 5.18 is located in the middle of the therapeutic domain, over $\Gamma_{\text{sym, }z}$, and the pressure behaviour across it indicates that the effect of DCB deployment is pronounced in the entire arterial wall. Lacking its protective layer of endothelial cells, assumed removed due to DCB deployment, the denuded endothelium behaves differently than its intact counterpart regarding the regulation of pressure from the lumen, even at normal conditions. Remarkably, the transmural pressure limits due to the luminal and perivascular pressure constraints ($p_{\text{lum}} = 100$ mmHg and $p_{\text{peri}} = 30$ mmHg) are only noticeable under normal conditions at the denuded endothelium. The protective role of the intact endothelium may be appreciated, greatly regulating the transmural behaviour over its length. Moreover, on closer inspection of the curve, small discontinuities of pressure are noticeable where the elastic laminae separates the layers.

The dotted line (b) crosses the intact endothelium ($\Gamma_{\text{ET, de}}$) closely below the intervention site.

Even in the vicinity of the deployment site, its pressure behaviour indicates that this region is considerably less affected by the deployment. In conclusion, Figure 5.18 highlights the impact of DCB deployment and the protective role of the endothelium.

Transmural velocity field

The behaviour of convective velocity due to transmural filtration is derived from the transmural pressure, as detailed in Section 5.3. Figure 5.20 provides a qualitative representation of the transmural velocity field for different inflation pressures. The velocity direction is depicted with arrows, and the colour scale is chosen to enhance visualisation, producing contrast between the cases.

This field seems remarkably affected by the transitory region between intact and denuded endothelium, where the pressure gradient is brisk, and by the DCB deployment. Also, due to the pressure gradient across the arterial wall, the convective field generally points radially outwards. Considering advective drug transport, this facilitates the drug drift towards the perivascular surface of the arterial wall, where the perivascular sink is located. This was previously observed in [55], in a comparison between endovascular and perivascular drug delivery modalities.

For instance, Figure 5.19 observes the transmural velocity magnitude in the radial direction (u_r) over a middle radial line can illustrate the early instants of DCB deployment.

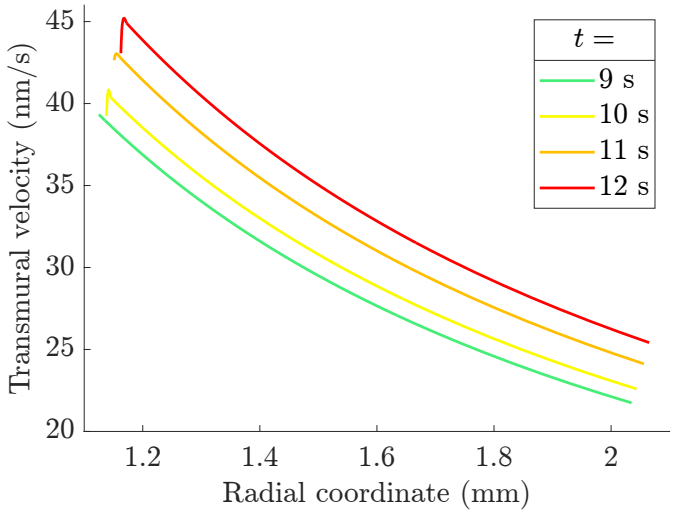

Figure 5.19: Transmural velocity magnitude in the radial direction (u_r) over a radial line through the middle of the arterial wall, for different instants during DCB deployment. The baseline scenario of procedural parameters is considered in the simulation (inflation pressure of 8 atm, inflation duration of 60 s, and nominal drug load m_0).

The contact interaction due to DCB deployment temporarily disrupts the transmural fields of the arterial wall by altering the pressure constraint at the contact interface $\Gamma_{\text{ET, de}}$. The magnitude of the alteration is directly related to the contact pressure value and indirectly related to the inflation pressure value. Although brief, during approximately the time window of inflation

duration, this effect may be crucial because of its drug delivery implications. During contact, the magnitude of advection is locally amplified, contributing towards deeper drug penetration as originally reported in [72].

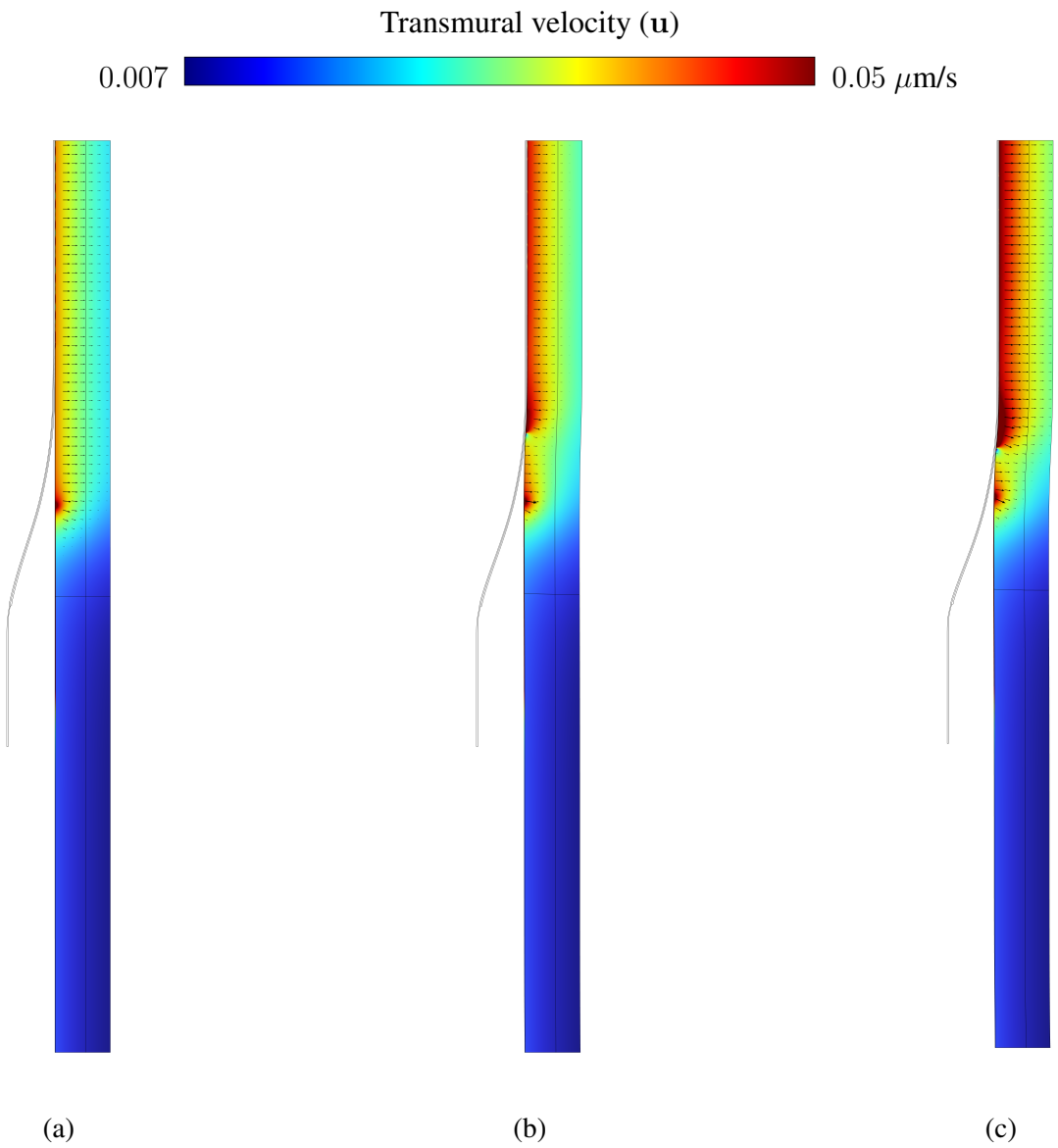

Figure 5.20: Mid-deployment transmural convective field, for inflation pressures of (a) 6 atm, (b) 8 atm, and (c) 10 atm, over half of the 2D-axisymmetric model geometry. The magnitude of transmural velocity is illustrated qualitatively using a linear colour scale from 0.007 to 0.05 μm/s.

The following subsections outline the main results of the drug delivery simulation for the Case Studies proposed and concisely explain their significance.

5.6.5 Drug release profile

Drug delivery from the DCB is quantified with a drug release profile. It can be inferred in the current model in multiple ways. For example, by measuring how much drug (I) is present in the coating domain (Ω_{coat}), (II) crosses the contacting surface (Γ_{coat} or $\Gamma_{ET,de}$), by integrating the inward fluxes J_{Src} or J_{Dst}, or (III) is present in the arterial wall domains (Ω_{int}, Ω_{med}, and Ω_{adv}) at a given time. Once the drug mass is calculated, it can be related to the initial drug load in the DCB coating to draw the drug release profile. Assuming well-behaved conservation of mass in the model, all three ways mentioned above are equivalent. For simplicity, the first option was used (calculating the drug mass in the coating domain).

Similarly to the definition from Chapter 4, the drug release profile is defined as a time-dependent function during the Deployment step as

$$\begin{aligned} DRP(t) &= \frac{m_0 - m_{\text{coat}}(t)}{m_0} \\ &= 1 - \frac{m_{\text{coat}}(t)}{m_0}, \end{aligned} \tag{5.6.1}$$

where m_0 is the initial drug load, post-tracking; DRP is the drug release profile, expressed as a percentage possibly ranging from 0 to 100%. The value of DRP represents the cumulative fraction of the drug load released until that time.

As exemplified in Figure 5.21 for the Case Studies, the cumulative amount of drug released from the coating of the DCB may be expressed as a fraction (in %) or drug mass (in μg). The drug release profile, as defined previously in Chapter 3, is a measurement of the cumulative fraction of drug released from a given drug reservoir, in this case, from the coating of the DCB. It is relative to the starting drug load at the beginning of the simulation, i.e. at $t = 0$ s, after tracking loss is deducted. Alongside it, a drug mass-based profile is proposed to facilitate the understanding and provide further depth to the comparison, outlining the magnitude of drug delivery. Axes ranges are equivalent to facilitate comparison between cases.

The magnitude of the drug release profile of the current model ($22\% - 37\%$) can be compared with other DCB modelling studies. For example, [66], [67], and [72] report that a typical DCB application is expected to release about 15–40 % of the drug load of the DCB. Remarkably, in these example studies the drug delivered from the DCB was modelled as a temporary inward flux of drug, behaving according to a predefined expression (as in Chapter 3). In contrast, the current model uses a thin diffusion barrier boundary condition enabled by contact between the inflating DCB and arterial wall.

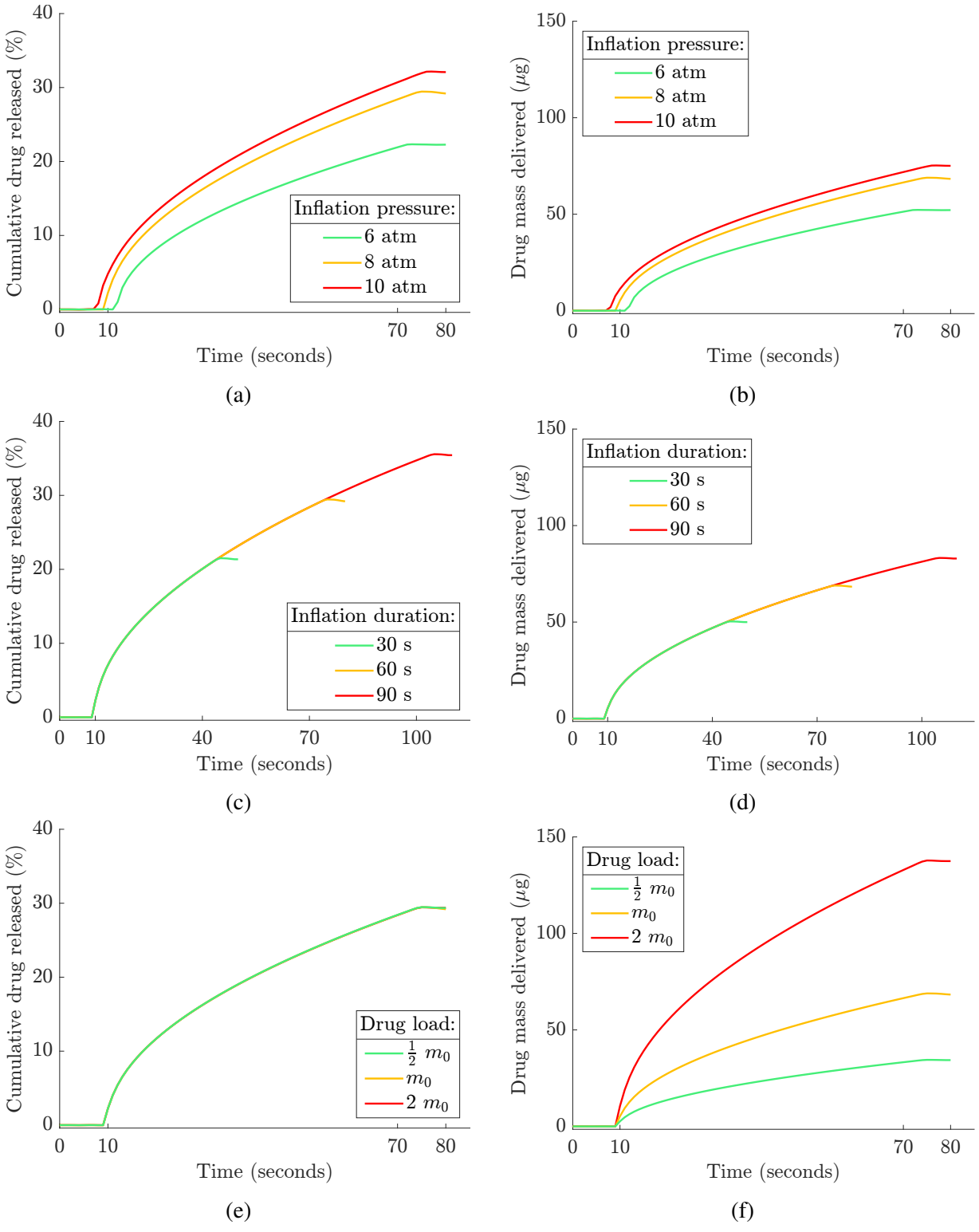

Figure 5.21: Drug release profile and drug mass delivered results for the three Case Studies, varying (a-b) inflation pressure, (c-d) inflation duration, and (e-f) drug load.

Figures 5.21 (a) and (b) show that increasing inflation pressure contributes towards greater drug release. Inflation pressure contributes towards drug delivery primarily by increasing the contact surface area between DCB and artery. Secondarily, amplification of transmural advec-

tion may enhance the drug concentration gradient, quickening drug delivery as drug is delivered deeper. A pertinent observation is that the total duration of contact, and consequently drug delivery, is slightly sensitive to inflation pressure since the DCB engages the artery at the nominal pressure value (6 atm) in the simulation. Figures 5.21 (c) and (d) indicate that longer inflation durations result in greater drug release, albeit at a diminishing rate. Concluding, Figures 5.21 (e) and (f) indicate that drug load substantially affects the drug mass delivered, at a quasi-linear proportion, while it only marginally affects the cumulative release rate.

Drug release profile and drug mass delivered concern only the Deployment step, as the DCB is removed afterwards, and the model assumes there is no delayed sustained release. Towards the end of each curve, a stagnation of the crescent behaviour can be noticed. At that moment, the DCB is undergoing deflation and loses contact with the arterial wall, ceasing drug delivery.

5.6.6 Drug distribution

The primary output of the drug transport and retention simulation is the spatiotemporal drug concentration field. It allows the analysis of drug distribution in the tissue at any given moment during the simulation in each drug phase — ultimately enabling the measurement of key indicators of the therapy.

This subsection presents the spatial distribution of drug in the arterial wall throughout the simulation as sequences of 2D plots. The drug distribution is observed at several instants, spanning over the Deployment and Follow-up steps, at $t = 40$ seconds, ten minutes, one hour, four hours, one day, seven days, and 28 days. A single baseline scenario of procedural parameters is considered, characterised by inflation pressure of 8 atm, inflation duration of 60 s, and nominal drug load m_0. Aiming to disregard numerical noise and enhance visualisation of the plots, drug is assumed detectable for concentrations greater than 10^{-6} mol/m^3.

Total drug distribution

Firstly, the overall spatial distribution of drug in the model is presented by the total drug concentration, including free and bound phases, over the model domains.

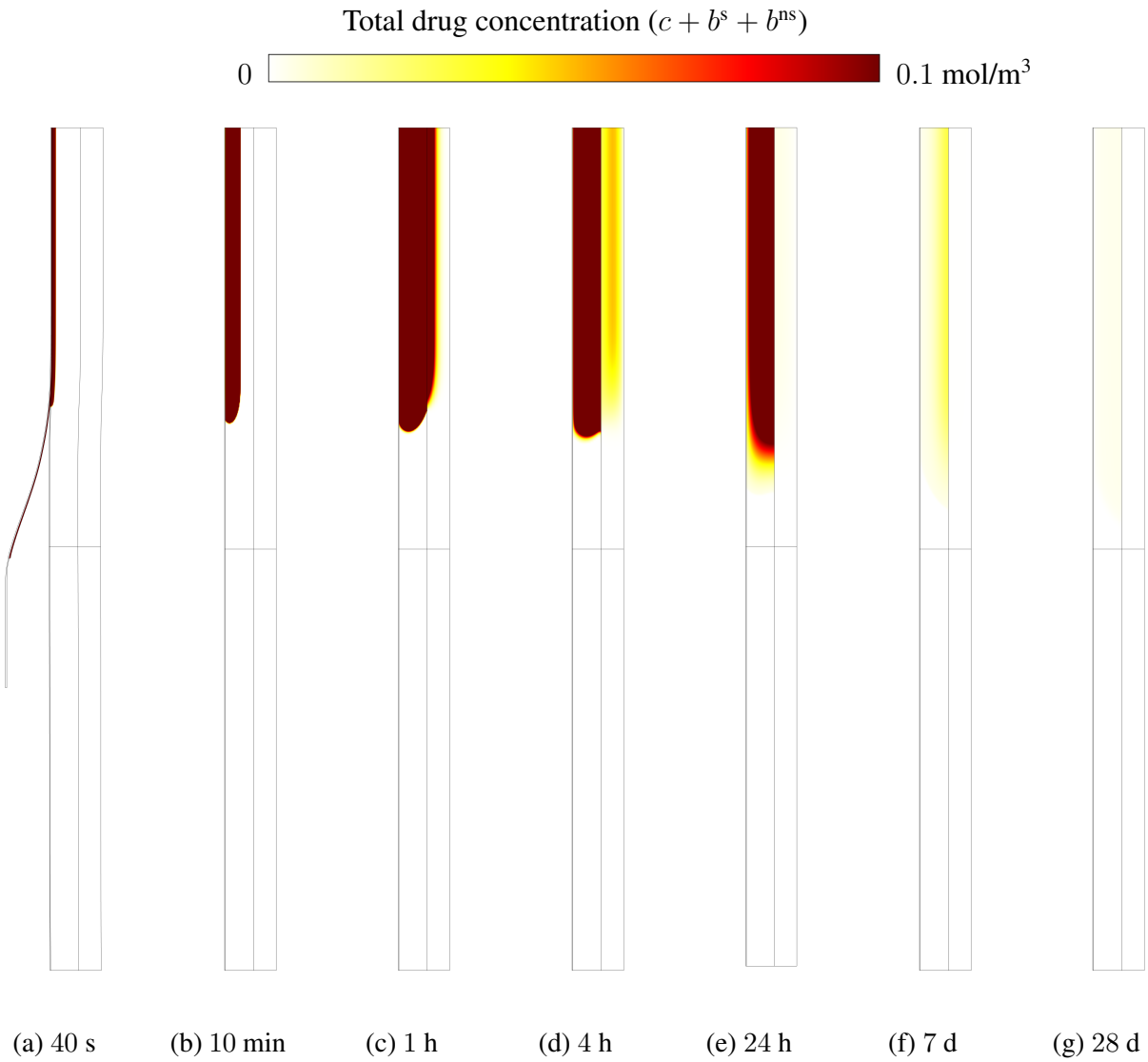

(a) 40 s (b) 10 min (c) 1 h (d) 4 h (e) 24 h (f) 7 d (g) 28 d

Figure 5.22: Spatial distribution of drug throughout the simulation. The magnitude of drug concentration is illustrated using a linear colour scale from 0 to 0.1 mol/m^3.

The temporal advancement of the simulation is depicted by the subfigures (a-g). The first time point, (a), depicts an early mid-deployment instant when the DCB is visible and the artery is deformed. Later points mainly depict the penetration of drug into the arterial wall, with a preference for transport in the radial direction. Figures 5.22 (c-g) show greater retention of drug in the media layer, where drug binding is modelled. Drug concentration in the adventitia layer is notably low throughout the observed times.

Drug concentration is mostly contained within the therapeutic domain, where similar drug measurements are performed in preclinical experiments. This corroborates the rationale of the therapeutic domain, focussing on the site of drug distribution and the length of the artery segment in the model, as sufficient to allow unconstrained drug distribution.

Free drug distribution

The behaviour of each of the drug phases can be observed separately in additional drug distribution plots. Next, free drug distribution is presented in Figure 5.23.

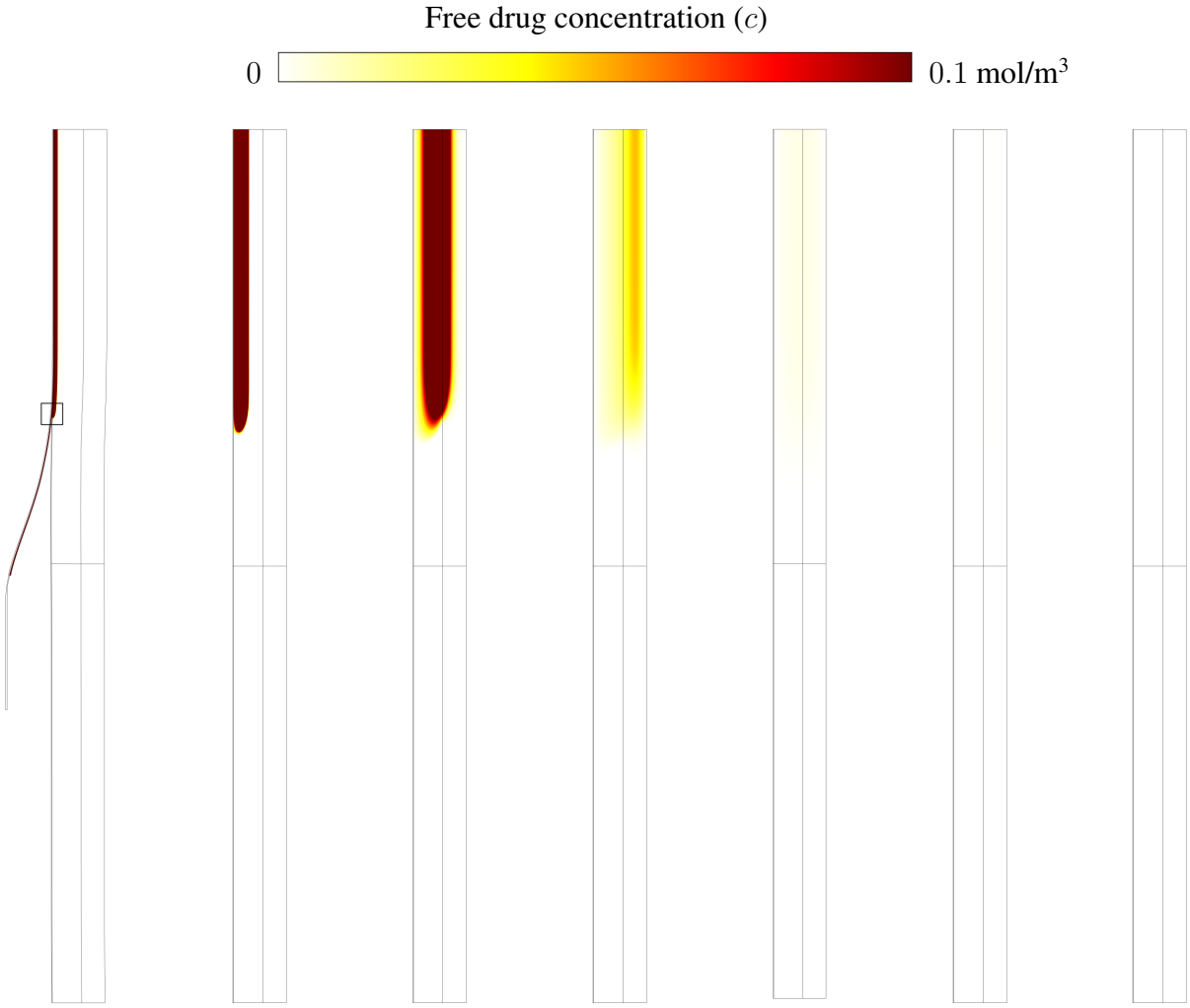

(a) 40 s (b) 10 min (c) 1 h (d) 4 h (e) 24 h (f) 7 d (g) 28 d

Figure 5.23: Spatial distribution of free drug throughout the simulation. The magnitude of drug concentration is illustrated using a linear colour scale from 0 to 0.1 mol/m^3.

In contrast to the total drug distribution, subfigures (c-g) show rapid depletion of free drug. This indicates that drug is retained preferably in bound phases within the arterial wall.

Furthermore, the distribution of free drug concentration also concerns the coating of the DCB. The coating domain is characteristically embedded with a high concentration of drug, c_0, three orders of magnitude greater than the value used in the previous plotting scales of total and free drug concentration. On contact, part of its drug load is delivered to the tissue.

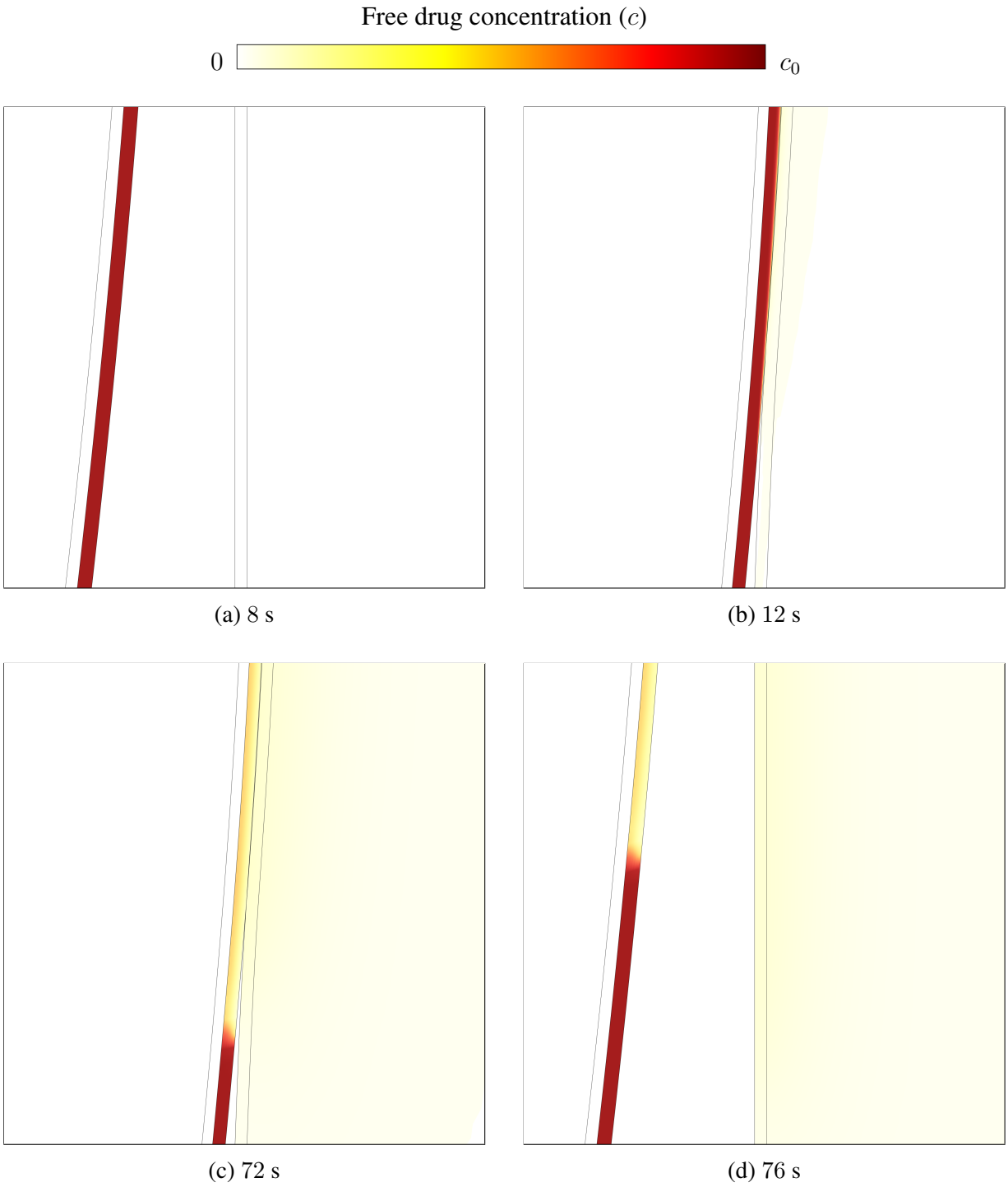

(a) 8 s

(b) 12 s

(c) 72 s

(d) 76 s

Figure 5.24: Highlight of the spatial distribution of free drug in part of the coating domain, at early moments near the beginning (a-b) and end (c-d) of the drug delivery simulation. The magnitude of drug concentration is illustrated qualitatively using a linear colour scale from 0 to c_0, i.e. the initial drug concentration in the coating, 224 mol/m^3, when the nominal drug dose is considered.

Figure 5.24 illustrates the draining effect in the coating, by observing a contacting region at different moments during the deployment simulation. The region shown is a magnified inset of Figure 5.23 (a). The simplifying assumptions of the coating must be noted alongside this

analysis.

Specifically-bound drug distribution

The distribution of drug bound to the specific receptors in the tissue (i.e. cells) can be observed in its characteristic concentration scale.

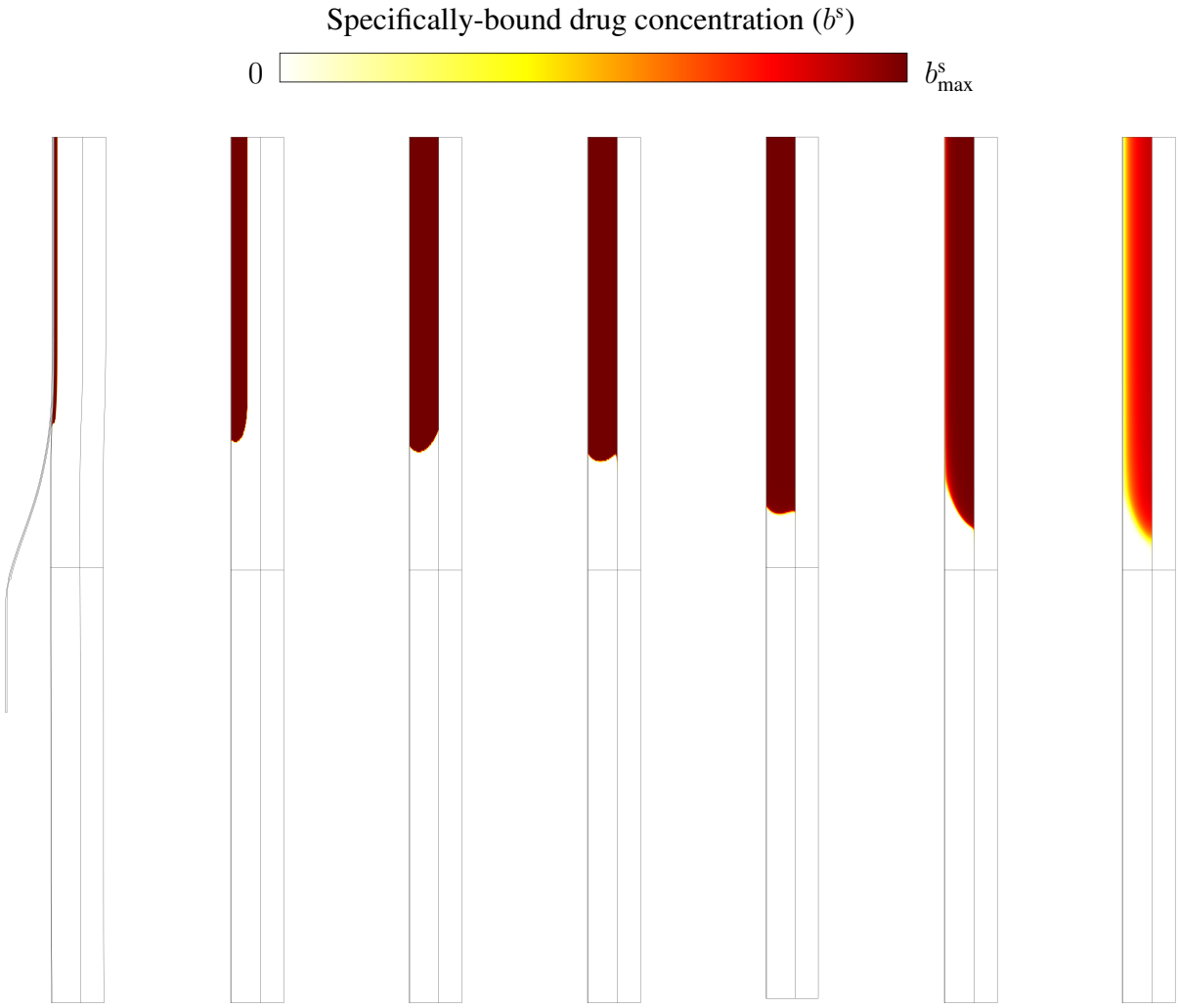

(a) 40 s (b) 10 min (c) 1 h (d) 4 h (e) 24 h (f) 7 d (g) 28 d

Figure 5.25: Spatial distribution of specifically-bound drug throughout the simulation. The magnitude of drug concentration is illustrated using a linear colour scale from 0 to $b^s_{max} = 0.0033$ mol/m^3.

The specific binding site density (b^s_{max}) defines the ceiling value of drug in specifically-bound phase, at which saturation occurs. Its magnitude is remarkably low ($b^s_{max} = 0.0033$ mol/m^3). This means that little drug mass is sufficient to completely fill the specific binding sites and thus achieve maximum retention of drug in the tissue.

Figure 5.25 illustrates well the concept of receptor saturation. After 7 days of the delivery procedure, drug appears to have soaked the entire media layer within the therapeutic domain,

as shown in subfigure (f). If the specific receptors are completely saturated, it means that specific receptor saturation is at 100%. High saturation of the specific receptors throughout the therapeutic window is the target of the drug therapy [61].

Over time, drug continuously unbinds from the binding sites, returning to the free drug phase and continuing its radial drift towards the perivascular end. This showcases the reversible behaviour of drug binding and may be observed in subfigure (g) where the bound drug concentration is slowly decreasing. At later times, it is expected that all drug is washed off from the arterial wall through its drug sinks.

Non-specifically-bound drug distribution

Likewise, the distribution of drug bound to the non-specific receptors in the tissue (i.e. interstitial tissue and extracellular matrix) can be observed in its characteristic concentration scale.

The behaviour of non-specific binding differs from that of its specific bound counterpart. The former peaks earlier, covering a smaller part of the therapeutic domain, and declines more rapidly. A combination of two main factors may explain the difference: (I) a much larger binding site density ($b^{\text{ns}}_{\text{max}} >> b^{\text{s}}_{\text{max}}$) and (II) a weaker binding-on rate ($k^{\text{ns}}_{on} << k^{\text{s}}_{on}$).

The previous spatial distribution figures stressed that each of the drug phases has its characteristic concentration range. The colour scale for total and free drug concentration (from 0 to 0.1 mol/m^3) was chosen to produce contrast over the chosen time points. Bound drug concentrations b^{s} and b^{ns} were shown limited by their respective saturation values, $b^{\text{s}}_{\text{max}}$ and $b^{\text{ns}}_{\text{max}}$ — which differ in magnitude 110-fold. It is crucial to emphasise the concept of receptor capacity, also known as binding site density. It determines how much drug can be retained in each of the bound phases until saturation.

The drug distribution plots can be observed in conjunction with the further drug content and receptor saturation plots.

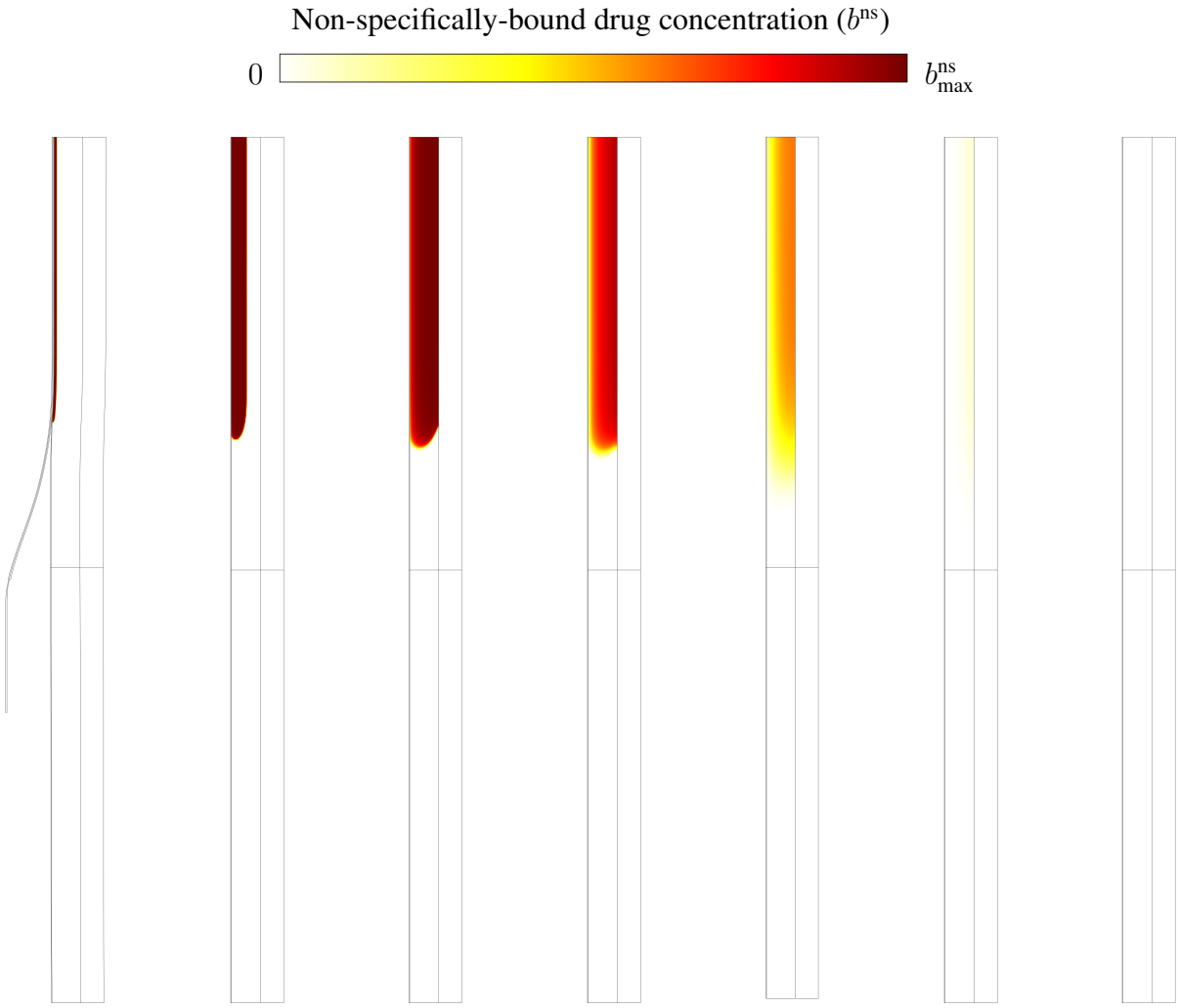

(a) 40 s (b) 10 min (c) 1 h (d) 4 h (e) 24 h (f) 7 d (g) 28 d

Figure 5.26: Spatial distribution of non-specifically-bound drug throughout the simulation. The magnitude of drug concentration is illustrated using a linear colour scale from 0 to $b^{ns}_{max} = 0.363$ mol/m^3.

Drug mass distribution

Additionally, the total drug mass in each of the model domains over time can be quantified via the integration of the spatial drug distributions. This perspective was used during the development of the model, mainly concerning the conservation of mass during the transmission of drug between DCB and arterial wall and the moving geometry problem; nonetheless, the analysis of drug mass distribution by domain can provide further insights from the simulation results.

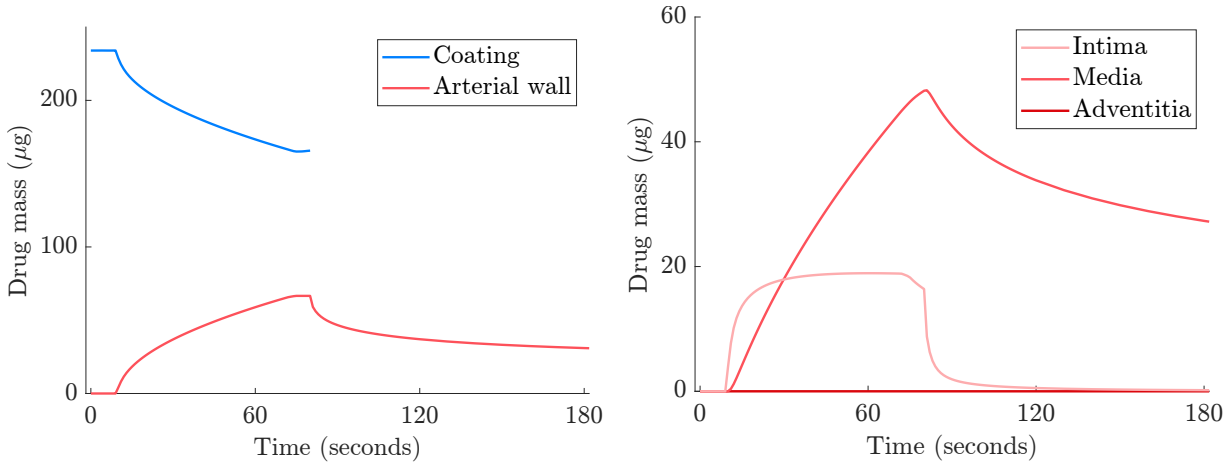

(a) (b)

Figure 5.27: Total drug mass distribution in the early moments of the simulation, at (a) a macro level of coating and arterial wall and (b) a micro level on a layer-specific basis. A single baseline scenario of procedural parameters was considered.

Measuring the total drug mass in the entire model shows a negative fluctuation of 0.987% during the early moments of drug delivery. Drug clearance should not happen via luminal sink as it is disabled during the Deployment step; thus this fluctuation is unnatural and is assumed to be related to numerical error in the calculation of drug transfer between domains. While this magnitude of violation of conservation is acceptable, further improvement of meshing and tuning of the penalty contact method (to lessen penetration) could lower it even more. After the Deployment step, the DCB is removed and drug stops being quantified in the coating domain, as illustrated by the blue curve in Figure 5.27 (a).

For conciseness, Figure 5.27 only presents the total drug mass distribution during the first three minutes of the simulation. Other scenarios can deepen the understanding of the simulation results, for instance observing the distribution of drug mass in free and bound phases, at later times, and while varying procedural parameters.

A single example scenario is presented in Table 5.15. Late drug retention in the tissue majorly occurs in bound drug phases — 99.7% when considering drug bound to both specific and non-specific binding sites.

Table 5.15: Composition of drug mass retained in the tissue at 28 days after delivery, by phase, considering the baseline Case Study (8 atm, 60 s, and m_0) and the therapeutic region.

Total	Free	Bound, specific	Bound, non-specific
158.0 ng (100%)	0.38 ng (0.24%)	144.0 ng (91.14%)	13.6 ng (8.62%)

5.6.7 Drug content

Preclinical studies commonly use drug content (DC) to evaluate the permanence of drug in an artery segment throughout the therapeutic window. Within a predefined therapeutic region, the amount of drug mass per arterial tissue mass determines the value of DC at any given moment, usually in nanograms of drug per microgram of tissue. To achieve a therapy that is both efficacious and safe, the DC value is desirable between a therapeutic limit and a toxic limit.

On the therapeutic limit of drug content

The concentration threshold over which the drug exerts a therapeutic effect, referred to as the therapeutic limit, is commonly reported in preclinical studies as DC greater than 1 ng/mg for coronary artery tissue [33, 47], evaluated at 28 days after the drug delivery. Values above this limit indicate sufficient effect of the antiproliferative drug, highlighting the usage of DC as an indirect indicator of therapeutic efficacy. From the *in silico* experimentation performed in this study, this value is found to correspond to the resultant DC value when the specific receptors are mostly saturated. How this therapeutic value may relate to receptor binding is discussed in Section 5.7.

On the toxic limit of drug content

Although this study specifically considers a cytostatic drug (sirolimus) and not a cytotoxic drug (such as paclitaxel), the concept of toxic limit intends to illustrate a scenario where excessive exposition to a therapeutic agent is potentially harmful or undesired. Thus, values above this limit indicate a potentially harmful effect of the antiproliferative drug, highlighting the usage of DC as an indicator of therapeutic safety.

The toxic limit may be estimated by using a point-wise drug concentration as suggested in [134]. There, the drug concentration value 0.73 mol/m^3 was used as a toxic threshold for the optimisation of sirolimus delivery from DESs. The translation of the point-wise concentration to a drug content value is proposed below from the definition of DC, and assuming a constant free drug concentration averaged over the entire domain, $\bar{c}$, in order to simplify the volume terms in the equation:

$$\begin{aligned} DC &= \frac{m_{\text{wall}}^{\text{drug}}}{m_{\text{tissue}}} \\ DC_{\text{tox}} &= \frac{\int_V \bar{c}\, M_{\text{sir}}\, dV}{\int_V \rho\, dV} \\ &= \frac{\bar{c}\, M_{\text{sir}}}{\rho} \end{aligned} \tag{5.6.2}$$

$$\approx 679 \frac{\text{ng}}{\text{mg}},$$

where $\bar{c}$ is the toxic concentration threshold, M_{sir} is the molar mass of sirolimus, and ρ is the tissue density, as defined previously.

The results of drug content for the proposed Case Studies are presented in Figure 5.28. The increasing magnitude of the varying procedural parameters is denoted by the colour progression from green to yellow to red. Due to the "one-shot" nature of DCB delivery, all DC results exhibit a large early peak followed by an abrupt decline. This behaviour is in line with the experimental results observed by [43] after DCB application in coronary arteries, which reported a rapid decrease in drug levels in the tissue within the first 60 minutes, and a greater than 90% decay by 72 hours — vs 94% in the baseline simulation of this work. The declining behaviour is because drug is allowed to leave the tissue through the luminal and perivascular sinks soon after the Deployment step, as the Follow-up step begins. The magnified inset shows the Deployment step in detail, in the time scale of seconds, where the peak values occur and are denoted with a black dot. Noticeably, the early DC behaviour is somewhat proportional to the amount of drug mass delivered, presented previously in Figure 5.21. The most drastic increase in drug content is observed when the drug load is varied. Some combinations of procedural parameters result in infringement of the toxic limit of drug content, estimated in Equation 5.6.2. While a two-fold increase in drug load may not be sensible, these results illustrate a potentially alarming scenario of toxic DC levels.

The tables beside each subfigure summarise the peak and final DC values for that Case Study. The main conclusion regarding these is the observation of marginal difference in final DC values at later times (28 days after the procedure), regardless of the contrasting early peak values.

The drug transport and retention properties of sirolimus are considered here, as gathered from the literature. Other relevant antiproliferative drugs, e.g. Biolimus A9™, everolimus, zotarolimus, have not been unexplored to the same extent and may result in different DC behaviours.

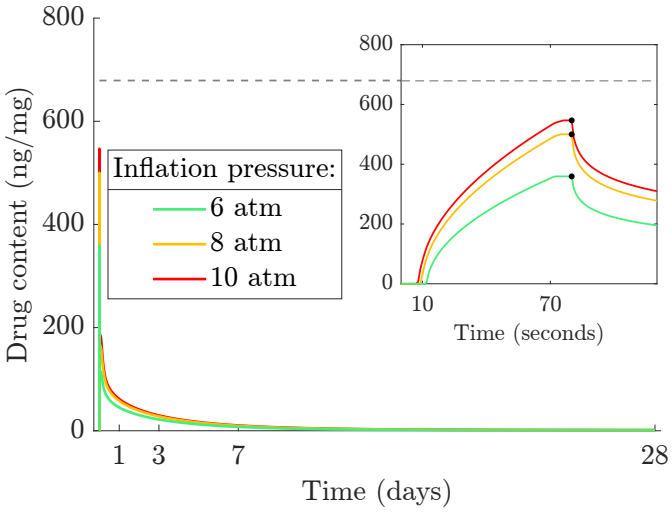

(a)

Inflation pressure (atm)	Peak DC (ng/mg)	Final DC (ng/mg)
6	359.31	0.94
8	500.02	1.19
10	546.74	1.27

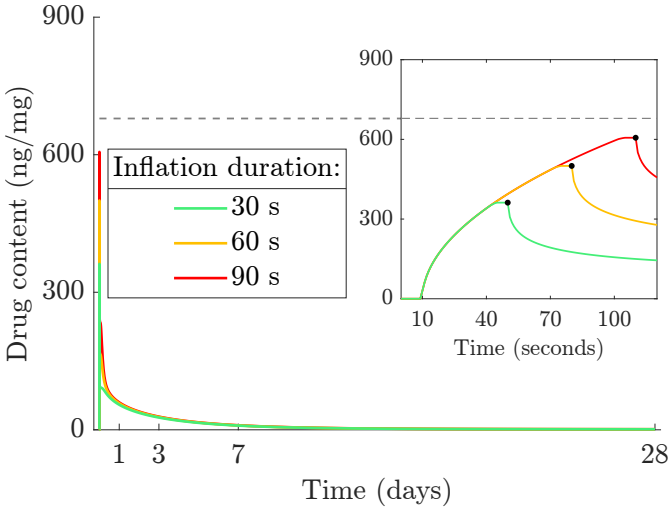

(b)

Inflation duration (s)	Peak DC (ng/mg)	Final DC (ng/mg)
30	361.83	1.13
60	500.02	1.19
90	606.11	1.22

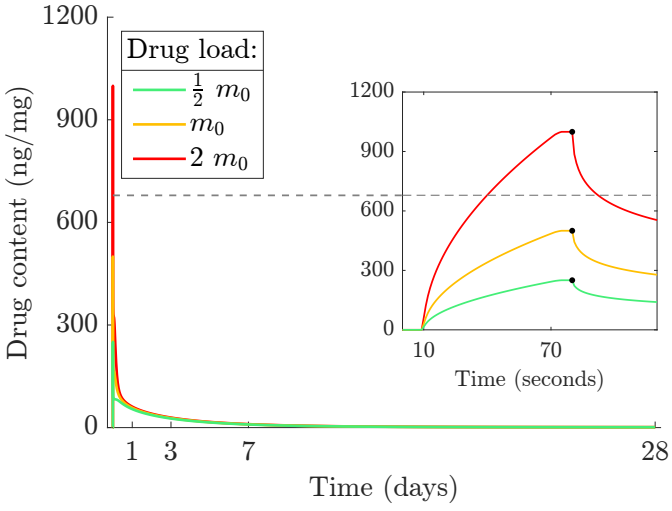

(c)

Drug load (μg)	Peak DC (ng/mg)	Final DC (ng/mg)
$\frac{1}{2}\ m_0$	250.28	1.13
m_0	500.02	1.19
$2\ m_0$	999.24	1.24

Figure 5.28: Drug content results while varying (a) inflation pressure, (b) inflation duration, and (c) drug load. The magnified inset shows the Deployment step in detail. The dotted horizontal line illustrates the concept of toxic limit, according to the aforementioned estimation.

5.6.8 Receptor saturation

Figure 5.29 presents the results of receptor saturation levels for the proposed Case Studies, concerning the behaviour of drug binding to the drug receptors in the media layer.

The subfigures (a), (c), and (e) show the saturation of specific drug receptors (sRS). Importantly, sRS is strongly related to the residence time of drug in the arterial tissue, which seems to be a predictor of success of the endovascular drug delivery [**?**]. Its value is desired to be as high as possible during the therapeutic window.

The remaining subfigures of Figure 5.29, (b), (d), and (f), show the saturation of non-specific drug receptors ($nsRS$). As a collateral form of drug binding, the role of $nsRS$ is relatively unexplored. From the preliminary observations *in silico*, this type of binding effectively produces a drug reservoir in the tissue, which peaks early, contributing to the overall drug uptake by the tissue. The large difference between the two saturation behaviours is due to the parameters governing drug binding in the model: binding site densities and binding-on and off rates.

Intrinsically, the behaviour of the curves of Figure 5.29 depends on having sufficient drug mass to saturate the receptors in the tissue. Consequently, saturation levels are expected to be influenced by the amount of drug mass delivered, and thus by the procedural parameters considered in the Case Studies.

Figure 5.29 (a) shows a pronounced saturation difference between inflation pressure values of 6 and 8 atm, while a marginal difference between 8 and 10 atm. Marginal improvement in specific receptor saturation is observed even with a substantial increase in the amount of drug delivered, as proposed in Case 3. Due to the modelling assumptions of drug binding, drug retention is limited by the binding site density values. Once the cell receptors saturate, i.e. specific saturation reaches 100%, further increase in drug availability does not increase retention nor would contribute towards increased antiproliferative effects of the drug. In this case, the drug excess in the tissue would primarily raise the drug content levels and, eventually, lead to toxicity. In summary, it is desirable to maintain consistently high values of sRS throughout the therapeutic window, while keeping DC values below the toxic threshold.

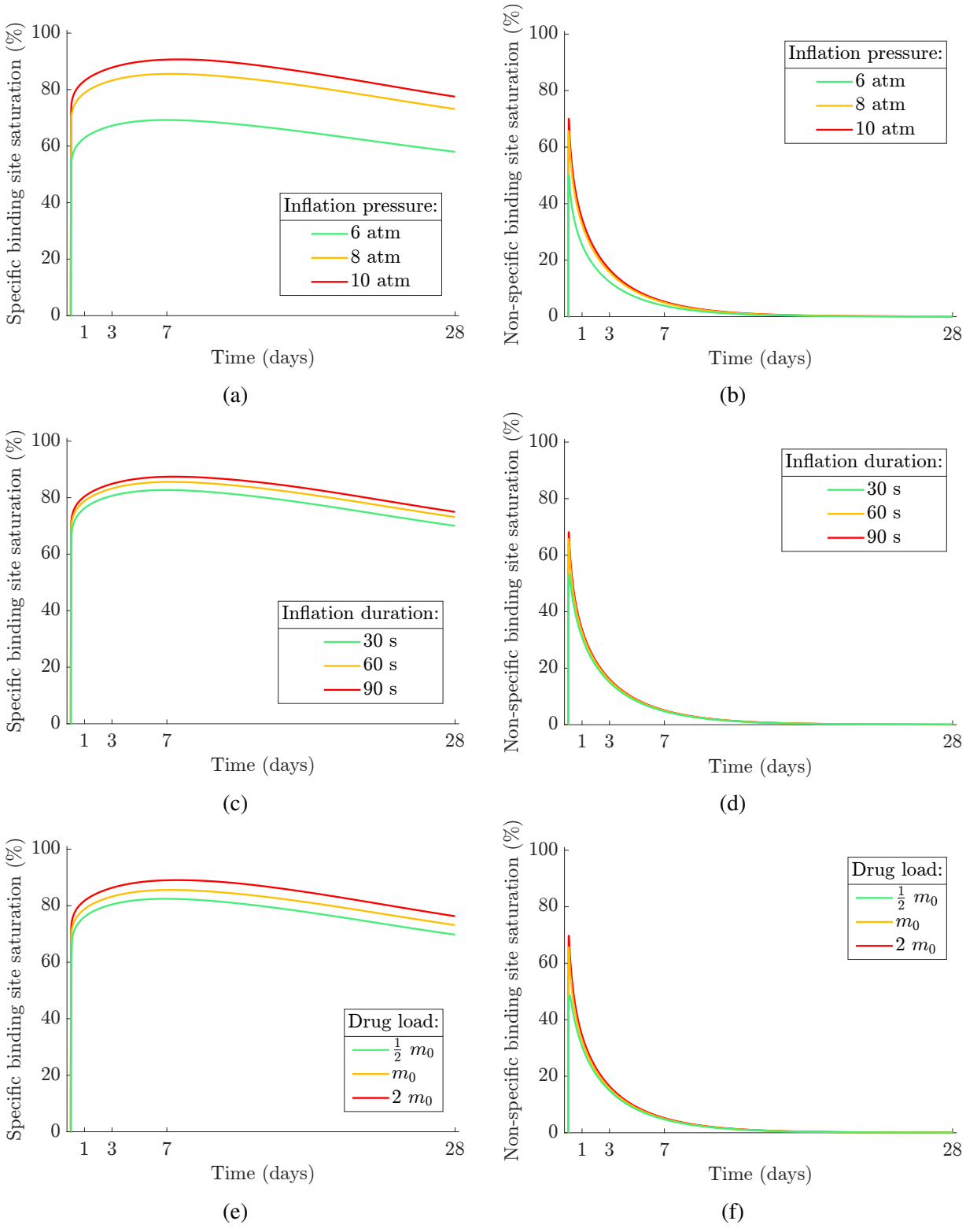

Figure 5.29: Specific and non-specific receptor saturation results while varying (a-b) inflation pressure, (c-d) inflation duration, and (e-f) drug load.

5.7 Discussion

This Section presents a summary of the milestones achieved, key novelties, and limitations of the work developed.

This Chapter presented the modelling and simulation of an idealised DCB deployment and drug delivery procedure. The work builds upon pre-existing computational modelling works of endovascular drug delivery, contributing to the field by incorporating a representation of the DCB device and its deployment procedure. At the time of the report, this is the first *in silico* model of DCB that accounts for deployment, drug delivery, and drug transport and retention within a single modelling framework. To some extent, it demonstrated the feasibility of coupling the structural mechanics and drug delivery parts of DCB deployment, incorporating the multiphysics and time-dependent interaction between the device and target vessel with success. Moreover, the coupling of DCB deployment with transmural filtration was proposed as a novel feature. Finally, the model enabled drug release and uptake to be fully quantified, including the assessment of both early-time peaks and long-term drug retention in tissue, both intimately linked to the release kinetics. The main indicators of safety and efficacy of the therapy were assessed from the simulation results, as measured in the preclinical studies. Further studies envisage a direct comparison of the model against experimental data for potential calibration and validation.

On modelling the DCB

Representing the DCB geometry in the model permits the study and learning of various relevant processes, such as balloon inflation, contact mechanics, arterial wall deformation, and contact-based drug delivery. The study of these was unfeasible in the previous modelling works without a geometrical representation of the DCB.

Observation of simulation results over a radial line, as illustrated in Figure 5.30, may facilitate understanding and allow comparison with simpler geometries such as 1D models. For conciseness, the set of results presented in Section 5.6 only depicted 2D-dimensional fields. Future works shall scrutinise the results from different perspectives.

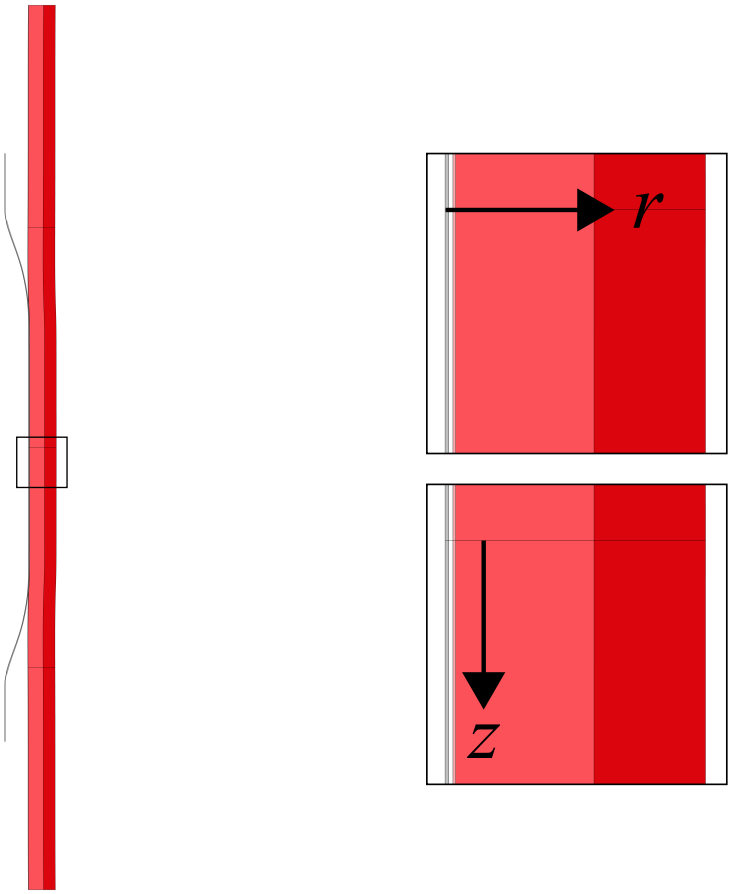

Figure 5.30: Model geometry overview at the moment of DCB deployment. The magnified insets show radial and longitudinal lines intended to assess simulation results on a 1D basis and facilitate understanding.

Below are some comments about pertinent modelling aspects.

Balloon inflation

The Gent hyperelastic material model was suitable for describing the deformation behaviour of a semi-compliant balloon within the operation range. In Chapters 4 and 5, free DCB expansion was considered, assuming the resistance of the solution medium and luminal blood flow were negligible, respectively. In the latter, the DCB was paired with the arterial wall model and insights into the interaction could be gathered. With the balloon-to-artery ratio chosen ($1 : 1$), particularly small arterial deformations were observed (up to 5% radially). From the simulations performed, it was noted that the multilayered arterial wall complied with the high-pressure inflated balloon. Importantly, DCB inflation was modelled with a time-dependent pressure load and not a prescribed displacement. In the case of sclerotic disease, where plaque or calcified lesions may alter the arterial composition, the compliance behaviour would likely differ. However, it must be emphasised that the role of DCB is for drug delivery and not for dilating the

lumen.

Reiterating, the pressurised environment of the artery lumen is neglected in the model, which implies that balloon inflation is simplified as a consequence. Nevertheless, the balloon compliance was calibrated to reflect the expected deformation behaviour of the device.

The simplicity of the material model permitted a straightforward and effective adjustment of material parameters via a parameter-fitting routine based on the available compliance information. Spatiotemporal smoothing of the pressure ramp provided satisfactory results, concerning simulation stability and deformation realism. Further experimentation, in the form of inflation tests with DCBs of different sizes, can validate the deformation behaviour of the model and the assumption of 2D-axisymmetry.

Contact

Multi-body interaction is a distinguishable feature of this model. The importance of contact mechanics has been eloquently described in [127] from an engineering point of view, and its modelling was a crucial challenge of the problem of the present work, as it is time-dependent and involves multiple physics. As reported by other endovascular modelling works focussed on structural mechanics, severe non-convergence difficulties were encountered when modelling the contact interaction between the device and the arterial wall in the context of stent deployment [70] and alternative contact algorithms were proposed to avoid numerical problems of standard facet-based contact [123]. Time-dependent deformation and contact modelling were central and challenging pieces of the modelling puzzle, and similar non-converging solution difficulties were eventually overcome with an exhaustive manual tuning of the mesh and solver settings. As a reward, including the DCB as a separate entity and modelling contact in the model led to pertinent observations.

Common intravascular pressure values in coronary arteries, as used in the referenced studies [62], [82], [63], [83], are in the order of 100 mmHg. Previous modelling works, although not including DCB deployment and artery deformation, assumed that the full inflation pressure of 8 atm would act on the lumen-wall interface during the procedure [67, 72]. This would configure a 60-fold increase of intravascular pressure during DCB inflation, which seems unnatural as previously discussed in Chapter 3. Although interventional balloons are inflated to extraordinarily high-pressure magnitudes (e.g. 8 atm $= 6080$ mmHg), the contact pressure transmitted to the arterial wall during inflation depends on the contact interaction between the bodies. Therefore, balloon inflation pressure should be included but with proper consideration of the contact interaction between the DCB and arterial wall. In the model presented in Chapter 5, the balloon pressure acting on the arterial wall during deployment is not imposed but is an indirect product of the contact simulation. In the results of Section 5.6, the magnitude of contact pressure was shown to be only a small fraction of the total inflation pressure value. *In silico* studies dedicated to the investigation of contact pressure and DCB unfolding mechanisms can be found in [71],

and show results in line with the findings of the present model. The different balloon-to-artery ratios between the studies must be appreciated before a quantitative comparison.

It must be emphasised that the coating structure considered in this Chapter assumes artificial mechanical resistance. In Chapter 4, the DCB model geometry was proposed as a geometry merging Ω_{B} and Ω_{coat} with the same structural properties. Notably, this simplifying assumption produces a thicker structure of less stiffness to achieve the desired compliance. An initial discussion was provided in that Chapter, comparing DCBs of comparable compliance with and without a mechanically resistive coating structure. To further justify the assumption of merged structural mechanics for the balloon and coating geometries, comparisons are proposed concerning contact mechanics and stress. When the DCB is inflated against the arterial wall, the observation of contact pressure behaviour is relevant. Figure 5.31 compares the two cases of DCB geometry mid-deployment, for an inflation pressure of 8 atm. Remarkably, contact pressure is comparable in shape and magnitude between the cases, with a relative decrease of 5.9 % in average contact pressure when simulating a DCB with the coating.

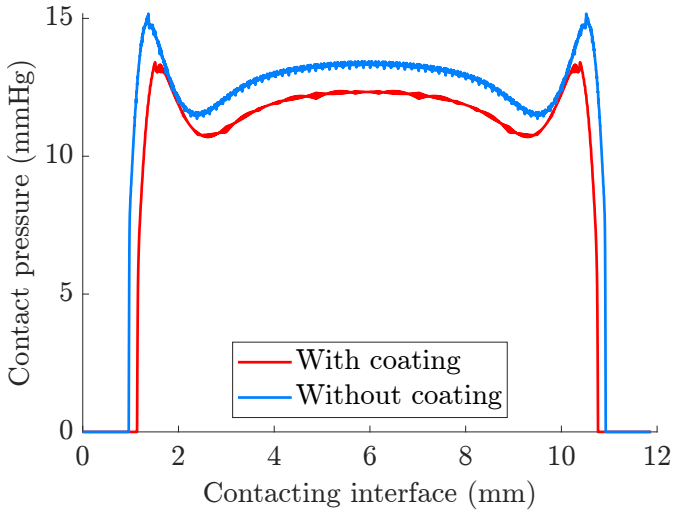

Figure 5.31: Magnitude of normal contact pressure over the contacting interface between coating and denuded endothelium boundaries (in mmHg), comparing the DCB geometry with and without coating. The observation instant is mid-deployment ($t = 40$ s).

A preliminary stress analysis is proposed over a radial line across the DCB and multilayered arterial wall during deployment as illustrated in 5.30. The first principal stress value is assessed as in [135]. This stress analysis is, however, severely limited due to the lack of longitudinal *in situ* stretch and effect of transmural pressures on arterial deformation. It serves simply to illustrate the incremental effect of balloon inflation on a resting geometry, and the difference between having it caused by DCB geometries with different stiffness (with or without a stiff coating). Figure 5.32 (a) conveys that the uncoated balloon has increased stiffness and reduced thickness. Figure 5.32 (b) shows that the artery exhibits strong layer-specific behaviours, deployment stress is mainly received by the intima layer, and difference between cases is marginal. The

observed arterial stress values are within the physiological range of tissue stresses, as assumed in Holzapfel et al. [136] in the order of $50 - 100$ kPa. Future works dedicated to the subject of structural mechanics may elaborate on this.

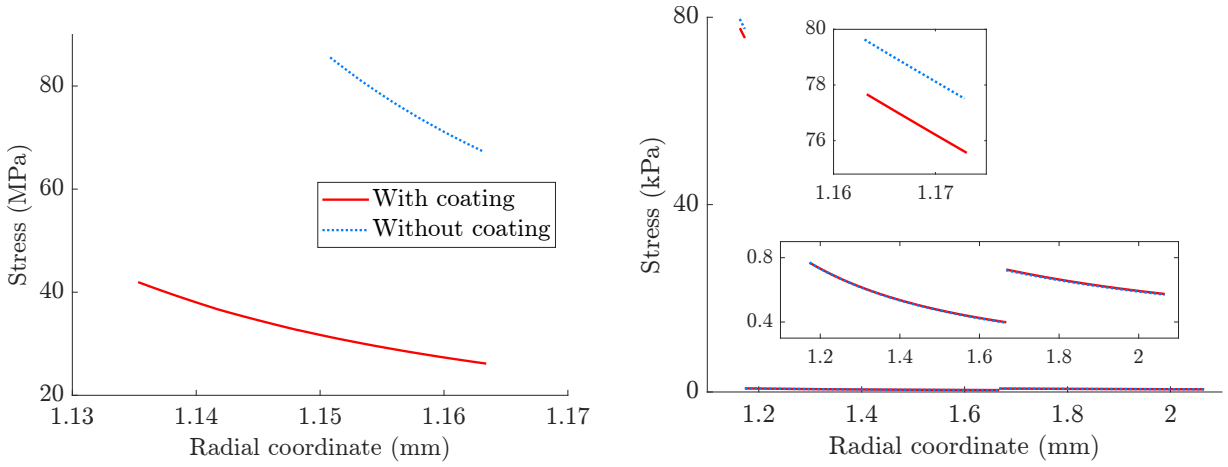

(a) (b)

Figure 5.32: Comparison of spatial stress distribution over a middle radial line at mid-deployment ($p_{\max} = 8$ atm), considering the first principal stress across (a) the DCB geometry and (b) the multilayered arterial wall. The magnitude of each stress scale is notably different, due to the different material models and stiffness, in MPa for the balloon, and in kPa for the arterial wall. The magnified insets in (b) show the stress across the intima, and media and adventitia layers in their characteristic scales.

Overall, the inclusion of contact in the current work contributes to the understanding of balloon inflation pressure affecting arterial deformation, amplification of transmural filtration, drug release from DCB, and early drug transport in the tissue. Furthermore, it refines the *in silico* insights of [72], which emphasise that balloon inflation pressure, although active for only a short time window during deployment, critically affects the drug distribution behaviour and must be considered in the simulation of DCB drug delivery. Expanding the interpretation of contact to Levels 2 and 3 also indicates respectively that the transmural filtration velocity is locally amplified and the contacting interface length increases with higher inflation pressures, both potentially increasing drug transfer during DCB deployment.

The fundamental limitations of this modelling work are related to modelling simplifications and the availability of experimental parameters. They could be addressed in the future with further development of the modelling assumptions and experimental studies. A brief discussion about the limitations of the model is provided below.

Simplified geometry

Firstly, the model uses a simplified geometry, based on an idealised artery segment and DCB exploiting two types of symmetries. Due to the use of 2D-axisymmetry, the model geometries

are always symmetric around the radial axis. Due to symmetry over a middle longitudinal line (mirroring), the behaviours downstream and upstream are identical. Consequently, this excludes the depiction of any non-symmetries of the problem. While the current methodology is likely reasonable for the preclinical case with healthy animal arteries, the advancement of this work to more realistic patient-specific artery geometries will demand reconsidering the simplifying modelling assumptions.

As exemplified in Chapter 3, symmetry considerably lowered the geometric complexity of a drug-eluting stent to a series of disconnected rings. While it was part of the many acceptable assumptions of that model, such simplification should have perceptible effects on drug distribution. However, the loss of realism should be less pronounced in the case of DCBs, which feature a somewhat simpler design. The device is, by design, symmetrical around the radial axis, readily enabling 2D-axisymmetry. Furthermore, its proximal and distal parts are sufficiently similar and should play a much smaller role in drug delivery when compared to the middle part. However, simplifying the DCB geometry excludes parts of the problem, such as the crimping procedure, that describes how the balloon is folded into the catheter pre-delivery. Crimping strategies typically aim to preserve the drug concentration in the coating of the DCB while in transit to the lesion site, minimising tracking loss. Despite disregarding crimping, the DCB's mechanical behaviour in the simulation was satisfactory, successfully mimicking the desired compliance. The assumption of a non-crimped and initially-uninflated DCB in the deployment simulation is related to the preliminary DCB model presented in Chapter 4, where the balloon undergoes free inflation. Future modelling may ponder the role of the crimping process and reconsider the geometrical symmetries. Concluding, symmetric modelling is more suitable for DCBs than for stents.

Coating behaviour

For the purpose of drug delivery simulations, the coating is the most relevant part of the DCB device. During the intervention, the drug-embedded coating is exposed to the lumen, where blood normally flows. However, the haemodynamics are considerably simplified considering the lumen simplification proposed in Chapter 3. In the absence of blood flow, drug wash-off from the DCB coating due to exposure to the lumen during the deployment simulation is also simplified. Unlike in Chapter 4, the effect of drug loss to the "solution medium" that the DCB is immersed in, i.e. the luminal flow here, is not regarded during the deployment simulation. Instead, only tracking loss is included prior to the time-dependent simulation, at $t = 0$ s in the form of a uniform deduction of the initial drug concentration in the coating. Further studies are necessary to elucidate the relevance of these effects.

In Chapters 4 and 5, the coating was assumed as a solid nonporous geometry. Its structural properties are notably assumed artificial, as discussed in detail throughout the discussions of these Chapters, and the main rationale for the simplifying assumption of a stiff coating in the

proposed modelling is to enable the simulation of DCB deployment featuring a drug-embedded domain Ω_{coat}, where drug transport physics are calculated, avoiding its crushing during the multiphysics contact interaction. The consequence of this artificial coating behaviour was studied, as illustrated in Figures 5.31 and 5.32, and deemed to be acceptable for the current model.

Having a drug-embedded coating geometry prompted the use of continuity of concentration to transfer drug between DCB and arterial wall domains. However, two options were considered throughout the extensive *in silico* experimentation performed — with a thin diffusion barrier or continuity of concentration. For illustration, comparisons between these were performed using a smaller pseudo-1D model, with only 2 mesh elements in the longitudinal direction. It replicates all the physics of the regular model. An overview of the simulation results with different modelling approaches for the drug transfer between the drug-embedded coating and arterial wall is provided below. Figure 5.33 (a) compares the drug release profile. In Figure 5.33 (b), the conservation of mass is assessed by the relative total drug mass in the system, given by

$$\frac{\displaystyle\sum_i \int_{\Omega_\text{i}} (c + b^\text{s} + b^\text{ns})\, d\Omega_\text{i}}{\displaystyle\int_{\Omega_\text{coat}} c_0\, d\Omega_\text{coat}} \qquad \text{in } \Omega_i, \text{ for } i = \{\text{int, med, adv}\}. \tag{5.7.1}$$

$$= \frac{m_\text{coat}(t) + m_\text{wall}(t)}{m_0}$$

Ideally, this value should remain as close to 100% as possible during the Deployment step, when drug clearance is disabled. The value of the relative total drug mass fluctuates; that is, mass is not perfectly conserved due to numerical error. This behaviour is more abrupt with the continuity condition; likely since continuity is only suitable for pairs where the boundaries match, according to COMSOL documentation [137]. Further mesh refinement should lower it even more. However, in the present model, there is no guarantee that the deformed coating with its deformed mesh will engage contact while having a "matching" boundary with the wall.

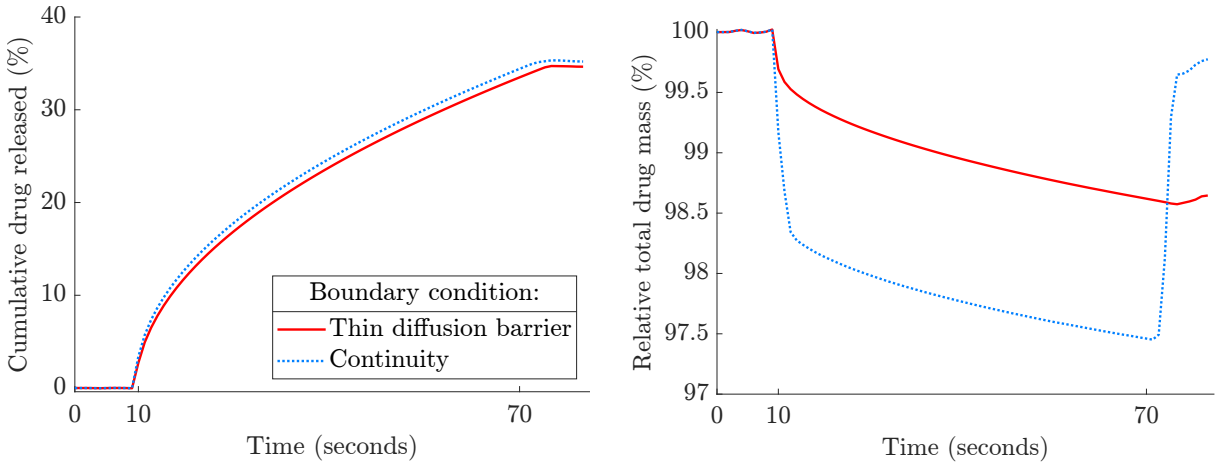

(a) (b)

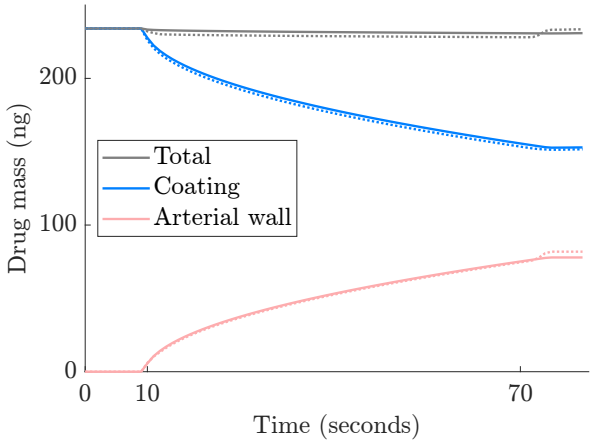

(c)

	Thin diffusion barrier	Continuity
Cumulative drug released in 60 s	34.6%	35.2%
Conservation of mass after delivery	−1.35%	−0.23%
Computation time	2 min 23 s	6 min 53 s

Figure 5.33: Comparison between thin diffusion barrier and continuity of concentration, regarding (a) drug release profile, (b) conservation of mass, and (c) the drug mass distribution in the coating and artery domains, and the entire model (in nanograms due to the reduced model size). Solid and dotted lines refer respectively to results with the thin diffusion barrier and the continuity condition.

The results show that the difference in simulation results was not dramatic, only in computation time as in Figure 5.33 (c). Therefore, the thin diffusion barrier was preferred over the continuity of concentration. The notable disadvantages of continuity of concentration in the present model are (I) the increase in computation costs and (II) the requirement of matching meshes at the contacting boundaries. Since the diffusion coefficient in the coating domain is 2

orders of magnitude slower than in the intima layer ($8.2 \cdot 10^{-13}$ vs $1.67 \cdot 10^{-11}$ m^2/s), future works will continue pondering the modelling of the drug-embedded coating of DCBs, and review the flux dependency on h_{coat}.

The thin diffusion barrier was proposed as an alternative to a continuity condition. The continuity condition would connect the drug concentration fields of the contacting domains. The distinctive features of the thin diffusion barrier are (I) the additional dependency on coating parameters, namely D_{coat} and h_{coat}, and (II) reduced computational expense, as observed in preliminary *in silico* experimentation of own authorship.

The distinctive features of the thin diffusion barrier are (I) the additional dependency on coating parameters, namely D_{coat} and h_{coat}, and (II) reduced computational expense, as observed in preliminary *in silico* experimentation of own authorship. Future studies may ponder the modelling of the drug-embedded coating with different modelling approaches.

As an addendum, the potential effect of coating adhesion acting as a drug reservoir is absent in this model. Coating adhesion is a phenomenon where part of the coating is mechanically detached from the DCB and retained by the arterial tissue during deployment. While the blood flow should vigorously and rapidly wash off the coating adhered to the luminal surface, particles of the coating delivered deeper into the arterial wall may serve as a drug reservoir of sustained release [69]. The interaction between the coating and endothelial surface during deployment is mentioned in other studies as an understudied factor of DCBs [53]. This additional drug delivery mechanism is out of the scope of this modelling work.

Therapeutic agent

Since the focus of the model and this work is on the distribution and not on the action of the drug, the drug definition is reduced to a set of drug transport and retention parameters. Sirolimus was the therapeutic agent of choice in the simulations reported since it is a more extensively studied substance and presents a wider availability of parameters. Notwithstanding, the model is adaptable to test any other drug as long as sufficient information is provided.

Notably, the value of the diffusion coefficient in the coating comes from the previous drug release studies of Chapter 4 — based on a Biolimus A9™ experiment. Although the diffusion coefficient of Biolimus A9™ is expected to be very similar to that of sirolimus, due to their analogous chemical structure, this incongruence must also be noted. Considerable effort was made to harvest additional drug transport and retention parameters of Biolimus A9™ from available data, however, this is currently an unfinished endeavour. Additional and objective drug-on-tissue experimentation is required to advance the understanding of Biolimus A9™ parameters for modelling drug transport and retention.

Arterial tissue

The largest simplification of the endovascular modelling presented in this work was the arterial wall. Firstly, the artery geometry is idealised as a straight axisymmetric tube. It must be emphasised carefully that the model uses a generalisation of a coronary artery model. Parameters and dimensions come from multiple sources, which fatefully enhances model idealisations. Importantly, while the model aims to represent the drug delivery of sirolimus into a porcine arterial environment, some of the parameters used were obtained from different animal species and drug types. A rigorous review of the parameters is necessary to ensure a fair comparison with a particular experimental setting.

The simplified mechanical behaviour of arterial tissue must also be regarded. While it is programmed to deform according to a sophisticated hyperelastic material model, including layer-specific and anisotropic fibre orientation and dispersion, it does so with limited conditions. Arterial deformation in the simulation happens only during the Deployment step and according to external stimuli, i.e. due to DCB contact. As balloon deflation happens, the artery returns to its original position in an effectively elastic manner, which, in reality, would not happen. The model does not include the effect of plasticity; indeed, hyperelastic constitutive models are unable to fully characterise the non-elastic deformation of arteries [107]. Moreover, the GOH material model utilised may have a set of limitations, as critiqued in [125]. During Follow-up, structural mechanics are disabled and the arterial wall is assumed rigid and immutable. Hence, any further time-dependent alteration of the artery geometry, for mechanical or biological reasons, is disregarded. Briefly, the former relates to the phenomenon of elastic recoil, which originally prompted the usage of stents as permanent scaffolding devices post-intervention. The latter refers to another major subject of research: arterial remodelling.

Remodelling is a relevant concern regarding the long-term behaviour of arterial tissue following traumatic injury. Although the arterial wall model in Chapter 5 includes a geometry responsive to structural deformation, it ignores all histological responses to the drug, such as growth and remodelling behaviours that may occur in the biological tissue following the DCB intervention, as well as the effect of the drug in the inhibition of neointimal proliferation. For instance, other modelling works focussed on the biological species in the arterial tissue and the effect of drug on them, proposing a time-dependent alteration of the density of the cell population and thus the density of drug receptors [80, 85]. Moreover, the modelling of cell proliferation may inform the process of arterial remodelling post-drug delivery therapy, also altering the artery geometry. This was done at discrete time intervals in [75]. However, while these studies incorporated biological aspects, they lacked an in-depth representation of the deployment procedure, such as presented in Chapter 5 of this thesis. Future work may combine the novel modelling of DCB deployment and delivery process presented here with the central biological aspect of the problem: cell proliferation and the effect of antiproliferative drugs on it. This endeavour could be implemented as an additional Level to the model, such as "Level 4: Remodelling". Hypo-

thetically, Level 4 could feedback information to Level 1, updating arterial wall geometry, and to Level 3, updating the binding site density. The simplifying assumption of media-only binding may also be questioned in future studies.

Another possible implication of cell proliferation is the healing of the denuded endothelium, which notably remained denuded for the entirety of the 28-day simulation. This could represent a restoration of the endothelium, reverting its boundary conditions to those of an intact endothelium.

As the current model's focus is on the drug delivery and subsequent distribution of drug in the tissue, these simplifications are assumed valid. Moreover, the time frame of 28 days considered in the simulation may be short for observing a considerable arterial remodelling phenomenon. Lingering post-deployment mechanical and biological effects can be the subject of future studies.

On disease

Another crucial simplification in the artery model is the absence of disease or stenosis. As the vessel commonly targeted with endovascular intervention and drug therapy suffers from severe atherosclerotic disease or in-stent restenosis, this configures a highly idealised scenario. However, two main arguments can be made: (I) before DCB utilisation, the vessel ideally undergoes lesion preparation, a technique for clearing the lumen of excessive obstructive plaque, and (II) preclinical studies often test drug delivery on healthy porcine arteries. Since the available preclinical data used to inform the modelling came from *in vivo* porcine studies with healthy subjects, the latter argument is pertinent.

The modelling of disease considering different types of plaque is the scope for future studies. A preliminary modelling study was performed considering heterogenous lesion composition over a cross-sectional artery, using virtual histology intravascular ultrasound (VH IVUS) [138]. While this work was ongoing, Sarifuddin and Mandal [74] published a pertinent work on the same subject. However, the relevance of including severe disease in a DCB-only simulation also deserves questioning. Because drug delivery from DCBs is recommended after optimal lesion preparation, clinicians may avoid DCB-only procedures depending on the lesion severity — and then recur to lesion preparation to alleviate it, as advised by DCB consensus groups in [45] and [30].

Levels

The design of a system of Levels was immensely helpful to (I) maintain and develop the model in an organised fashion, (II) provide a comprehensive explanation of the complex multiphysics model structure, and (III) facilitate further model development in the sense that new "Levels" can be added.

Each level can operate independently in a somewhat modular fashion as long as sufficient input is provided. During model development, this permitted the execution of faster test simulations with only part of the model enabled. For instance, only Level 1 is required to test the deformation physics.

Parameter optimisation

It is envisaged that the model developed in this work be used as a design development tool. Currently, a single simulation of DCB deployment followed by 28 days of drug distribution expends approximately 6 hours of computation time. The computational burden of the simulation limits any sensitivity and uncertainty analysis of model output to variation in the model inputs. Some techniques, such as statistical emulation, GPU computing, and surrogate modelling, may substantially improve computation speed and be imperative to permit feasible parametric exploration and optimisation. In one preliminary study of co-authorship, a simple drug delivery model underwent parameter estimation to optimise the safety and efficacy indicators of the drug therapy [119]. For example, the requirement of having sRS as high as possible during the therapeutic window was quantified as the area under the receptor saturation curve and was used as an optimisation constraint alongside a maximum tolerable value of DC. The statement of this study exemplifies the concept of expanding the model's application as a tool for design development. Ideally, future research will bring such models to the clinic as a decision-making tool, combining real-time imaging and fast simulations to provide timely insights to clinicians.

Significance of results

The usefulness of the model is given in terms of the computational results obtained. The key significance of the findings is preliminary mechanistic insights into the effect of DCB deployment on drug delivery and subsequent drug distribution in the tissue. Contact interaction between the DCB and the artery actively influences drug delivery and retention and must be explored in detail.

Remarkably, the present model enabled the generation of a non-prescribed drug influx, dependent on the multiple procedural parameters of the simulation of DCB deployment. This builds upon the drug flux expressions of [66] and [67], which were derived experimentally and fitted to exponential behaviours, previously used in the simplified representation of drug delivery from DCB in Chapter 3. Figure 5.34 compares the three expressions over the brief time window of DCB drug delivery.

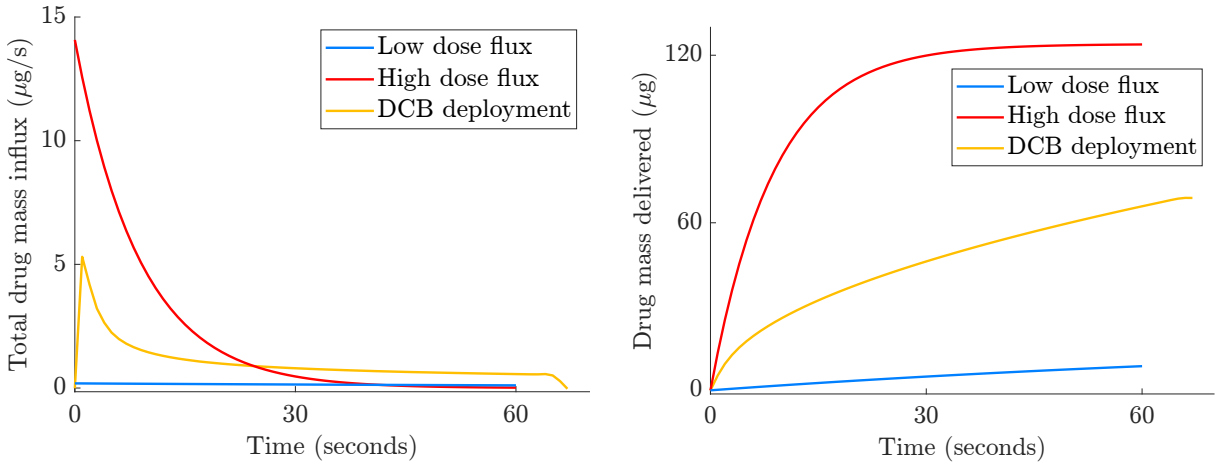

Figure 5.34: Comparison of drug delivery due to the prescribed drug flux expressions used in Chapter 3 ("Low dose" and "High dose") and resultant from the DCB deployment model of Chapter 5, in terms of mass-based (a) drug delivery rate and (b) cumulative drug delivered. The latter plot results from the temporal integration of the former.

The comparison between these drug release behaviours instigates pertinent discussion points. For example: (I) the length of drug delivery was fixed to be uniform over the denuded endothelium ($\Gamma_{\text{ET, de}}$) in Chapter 3, then became the variable contact length resultant from the simulation of DCB deployment in Chapter 5; (II) the delivery duration was fixed at 60 seconds, then, likewise, became dependent on contact from the DCB deployment simulation, which, for the baseline parameters, is about 10% larger due to premature contact before full inflation pressure is reached; (III) the magnitude of drug delivered when having DCB deployment is somewhat intermediate to the "Low dose" and "High dose" cases, showing reasonably comparable results. In future work, the drug flux obtained from the more sophisticated simulation of DCB deployment may be prescribed to the simpler model. This would allow observation of the relevance of having time-dependent deformation and their underlying multiphysical effects included in the simulation.

The percentage-based drug release profile, presented in Figure 5.21, may be compared to preclinical studies. One example reports that approximately 10% to 15% of the total DCB dose is immediately transferred, using early paclitaxel DCBs in healthy porcine coronary arteries [43]. Similarly, others reported approximate values of 16% and 14% of the total dose transferred, respectively with paclitaxel and sirolimus DCBs [36, 42]. The drug transfer mechanism proposed in the current model caused a noticeably higher drug release than these experimental studies (22% – 32%). The equivalence of procedural parameters is required to allow a clear comparison.

Since the models of Chapters 3 and 5 were based on a healthy porcine model, it is pertinent to compare their results with a reference animal study. For instance, the *in silico* results of DC obtained as continuous curves throughout the time-dependent simulations can be compared

with similar measurements taken as discrete time points in preclinical *in vivo* testing. Figure 5.35 presents a single example of comparison, provided by [81].

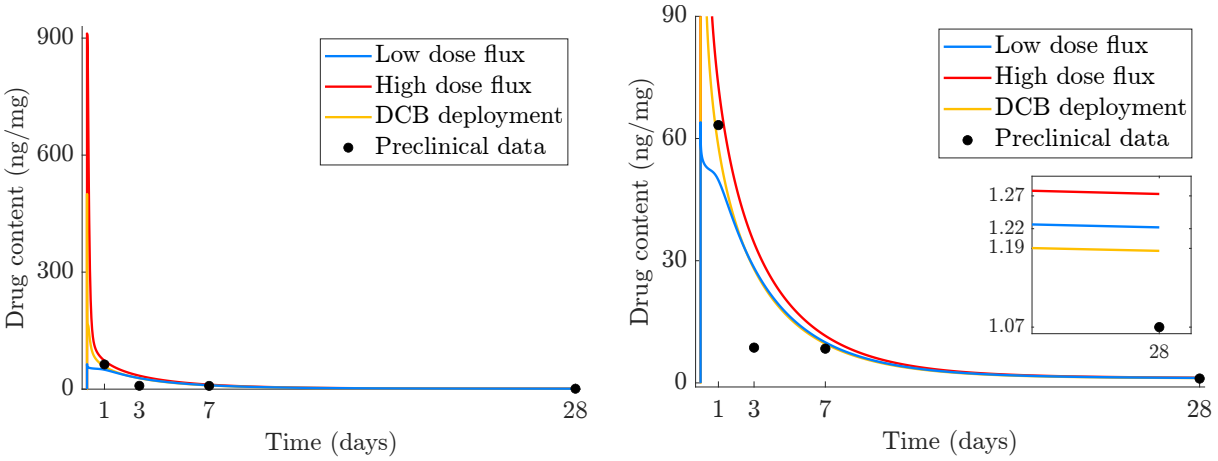

(a) (b)

Case	DC (ng/mg)			
	1 day	3 days	7 days	28 days
Low dose flux	49.8	28.3	9.95	1.22
High dose flux	72.9	34.4	11.56	1.27
DCB deployment	58.0	28.0	9.61	1.19
Preclinical data	63.3	8.66	8.41	1.07

(c)

Figure 5.35: Comparison of the DC results obtained *in silico*, in Chapter 3 using the prescribed drug fluxes ("Low dose flux" and "High dose flux") and through the "DCB deployment" simulation, with preclinical studies using a healthy porcine model ("Preclinical data"). Subfigure (a) depicts the total DC behaviour, while (b) magnifies a lower DC range and the final results at 28 days. The table in (c) compares the DC values at each of the instants of available preclinical data.

Although brief, due to the modelling character of this work, the comparison with a reference *in vivo* model permits noteworthy points of discussion:

1. The results featured as "Preclinical data" are part of a preliminary animal study using an early iteration of Biosensors's BA9™ DCB. Six balloons were deployed to obtain a single time point ($n = 6$), totalling twenty-four DCBs in eight healthy mini-pigs for the pharmacokinetic cohort featured in this work. The uncertainty of the measurements, in the form of error bars, was not available for this comparison.

2. Sufficient similarity between human and porcine coronary artery geometries must be assumed to allow comparison between results. Moreover, the animal study tested multiple

arteries per animal and different artery types (right coronary artery, left anterior descending, and/or circumflex branch of the left coronary artery).

3. The study that generated this preclinical dataset used Biolimus A9™ as the drug, also known as umirolimus. It is an analogue drug obtained from the modification of a chemical branch of sirolimus [81, 100]. While it may have different transport and retention properties than sirolimus, the current work assumes a hypothetical similarity between the two drugs for modelling convenience. Nevertheless, the model made an effort to maintain the generality of the drug type, and future studies may update drug parameters freely.

4. Animal experiments are often limited by the extraction of data points, for practical reasons. The participating animals need to be sacrificed, and the tested arteries harvested for measurement. While the four discrete time points from the example above are somewhat capable of describing the DC behaviour over a large period, they lack information at early times, such as the acute early peak followed by abrupt decay — which is crucial for understanding the rapid drug delivery from the DCB.

5. At $t = 1$ day, the "DCB deployment" best resembled the preclinical results. The method by which the "Low dose" and "High dose" fluxes were derived was questioned in Chapter 3, and may not be representative of a contact-based drug transfer.

6. Over time, depletion of drug due to wash-off causes DC levels to converge to similar values, around 1 ng/mg.

7. While these preclinical results are preliminary, they suggest a plateau between 3 and 7 days. The "Low dose flux" best depicted this behaviour, despite the insufficient drug released. It may be inferred that drug tissue levels are expected to reach high amounts, decay within 3 days, and then substantially slow down its decaying rate. The drug transport and retention parameters in the model may be probed to investigate such mechanisms.

8. While the time frame of the comparison proposed was 28 days, the animal study also observed the behaviour of drug retention in the tissue up to 180 days after the procedure. The simulation time range could be adjusted to reproduce this analysis.

9. *In vivo* as well as *in silico*, the results showed drug retention 28 days after the procedure, indicating therapeutic efficacy.

Despite substantial limitations and idealisations, the model broadly captures the DC behaviour of experimental results internally available within the collaborating industrial partner. The magnitude of drug delivery evaluated in the multiphysics model of DCB deployment has shown promise. However, before further comparisons with multiple studies and exploration of particular procedural parameters are carried out, the model must be scrutinised thoroughly.

The study of the time-dependent drug distribution with different scenarios is a remarkable advantage conferred by *in silico* experimentation. The model presented was capable of providing mechanistic insights into the effect of varying procedural parameters — inflation pressure, inflation duration, and drug load — on the drug release profile and key indicators DC and sRS. This outlined the importance of procedural parameters on the outcome of drug delivery from DCB and illustrated the balance between the safety and efficacy of the therapy. Due to the strong specific binding behaviour, drug concentration levels in the tissue tend towards the specific binding site density value at later times. That is, the tissue retains approximately the drug mass required to fully saturate the specific receptors in the media, whilst drug excess tends to be washed away by the luminal and perivascular sinks.

An exercise relating the concepts of drug content and receptor saturation is proposed. Considering the specifically-bound drug capacity in the current model geometry:

$$\begin{aligned} m_{b^{\mathrm{s}}_{\mathrm{max}}} &= M_{\mathrm{sir}} \int_{\Omega_{\mathrm{med}}} b^{\mathrm{s}}_{\mathrm{max}} \, d\Omega_{\mathrm{med}} \\ &\approx 196.9 \text{ ng}, \end{aligned} \tag{5.7.2}$$

where M_{sir} is the molar mass of the drug, in g/mol, $b^{\mathrm{s}}_{\mathrm{max}}$ is the specific binding site density, in mol/m^3, and the spatial integration of the media domain results in its tissue volume, in m^3.

That is, Equation 5.7.2 states that the specific binding sites in the therapeutic domain can retain up to 196.9 ng of drug. As shown previously in Table 5.15, it is sensible to assume a predominance of drug retention to specific binding sites at later times. Assuming a late scenario where this amount of drug mass is concentrated in the media layer purely in specifically-bound phase, which fully saturates the specific binding sites ($sRS = 100\%$), a resultant drug content is calculated:

$$\begin{aligned} DC &= \frac{m_{b^{\mathrm{s}}_{\mathrm{max}}}}{m_{\mathrm{tissue}}} \\ &\approx 1.45 \, \frac{\text{ng}}{\text{mg}}, \end{aligned} \tag{5.7.3}$$

where $m_{\mathrm{tissue}} = m_{\mathrm{int}} + m_{\mathrm{med}} + m_{\mathrm{adv}}$, each given by the spatial integration of the respective domain times the tissue density.

Endovascular drug delivery efficacy is often related to the ability to retain the drug delivered in the arterial tissue during a sufficient time window, to supply the target cell receptors with sustained levels of drug and induce its desired antiproliferative treatment effect — a persistent inhibition of hyperplasia [64, 68, 78]. The DC value at full specific saturation resembles the therapeutic limit of 1 ng/mg, targeted in [33] and [47]. This suggests that the therapeutic limit of DC may be intrinsically related to the concept of receptor saturation.

In the experimentation of procedural parameters showcased in this work, only a marginal

improvement in the therapy efficacy was noticed when increasing the amount of drug delivered. This suggests that (I) the drug mass delivered may be sufficient to saturate the target receptors, exemplified by Case Study 3 with a smaller drug load ($\frac{1}{2}\ m_0$), which tackles the question of how much drug is necessary to promote sufficiently high sRS levels throughout the therapeutic window. And, that (II) drug distribution after DCB delivery may be governed by other sets of parameters, such as drug-related parameters, and slower pharmacokinetics may be required to reach higher drug retention. That is, so the drug is "absorbed" more slowly into the vessel wall. Different parameter types and ranges can be investigated to understand why certain DCBs achieve greater drug content values at later times [42]. Points (I) and (II) are entwined to determine the outcome of drug delivery. Therefore, the understanding of receptor binding mechanics is crucial for designing effective drug delivery.

Chapter 6

Conclusion

Despite the eventual modelling challenges, this work has shown novel advances in DCB modelling. Chapter 3 appreciated the multiphysics aspect of the problem and discovered that the temporary increase in transmural pressure during DCB delivery has a considerable effect on the drug distribution in the tissue. Moreover, it demonstrated that the previous approaches of including balloon inflation pressure were flawed, showing that the current state of the literature presents room to grow.

Chapter 4 reproduced a DCB testing procedure *in silico*, yielding a novel DCB model and insights on how DCBs release drug. Although the model has been calibrated to the single experimental data set available, its simulation largely captured the behaviour of the phenomenon of interest and shall fulfil its validation against different scenarios in future studies.

Chapter 5 showed the feasibility of time-dependent DCB simulations with simultaneous deformation, contact, and drug delivery. This work built multiphysics models of increasing complexity, developed within an original system of Levels, culminating in the first reported model that incorporates balloon deployment and drug delivery simultaneously and included a representation of the DCB. Remarkably, in this model, no parameter was adjusted or calibrated a posteriori to fit results into the experimental data available, which originated from animal studies at the preclinical stage provided by the collaborating company. Still, the model was able to capture the trend of drug content in the tissue for a therapeutic window of 28 days. All this progress paves the way for using the *in silico* modelling framework developed in the real world to help design effective implantless drug delivery that provides steady, sustained drug levels throughout the treatment duration.

Considerations must be made before these promising outcomes. Although this work represents a significant mathematical modelling and computational challenge, ultimately *in silico* models need to be validated before they can be used in a truly predictive sense. In subsequent efforts, the present model hopes to be validated against experimental and clinical data — as per the example of many of the studies referenced in Chapter 2, which were instrumental in advancing the technology of endovascular drug delivery because they combined computational and the

standard experimental practices augmenting each other. Moreover, the model produced can potentially be used to make the best of existing DCBs, by exploring the performance of different commercial devices regarding several conditions e.g. inflation pressure and duration, drug dose and type, balloon-to-artery ratio, etc. and helping inform procedural parameters.

The model limitations are numerous yet justifiable to allow feasible simulations of the environment of endovascular drug delivery with the resources made available for the present work. These limitations have been described in each of the Discussion Sections throughout the thesis, and, concisely, are mainly related to (I) the simplifying assumptions of the DCB and arterial wall geometries, (II) the physiological arterial surroundings e.g. haemodynamics, and (III) the effect of the drug in the tissue beyond its spatiotemporal distribution. In the future, the model may be developed according to the necessity to depict particular additional aspects of the DCB procedure. As discussed in the previous Section 5.7, coating adhesion, patient-specific artery geometry, and arterial remodelling are candidates to be incorporated. Although it is not the model's aspiration to be all-encompassing, and modelling parsimony must be regarded, the depiction of complex phenomena demands further efforts.

Concluding, *in silico* modelling and simulation offer a powerful and convenient platform for medical device development and decision making. Future studies may achieve further validation, increase realism, focus on different procedural and design parameters, and be used as digital twins alongside real experiments and procedures. The general impact of the work should be perceived in how the industry designs drug delivery devices, and in how they are used in the clinic — by prompting the application of *in silico* tools alongside the traditional preclinical and clinical experimentation, and to help inform clinical procedures.

Acknowledgements

Biosensors International provided technical information in addition to a contribution towards University tuition fees and software consumables.

Bibliography

[1] George EP Box. Robustness in the strategy of scientific model building. In *Robustness in statistics*, pages 201–236. Elsevier, 1979.

[2] World Health Organization. Global Health Estimates 2020: Deaths by Cause, Age, Sex, by Country and by Region, 2000-2019, Geneva, World Health Organization; 2020.

[3] Robert A Byrne, Gregg W Stone, John Ormiston, and Adnan Kastrati. Coronary balloon angioplasty, stents, and scaffolds. *The Lancet*, 390(10096):781–792, 2017.

[4] Michael R Lepore, Moises Yoselevitz, W Charles Sternbergh, and Samuel R Money. Minimally invasive vascular techniques. *Ochsner Journal*, 2(3):145–152, 2000.

[5] Patrick W Serruys, Hector M Garcia-Garcia, and Yoshinobu Onuma. From metallic cages to transient bioresorbable scaffolds: change in paradigm of coronary revascularization in the upcoming decade? *European heart journal*, 33(1):16–25, 2012.

[6] Javaid Iqbal, Julian Gunn, and Patrick W Serruys. Coronary stents: historical development, current status and future directions. *British medical bulletin*, 106(1), 2013.

[7] Sean McGinty. A decade of modelling drug release from arterial stents. *Mathematical biosciences*, 257:80–90, 2014.

[8] Dario Buccheri and Bernardo Cortese. *History of Drug-Coated Balloons*, pages 9–13. Springer International Publishing, Cham, 2019.

[9] Farhad Rikhtegar Nezami, Lambros S Athanasiou, and Elazer R Edelman. Endovascular drug-delivery and drug-elution systems. In *Biomechanics of Coronary Atherosclerotic Plaque*, pages 595–631. Elsevier, 2021.

[10] Trevor Simard, Benjamin Hibbert, F Daniel Ramirez, Michael Froeschl, Yong-Xiang Chen, and Edward R O'Brien. The evolution of coronary stents: a brief review. *Canadian Journal of Cardiology*, 30(1):35–45, 2014.

[11] Michael Haude, Raimund Erbel, Hassan Issa, and Jürgen Meyer. Quantitative analysis of elastic recoil after balloon angioplasty and after intracoronary implantation of balloon-expandable palmaz-schatz stents. *Journal of the American College of Cardiology*, 21(1): 26–34, 1993.

[12] Raimund Erbel, Michael Haude, Hans W Höpp, Damian Franzen, Hans Jürgen Rupprecht, Bernd Heublein, Klaus Fischer, Peter de Jaegere, Patrick Serruys, Wolfgang Rutsch, et al. Coronary-artery stenting compared with balloon angioplasty for restenosis after initial balloon angioplasty. *New England Journal of Medicine*, 339(23):1672–1678, 1998.

[13] Gary S Roubin, Adam D Cannon, SK Agrawal, PJ Macander, LS Dean, WA Baxley, and J Breland. Intracoronary stenting for acute and threatened closure complicating percutaneous transluminal coronary angioplasty. *Circulation*, 85(3):916–927, 1992.

[14] National Heart, Lung, and National Institutes of Health. Blood Institute; U.S. Department of Health Human Services. What are stents? URL `https://www.nhlbi.nih.gov/health/stents`. Accessed: December 2019.

[15] Alistair K McQueen. *Understanding how anti–proliferative drug modulates arterial healing following stent deployment*. PhD thesis, University of Glasgow, 2022.

[16] A Michael Lincoff, Eric J Topol, and Stephen G Ellis. Local drug delivery for the prevention of restenosis. fact, fancy, and future. *Circulation*, 90(4):2070–2084, 1994.

[17] J Eduardo Sousa, Marco A Costa, Alexandre Abizaid, Andrea S Abizaid, Fausto Feres, Ibraim MF Pinto, Ana C Seixas, Rodolfo Staico, Luiz A Mattos, Amanda GMR Sousa, et al. Lack of neointimal proliferation after implantation of sirolimus-coated stents in human coronary arteries: a quantitative coronary angiography and three-dimensional intravascular ultrasound study. *Circulation*, 103(2):192–195, 2001.

[18] Raúl Moreno. Drug-eluting stents and other anti-restenosis devices. *Revista Española de Cardiología (English Edition)*, 58(7):842–862, 2005.

[19] Craig Bonsignore. A decade of evolution in stent design. In *Proceedings of the International Conference on Shape Memory and Superelastic Technologies*, pages 519–528, 2003.

[20] Xiaoxiang Zhu and Richard D Braatz. A mechanistic model for drug release in plga biodegradable stent coatings coupled with polymer degradation and erosion. *Journal of Biomedical Materials Research Part A*, 103(7):2269–2279, 2015.

[21] Sean McGinty, Sean McKee, Roger M Wadsworth, and Christopher McCormick. Modeling arterial wall drug concentrations following the insertion of a drug-eluting stent. *SIAM Journal on Applied Mathematics*, 73(6):2004–2028, 2013.

[22] Gennaro Giustino, Antonio Colombo, Anton Camaj, Keisuke Yasumura, Roxana Mehran, Gregg W Stone, Annapoorna Kini, and Samin K Sharma. Coronary in-stent restenosis: Jacc state-of-the-art review. *Journal of the American College of Cardiology*, 80(4):348–372, 2022.

[23] Evan Shlofmitz, Micaela Iantorno, and Ron Waksman. Restenosis of drug-eluting stents: a new classification system based on disease mechanism to guide treatment and state-of-the-art review. *Circulation: Cardiovascular Interventions*, 12(8):e007023, 2019.

[24] Philip Urban, Alex Abizaid, Bernard Chevalier, Samantha Greene, Ian Meredith, Marie-Claude Morice, and Stuart Pocock. Rationale and design of the leaders free trial: A randomized double-blind comparison of the biofreedom drug-coated stent vs the gazelle bare metal stent in patients at high bleeding risk using a short (1 month) course of dual antiplatelet therapy. *American heart journal*, 165(5):704–709, 2013.

[25] Philip Urban, Ian T Meredith, Alexandre Abizaid, Stuart J Pocock, Didier Carrié, Christoph Naber, Janusz Lipiecki, Gert Richardt, Andres Iñiguez, Philippe Brunel, et al. Polymer-free drug-coated coronary stents in patients at high bleeding risk. *New England Journal of Medicine*, 373(21):2038–2047, 2015.

[26] Dietmar Schranz, Peter Zartner, Ina Michel-Behnke, and Hakan Akintürk. Bioabsorbable metal stents for percutaneous treatment of critical recoarctation of the aorta in a newborn. *Catheterization and Cardiovascular Interventions*, 67(5):671–673, 2006.

[27] Huda Hamid and John Coltart. 'miracle stents'-a future without restenosis. *McGill Journal of Medicine: MJM*, 10(2):105, 2007.

[28] Andreas H Mahnken. Ct imaging of coronary stents: past, present, and future. *International Scholarly Research Notices*, 2012, 2012.

[29] Enda L Boland, Connor J Shine, Nicola Kelly, Caoimhe A Sweeney, and Peter E McHugh. A review of material degradation modelling for the analysis and design of bioabsorbable stents. *Annals of biomedical engineering*, 44:341–356, 2016.

[30] Raban V Jeger, Simon Eccleshall, Wan Azman Wan Ahmad, Junbo Ge, Tudor C Poerner, Eun-Seok Shin, Fernando Alfonso, Azeem Latib, Paul J Ong, Tuomas T Rissanen, et al. Drug-coated balloons for coronary artery disease: third report of the international dcb consensus group. *Cardiovascular Interventions*, 13(12):1391–1402, 2020.

[31] Yariv Gerber, Charanjit S Rihal, Thoralf M Sundt, Jill M Killian, Susan A Weston, Terry M Therneau, and Véronique L Roger. Coronary revascularization in the community: a population-based study, 1990 to 2004. *Journal of the American College of Cardiology*, 50(13):1223–1229, 2007.

[32] Robert A Byrne, Michael Joner, Fernando Alfonso, and Adnan Kastrati. Drug-coated balloon therapy in coronary and peripheral artery disease. *Nature Reviews Cardiology*, 11(1):13–23, 2014.

[33] Juan F Granada, Armando Tellez, William R Baumbach, Brendan Bingham, Yen-Fang Keng, Jeffrey Wessler, Gerard Conditt, Jennifer McGregor, Gregg Stone, Greg L Kaluza, et al. In vivo delivery and long-term tissue retention of nano-encapsulated sirolimus using a novel porous balloon angioplasty system. *Eurointervention: Journal of Europcr in Collaboration with the Working Group on Interventional Cardiology of the European Society of Cardiology*, 12(6):740–747, 2016.

[34] Charan Yerasi, Brian C Case, Brian J Forrestal, Rebecca Torguson, William S Weintraub, Hector M Garcia-Garcia, and Ron Waksman. Drug-coated balloon for de novo coronary artery disease: Jacc state-of-the-art review. *Journal of the American College of Cardiology*, 75(9):1061–1073, 2020.

[35] *Drug-Coated Balloons: Applications in Interventional Cardiology*. Springer International Publishing, 2019.

[36] Bruno Scheller, Ulrich Speck, Claudia Abramjuk, Ulrich Bernhardt, Michael Bohm, and Georg Nickenig. Paclitaxel balloon coating, a novel method for prevention and therapy of restenosis. *Circulation*, 110(7):810–814, 2004.

[37] Ron Waksman and Rajbabu Pakala. Drug-eluting balloon: the comeback kid? *Circulation: Cardiovascular Interventions*, 2(4):352–358, 2009.

[38] Bernardo Cortese, Sergio Berti, Giuseppe Biondi-Zoccai, Antonio Colombo, Ugo Limbruno, Francesco Bedogni, Alberto Cremonesi, Pedro Leon Silva, and Gregory A Sgueglia. Drug-coated balloon treatment of coronary artery disease: a position paper of the italian society of interventional cardiology. *Catheterization and Cardiovascular Interventions*, 83(3):427–435, 2014.

[39] Franz X Kleber, Detlef G Mathey, Harald Rittger, Bruno Scheller, et al. How to use the drug-eluting balloon: recommendations by the german consensus group. *EuroIntervention*, 7(Suppl K):K125–K128, 2011.

[40] Ron Waksman, Antonio Serra, Joshua P Loh, FT Malik, Rebecca Torguson, Stefanie Stahnke, Rembert Pogge von Strandmann, and Alfredo E Rodriguez. Drug-coated balloons for de novo coronary lesions: results from the valentines ii trial. *EuroIntervention*, 9(5):613–619, 2013.

[41] Patrick W. Serruys and Kuniaki Takahashi. *From Drug-Eluting Balloon to Drug-Coated Balloon ... to Eradication of Intracoronary Metal, a New Ending Story*, pages 1–7. Springer International Publishing, Cham, 2019.

[42] Yvonne Patricia Clever, Daniel Peters, Jorge Calisse, Stephanie Bettink, Madeleine-Caroline Berg, Christian Sperling, Michael Stoever, Bodo Cremers, Bettina Kelsch, Michael Böhm, et al. Novel sirolimus–coated balloon catheter: in vivo evaluation in a porcine coronary model. *Circulation: Cardiovascular Interventions*, 9(4):e003543, 2016.

[43] William A Gray and Juan F Granada. Drug-coated balloons for the prevention of vascular restenosis. *Circulation*, 121(24):2672–2680, 2010.

[44] Alexandre Abizaid, Martin B. Leon, and Antonio Colombo. URL `https://www.pcronline.com/Cases-resources-images/Resources/Educational-interviews/2019/EuroPCR/DCB-technology`. Interview at EuroPCR 2019.

[45] Franz X Kleber, Harald Rittger, Klaus Bonaventura, Uwe Zeymer, Jochen Wöhrle, Raban Jeger, Benny Levenson, Sven Möbius-Winkler, Leonhard Bruch, Dieter Fischer, et al. Drug-coated balloons for treatment of coronary artery disease: updated recommendations from a consensus group. *Clinical Research in Cardiology*, 102:785–797, 2013.

[46] Mark Rosenberg, Matthias Waliszewski, Kenneth Chin, Wan Azman Wan Ahmad, Giuseppe Caramanno, Diego Milazzo, Amin Ariff Nuruddin, Houng Bang Liew, Oteh Maskon, Pierre Aubry, et al. Prospective, large-scale multicenter trial for the use of drug-coated balloons in coronary lesions: The dcb-only all-comers registry. *Catheterization and cardiovascular interventions*, 93(2):181–188, 2019.

[47] Bryan P Traynor, Sean Fitzgerald, Fernando Alfonso, Peter O'Kane, Manel Sabaté, Ralph Tölg, Jasper Trevelyan, Joo-Yong Hahn, Darren Mylotte, Jochen Wöhrle, et al. Design and rationale of a prospective, randomized, non-inferiority trial to determine the safety and efficacy of the Biolimus A9™ drug coated balloon for the treatment of in-stent restenosis: First-in-man trial (REFORM). *Cardiovascular Revascularization Medicine*, 2023.

[48] Boston Scientific. URL `https://www.bostonscientific.com/en-EU/products/balloons--drug-coated/agent.html`. Acessed: March 2024.

[49] Boston Scientific Receives FDA Approval for the AGENT™ Drug-Coated Balloon. URL `https://www.prnewswire.com/news-releases/boston-scientific-receives-fda-approval-for-the-agent-drug-coated-balloon-302076861.html`. Acessed: March 2024.

[50] Robert W Yeh, William Bachinsky, Robert Stoler, Cinthia Bateman, Jennifer A Tremmel, J Dawn Abbott, Suhail Dohad, Wayne Batchelor, Paul Underwood, Dominic J Allocco, et al. Rationale and design of a randomized study comparing the agent drug coated balloon to plain old balloon angioplasty in patients with in-stent restenosis. *American Heart Journal*, 241:101–107, 2021.

[51] Bernardo Cortese, Harkaran Kalkat, Gurbir Bathia, and Sandeep Basavarajaiah. The evolution and revolution of drug coated balloons in coronary angioplasty: An up-to-date review of literature data. *Catheterization and Cardiovascular Interventions*, 102(6):1069–1077, 2023.

[52] Marco Ferrone and Juan F Granada. Current technical challenges and the future of drug-coated balloons. *Drug-Coated Balloons: Applications in Interventional Cardiology*, pages 227–234, 2019.

[53] Tarek Shazly, William M Torres, Eric A Secemsky, Vipul C Chitalia, Farouc A Jaffer, and Vijaya B Kolachalama. Understudied factors in drug-coated balloon design and evaluation: A biophysical perspective. *Bioengineering & Translational Medicine*, 8(1):e10370, 2023.

[54] Elazer R Edelman, David H Adams, and Morris J Karnovsky. Effect of controlled adventitial heparin delivery on smooth muscle cell proliferation following endothelial injury. *Proceedings of the National Academy of Sciences*, 87(10):3773–3777, 1990.

[55] Christopher J Creel, Mark A Lovich, and Elazer R Edelman. Arterial paclitaxel distribution and deposition. *Circulation research*, 86(8):879–884, 2000.

[56] Stefano Morlacchi and Francesco Migliavacca. Modeling stented coronary arteries: where we are, where to go. *Annals of biomedical engineering*, 41:1428–1444, 2013.

[57] Mark A Lovich and Elazer R Edelman. Computational simulations of local vascular heparin deposition and distribution. *American Journal of Physiology-Heart and Circulatory Physiology*, 271(5):H2014–H2024, 1996.

[58] Chao-Wei Hwang, David Wu, and Elazer R Edelman. Physiological transport forces govern drug distribution for stent-based delivery. *Circulation*, 104(5):600–605, 2001.

[59] Andrew D Levin, Neda Vukmirovic, Chao-Wei Hwang, and Elazer R Edelman. Specific binding to intracellular proteins determines arterial transport properties for rapamycin and paclitaxel. *Proceedings of the National Academy of Sciences*, 101(25):9463–9467, 2004.

[60] Paolo Zunino. Multidimensional pharmacokinetic models applied to the design of drug-eluting stents. *Cardiovascular Engineering: An International Journal*, 4:181–191, 2004.

[61] A Rami Tzafriri, Andrew D Levin, and Elazer R Edelman. Diffusion-limited binding explains binary dose response for local arterial and tumour drug delivery. *Cell proliferation*, 42(3):348–363, 2009.

[62] Franz Bozsak, Jean-Marc Chomaz, and Abdul I Barakat. Modeling the transport of drugs eluted from stents: physical phenomena driving drug distribution in the arterial wall. *Biomechanics and modeling in mechanobiology*, 13:327–347, 2014.

[63] Javier Escuer, Martina Cebollero, Estefania Pena, Sean McGinty, and Miguel A Martínez. How does stent expansion alter drug transport properties of the arterial wall? *Journal of the Mechanical Behavior of Biomedical Materials*, 104:103610, 2020.

[64] Abraham R Tzafriri, Adam Groothuis, G Sylvester Price, and Elazer R Edelman. Stent elution rate determines drug deposition and receptor-mediated effects. *Journal of Controlled Release*, 161(3):918–926, 2012.

[65] Sean McGinty and Giuseppe Pontrelli. On the role of specific drug binding in modelling arterial eluting stents. *Journal of mathematical chemistry*, 54:967–976, 2016.

[66] Vijaya B Kolachalama, Stephen D Pacetti, Joseph W Franses, John J Stankus, Hugh Q Zhao, Tarek Shazly, Alexander Nikanorov, Lewis B Schwartz, Abraham R Tzafriri, and Elazer R Edelman. Mechanisms of tissue uptake and retention in zotarolimus-coated balloon therapy. *Circulation*, 127(20):2047–2055, 2013.

[67] Karthic Anbalakan, Han Wei Toh, Hui Ying Ang, Martin Lindsay Buist, and Hwa Liang Leo. Assessing the influence of atherosclerosis on drug coated balloon therapy using computational modelling. *European Journal of Pharmaceutics and Biopharmaceutics*, 158:72–82, 2021.

[68] Abraham R Tzafriri, Sahil A Parikh, and Elazer R Edelman. Taking paclitaxel coated balloons to a higher level: Predicting coating dissolution kinetics, tissue retention and dosing dynamics. *Journal of Controlled Release*, 310:94–102, 2019.

[69] Abraham R Tzafriri, Benny Muraj, Fernando Garcia-Polite, Antonio G Salazar-Martín, Peter Markham, Brett Zani, Anna Spognardi, Mazen Albaghdadi, Steve Alston, and Elazer R Edelman. Balloon-based drug coating delivery to the artery wall is dictated

by coating micro-morphology and angioplasty pressure gradients. *Biomaterials*, 260: 120337, 2020.

[70] VV Shukla, PM Padole, S Deshpande, and HM Mardikar. Assessment of vascular injury during stent placement using contact mechanics. *International Journal for Computational Vision and Biomechanics*, 2010:3, 2010.

[71] Efstathios Stratakos, Luca Antonini, Gianluca Poletti, Francesca Berti, Abraham R Tzafriri, Lorenza Petrini, and Giancarlo Pennati. Investigating balloon-vessel contact pressure patterns in angioplasty: In silico insights for drug-coated balloons. *Annals of Biomedical Engineering*, 51(12):2908–2922, 2023.

[72] Javier Escuer, André Fensterseifer Schmidt, Estefania Pena, Miguel A Martínez, and Sean McGinty. Mathematical modelling of endovascular drug delivery: Balloons versus stents. *International Journal of Pharmaceutics*, 620:121742, 2022.

[73] Monika Colombo, Anna Corti, Scott Berceli, Francesco Migliavacca, Sean McGinty, and Claudio Chiastra. 3d modelling of drug-coated balloons for the treatment of calcified superficial femoral arteries. *PLoS one*, 16(10):e0256783, 2021.

[74] Sarifuddin and Prashanta Kumar Mandal. Plaque heterogeneity and the spatial distributions of its components dictate drug-coated balloon therapy. *Scientific Reports*, 14(1): 4412, 2024.

[75] Anna Corti, Claudio Chiastra, Monika Colombo, Marc Garbey, Francesco Migliavacca, and Stefano Casarin. A fully coupled computational fluid dynamics–agent-based model of atherosclerotic plaque development: multiscale modeling framework and parameter sensitivity analysis. *Computers in biology and medicine*, 118:103623, 2020.

[76] Our World in Data. URL `https://ourworldindata.org/grapher/transistors-per-microprocessor`. Accessed: March 2024.

[77] Cardiovascular News. URL `https://cardiovascularnews.com/reform-study-results-biolimus-dcb/`. Accessed: March 2024.

[78] Abraham R Tzafriri and Elazer R Edelman. Endovascular drug delivery and drug elution systems: first principles. *Interventional cardiology clinics*, 5(3):307, 2016.

[79] Pujith RS Vijayaratnam, John A Reizes, and Tracie J Barber. Flow-mediated drug transport from drug-eluting stents is negligible: Numerical and in-vitro investigations. *Annals of Biomedical Engineering*, 47:878–890, 2019.

[80] Alistair McQueen, Javier Escuer, André Fensterseifer Schmidt, Ankush Aggarwal, Simon Kennedy, Christopher McCormick, Keith Oldroyd, and Sean McGinty. An intricate

interplay between stent drug dose and release rate dictates arterial restenosis. *Journal of Controlled Release*, 349:992–1008, 2022.

[81] Personal correspondence with Biosensors International Group, Ltd., 2021–2024.

[82] Javier Escuer, Miguel A Martínez, Sean McGinty, and Estefanía Peña. Mathematical modelling of the restenosis process after stent implantation. *Journal of the Royal Society Interface*, 16(157):20190313, 2019.

[83] Javier Escuer, Irene Aznar, Christopher McCormick, Estefanía Peña, Sean McGinty, and Miguel A Martínez. Influence of vessel curvature and plaque composition on drug transport in the arterial wall following drug-eluting stent implantation. *Biomechanics and Modeling in Mechanobiology*, 20:767–786, 2021.

[84] J Theodore Dodge Jr, B Greg Brown, Edward L Bolson, and Harold T Dodge. Lumen diameter of normal human coronary arteries. influence of age, sex, anatomic variation, and left ventricular hypertrophy or dilation. *Circulation*, 86(1):232–246, 1992.

[85] Alistair McQueen, Javier Escuer, Ankush Aggarwal, Simon Kennedy, Christopher McCormick, Keith Oldroyd, and Sean McGinty. Do we really understand how drug eluted from stents modulates arterial healing? *International Journal of Pharmaceutics*, 601: 120575, 2021.

[86] Anouchska Autar, Aladdin Taha, Richard van Duin, Ilona Krabbendam-Peters, Dirk J Duncker, Felix Zijlstra, and Heleen MM van Beusekom. Endovascular procedures cause transient endothelial injury but do not disrupt mature neointima in drug eluting stents. *Scientific Reports*, 10(1):2173, 2020.

[87] Ora Kedem and Aharon Katchalsky. Thermodynamic analysis of the permeability of biological membranes to non-electrolytes. *Biochimica et biophysica Acta*, 27:229–246, 1958.

[88] Lisong Ai and K Vafai. A coupling model for macromolecule transport in a stenosed arterial wall. *International journal of heat and mass transfer*, 49(9-10):1568–1591, 2006.

[89] Vera Demarchi Aiello, Paulo S Gutierrez, Márcio JF Chaves, Antonio AB Lopes, Maria L Higuchi, and José AF Ramires. Morphology of the internal elastic lamina in arteries from pulmonary hypertensive patients: a confocal laser microscopy study. *Modern pathology*, 16(5):411–416, 2003.

[90] Giuseppe Vairo, Margherita Cioffi, Riccardo Cottone, Gabriele Dubini, and Francesco Migliavacca. Drug release from coronary eluting stents: a multidomain approach. *Journal of biomechanics*, 43(8):1580–1589, 2010.

[91] Sean McGinty and Giuseppe Pontrelli. On the role of specific drug binding in modelling arterial eluting stents. *Journal of Mathematical Chemistry*, 54:967–976, 2016.

[92] Martin A Wear and Malcolm D Walkinshaw. Determination of the rate constants for the FK506 binding protein/rapamycin interaction using surface plasmon resonance: an alternative sensor surface for ni2+-nitrilotriacetic acid immobilization of his-tagged proteins. *Analytical biochemistry*, 371(2):250–252, 2007.

[93] Mesh Element Quality, COMSOL Multiphysics® v. 5.6 Documentation. URL `https://doc.comsol.com/5.6/docserver/#!/com.comsol.help.comsol/comsol_ref_mesh.20.19.html`. COMSOL AB, Stockholm, Sweden.

[94] Craig M McKittrick, Sean McKee, Simon Kennedy, Keith Oldroyd, Marcus Wheel, Giuseppe Pontrelli, Simon Dixon, Sean McGinty, and Christopher McCormick. Combining mathematical modelling with in vitro experiments to predict in vivo drug-eluting stent performance. *Journal of Controlled Release*, 303:151–161, 2019.

[95] Karthic Anbalakan, Han Wei Toh, Hui Ying Ang, Martin Lindsay Buist, and Hwa Liang Leo. How does the nature of an excipient and an atheroma influence drug-coated balloon therapy? *Cardiovascular Engineering and Technology*, 13(6):915–929, 2022.

[96] Sean McGinty. *Stents and arterial flows*. PhD thesis, University of Strathclyde, 2010.

[97] Bogdan Ciszek, Krzysztof Cieślicki, Paweł Krajewski, and Stefan K Piechnik. Critical pressure for arterial wall rupture in major human cerebral arteries. *Stroke*, 44(11):3226–3228, 2013.

[98] IM Tiessen and MR Roach. Factors in the initiation and propagation of aortic dissections in human autopsy aortas. 1993.

[99] Jareer Heider Abu-Hmeidan, Arief Ismael Arrowaili, Raid Said Yousef, Sami Alasmari, Yasser M Kassim, Hamad Hamad Aldakhil Allah, Abdullah Mohammed Aljenaidel, Abdullah Abdulmohsen Alabdulqader, Muath Hamad Alrashed, Mulfi Ibrahim Alkhinjar, et al. Coronary artery rupture in blunt thoracic trauma: a case report and review of literature. *Journal of Cardiothoracic Surgery*, 11(1):1–6, 2016.

[100] Shona Rae, Jake Miller, Hannah Kerr, and Alasdair Hambrey. *Characterising drug release and tissue uptake kinetics from drug-coated balloons: towards more effective revascularisation treatments*. Unpublished MEng project dissertation, University of Strathclyde, 2023.

[101] Arkema. Technical data sheet, PEBAX© 7233 SA 01 MED. URL `https://mypolymer.materialdatacenter.com/pds/en/si/pebax7233sa01med`. Accessed: March, 2024.

[102] U. S. Food and Drug Administration. Inactive ingredient search for approved drug products (open access database), "Polyethylene oxide". URL `https://www.accessdata.fda.gov/scripts/cder/iig/index.cfm`. Accessed: March, 2024.

[103] Jordan A Anderson, Sujan Lamichhane, Tyler Remund, Patrick Kelly, and Gopinath Mani. Preparation, characterization, in vitro drug release, and cellular interactions of tailored paclitaxel releasing polyethylene oxide films for drug-coated balloons. *Acta biomaterialia*, 29:333–351, 2016.

[104] Kai Xu, GuoSheng Fu, Qian Tong, Bin Liu, XueBin Han, Jun Zhang, GenShan Ma, Qing Yang, Hui Li, Yujie Zhou, et al. Biolimus-coated balloon in small-vessel coronary artery disease: the bio-rise china study. *Cardiovascular Interventions*, 15(12):1219–1226, 2022.

[105] Juan F Granada, Renu Virmani, Daniel Schulz-Jander, Stefan Tunev, and Robert J Melder. Rate of drug coating dissolution determines in-tissue drug retention and durability of biological efficacy. *Journal of drug delivery*, 2019, 2019.

[106] Markus A Geith, Krzysztof Swidergal, Bernd Hochholdinger, Thomas G Schratzenstaller, Marcus Wagner, and Gerhard A Holzapfel. On the importance of modeling balloon folding, pleating, and stent crimping: An fe study comparing experimental inflation tests. *International journal for numerical methods in biomedical engineering*, 35(11):e3249, 2019.

[107] DK Liang, DZ Yang, M Qi, and WQ Wang. Finite element analysis of the implantation of a balloon-expandable stent in a stenosed artery. *International journal of cardiology*, 104(3):314–318, 2005.

[108] Francesca Gervaso, Claudio Capelli, Lorenza Petrini, Simone Lattanzio, Luca Di Virgilio, and Francesco Migliavacca. On the effects of different strategies in modelling balloon-expandable stenting by means of finite element method. *Journal of Biomechanics*, 41(6): 1206–1212, 2008.

[109] Houman Zahedmanesh, Daniel John Kelly, and Caitriona Lally. Simulation of a balloon expandable stent in a realistic coronary artery—determination of the optimum modelling strategy. *Journal of Biomechanics*, 43(11):2126–2132, 2010.

[110] Jakub Bukala, Piotr Kwiatkowski, and Jerzy Malachowski. Numerical analysis of crimping and inflation process of balloon-expandable coronary stent using implicit solution. *International journal for numerical methods in biomedical engineering*, 33(12):e2890, 2017.

[111] Alan N Gent. A new constitutive relation for rubber. *Rubber chemistry and technology*, 69(1):59–61, 1996.

[112] Cornelius O Horgan. The remarkable gent constitutive model for hyperelastic materials. *International Journal of Non-Linear Mechanics*, 68:9–16, 2015.

[113] Víctor Jesús Amores, José María Benítez, and Francisco Javier Montáns. Average-chain behavior of isotropic incompressible polymers obtained from macroscopic experimental data. a simple structure-based wypiwyg model in julia language. *Advances in Engineering Software*, 130:41–57, 2019.

[114] Sai Kumar Siliveri, Ashok Orepalli, and Nelson Muthu. Hyperelastic analysis of adventitial layer using isotropic gent model. In *North-East Research Conclave*, pages 405–417. Springer, 2022.

[115] Gerhard A Holzapfel. Similarities between soft biological tissues and rubberlike materials. In *Constitutive models for rubber IV*, pages 607–617. Routledge, 2017.

[116] pyMechT. URL `https://pymecht.readthedocs.io/en/latest/`. A Python package for mechanics of soft tissues.

[117] Zhaowei Liu, Andrew McBride, Abhishek Ghosh, Luca Heltai, Weicheng Huang, Tiantang Yu, Paul Steinmann, and Prashant Saxena. Computational instability analysis of inflated hyperelastic thin shells using subdivision surfaces. *Computational Mechanics*, 73(2):257–276, 2024.

[118] Morris G Rogers. Some studies on the swelling behavior of polyethylene. *Journal of Applied Polymer Science*, 14(7):1679–1689, 1970.

[119] L Mihaela Paun, André Fensterseifer Schmidt, Sean McGinty, and Dirk Husmeier. Statistical inference for optimisation of drug delivery from stents. 2022.

[120] Robert J. Cipolle, Linda M. Strand, and Peter C. Morley. *Chapter 8. Follow-Up Evaluation*. The McGraw-Hill Companies, New York, NY, 2012. URL `accesspharmacy.mhmedical.com/content.aspx?aid=56173564`.

[121] T Christian Gasser, Ray W Ogden, and Gerhard A Holzapfel. Hyperelastic modelling of arterial layers with distributed collagen fibre orientations. *Journal of the royal society interface*, 3(6):15–35, 2006.

[122] Thomas E Carew, Ramesh N Vaishnav, and Dali J Patel. Compressibility of the arterial wall. *Circulation research*, 23(1):61–68, 1968.

[123] Gerhard A Holzapfel, Michael Stadler, and Thomas C Gasser. Changes in the mechanical environment of stenotic arteries during interaction with stents: computational assessment of parametric stent designs. *J. Biomech. Eng.*, 127(1):166–180, 2005.

[124] Anthony James Merrill Spencer. Constitutive theory for strongly anisotropic solids. In *Continuum theory of the mechanics of fibre-reinforced composites*, pages 1–32. Springer, 1984.

[125] CO Horgan and JG Murphy. Some unexpected behaviour in shear for elasticity models of arterial tissue that only use the i 1, i 4, i 6 invariants. *IMA Journal of Applied Mathematics*, 79(5):820–829, 2014.

[126] Gerhard A Holzapfel, Gerhard Sommer, Christian T Gasser, and Peter Regitnig. Determination of layer-specific mechanical properties of human coronary arteries with nonatherosclerotic intimal thickening and related constitutive modeling. *American Journal of Physiology-Heart and Circulatory Physiology*, 289(5):H2048–H2058, 2005.

[127] Peter Wriggers and Tod A Laursen. *Computational contact mechanics*, volume 2. Springer, 2006.

[128] Rosaire Mongrain, Richard Leask, Jean Brunette, Iam Faik, Neil Bulman-Feleming, and T Nguyen. Numerical modeling of coronary drug eluting stents. *Studies in health technology and informatics*, 113:443–458, 2005.

[129] Bettina Kelsch, Bruno Scheller, Melanie Biedermann, Yvonne P Clever, Silvio Schaffner, Dirk Mahnkopf, Ulrich Speck, and Bodo Cremers. Dose response to paclitaxel-coated balloon catheters in the porcine coronary overstretch and stent implantation model. *Investigative radiology*, 46(4):255–263, 2011.

[130] Gordon Minru Xiong, Huiying Ang, Jinjie Lin, Yuan Siang Lui, Jie Liang Phua, Jing Ni Chan, Subbu Venkatraman, Nicolas Foin, and Yingying Huang. Materials technology in drug eluting balloons: Current and future perspectives. *Journal of Controlled Release*, 239:92–106, 2016.

[131] Peter V Danckwerts. Continuous flow systems. distribution of residence times. *Chemical engineering science*, 50(24):3857–3866, 1995.

[132] Setting Up a Contact Problem, COMSOL Multiphysics® v. 5.6 Documentation. URL `https://doc.comsol.com/5.6/docserver/#!/com.comsol.help.sme/sme_ug_modeling.05.103.html`. COMSOL AB, Stockholm, Sweden.

[133] Mircea Teodorescu, Moshe Brand, Jacob Rosen, and Homer Rahnejat. The influence of post angioplasty stent implant profile on arterial wall stress. In *International Design*

Engineering Technical Conferences and Computers and Information in Engineering Conference, volume 44120, pages 413–420, 2010.

[134] Franz Bozsak, David Gonzalez-Rodriguez, Zachary Sternberger, Paul Belitz, Thomas Bewley, Jean-Marc Chomaz, and Abdul I Barakat. Optimization of drug delivery by drug-eluting stents. *PloS one*, 10(6):e0130182, 2015.

[135] C Lally, Fl Dolan, and PJ Prendergast. Cardiovascular stent design and vessel stresses: a finite element analysis. *Journal of biomechanics*, 38(8):1574–1581, 2005.

[136] Gerhard A Holzapfel, Michael Stadler, and Christian AJ Schulze-Bauer. A layer-specific three-dimensional model for the simulation of balloon angioplasty using magnetic resonance imaging and mechanical testing. *Annals of Biomedical Engineering*, 30:753–767, 2002.

[137] Continuity on Interior Boundaries, COMSOL Multiphysics® v. 5.6 Documentation. URL `https://doc.comsol.com/5.6/docserver/#!/com.comsol.help.comsol/comsol_ref_modeling.15.61.html?highlight=continuity+pair`. COMSOL AB, Stockholm, Sweden.

[138] Philips Healthcare. URL `https://www.philips.sa/en/healthcare/education-resources/technologies/igt/vh-ivus`. Accessed: March 2024.